Development and Non-invasive
Quality Assessment
of Advanced Therapy Medicinal Products

Dissertation

der Mathematisch-Naturwissenschaftlichen Fakultät

der Eberhard Karls Universität Tübingen

zur Erlangung des Grades eines

Doktors der Naturwissenschaften

(Dr. rer. nat.)

vorgelegt von

M. Sc. Ruben Daum

aus Stuttgart-Bad Cannstatt

Tübingen

2020

Gedruckt mit Genehmigung der Mathematisch-Naturwissenschaftlichen Fakultät der Eberhard Karls Universität Tübingen.

Tag der mündlichen Qualifikation:	12.03.2021
Stellvertretender Dekan:	Prof. Dr. József Fortágh
1. Berichterstatter:	Prof. Dr. Katja Schenke-Layland
2. Berichterstatter:	Prof. Dr. Ralf Kemkemer

Wir erkennen die Wahrheit nicht nur mit dem Verstand, sondern auch mit dem Herzen.

Blaise Pascal

Table of Contents

Abstract

In recent years, a new complex group of medicinal products known as Advanced Therapy Medicinal Products (ATMPs), has attracted increasing attention. Based on genes, cells or tissues, these products offer new treatment options for serious diseases such as hereditary diseases and blood cancers and they can also serve as a tissue replacement. However, due to the high complexity of these products, which affects their development, production, approval and quality control, their translation into clinical practice remains a challenge. This thesis presents solutions for addressing these hurdles. An important element in ensuring the safety and functionality of ATMPs is the non-destructive and non-invasive monitoring of their quality. As part of this thesis, a possibility for a non-invasive quality control of stem cells based on DNA methylation was developed. I successfully demonstrated that Raman microspectroscopy in combination with multivariate data analysis is capable of distinguishing between lower and higher global DNA methylation states indicating the pluripotency of stem cells. In the second part of this thesis, I fabricated an electrospun vascular graft with mechanical properties comparable to those of a native blood vessel. The surface of the graft was biofunctionalized with two different extracellular matrix proteins, decorin and fibronectin, of which the latter promoted the adherence and proliferation of primarily isolated vascular endothelial cells and endothelial progenitor cells in vitro. Due to the characteristics of the graft, it can be considered for future use in in-situ tissue engineering. In this case, a cell-free construct can be implanted, reducing biological complexity and simplifying production and storage, thus saving costs. Finally, I focused on investigating fibronectin adsorption on polyurethane surfaces with different chemical and topographic properties. I successfully demonstrated that surface roughness and chemistry influence the orientation and conformation of the adsorbed protein and thus its bioactivity. Using two different endothelial cell phenotypes, I was able to show that the adsorbed fibronectin on the different surfaces alters the cell response in terms of cell-cell and cell-material interaction. These findings can help to design surfaces that direct cell response by modulating protein adsorption, thereby improving the biocompatibility of biomaterials for the fabrication of ATMPs.

Zusammenfassung

In den letzten Jahren hat eine neue komplexe Gruppe von Arzneimitteln an zunehmender Aufmerksamkeit gewonnen, die als Arzneimittel für neuartige Therapien (Advanced Therapy Medicinal Products, ATMPs) bezeichnet wird. Basierend auf Genen, Zellen oder Geweben bieten diese Produkte neue Behandlungsmöglichkeiten für schwerwiegende Krankheiten wie Erbkrankheiten und Blutkrebs oder dienen auch als Gewebeersatz. Durch die hohe Komplexität der Produkte, was sich auf die Entwicklung, Herstellung, Zulassung und Qualitätskontrolle auswirkt, ist die Übertragung in die klinische Praxis jedoch eine Herausforderung. Diese Arbeit zeigt Lösungen auf, wie diesen Hürden begegnet werden kann. Ein wichtiges Element zur Gewährleistung der Sicherheit und Funktionalität von ATMPs ist die zerstörungsfreie und nicht-invasive Überwachung der Qualität. In einem Teil dieser Arbeit wird eine Möglichkeit für eine nicht-invasive Qualitätskontrolle von Stammzellen auf der Basis von DNA-Methylierung vorgestellt. Ich konnte erfolgreich nachweisen, dass die Raman-Mikrospektroskopie in Kombination mit multivariater Datenanalyse die Unterscheidung zwischen niedrigeren und höheren globale DNA-Methylierungszuständen ermöglicht, was auf die Pluripotenz der Zellen hinweist. Im zweiten Teil dieser Arbeit habe ich ein elektrogesponnenes Gefäßtransplantat hergestellt, dessen mechanische Eigenschaften mit denen eines nativen Blutgefäßes vergleichbar sind. Die Oberfläche des Transplantats wurde mit zwei verschiedenen Proteinen aus der extrazellulären Matrix biofunktionalisiert, Decorin und Fibronektin, wobei letzteres insbesondere die Adhärenz und Proliferation primär isolierter vaskulärer Endothelzellen und endothelialer Vorläuferzellen in vitro förderte. Aufgrund der Eigenschaften des Transplantats kann dieses zukünftig für die Verwendung im in-situ Tissue Engineering in Betracht gezogen werden. In diesem Fall kann ein zellfreies Konstrukt implantiert werden, welches die biologische Komplexität reduziert sowie die Herstellung und Lagerung vereinfacht. Durch die Einsparung dieser Kosten kann ein massiver wirtschaftlicher Vorteil gezogen werden. Ein weiterer Fokus dieser Arbeit lag in der Untersuchung der Adsorption von Fibronektin auf Polyurethan-Oberflächen, die unterschiedliche chemische und topographische Eigenschaften besitzen. Ich konnte erfolgreich zeigen, dass die Oberflächenrauheit und -chemie die Orientierung und

Konformation des adsorbierten Proteins und damit seine Bioaktivität beeinflusst. Anhand von zwei verschiedenen Endothelzell-Phänotypen konnte ich nachweisen, dass durch das adsorbierte Fibronektin auf den verschiedenen Oberflächen die Zellantwort in Bezug auf die Zell-Zell- und Zell-Material-Interaktion verändert wird. Diese Erkenntnisse können dazu beitragen, Oberflächen zu entwerfen, welche die Zellantwort durch Modulation der Proteinadsorption steuern und dadurch die Biokompatibilität von Biomaterialien für die Herstellung von ATMPs verbessern.

Abbreviations

ATMP	advanced therapy medicinal product
CCD	charge-coupled device
CVD	cardiovascular disease
CpG	5'-C-phosphate-G-3'dinucleotides
DCN	decorin
DAPI	4',6-diamidino-2-phenylindole
DNA	deoxyribonucleic acid
DNMT	DNA methyltransferase
ECFC	endothelial colony forming cell
ECM	extracellular matrix
ELISA	enzyme-linked immunosorbent assay
EPC	endothelial progenitor cell
FA	focal adhesion
FAK	focal adhesion kinase
FN	fibronectin
HMVECs	human microvascular endothelial cells
HUVEC	human umbilical vein endothelial cell
IF	immunofluorescence
mESC	murine embryonic stem cells
PC	principal components
PCA	principal component analysis
SEM	scanning electron microscopy
SMC	smooth muscle cell
TEP	tissue-engineered product
TEVG	tissue-engineered vascular graft
TPCU	thermoplastic polycarbonate urethane
vEC	vascular endothelial cell
vWF	Von Willebrand factor
WT	wildtype

List of Figures

List of Publications

Published Manuscripts

1. Brauchle E., Kasper J., **Daum R.** et al. Biomechanical and biomolecular characterization of extracellular matrix structures in human colon carcinomas. Matrix Biology 68-69, 8 (2018)

2. Wenzel T., Berrio, D.A.C., **Daum R.** et al. Molecular Effects and Tissue Penetration Depth of Physical Plasma in Human Mucosa Analyzed by Contact- and Marker-Independent Raman Microspectroscopy. ACS Appl. Mater. Interfaces 11, 46 (2019)

3. **Daum, R.**, Brauchle, E., Berrio, D.A.C. et al. Non-invasive detection of DNA methylation states in carcinoma and pluripotent stem cells using Raman microspectroscopy and imaging. Scientific Reports 9, 1 (2019)

4. **Daum, R.**, Visser, D., Wild, C. et al. Fibronectin Adsorption on Electrospun Synthetic Vascular Grafts Attracts Endothelial Progenitor Cells and Promotes Endothelialization in Dynamic In Vitro Culture. Cells 9, 3 (2020)

5. Ciarfaglia, N., Pepe, A., Piccirillo, G., Laezza, A., **Daum, R.** et al. Nanocellulose and Elastin Act as Plasticizers of Electrospun Bioinspired Scaffolds. ACS Appl. Polym. Mater. 2, 11 (2020)

6. Feuerer, N., Morschl, J., **Daum, R.** et al. Macrophage retrieval from 3D biomaterials: a detailed comparison of common dissociation methods. J. Immunol. Regen. Med. 11 (2021)

7. **Daum, R.**, Mrsic, I., Hutterer J. et al. Fibronectin adsorption on oxygen plasma-treated polyurethane surfaces modulates endothelial cell response. J. Mater. Chem B 9, 6 (2021)

Contributions

No.	Accepted for publiccation	Number of authors	Position of the candidate in the list of authors	Scientific ideas by candidate (%)	Data generation by candidate (%)	Interpretation and analysis by candidate (%)	Paper writing by candidate (%)
1	yes	8	3	10	30	20	5
2	yes	10	3	20	0	20	5
3	yes	5	1	60	85	80	70
4	yes	11	1	40	60	60	65
5	yes	7	5	10	15	10	10
6	yes	7	3	0	5	5	5
7	yes	9	1	40	50	40	60

Chapter 1

Introduction

1. Introduction

Preface

Over the last few decades, the complexity of medicinal products has steadily increased. Until the late 1960s, most patented medications were based on chemical synthesis, but from the 1970s onwards, a new class of pharmaceuticals appeared: the biopharmaceuticals [1]. These protein-based drugs, produced from microbial cells or mammalian cell lines, were already far more complex in their composition and production compared to previous chemical medicaments. In recent years, a new, even more complex group of pharmaceuticals has been emerging, based on genes, cells or tissues. In 2007, the European Medicines Agency designated them for the first time as Advanced Therapy Medicinal Products (ATMPs) [2]. This new class of therapies offers new possibilities for the treatment of diseases and injuries, including hereditary diseases, blood cancers or the replacement, repair or regeneration of tissue [3,4]. The latter, referred to as tissue-engineered products (TEPs), are attracting increasing attention in the treatment of vascular diseases (CVDs) [5]. One example in the field of vascular and cardiac surgery are tissue-engineered vascular grafts (TEVGs), for which several clinical studies have been successfully conducted in recent years [6–8]. However, TEVGs are not widely clinically used at this time [7]. The translation of these medicinal products into clinical practice remains a challenge due to their high complexity, which affects their development, manufacturing, approval and quality control. Some of these hurdles can be addressed by biofunctionalizing the material surface in order to improve endothelialization.

In addition, non-destructive and non-invasive methods for monitoring the quality of ATMPs can be an important step towards the industrialisation of these products. Moreover, quality criteria must be identified and defined. An interesting and promising quality criterion in the case of stem cell-based medicinal products could be epigenetic hallmarks such as DNA methylation.

1.1 DNA Methylation in Early Development, Disease and Aging

Cell identity and function is partly maintained by epigenetic mechanisms. The term epigenetic, which was first mentioned in the early 1940s, describes changes in

gene function that are mitotically and meiotically heritable but do not entail a change in the deoxyribonucleic acid (DNA) sequence [9,10]. This is achieved by semi-reversible covalent chemical modifications on nucleic acids and proteins with which the DNA is associated in the cell's nucleus. A major epigenetic mechanism that plays a critical role in the regulation of gene expression is DNA methylation. About 80 % of DNA methylations are found on the cytosine of 5'-C-phosphate-G-3'dinucleotides (CpG) [11]. By covalently binding a methyl group to the 5'-carbon of cytosine mainly to CpG dinucleotide sequences catalyzed by DNA methyltransferases (DNMTs), DNA methylation influences chromatin structure and, in promoter regions, the binding of transcription factors resulting in the silencing of genes [12,13]. This relatively stable epigenetic marker is inheritable by cell division, and therefore an important component of the cellular memory mechanisms that maintain cell identity [14].

Early embryogenesis is characterized by dramatic DNA methylation changes (Fig. 1). During early embryonic development, DNA methylation is reprogrammed into a totipotent state for the production of the next generation. This is achieved by removing the sex-specific germ cell methylation patterns in preimplantation embryos, with the maternal genome mainly undergoing passive demethylation and the paternal genome undergoing active demethylation [14]. Upon implantation, de novo methylation establishes the embryonic methylation pattern within a few days [14,15]. From the blastocyst stage onwards, global DNA methylation levels remain constant [16–18]. During embryogenesis, a genome-wide redistribution of DNA methylation occurs. For example, the pluripotency markers Nanog and Oct4 are initially unmethylated and undergo methylation during differentiation [19].

Throughout life, environmental and lifestyle factors such as diet, smoking, physical activity, psychological stress and air pollution influence DNA methylation [20]. Some of these DNA methylation modifications are associated with several diseases. Aberrant DNA methylation of promoter regions and global DNA methylation changes leads to altered gene expression as well as genomic instability [21]. In most cancers, a site-specific DNA hypermethylation and a global DNA hypomethylation takes place [22–24]. When promotors of tumor suppressor genes get hypermethylated, the genes are then switched off [25,26]. Global hypomethylation in turn leads to the activation of transposable elements and oncogenes [25]. It is still

not clear to what extent these epigenetic changes influence the tumour initiation, but it is very likely that they are involved carcinogenesis [27,28].
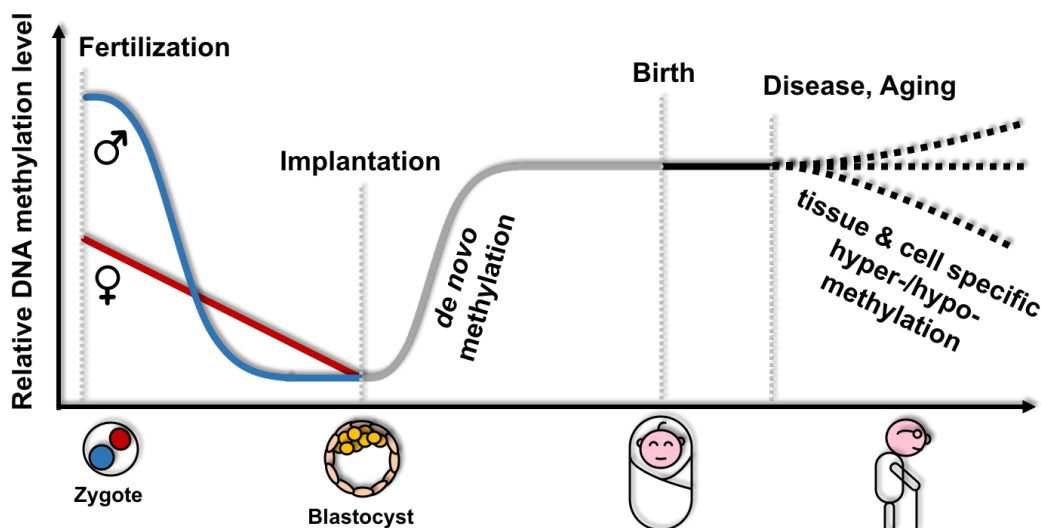
Figure 1. Dynamic changes in DNA methylation during early embryogenesis, disease and aging. Schematically shown is the global DNA demethylation and remethylation throughout life. After fertilization, the paternal genome undergoes active demethylation and the maternal genome undergoes passive demethylation. Upon implantation, de novo methylation establishes the embryonic methylation pattern. During differentiation, global DNA methylation levels do not dramatically change any more. Diseases such as cancer and atherosclerosis or ageing processes are mostly associated with cell & tissue specific global DNA hyper- or hypomethylation. Modified from Zeng et al. [14].

Aberrant DNA methylation is also known to be involved in neurological diseases, immunological diseases and age-related diseases such as osteoporosis and atherosclerosis [29]. For example, it has been reported that the DNA in atherosclerotic aortas from rabbits was hypomethylated compared to normal arteries [30,31].

Aging is accompanied by global DNA hypomethylation. However, most of these global DNA methylation changes are tissue- or cell-specific [32]. Interestingly, age-related changes in DNA methylation that occur at specific CpG sites in the genome have been shown to be quantitative biomarkers of chronological age, leading to the theory of the "epigenetic clock" [33]. This clock may be useful in predicting accelerated biological aging in humans [34]. However, it is not yet clear to what extent

DNA methylation is responsible for the development of age-related diseases. Therefore, further epigenome-wide association studies are needed to help identify methylation quantitative trait loci to determine any associations between DNA methylation and age-relating diseases such as cardiovascular disease [35].

1.2 Raman Microspectroscopy and Imaging

Existing methods to study DNA methylation in cells requires sample digestion that excludes the investigation of living matter. Raman spectroscopy can overcome this issue as it is a non-invasive and non-contact method based on the analysis of inelastic scattered light [36]. When a material is illuminated with light, most photons are scattered back at the same energy as the incident light, which is known as elastic or Rayleigh scattering. However, 1 out of $10^6 - 10^8$ photons is scattered with a shift from its original energy [37], described as inelastic or Raman scattering. Raman scattering can lead to emitted photons with either higher or lower energy levels than the incident photons. In Stokes scattering, the incident photon is absorbed by the molecule in its ground state resulting in an excited vibrational state. When the molecule returns to its ground state, photons with a lower energy level are emitted which leads to a reduction in the frequency of the scattered light. In Anti-Stokes scattering, the photon is absorbed by a molecule that is already in an excited vibrational state. When the molecule returns to its ground state, it releases the energy of the excited molecular mode, resulting in an increased frequency of the scattered light (Fig. 2) [38]. As these vibrational frequency shifts are specific for the chemical bonds and symmetry of a molecule, Raman spectroscopy provides specific fingerprint spectra [39].
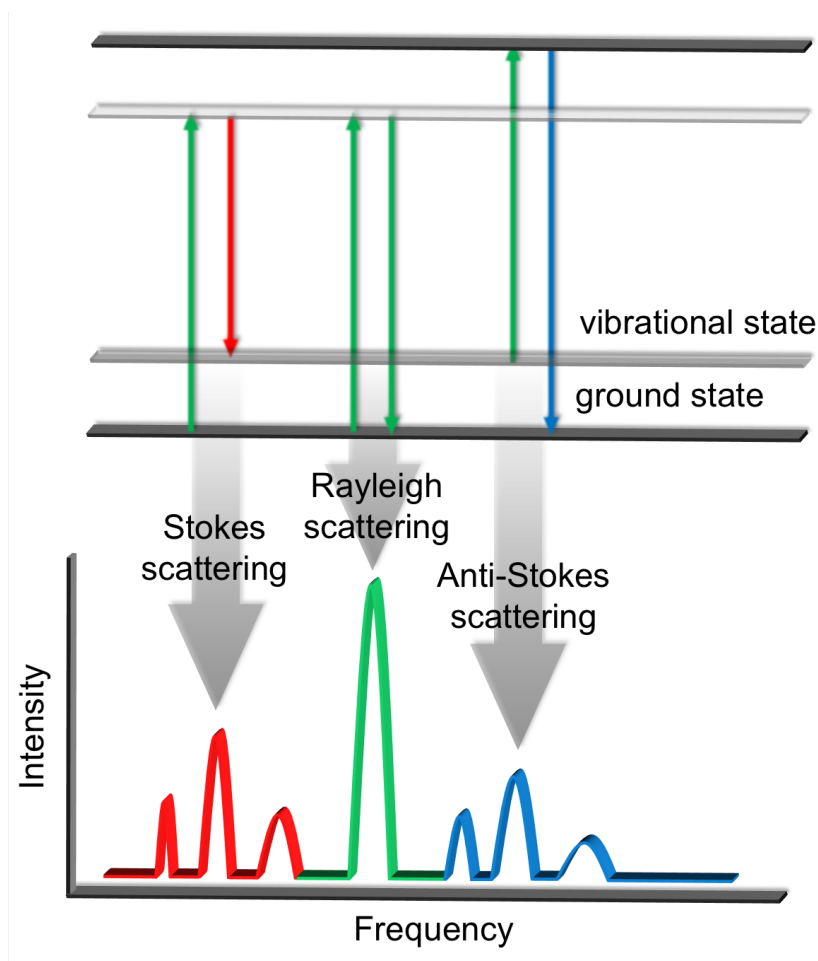
Figure 2. Molecular energy levels according to the type of light scattering. The elastic Rayleigh scattering and the inelastic Raman scattering subdivided into Stokes scattering and Anti-Stokes scattering. Adapted from Boyaci et al. [40].

The Raman measurement of biological samples provides signals from proteins, lipids, nucleic acids, carbohydrates and inorganic crystals that enables cells and tissues to be identified and distinguished based on their individual biochemical signature [36]. For this reason, Raman spectroscopy has become a popular tool in the field of biomedical research [41,42]. The analysis of biological processes within living cells, such as cell cycle dynamics, cell differentiation and cell death, has already been demonstrated with this marker-free technique [43]. It has also been shown to be useful in tissue diagnostics for the detection of carcinomas [44], the analysis of genetic disorders affecting connective tissue [45], and in degenerative disease imaging [46].

In a Raman microspectroscopy setup, the Raman system is coupled with an optical microscope, which allows a spatially-resolved analysis of the sample (Fig. 3) [43,47]. The sample is first focused and then excited with a laser through the microscopic

objective. Elastic scattered light is filtered out by a notch filter and the frequency shifted Raman scattered light is directed to a charge-coupled device (CCD) detector and converted into a Raman spectrum. While classical Raman microspectroscopy detects only individual points within the sample, Raman imaging is based on scanning an entire surface. Scanning an area with a defined pixel resolution allows the generation of a spectral map in which each pixel is defined by a separate spectrum.
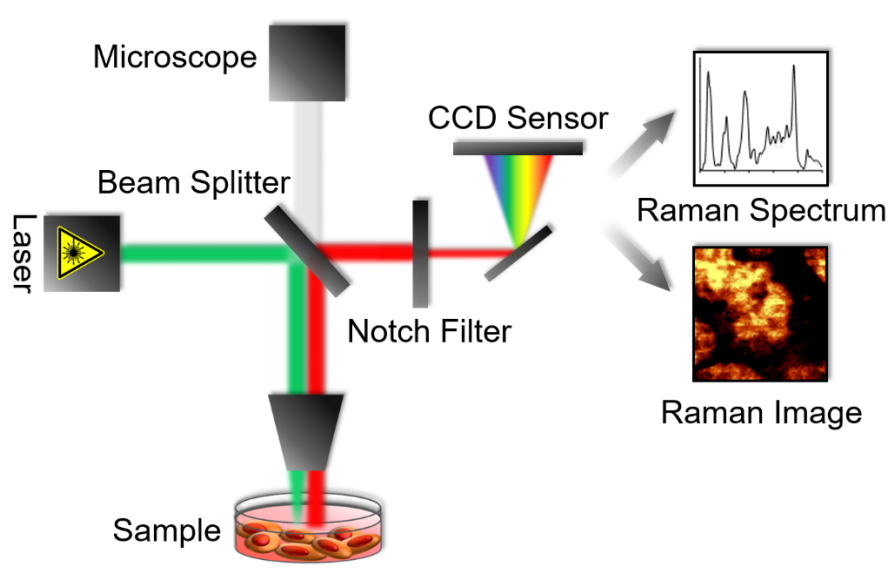
Figure 3. Schematic representation of a Raman microspectroscopy measurement. The sample is excited by a laser (green light path). Emitted photons of lower frequency (red light path) are separated from Rayleigh or higher frequency scattering by a notch filter and detected by the CCD sensor. The microscope is used to target the region of interest for Raman acquisition (grey light path). Adapted from Marzi et al. [48]

The evaluation of the spectral data is usually performed with multivariate statistical analysis tools such as principal component analysis (PCA). PCA reduces the dimensionality of the data set, which consists of many coherent variables, while preserving as much variation present within the data set as possible [49]. By resolving variance within the spectral data set, complex spectral peak shifts and peak correlations are revealed and can be graphically displayed [16,50]. This is achieved by projecting the original variables on a smaller set of variables, the principal components (PC) [49]. The PCs comprise a certain amount of the variance from the population. They are ordered so that the first PC explains most of the

variation present in all of the original variables. The subsequent PCs, which are orthogonal to the previous ones, represent lower variances in descending order, respectively. PCA takes into account that variables with large differences are attributed to a large amount of information, whereas variables, which exhibit little variation are expected to have no important amount of information. The output of the PCA can be described with the following equation (Equation 1). The original data matrix X forms the score matrix (T) assigning each data point to a new value based on its relative distance from the calculated PC. The loading vector P^T describes the influence of the original value on the modelling of the PC. Scores and loadings only provide a simplified approximation. The residues matrix E is added to cancel out the mathematical equation [51].

$$X = T \cdot P^T + E \qquad \text{(Equation 1)}$$

The spectral data analyzed by PCA are visualized by score plots. Each spectrum is displayed as a score value in a two-dimensional scatter defined by two selected PCs. The score plot can be used to investigate whether there is a separation between two or more data sets. Another output of the PCA is the loading plot. It helps to further interpret the data by explaining the spectral differences indicated by the corresponding PC. Positive peaks in the loading plot refer to spectral information of data points that are predominantly found in spectra with a positive score value. Negative loading values represent the spectral information of negative score values.

1.3 Therapies for Atherosclerotic Cardiovascular Diseases

1.3.1 The Classical Therapies for Atherosclerotic Cardiovascular Diseases

CVDs are the leading cause of death worldwide [52]. The World Health Organisation estimated that about 31 % of all deaths in 2015 could be attributed to CVDs [53]. Commonly, CVDs include all medical conditions, where blood flow to organs and limbs is reduced due to plaque deposition. The underlying cause is predominantly atherosclerosis, which in turn is caused by high blood pressure, smoking, diabetes mellitus, obesity and poor nutrition [54]. Initial therapies include lifestyle changes and

medication. In more severe cases, surgical intervention is required to reopen or replace the defective vessel. Usually, the first step is percutaneous transluminal angioplasty, in which an inflated balloon attached to a catheter dilates the constricted vessel and restores blood flow [55]. This therapy is typically combined with the placement of a stent at the affected site, to ensure that the vessel remains open [56]. If the intervention does not satisfactorily and permanently relieve the ischemic symptoms, a bypass operation is performed. Today, the standard clinical approach for the replacement of blood vessels is the use of autografts and homografts, such as the saphenous vein or the mammary artery [57]. However, due to scarce availability and mechanical or size-related mismatches, alternative graft sources are needed [58]. For large and medium diameter vessels such as the aorta, the iliac or the common femoral artery, synthetic grafts made of polyethylene terephthalate (Dacron®) or expanded polytetrafluorethylene (Goretex®) are relatively successfully used [59]. However, synthetic grafts of small diameter (<6 mm) show low patency rates due to their tendency to elicit thrombosis, inflammation or the formation of intimal hyperplasia. The main causes of failure are poor compliance mismatch and delayed or incomplete re-endothelialization after transplantation [60–62]. For this reason, further approaches are necessary to address the lack of biocompatibility.

1.3.2 The Anatomy of a Blood Vessel

An understanding of the structure and functions of a native blood vessel is essential for the development of a highly biocompatible vascular graft. For this reason, its structure is briefly described below. The walls of a native blood vessels can be subdivided into three layers (Fig. 4). The innermost layer, called tunica intima, consists of a continuous endothelial cell layer, which primarily regulates hemostasis. As the initial barrier inside the vessel, the endothelium plays an important role in permeability, leucocyte trafficking and regulation of vascular tone [63]. The endothelial cells are anchored to the basement membrane, which itself consists of two structures, the basal lamina and an external, fibrillary reticular lamina of collagen III [64–66]. The basal lamina is a thin dense sheet of self-assembled laminin and type IV collagen networks linked by extracellular matrix proteins, including nidogen, collagen VII and heparan sulfate proteoglycans such as

perlecan. In addition, various combinations of other proteins, glycoproteins and proteoglycans such as decorin are present in the lamina, creating biochemically and biophysically distinct structures and tethering growth factors [66–70]. The basement membrane not only provides structural support for the endothelium, but also initiates cellular signalling pathways through cell binding, presenting a barrier to the transmigration of cells. This in turn effects angiogenesis by storing and releasing growth factors [71,72].

In arteries, an internal elastic membrane separates the intima from the middle layer, the tunica media. This layer, which is thicker in arteries than in veins, is composed of circumferentially aligned smooth muscle cells (SMCs) and elastic fibers. The tunica media predominantly contributes to the mechanical strength of the blood vessel wall and is responsible for maintaining blood pressure by regulating vasoconstriction and vasodilatation [73].

The outer layer, the tunica adventitia, consists primarily of fibroblasts and fibrillary collagens anchoring the vessel to its surroundings [74]. In addition, it contains perivascular nerves, nervi vasorum, which innervate SMCs and thereby regulate local blood pressure [75]. In large vessels, the vasa vasorum, supplies the vessel's wall with nutrients [76]. In larger arteries, an external elastic membrane separates the tunica adventitia from the tunica media.
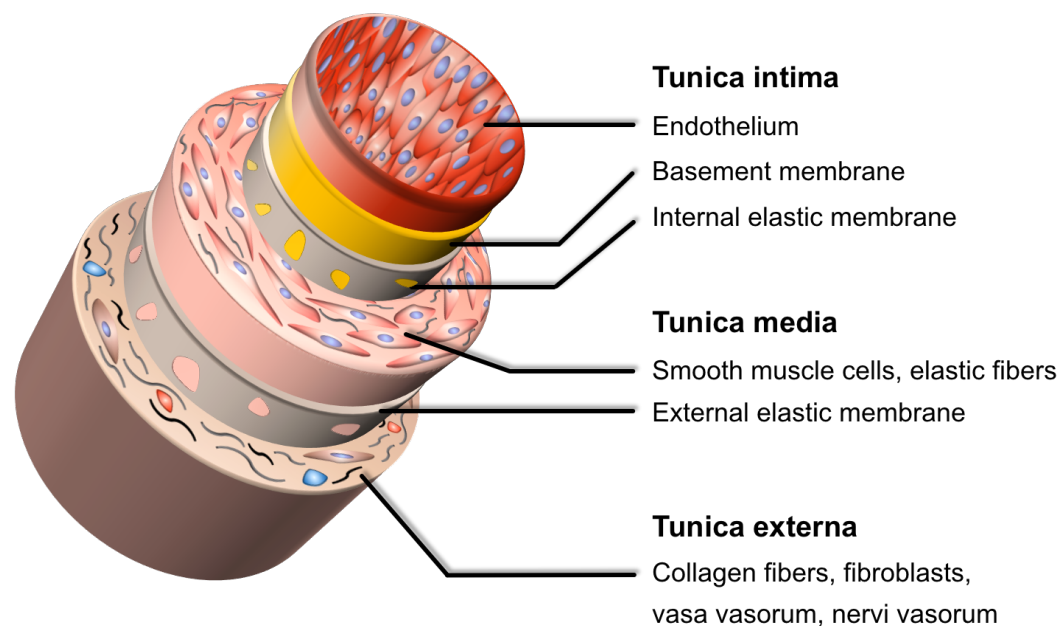

Figure 4. Three-layered structure of an artery. Shown are the three blood vessel layers, tunica intima, tunica media and tunica externa. Modified from Marieb and Hoehn [77].

1.3.3 In Vitro and In Situ Tissue-Engineered Vascular Grafts

The emerging field of tissue engineering has aimed to overcome the limitations of synthetic small diameter vascular grafts by creating highly biocompatible, autologous, living replacement structures, that reflect the functionality and structure of a native blood vessel [78]. The classical tissue engineering approach consists of designing and culturing a TEVG in vitro until it meets the biological and biomechanical requirements for implantation. To this end, four important factors must be considered: the cell source, the supporting structures, bioactive substances such as growth factors and physical and mechanical forces influencing cell differentiation and maturation.

Cell sources for in vitro vascular tissue engineering can be divided into three categories: mature somatic cells, adult multipotent progenitor cells and pluripotent stem cells [79]. The mature cells are usually primary endothelial cells and smooth muscle cells. Ideally, autologous, patient-derived cells are used, as this prevents an immune reaction or cell rejection during implantation [80]. A disadvantage of this cell source is the limited proliferation and thus expansion capacity of these terminally differentiated cells [80]. An alternative to this are adult multipotent stem cells, which have a greater proliferative potential and higher plasticity to differentiate in a particular lineage such as endothelial progenitor cells (EPCs) and mesenchymal stem cells [79,81]. A particular population of EPCs are endothelial colony forming cells (ECFCs), also known as late outgrowth endothelial cells. This cell population, which rarely circulates in peripheral blood, represents the most potent reparative cell type among all EPCs, as it has a robust clonal proliferative potential and the ability to form colonies and a capillary network in vivo [82,83]. However, the isolation and expansion of these cells from peripheral blood or bone marrow can be time consuming and expensive [84]. A further challenge of adult stem cells is the reduced proliferation and differentiation potential with increasing donor age [81]. Pluripotent stem cells circumvent this limitation through their unlimited capacity for self-renewal and their ability to differentiate into all three germ layers [79,85]. Whereas access to embryonic stem cells is again limited, induced pluripotent stem cells proved to be an attractive cell source for vascular tissue engineering [86,87].

Another important factor for in vitro vascular tissue engineering is the tubular three-dimensional scaffold that serves as a supporting structure to anchor and spatially distribute the different cell types. An essential feature of the scaffold is its porous structure, which mimics the in vivo cellular microenvironment to support cell adhesion, migration, proliferation and differentiation [80]. The most popular techniques to fabricate these structures are elelectrospinning, molding, 3D printing, cell sheet rolling and decellularization [88]. Electrospinning in particular proved to be a very promising and widespread method, which will be discussed in more detail later. Various materials have already been used for vessel engineering, including natural polymers, such as collagen or elastin, synthetic biostable and biodegradable polymers and decellularized vessels [80]. The advantages of synthetic materials to natural biomaterials are their reproducibility due to their defined chemical composition and their controllable mechanical properties. In this category, polycarbonate-based elastomeric polyurethanes proved to be very attractive materials as they offer ideal elastic properties and good biocompatibility for vascular grafts [89,90]. Synthetic polymers, however, lack the bioactivity of natural biopolymers, such as sites for cell adhesion. Possibilities to address this problem are the use of a blend of synthetic and natural polymers or the surface functionalization with cell-adhesive peptides such as the RGD or CAG sequence [91,92].

The creation and physical conditioning of TEVGs requires an environment, which simulates the physiological conditions in the human body [93]. For this purpose, vascular perfusion bioreactors are constructed, which usually consist of a pump, tubes, a medium reservoir and a flow chamber, in which the TEVG is placed (Fig. 5). Depending on the approach, the lumen and the outer surface of the TEVG are perfused separately, which enables the cultivation of different cells [94]. Perfusion of the luminal side not only provides fresh medium and nutrients and removes waste products, but it also exerts shear forces on the endothelial cells and mimics the natural blood flow. Thereby, the hemodynamic forces modulate the phenotype and gene expression of the cells. In this context, a correct flow is of great importance for the formation of a well-functioning endothelium [95].

TEGVs offer several advantages when compared to synthetic grafts as they allow growth, tissue modelling and self-repair. However, there is still limited use of

TEVGs clinically due to poor mechanical properties, the long in vitro production time and the high regulatory hurdle [7,96].
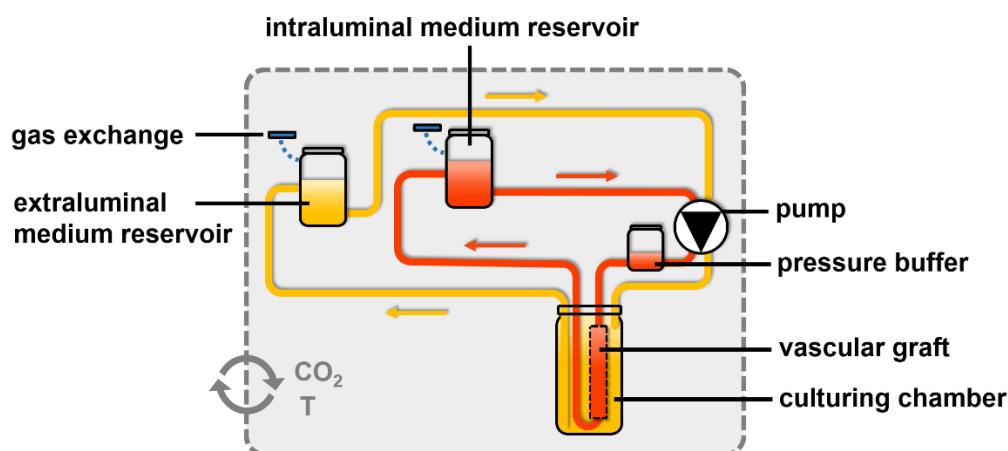
Figure 5. Schematic representation of a simplified bioreactor set-up for culturing a tissue engineering vascular graft. The vascular graft is clamped into the culturing chamber and perfused by an extraluminal and intraluminal circulation. Adapted from Daum et al. [97].

An attractive alternative is the use of an acellular synthetic graft that enables the targeted adhesion, migration and proliferation of specific cells in situ [98]. In this approach, the porous scaffold has to provide the mechanical strength comparable to that of a native blood vessel. In addition to the mechanical properties, the surface chemistry of the scaffold is crucial for the success of this strategy [96]. To achieve rapid and complete endothelialization of the lumen after implantation, the surface is biofunctionalized with bioactive substances that promote the attraction, adhesion, proliferation and differentiation of mature endothelial cells and endothelial progenitor cells. Strategies to address this issue are the immobilization of antibodies against specific endothelial cell markers and the modification with growth factors, aptamers and phospholipids [99–102]. In addition, extracellular matrix (ECM) proteins such as collagen or fibronectin, are attractive candidates, since they not only mediate cell interaction, but can also store growth factors and interact with other ECM proteins [103,104].

_____

1.3.4 Scaffolds for Tissue Engineering Produced by Electrospinning

Electrospinning is a method for the facile production of continuous, ultra-thin fibers with diameters ranging from a few nanometers to several micrometers, enabling the manufacture of non-woven, fibrous scaffolds for tissue engineering [105]. The principle of electrospinning is based on the use of a high voltage to electrify a polymer followed by the ejection of liquid jets. The basic electrospinning setup is shown below (Fig. 6).
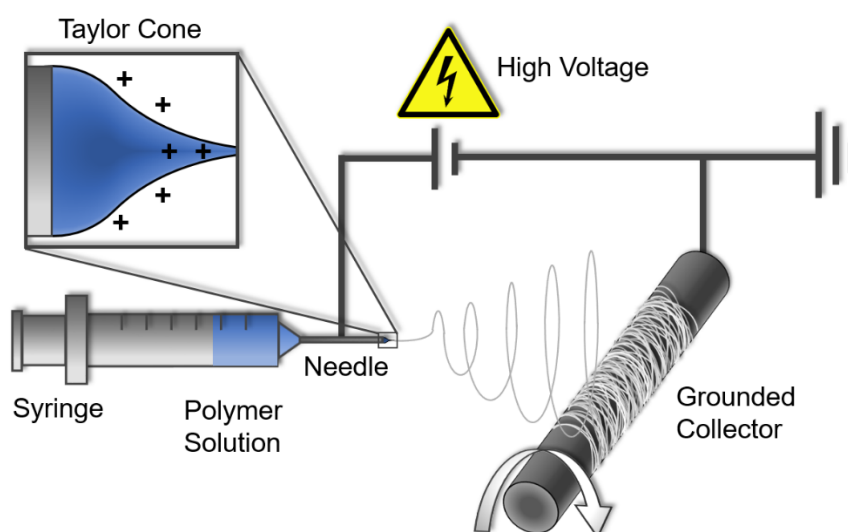
Figure 6. Electrospinning of a tubular scaffold. A polymer solution is pumped through the syringe to the needle where a droplet is formed. When an electric field is applied, the polymer droplet at the tip of the needle gets charged, a Taylor cone is formed, from which a jet is ejected. In the electric field, the jet is accelerated towards the grounded collector. The solvent evaporates and the solid fiber is deposited on the rotating, tubular collector. Modified from Gonzales et al. [106].

It requires a high-voltage power supply, a syringe pump, a syringe with a metal needle and a conductive grounded collector. During electrospinning, a polymer solution is pumped through the needle to produce a droplet as a result of surface tension on the tip. When an electric field is applied, the polymer droplet gets electrified and deforms into a Taylor cone. As soon as the electrical force exceeds the surface tension of the polymer droplet, a charged jet is ejected. The jet initially extends in a straight line and is then accelerated towards the collector undergoing whipping motions because of bending instabilities. The polymer jet is stretched,

thinned and the solvent evaporates, resulting in the deposition of solid fibers on the grounded collector [105].

The electrospinning process relies on an intricate interplay of a variety of parameters, which can be classified in solution properties, process parameters and environmental conditions (Table 1) [107]. Varying these parameters modulate both the electrospinning process as well as the morphology and size of the electrospun fibers. Consequently, it is necessary to optimize all process parameters to control an electrospinning process.

Table 1: Electrospinning parameters that affect the fiber size. Adapted from Vlachou et al. [107]

Electrospinning parameters	Effect on fiber size
Solution properties	
Polymer concentration ↑	↑
Viscosity ↑	↑
Solution conductivity ↑	↓
Process parameters	
Flow rate ↑	↑
Applied voltage ↑	↓
Needle size↑	↓
Needle tip to collector distance ↑	↓
Environmental conditions	
Relative humidity	-
Temperature ↑	↓

Electrospun scaffolds have found use in a variety of biomedical applications as they mimic the highly porous structure and physical properties of the extracellular matrix (ECM) of the native tissue. Due to their high porosity and large surface area, the fibrous scaffolds have been shown to promote cell adhesion, cell migration and cell alignment [108–111]. A variety of biostable and biodegradable polymers, including both natural polymers such as collagen or gelatine and synthetic polymers such as poly (lactic acid), polyurethane and polycaprolactone, to name only a few, have been successfully electrospun into nanofibers [105,112,113]. Depending on the collector type, the electrospun scaffold shape also can be varied. For example for cardiovascular applications, in addition to flat collectors for the production of heart patches and rotating thorns for the production of vascular grafts, the use of heart valve-shaped collectors is also described [108,114].

1.4 Biological Interactions with Cardiovascular Implants

1.4.1 Protein Adsorption on Biomaterial Surfaces

Immediately after the implantation of a cardiovascular graft, its surface comes into contact with blood, which leads to the adsorption of a whole range of blood components, particularly plasma proteins [115]. The main driving force for the protein adsorption process is an entropy gain, which results from the release of water molecules and salt ions adsorbed on the surface and from structural rearrangements inside the protein [116,117]. However, the affinity, composition and bioactivity of the adsorbed protein layer is influenced by numerous additional factors such as external parameters, surface properties and protein properties (Fig. 7). Once adsorbed, the proteins further determine the cellular and subsequent host response [118]. Understanding the underlying mechanisms of protein adsorption could enable the targeted deposition of proteins in vitro to influence subsequent biological processes such as cell interaction and immune response in vivo.

External parameters
temperature, pH,
ionic strength

Protein properties
size, structural stability,
composition

Surface properties
surface energy, polarity,
charge, morphology

Diffusion   **Initial Contact**   **Spreading**
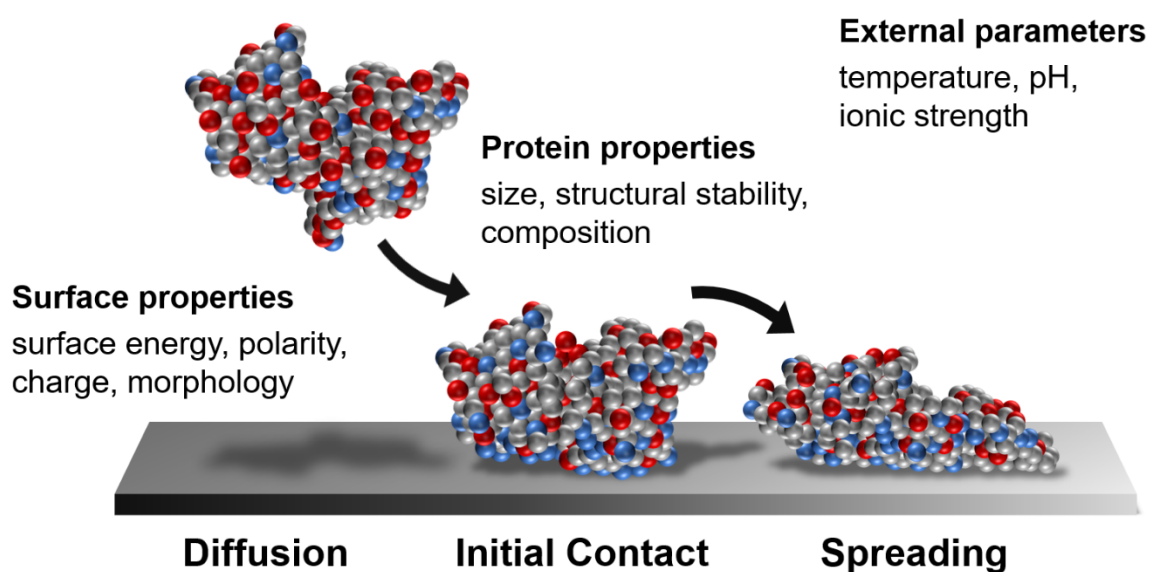
Figure 7. Protein adsorption process on a solid surface. Through diffusion, the protein initially comes into contact with the surface, followed by the spreading of the protein. These steps are influenced by external parameters, protein properties and surface properties. Modified from Andrew White [119].

External parameters influencing protein adsorption are temperature, pH, ionic strength and buffer composition. Higher temperature and a pH value equal to the isoelectric point of the protein generally increases the amount of adsorbed protein on the surface [120,121]. The ionic strength can influence the protein adsorption in such a way that a high ionic strength reduces the adsorption of proteins to oppositely charged substrates, while the adsorption to equally charged substrates is increased [122].

Each protein has a unique molecular signature consisting of long, individual polypeptide chains that fold into unique 3D structures, which usually undergo additional post-translational modification [123]. For this reason, the adsorption behaviour of each protein must be examined individually. A simplified classification regarding its interfacial behaviour can be achieved by considering the size, structural stability and composition of the protein [124]. These properties affect the orientation and conformation of the protein during adsorption, which ultimately determines its bioactivity (Fig. 7). Small, rigid proteins are generally considered as "hard" and have a low tendency for structural changes upon surface contact [125]. Intermediate size proteins such as the majority of the abundant plasma proteins like Albumin and high molecular weight proteins like fibronectin are usually able to undergo conformational reorientations when adsorbed on the surface [124]. While for smaller proteins the properties of the outer protein domains determine the initial adsorption, for larger lipoproteins or glycoproteins it is dominated by the lipid layer and glycans [123,126]. When a material comes into contact with a complex protein mixture such as blood, the composition of the adsorbed proteins can change over time, which is described by the Vroman effect [127]. Smaller, highly mobile proteins like albumin are the dominating species in the early adsorption stage. Larger proteins such as fibronectin are less mobile, but bind more strongly to the surface due to a larger contact area. Over time, these high-affinity proteins replace the pre-adsorbed lower-affinity proteins [124]. The competitive protein adsorption is a key determinant of the subsequent cell response to the surface [128].

In this context, the ultimate composition of the adsorbed proteins is closely related to the chemical and physical properties of the surface [129]. In particular, surface energy, polarity, charge and roughness have been characterized as key determinants [130]. Regarding the wettability, which mainly depends on the surface energy, it is reported that hydrophobic surfaces generally adsorb more protein than

hydrophilic surfaces, which can be explained by an entropy gain of the system [131,132]. However, this is not a universal result, as it also depends on the protein's properties. In comparison to hydrophilic surfaces, adsorption on hydrophobic surfaces is usually accompanied by strong conformational changes of the protein, which to a certain extent can lead to an activation of the protein, as in the case of fibronectin. In most cases, however, it rather leads to an impairment of its functionality [128]. While on hydrophobic surfaces mainly conformational changes are the driving force for protein adsorption, on hydrophilic surfaces it is mainly driven electrostatically by global charges on proteins and surfaces [128,133]. Thereby, it was shown that both positively and negatively charged surfaces are able to bind adhesion proteins [128].

1.4.2 Influence of Adsorbed Proteins on Endothelialization

Early endothelialization of the blood contact surfaces of a cardiovascular implant is crucial for a long-term graft performance. In this context, the surface properties of the biomaterial play a decisive role. Random protein adsorption can lead to platelet adhesion, thrombosis, intimal hyperplasia and occlusion [134]. However, targeted biofunctionalization of the surface can promote the adhesion of endothelial cells and thus enable the early formation of a functional endothelium. Cell-adhesive structures are necessary for the anastomotic ingrowth of endothelial cells from the adjacent blood vessel and for the homing of EPCs [135]. EPC adhesion in vivo is mainly mediated by specific transmembrane receptors called integrins, specifically integrin β1, β2, αvβ3 and αvβ5. Defined by the integrin subunits, they bind to various ECM proteins such as laminins, collagens and fibronectin [134,135]. The functionalization of a biomaterial surface with these proteins or derived peptides has been shown to promote the adhesion of endothelial cells while inhibiting platelet adhesion and smooth muscle cell proliferation [134]. Minutes after binding to the ligands, the integrin receptors cluster together and form focal complexes, which can mature into more stable focal adhesions (FA) [136,137]. These macromolecular complexes, which consist of many additional proteins, transmit mechanical force and regulatory signals between the ECM and the cell. The FA architecture can be represented in four functional layers (Fig. 8). The extracellular integrin domains form the matrix-receptor binding outside the cell. The integrin

signalling layer, which is located on the intracellular side of the cell membrane, consists of intracellular integrin domains, paxillin, the focal adhesion kinase (FAK) and many other proteins that mediate cell signalling. Above this, a force transduction layer, consisting of proteins such as talin and vinculin, connects the integrins with the actin filaments. Finally, the actin regulatory layer, which consists of actin stress fibers cross-linked by α-actinin and myosin, is involved in focal adhesion strengthening [138,139]. Integrin-mediated cell-ECM adhesion has profound effects on cells by regulating the downstream signalling pathways that regulate proliferation, differentiation and survival [137]. The functionalization of a suitable surface with promising proteins thus enables not only the adhesion of endothelial cells but also the rapid formation of a functional endothelium.
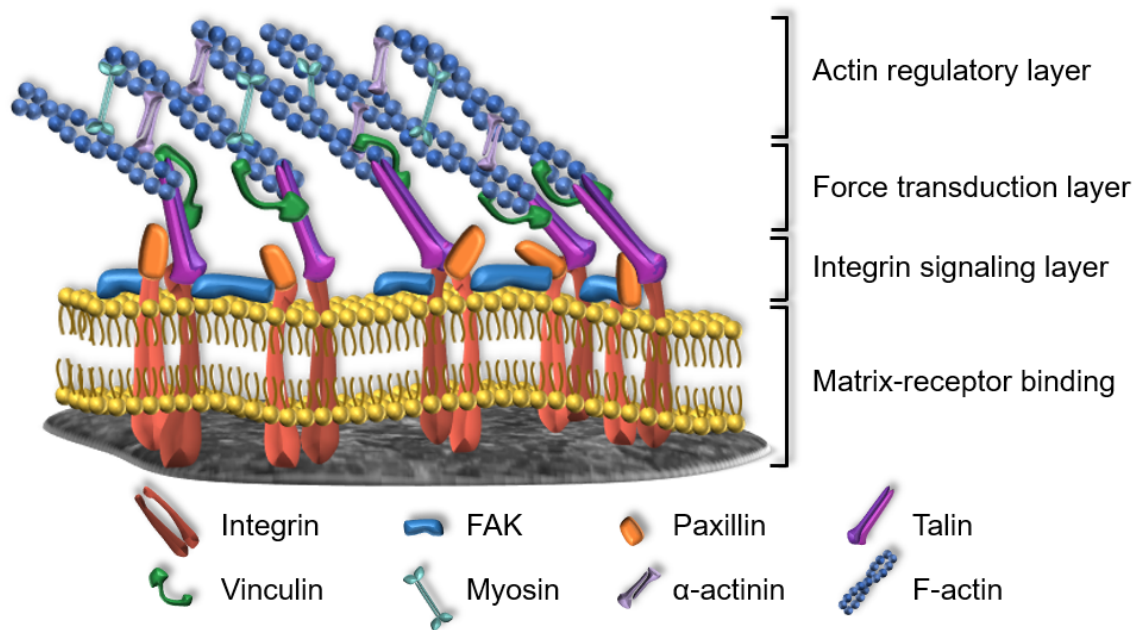

Figure 8. Schematic model of a mature focal adhesion complex. The architecture can be classified in several functional layers that transmit mechanical strength and regulatory signals. Modified from Kanchanawong et al. [138].

Chapter 2

Objectives of the Thesis

Objectives of the Thesis

This thesis has two main focuses, the application of Raman microspectroscopy for the non-invasive assessment of epigenetic states in human cells, and the development of a highly biocompatible TEGV. In the first study, Raman microspectroscopy and imaging were used to detect altered global DNA methylation states in carcinoma and pluripotent stem cells by identifying specific DNA methylation markers. Immunofluorescence staining and 5mC ELISA served as references in order to verify the results from the Raman measurements. The aim of the study was to establish a non-invasive method for tracking epigenetic changes in living cells, which could serve as a quality control tool for further applications in stem cell research or diagnostics.

The aim of the second study was to develop an electrospun vascular graft with mechanical properties that are comparable to native vascular tissues and a bioactive surface that attracts endothelial progenitor cells or promotes endothelialization. For this approach, a newly developed biostable polyurethane elastomer was used to biofunctionalize planar and tubular electrospun scaffolds with FN, DCN, or both in combination. First, the simulation of endothelial cell homing in vitro by attracting endothelial colony forming cells was addressed. Secondly, in vitro endothelialisation was investigated with a classical TEGV approach, in which primarily isolated endothelial cells were cultivated in a custom-made bioreactor to create an ATMP. From this work, the study of FN adsorption on polyurethane films with different surface chemistry and roughness was further examined. The aim of the study was to investigate the conformation and orientation of the adsorbed FN and the FN-cell interaction. For this purpose, polyurethane surfaces with different wettabilities were coated with FN and seeded with human umbilical vascular endothelial cells and human microvascular endothelial cells. The study aimed to provide a deeper understanding of how the surface properties of a biomaterial influence protein adsorption and cell behaviour, which may help to design surfaces in order to control the bioactivity of the adsorbed protein and thus direct cell response.

23

Chapter 3

Results I:

Non-invasive Detection of DNA Methylation States

3 Results I: Non-invasive Detection of DNA Methylation States

Early embryogenesis is characterized by massive changes in DNA methylation. After fertilization, DNA methylation in the genome is initially erased before later increasing around implantation [140,141]. After the blastocyst stage, the global DNA methylation levels remain almost the same. However, during carcinogenesis, a global DNA hypomethylation takes place [23]. Tracking these dramatic changes in global DNA methylation could provide new insights into early embryogenesis and provide evidence of cancerous tissue.

There are various approaches to study global DNA methylation such as immunofluorescence (IF) staining, bisulfite conversion or liquid chromatography-mass spectrometry [142,143]. However, these methods are based on cell fixation, cell lysis and DNA isolation, which excludes the examination of living cells. To track DNA methylation levels in living cells, Raman microspectroscopy is a promising tool, as it is a non-invasive and marker-independent technique based on light scattering of the illuminated material [36].

This study aimed to detect DNA methylation states in mouse pluripotent stem cells and human colon cancer cells in situ using Raman microspectroscopy and imaging (Fig. 9). To identify relevant DNA methylation Raman shifts, principal component analysis was applied. IF staining and 5mC enzyme-linked immunosorbent assay (ELISA) were used as reference methods to verify the results from the Raman measurements.
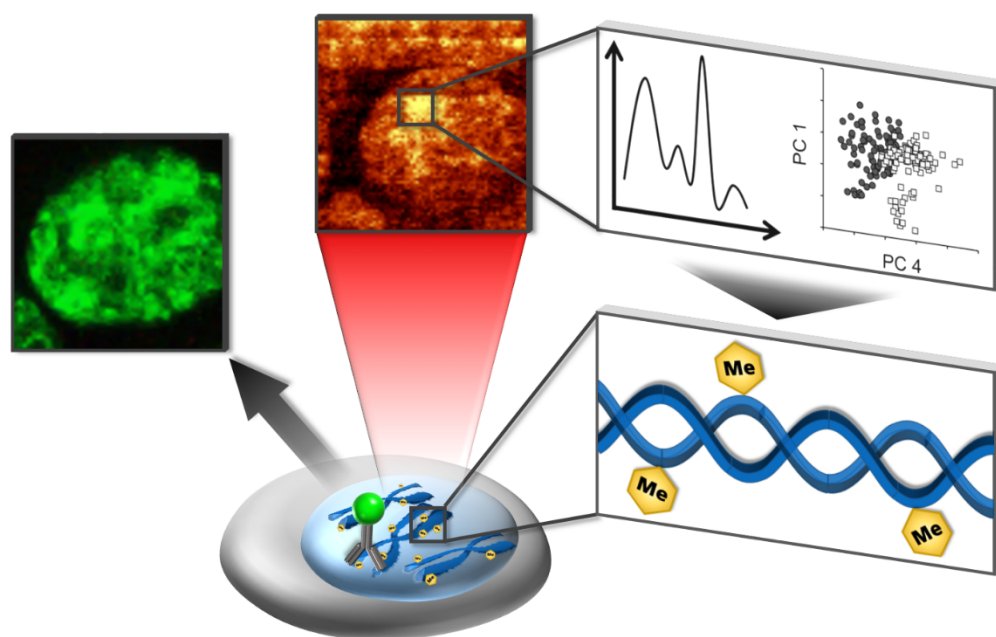
Figure 9. Non-invasive detection of DNA methylation states. Raman imaging and Raman microspectroscopy with subsequent PCA analysis was performed to detect DNA methylation states in carcinoma and pluripotent stem cells. DNA methylation was confirmed by anti-5 methylcytosine immunofluorescence staining.

3.1 Raman Microspectroscopy of Methylated DNA

Initially, relevant Raman bands related to DNA methylation had to be identified. For this purpose, cytidine and 5-Methylcytidine as well as methylated and non-methylated DNA were investigated by Raman microspectroscopy (Daum et al., **Appendix I**, Suppl. Fig. 1). All substances were analysed in a crystalline state. When compared to the Raman spectra of 5-Methylcytidine, the Raman spectra of cytidine revealed a notably increased Raman band at 1335 cm^{-1}, which can be assigned to CH_3CH_2 deformation vibrations [144]. In addition, increased signals were found at 788 cm^{-1} and 1248 cm^{-1}. Both peaks were previously described as characteristic Raman bands for cytosine [145,146].

Similar to 5-Methylcytidine, the Raman spectra of methylated DNA showed at 1335 cm^{-1} increased intensities compared to non-methylated DNA. In addition, significantly higher Raman bands were found at 1379 cm^{-1} ($p<0.05$) and 1579 cm^{-1} ($p<0.01$), which are correlated to the CH_3 group and the pyrimidine ring, respectively (Daum et al., **Appendix I**, Suppl. Fig. 1) [145,147]. Another prominent difference was detected at 1257 cm^{-1} ($p=0.106$) indicating nucleic acids [146]. These

results demonstrated that Raman spectroscopy enables the discrimination of methylated and non-methylated cytidine and DNA in a cell-free environment. Based on this data, Raman microspectroscopy and imaging was applied to pluripotent stem cells and carcinoma cells.

3.2 Raman Microspectrosopy and Imaging of Pluripotent Stem Cells and Carcinoma Cells

Mouse embryonic stem cells (mESCs) were used as a model system to study global DNA methylation changes in early embryogenesis. When cultured in serum-free medium, supplemented with leukemia inhibitory factor and the inhibitors GSK3β and Mek 1/2 (2i medium), the cells return to a "naïve pluripotent ground state", which is associated with a genome-wide DNA hypomethylation due to a reduced expression of the DNA methyltransferase 3 family [148–150]. After two weeks of 2i medium adaption, the cells revealed an increased gene and protein expression of the pluripotency markers Nanog and Oct4, confirming the pluripotent ground state (Daum et al., **Appendix I**, Suppl. Fig. 2). DNA methylation was first investigated by IF staining and 5mC ELISA. Exposure to 2i medium revealed a significant reduction in global DNA methylation. More precisely, a decrease from 4 % to 1 % methylated cytosines was observed. In addition, significant less 5mC-foci were found in the nuclei of the 2i mESCs compared to control.

Subsequently, using Raman microspectroscopy and imaging, the DNA methylation levels of mESCs cultured in serum-containing (control) and serum-free 2i medium (2i mESCs) were compared. First, high resolution Raman imaging of control and 2i mESCs was performed in order to obtain laterally resolved spectral information of the 5mC-foci within the cell nuclei. For this purpose, cells were fixed with paraformaldehyde. The acquisition time was one hour per cell. The Raman images were then analysed by creating a heat map with the sum of the intensities at 1257 cm^{-1}, 1331 cm^{-1} and 1579 cm^{-1} (Daum et al., **Appendix I**, Fig. 6 e-h), since these regions were found to exhibit major differences between methylated and non-methylated DNA, as previously shown. The heat maps of the control mESC Raman images revealed specific structures within the cell nuclei that were similar to those of the anti-5mC staining. By comparing the average spectra of these structures ("highly methylated") with average spectra of the lower intensity regions

("background"), increased Raman peaks were found for the "highly methylated" structures in the entire spectral range from 1250 cm^{-1} to 1390 cm^{-1}. This region is characterized by several Raman bands, which can be assigned to nucleic acids and CH_3CH_2 bonds [151]. When comparing the heat maps of the Raman images from the control and the 2i mESCs, the semi-quantitative pixel intensity analysis showed a significantly lower intensity per cell for the 2i mESCs compared to the control (Daum et al., **Appendix I**, Fig. 6 h; $p<0.05$).

For the analysis of living cells, the acquisition time of the Raman measurement was reduced to 100 seconds per cell. In this setup, the whole living cell was measured, showing a Raman spectrum with complex overlapping signals from lipids, proteins, carbohydrates and nucleic acids (Daum et al., **Appendix I**, Fig. 4) [151]. As a result, the spectral information of DNA methylation was much less apparent in the Raman spectrum. Nevertheless, some minor but significant changes were found at 1257 cm^{-1} ($p<0.01$), 1331 cm^{-1} ($p<0.001$) and 1575 cm^{-1} ($p<0.001$). Principal component analysis showed separate clusters for control and 2i mESCs in PC 4, which explain 3 % of the total spectral variance. Peaks in PC 4 loadings plot were found at 786 cm^{-1}, 896 cm^{-1}, 1257 cm^{-1} and 1331 cm^{-1} that correlated to nucleic acids, phosphodiester and deoxyribose [151].

In order to exclude cell-type specific factors, the same study was carried out with carcinoma cells. For this purpose, WT cells of the human colon cancer cell line HCT116 and their DNMT1-hypomorph progeny (DNMT1$^{-/-}$ cells) were used. A decreased global DNA methylation in DNMT1$^{-/-}$ cells was confirmed by anti-5mC IF staining and 5mC ELISA, showing a relative global DNA methylation difference of 0.6 % between the samples (Daum et al., **Appendix I**, Fig. 1). Similar to the results of mESCs Raman imaging, the heat maps of the WT cells, considering the same spectral regions at 1257 cm^{-1}, 1331 cm^{-1} and 1579 cm^{-1}, specific structures were found within the cell nucleus that were comparable to the structures seen when performing the 5mC IF staining (Daum et al., **Appendix I**, Fig. 6 a-d). The comparison of average spectra from highly methylated and background regions showed increased Raman bands in the range from 1250 cm^{-1} to 1390 cm^{-1}, but the difference was not as pronounced as with the mESCs. Nevertheless, the semi-quantitative pixel intensity analysis of the heat maps exhibited significant lower values for the HCT116 DNMT1$^{-/-}$ cells compared to the WT cells ($p<0.05$). The Raman spectral signature of living HCT116 WT and DNMT1$^{-/-}$ cells displayed

slightly but significant changes in intensity at 1257 cm^{-1} (p<0.001), 1330 cm^{-1} (p<0.01) and 1579 cm^{-1} (p<0.001). In the PC 4 scores plot of the PCA, which describes 3% of the total spectral variances, WT cells and DNMT1$^{-/-}$ cells showed a separation tendency (Daum et al., **Appendix I**, Fig. 2). Peaks described by the loadings plot of PC 3 correlated to 786 cm^{-1}, 1257 cm^{-1}, 1330 cm^{-1} and 1579 cm^{-1} referring to nucleic acids.

Finally, in order to investigate whether the differences in Raman spectra of the low and high global DNA methylation status are independent of species and cell types, PCA was performed on the data sets from both, the mESCs (control and 2i mESCs) and human colon cancer (HCT116 WT and DNMT1$^{-/-}$) cells. While the separation observed in PC 2 (12 %) and PC 4 (3 %) primarily explained cell type-specific differences, PC 5 (2 %) revealed a separation tendency between high-methylated and low-methylated cells (Daum et al., **Appendix I**, Fig. 5).

These results demonstrate that Raman microspectroscopy in combination with PCA possesses the required sensitivity to detect changes in the DNA methylation status of living cells, independent of the cell type. Furthermore, the data shows that Raman imaging can resolve DNA methylation patterns on a nano- and microscale within the cell nuclei. The non-invasive technology can be used to track epigenetic changes in living cells which may allow scientists to further investigate and understand epigenetic dynamics in early human embryogenesis and diseases. In addition, Raman spectroscopy has the potential to be used in the future as a tool for quality assessment in stem cell research or as a diagnostic tool for determining cancer tissue or cells.

Chapter 4

Results II:

Engineering of a Biofunctionalized Synthetic Vascular

Graft

4 Results II: Engineering of a Biofunctionalized Synthetic Vascular Graft

Large-diameter synthetic vascular grafts made of non-biodegradable polymers proved to be effective when replacing defective vessels [152]. However, small diameter grafts (<6 mm) show low patency rates due to their tendency to form thromboses and intimal hyperplasia [60–62]. Reasons for this include mechanical mismatches and too slow and insufficient endothelialization after implantation. Therefore, in addition to possessing the appropriate mechanical properties, the design of the vascular graft is crucial. Electrospinning enables the production of fibrous scaffolds that imitate not only the porous structure but also the physical properties of a native tissue, which improves the performance of the vascular graft. In order to induce a targeted reaction of the body after implantation, in our case a rapid endothelialization, the surface of the graft must be bioactivated. Immobilized decorin (DCN), a small-leucine-rich proteoglycan, has been shown to attract endothelial progenitor cells in vitro [153]. In addition, the protein is strongly involved in angiogenesis due to its binding to VEGFR2 [68]. Another highly relevant ECM protein is fibronectin (FN) as it is involved in wound healing [154,155]. Both proteins are therefore promising candidates to promote the attraction, adherence and proliferation of endothelial cells. A further challenge in the development and especially testing of medical devices is to replace, refine and reduce in vivo studies. For this purpose, appropriate in vitro test systems are required to mimic in vivo conditions as closely as possible.

The aim of this study was the fabrication of a small diameter electrospun vascular graft with mechanical properties comparable with those of a native blood vessel. For this purpose, a newly developed thermoplastic polycarbonate urethane (TPCU) was used, which combines softness with elasticity [156,157]. The electrospun graft was biofunctionalized with DCN and FN in order to promote endothelialization. Subsequently, the functionality of the electrospun scaffold was investigated in vitro. First, endothelial progenitor homing was simulated by attracting ECFCs. Subsequently, a tissue-engineering approach was performed by culturing primary-isolated vascular endothelial cells (vECs) in a custom-made bioreactor (Fig. 10).
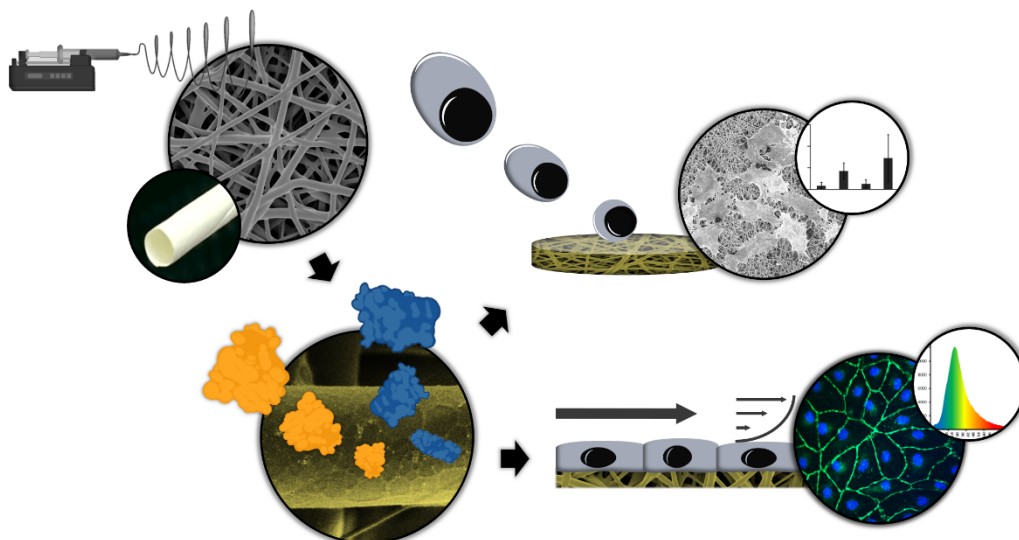
Figure 10. Fabrication and evaluation of a tissue-engineered vascular graft. A newly developed polyurethane is used to produce electrospun vascular grafts, which are biofunctionalized with fibronectin and decorin. Besides investigating the attraction of endothelial progenitor cells, endothelialization was investigated in dynamic in vitro culture.

4.1 Characterization of the Biofunctionalized Tubular Electrospun Scaffolds

Tubular scaffolds with a length of 110 mm, an inner diameter of 5 mm and a thickness of 0.40 ± 0.06 mm were produced by electrospinning 6 mL of 0.1 g/mL TPCU dissolved in 1,1,1,3,3,3 hexafluoro-2-propanol. The scaffolds were biofunctionalized with FN or DCN individually or in combination via protein adsorption. Subsequently, the influence of the biofunctionalization on the morphological and mechanical properties of the material was investigated. The electrospun TPCU scaffolds were examined by scanning electron microscopy (SEM) followed by the analysis of the pore and fiber sizes (Daum et al., **Appendix II**, Fig. 3). Both fiber and pore size, were not altered due to protein adsorption. The fiber sizes of our constructs ranged from 699 ± 61 nm to 776 ± 163 nm, which is much larger compared to collagen type IV fibers (20 to 52 nm). However, other studies that developed electrospun vascular grafts reported comparable or even larger fiber sizes on which a functional endothelium was formed. The pore sizes ranged between 0.08 ± 0.01 μm² and 0.12 ± 0.05 μm², which was comparable to the pore sizes of the extracellular matrix in native vessels (5 nm to 8 μm) [158–163].

36

A closer examination of the electrospun fiber surface showed a net-like deposition of FN in the nanometer range (Daum et al., **Appendix II**, Fig. 3). This phenomenon can be described as material-driven fibrillogenesis [164]. Depending on surface properties such as wettability, the adhesion of FN molecules can lead to spontaneous organization into FN networks. It has been reported, that the FN network influences cell growth, cell differentiation, and cell-cell interaction [165]. However, whether the FN network in our study significantly influences the cell behaviour compared to globularly deposited FN would need further investigation. The coated DCN formed randomly distributed aggregates on the TPCU scaffold. In combination with FN, even larger aggregates were observed, deposited on the FN network. In addition to these observations, FN and DCN biofunctionalization was successfully confirmed by IF staining.

For the investigation of the mechanical properties of the TPCU scaffolds, a ring tensile test was performed based on a method previously described [166]. Based on this data, the elastic modulus, the ultimate tensile strength and burst pressure were determined. The mechanical properties were not significantly influenced by the biofunctionalization. The elastic modulus was in the range from 3.7 ± 0.5 MPa to 5.6 ± 0.9 MPa, the ultimate tensile strength was between 21.1 ± 3.5 MPa and 22.1 ± 3.7 MPa. Burst pressures ranged from 3124 ± 466 mmHg to 3326 ± 78 mmHg. Most importantly, the mechanical properties were comparable to those of native vessels. Comparing our constructs with that of autologous grafts, which are the gold standard for vascular bypass surgery, the elastic modulus lied within the range of saphenous veins (2.25–4.2 MPa) and were similar to iliofemoral veins (3.11 MPa) and arteries (1.54 MPa), internal mammary arteries (8 MPa) and femoral arteries (10.5 MPa) (Daum et al., **Appendix II**, Table 2). The burst pressure of our constructed grafts was comparable to those of the saphenous vein (1250-3900 mmHg) and the internal mammary artery (2000-3196 mmHg). These results demonstrate that our construct has suitable morphological and mechanical properties to serve as a vascular graft.

4.2 In Vitro Simulation of Endothelial Progenitor Cell Homing

A crucial step for the in vivo endothelialization of an artificial vascular graft is the ability of the implanted material to attract endothelial progenitor cells. In our study,

we simulated this process in vitro under static and dynamic conditions. Briefly, ECFCs were cultured for 24 hours on planar (static) and tubular (dynamic) biofunctionalized scaffolds. Dynamic conditions were simulated by rotating the tubular scaffolds on a roller mixer. For both conditions, FN-coating and FN + DCN-coated samples showed a significantly increased number of adherent cells compare with controls and DCN-coated samples (Daum et al., **Appendix II**, Fig. 5 + Fig. 6). Under dynamic conditions, slightly but not significantly more cells were found on the FN + DCN coating compared to the FN coating. Under static conditions this tendency was not observed. For both conditions, the cell morphology differed significantly on the different protein coated surfaces. The ECFCs on the TPCU scaffolds that were coated with FN- and FN + DCN showed a stretched morphology, whereas the cells on the control and DCN-coated TPCU scaffold had a spherical shape. These findings indicate a cell-repellent effect of the control and DCN-coated scaffolds. Since cells prefer to adhere to hydrophilic surfaces, we assume that the hydrophobic surface of the TPCU scaffold impeded the adhesion of cells [167]. In our study, DCN-coating was not able to reduce this effect. Interestingly, it has been reported that DCN coated on a blend of polyethylene glycol dimethacrylate and polylactide favoured the adhesion of ECFCs [153]. Since the orientation and conformation and thus the bioactivity of an adsorbed protein can be influenced by the underlying surface properties, one can assume that the functionality of the adsorbed DCN is also influenced by the material surface [168–170]. FN-coating reversed the cell-repellent effect of the TCPU, both with and without DCN. IF staining of the statically cultured ECFCs showed a significantly higher VEGFR2 expression and a significantly lower PECAM-1 expression in the cells on the FN+DCN coated samples compared to the ECFCs grown on the FN coating (Daum et al., **Appendix II**, Fig. 5). These observations suggest that both DCN and FN in combination may have a different bioactivity [171]. Overall, we can conclude that the ECFC attraction was supported by FN but not affected by DCN.

4.3 In Vitro Endothelialization under Static and Dynamic Conditions

The formation of an endothelial cell layer on the electrospun TPCU scaffold was investigated with primary isolated vascular endothelial cells (vECs). Under static

conditions, the cells were cultured for seven days on planar scaffolds biofunctionalized with FN, DCN and FN+DCN. An almost confluent endothelial cell layer was formed on the FN and FN+DCN-coated scaffolds after one week (Daum et al., **Appendix II**, Fig. 7). IF staining confirmed the expression of the specific endothelial cell type marker VE-cadherin and PECAM-1 in the vECs on both coatings, indicating a functional endothelium. Vinculin expression showing cell-material interaction, was found in vECs on both coatings. In contrast, the vECs cultured on the DCN-coating and control did not form a confluent endothelial cell layer. Similar to the results obtained with the ECFCs, the cells on the control and DCN coating showed a spherical shape, while on the FN and FN+DCN-coated scaffolds, vECs were stretched. These findings demonstrated that the DCN coating on the TPCU scaffolds did not have a substantial advantage in the intended endothelialization.

Because of this, under dynamic conditions only FN-biofunctionalized TPCU scaffolds were used. For this purpose, a bioreactor system previously designed for this study was further developed and optimized (Daum et al., **Appendix II**, Fig. 2). In brief, the system consisted of a 250 mL glass bottle as culture chamber enclosing a removable previously custom-designed graft frame that holds the vascular graft. The graft frame was connected to a medium reservoir and a bubble trap via flexible silicone tubes. Gas exchange was provided by sterile filters, which were connected to the medium reservoir and the culture chamber. A multi-channel roller pump was used to circulate the cell culture medium through the system. The vECs were seeded into the tubular FN-functionalized TPCU scaffolds, and after an initial culture for three days under static conditions to allow cell attachment, a flow was employed that was stepwise increased to 25 mL/min within one and a half days. Under this flow, which caused a shear stress of about 0.03 Pa, the vEC-seeded FN-biofunctionalized scaffolds were cultured for seven days. Using IF staining and SEM, we successfully showed that after one week, a layer of confluent vECs with a unidirectional cell orientation in the direction of the flow was formed (Daum et al., **Appendix II**, Fig. 8). Curiously, the F-actin staining revealed a rather fibroblast-like cell morphology. As endothelial cells are highly plastic, it can be assumed that culturing the cells in vitro in an artificial environment can lead to cellular dedifferentiation [172,173]. These findings highlight the importance of fine-tuning the parameters for in vitro testing and tissue engineering.

This work showed that FN-coated on TPCU scaffolds promotes endothelialization. In contrast, DCN-biofunctionalized TPCU scaffolds showed a cell-repellent effect, most likely due to the high hydrophobic properties of the TPCU. Overall, we have successfully engineered a TPCU electrospun vascular graft with mechanical properties comparable to those of a native blood vessel. In addition, in vitro test systems were established which allow the culturing of endothelial cells under static and dynamic conditions.

Chapter 5

Results III:

Modulation of Fibronectin Adsorption to Direct

Endothelial Cell Fate

5 Results III: Modulation of Fibronectin Adsorption to Direct Endothelial Cell Fate

The functionalization of cardiovascular implants with peptides and proteins bioactivates the surface of the implant [174]. Depending on the molecule, it enables specific reactions in the body, such as reducing blood clotting, attracting certain cells or inducing a specific immune response [153,175,176]. An attractive candidate in this context is FN, a well-studied glycoprotein of the extracellular matrix, which is known to promote cell adhesion, proliferation and migration [177], while also being involved in wound healing [154,155]. Functionalization of the protein via physical adsorption has already been reported to support endothelialization [178,179]. However, it has been shown that the conformation and orientation of adsorbed FN and thus its bioactivity can change depending on surface properties such as the wettability [180–184]. This in turn has an effect on cell attachment, proliferation and differentiation [185–188]. Based on this knowledge, a controllable surface for the modulation of FN deposition, which in turn allows to direct endothelial cell behaviour, is very attractive.

The aim of the study was to investigate the conformation and orientation of FN adsorbed on surfaces with different surface chemistry and roughness and the FN-cell interaction (Fig. 11). For this purpose, spin-coated polyurethane surfaces were provided, whose surface wettability was finely tuned in the range of 15° to 72° using oxygen plasma treatment. The conformation and orientation of the adsorbed FN was investigated with anti-FN IF staining. Subsequently, the behaviour of human umbilical vascular endothelial cells (HUVECs) and human microvascular endothelial cells (HMVECs) on the FN-adsorbed surfaces was analysed with respect to cell adhesion and cell morphology as well as cell-cell and cell-material interaction.
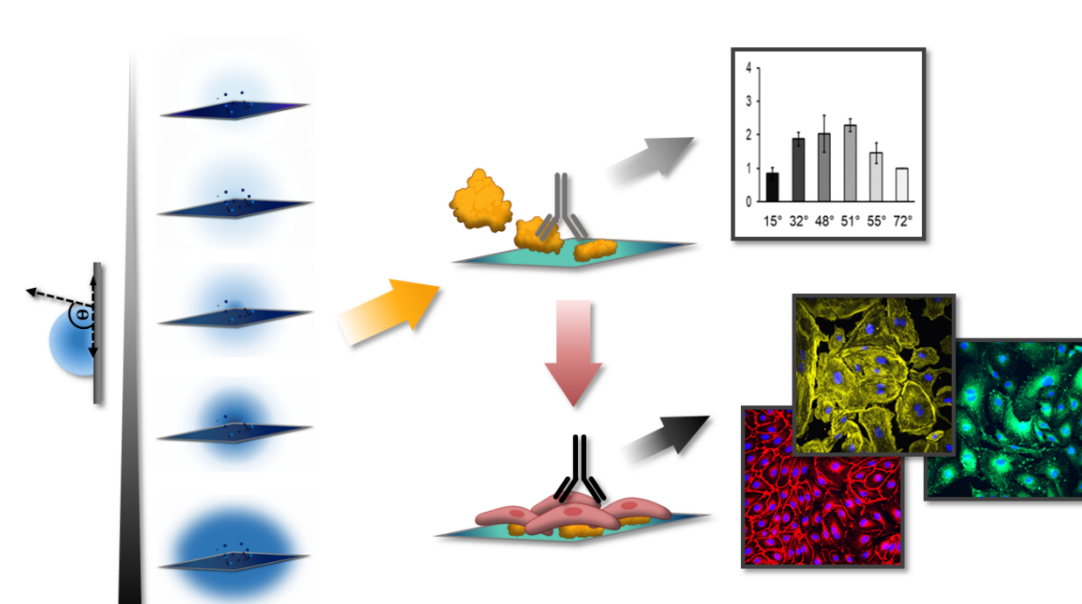
Figure 11. Investigation of fibronectin adsorption and endothelial cell behaviour on oxygen plasma-treated polyurethane. Spin-coated polyurethane (Pellethane®) films are treated with oxygen plasma using defined parameters to obtain different wettabilities. Oxygen plasma-treated samples are coated with 10 µg/ml human plasma fibronectin for 1 hour at 37°C. The orientation and conformation of adsorbed fibronectin is analyzed. The FN-cell interaction is studied using HMVECs and HUVECs seeded on the fibronectin coated samples.

5.1 Fibronectin Adsorption on Oxygen plasma-treated Polyurethane Surfaces

The amount of adsorbed FN on the fine-tuned oxygen plasma-treated polyurethane surfaces was investigated externally to this work by fluorescent labelling of FN. In addition, the coated FN was stained with a polyclonal anti-FN antibody and the monoclonal antibody HFN7.1, which is described to bind near the cell binding side of the FN [189]. The ratio of the results from the polyclonal and monoclonal antibody staining to the fluorescently labelled FN indicated the varying conformation and orientation of the adsorbed FN on the different surfaces (Daum et al., **Appendix III**, Fig. 3). On surface A and F, strong conformational changes of the adsorbed FN are suspected, since the signal of the polyclonal antibody is reduced compared to surface B, C, D and E indicating that fewer epitopes are present or accessible to the antibody. The surfaces C and D exhibit similar increased signals of the polyclonal antibody staining, suggesting only minor conformational changes of the

FN. Interestingly, especially on the surfaces A and D, the cell binding side of the adsorbed protein is exposed, demonstrated by an increased signal of the monoclonal HFN7.1 antibody staining compared to the B, C, E and F surfaces (Daum et al., **Appendix III**, Fig. 3). These observations suggest that the accessibility of the cell binding domain is related to both the conformational change and the orientation of the adsorbed FN.

5.2 Endothelial Cell Adhesion, Morphology and Cell-Cell Interaction

The influence of the altered conformation and orientation of the adsorbed FN on endothelial cells was investigated with HUVECs and HMVECs. First, the ability of the cells to adhere to the surface within 24 hours was investigated. Both cell types showed a similar trend regarding the cell count on the different surfaces. Significantly more cells were found on the moderate hydrophilic surfaces (B, C, D) compared to the most hydrophilic surface A and the less hydrophilic surfaces (E and F) (Daum et al., **Appendix III**, Fig. 4). Interestingly, the curve profile correlated with the polyclonal anti-FN staining, except for surface F (Daum et al., **Appendix III**, Fig. 3). It has been previously described that certain domains of FN influence cell cycle. Depending on the FN deposition, cell proliferation can be reduced or elevated [190–192]. Regarding the cell size, no differences were found on all surfaces. Only on the B sample, the size of the HUVECs tended to be smaller, although not significantly (Daum et al., **Appendix III**, Suppl. Fig. 7).

Since the organization of the cytoskeleton provides information about the status of the endothelial cell barrier function, the distribution of F-actin in the cells was further investigated. HUVECs and HMVECs showed distinct differences in the distribution of the microfilaments (Daum et al., **Appendix III**, Fig. 5). Peripheral F-actin was found in the cells on the F samples. Even more prominent cortical actin rings were found in both cell types on the A surface. This F-actin distribution is typically found in resting endothelium with a functional barrier function. On the other surfaces, HUVECs and HMVECs formed F-actin stress fibers, indicating activated and migratory endothelial cells [193]. The interaction of cells with FN induces the formation of focal adhesions complexes [194]. Vinculin, which is enriched in focal adhesions and mechanically cross-links integrins and other adhesion adaptor proteins to the actin cytoskeleton [195], was significantly more highly expressed in

HUVECs and HMVECs on the A surface (Daum et al., **Appendix III**, Fig. 6). In addition, the HMVECs showed a significant higher number of vinculin foci per cell on the F surface. Since the protein is not required at early stages of adhesions, but is mainly associated with mature focal adhesions, it can be assumed that the cells on the A and F surface have a stronger and more mature interaction with the surface [196]. Presumably, the stronger adhesion of the FN to these surfaces (Daum et al., **Appendix III**, Fig. 5) allows a proper transmission of force through the actin cytoskeleton allows the maturation of vinculin-associated focal adhesions as well as the formation of actin bundles [197,198]. Another protein of the focal adhesion complex, the FAK, showed different expression levels between the two cell types (Daum et al., **Appendix III**, Fig. 6). For the HUVECs, significant more FAK foci per cell were found in the cells on the C surface compared to the F sample. The HMVECs revealed the highest numbers of FAK foci on the C and D surfaces. Phosphorylated FAK enhances cell proliferation and motility [199–201]. In addition, it has been reported to enhance actin polymerization. These findings in turn overlap with the observations of cytoskeleton data, where increased F-actin stress fibers were found in the cells on these surfaces (Daum et al., **Appendix III**, Fig. 5).

The permeability of an endothelium is determined by the integrity of intercellular junctions [202]. Two major components that mediate these endothelial cell-cell interactions are VE-cadherin and PECAM-1. IF staining of these two proteins showed few differences on the different samples (Daum et al., **Appendix III**, Fig. 7). The VE-cadherin expression in the HUVECs was the same on all surfaces. For the HMVECs, significant higher expression levels were found on the A and C surfaces, which may indicate a more advanced formation of a functional endothelium compared to the other samples. The PECAM-1 analysis showed a significantly higher expression level in the HUVECs on the A surface, while the HMVECs showed no differences.

In this study, only minor parameter changes in oxygen plasma treatment induced large variations in the conformation and orientation of the adsorbed FN, which in turn affected both HUVECs and HMVECs in a similar manner with respect to cell number, cytoskeletal reorganization, formation of FAs and cell-cell interaction. Both the roughness and the surface chemistry affected the material-FN interaction, which in turn influenced the cell behaviour. In summary, oxygen plasma treatment of PU surfaces is a suitable method for designing surfaces in order to modulate the

bioactivity of FN and thus to direct cell adhesion, migration and proliferation. This makes it an attractive method with a high application potential in cardiovascular tissue engineering.

Chapter 6

General Discussion & Conclusion

General Discussion & Conclusion

6.1 Non-Invasive Quality Assessment of Advanced Therapy Medicinal Products

Since 2007, when the European Medicines Agency published a joint action plan for ATMPs to facilitate their development and authorisation [2], the number of clinical trials with ATMPs increased steadily. During the 2014-2018 period, 2.097 new clinical trials were initiated [203]. The regulatory hurdle for such a product is, among other things, to prove the benefit for the patient and to guarantee the consistency and reproducibility of the product, which is a major challenge due to its biological complexity. A cost-effective, reliable and ideally non-invasive method for quality assessment of the ATMP could be a step towards meeting this challenge. Raman microspectroscopy is a powerful label-free technique to monitor cell death stages, pathological cell states and differentiating pluripotent stem cells [36,204,205]. Interestingly, 23 % of the industry-driven and 93 % of the academia applied ATMPs, which are currently in clinical phase III and IV, are based on stem cells [206]. An obvious quality criterion of stem cells is their pluripotency. For this reason, determining and assessing the pluripotency of these cells ex vivo could be an attractive approach to ensure the quality of the product. Brauchle et al. successfully demonstrated that Raman spectroscopy is capable to distinguish between pluripotent and differentiated cells [205]. Most of the observed differences were attributed to cholesterol and other lipid molecules. However, epigenetic changes have never been considered in this context, although they occur extensively in early embryogenesis. As already mentioned earlier, after fertilization, the global DNA methylation initially decreases and then increases again around implantation. This phenomenon can be observed in vitro by culturing embryonic stem cells in serum-free "2i medium". Through this, the cells undergo genome-wide DNA hypomethylation, which is described as a return to a "naïve pluripotent ground state" [148]. If a stem cell-based therapy product must possess this pluripotent state, the measurement of global DNA methylation could be a possible quality criterion. Our study showed that Raman spectroscopy and Raman imaging in combination with PCA is able to detect changes in global DNA methylation status in living embryonic stem cells cultured in serum-containing and serum-free 2i medium.

Since in the early stages of embryonic development, the global DNA methylation level is an indication of cell pluripotency, we believe that this non-invasive technique is a promising way to monitor the quality of stem cell-based ATMPs. Interestingly, slight global DNA methylation changes occur also in most cancers, cardiovascular diseases such as arteriosclerosis and during ageing [22,30–32]. Our study examined altered global DNA methylation levels in cancer cells caused by decreased activity of DNMT1 revealing similar altered Raman bands as with the embryonic stem cells. These observations show that Raman spectroscopy might also be applicable as a tool for screening somatic cell therapy products with regard to their epigenetic stability.

However, one of the challenges is the duration of the analysis with Raman spectroscopy, which so far has been within minutes per cell. The step into applicability requires the measurement to be performed in a few seconds, which makes it necessary to further develop the devices. Furthermore, data analysis could be further optimized through the use of improved machine learning tools, making measurement not only faster but also more reliable.

6.2 Raman Spectroscopy as a Diagnostic Tool for Cardiovascular Diseases

Raman spectroscopy is not only convenient for the non-invasive quality assessment of cells but can also be used as diagnostic tool for diseases. For example, there are numerous studies describing Raman spectroscopy as a method to detect cancerous tissue [44,207,208]. While most of these studies focus on the analysis of tissue biopsies in vitro, researchers are also developing systems for in situ analysis, such as coherent Raman endoscopes [209]. This technique not only enables the analysis of cancer but could also serve as a diagnostic tool for cardiovascular diseases such as atherosclerosis. Classed as a disease of aging, atherosclerosis is accompanied by epigenetic changes such as global DNA hypomethylation [210]. In our study, genetically modified carcinoma cells were examined with regard to global DNA methylation states, which allowed the identification of distinct DNA methylation markers. Using these markers, atherosclerotic tissue could be identified and diagnosed in situ, based on the detection of DNA methylation by Raman spectroscopy.

Nevertheless, not only epigenetic markers, but also changes in ECM composition and in especially the calcification of the tissue could serve as promising biomarkers, since calcium salts reveal distinct Raman signals in biological tissues [151,211,212]. The non-destructive in situ observation of calcified tissue could be helpful in determining suitable therapies for treating the disease. Furthermore, monitoring disease progression could provide further insights into the formation and progression of atherosclerosis and thus lead to new therapeutic approaches.

6.3 From In Vitro to In Situ Tissue Engineering

In our study, a TEGV was fabricated, which could serve as an ATMP for vascular repair. Considering the current development of ATMPs, more marketing authorization applications can be expected in the next few years [203,213]. However since 2007, only 10 ATMPs approved in the European Union through a centralized procedure have been commercially available [214]. Reasons for this are the slow translation of new therapeutic approaches from research into clinical trials due to the inherent complexity of these products, especially with regard to quality. Besides the regulatory challenge of demonstrating the efficacy and safety of ATMPs, the costs of developing and producing these complex products can be quite high [215]. Opportunities to address these challenges include advisory services and incentives from the European Medicines Agency, cost reductions through "value-based payment systems" and simplification of the regulatory framework [216,217]. But what are the possibilities on the developer side? Regarding TEVGs, the classical in vitro tissue engineering approach is expensive, time-consuming and associated with high authorization hurdles due to the high complexity of the product [7]. An attractive way to meet these challenges is to use the regenerative capacity of the body to engineer the blood vessel in situ [218]. In this case, a highly biocompatible tubular scaffold without cells would be implanted and then remodeled and replaced by the body's own substances. In this approach, the role of the scaffold is to resist the stresses upon implantation and to control tissue development by providing a suitable microenvironment for the cells. The latter is pursued by bioactivating the material surface that comes into contact with blood to trigger a targeted reaction in the body, such as an anti-inflammatory response and a rapid endothelialization. This includes the initial protein adsorption, the immune response and the adhesion

of certain cells such as EPCs [219]. In our study, we functionalized the electrospun scaffold with a combination of the ECM proteins FN and DCN. FN in particular, enabled the adhesion and proliferation of ECFCs in vitro. By contrast, DCN led to an increased expression of VEGFR2 in the ECFCs, although this did not show any advantages with respect to ECFC adhesion. Even if DCN did not fulfil the expectation of supporting EPC homing, it could still be a promising protein for the functionalization of vascular grafts as it has been shown to inhibit the proliferation and migration of vascular smooth muscle and the formation of intimal hyperplasia [220,221].

The challenge of generating TEGVs in situ remains to elicit the desired response in the body by functionalizing the surface of the implant with promising bioactive substances such as ECM proteins, while keeping the complexity of biofunctionalization as low as possible. By further deepening our understanding of vascular regeneration mechanisms, in situ vascular tissue engineering will have great potential for vascular medicine by minimizing the risks and costs associated with cell handling and possibly enabling the availability of an "off-the-shelf" product.

6.4 Modulating Protein Adsorption on Biomaterial Surfaces

The biocompatibility of a vascular implant is determined not only by the material and its mechanical properties, but also by its surface properties. After implantation, the biomaterial is immediately coated with proteins from blood and interstitial fluids to which the cells first react and through which they can sense the foreign surface [128]. It is well known that the composition, conformation and orientation of the adsorbed proteins has a huge impact on cell adhesion, activation and wound healing responses. Albumin, the most abundant blood protein, promotes platelet adhesion if it denatures on a surface beyond a critical level [222]. The conformation of adsorbed fibrinogen is also a critical determinant of platelet adhesion, since the polymerization of fibrin is affected by the surface chemistry [223,224]. For this reason, some researchers advocate on creating materials with surface properties that show reduced protein adsorption. However, with regard to in situ tissue engineering, surface chemistries and topographies must be designed that affect the composition of the protein layers as well as the orientation and conformation of the proteins in order to evoke a desired tissue response [184,225]. In our study, FN was adsorbed on

electrospun PU scaffolds and on spin-coated PU surfaces. On both substrates, a material-driven FN fibrillogenesis was observed, which has already been shown to elicit beneficial biological signals [164,226]. Although the in vitro studies showed the adhesion and proliferation of endothelial cells on both substrates using different endothelial cell phenotypes, it remains to be proven whether the fibrillary structure of the adsorbed FN has any significant beneficial effect on endothelialization in vivo. To further investigate FN adsorption, the surface chemistry and topography of the spin-coated PU surfaces were modified by oxygen plasma treatment, which in turn influenced the amount, orientation and conformation of the adsorbed FN (Figure 11). The altered orientation and conformation of the FN on the different surfaces significantly affected the endothelial cells with regard to the amount of adherent cells, the cytoskeletal organization and the formation of focal adhesions. With this study, we demonstrated that the surface properties of a biomaterial are crucial as they determine the bioactivity of the adsorbed protein and thus the cell behavior. Using oxygen plasma treatment of the PU surfaces, we have established a simple and robust method that allows us to induce large variations in affinity, conformation and orientation of the adsorbed FN. By minor changes of the plasma treatment parameters, a finely tuned gradation of the surface wettability can be achieved, which in turn allows a systematic investigation of the relationship of surface chemistry and surface roughness to protein adsorption. Investigating the influence of the adsorbed protein or protein mixture on blood, immune cells and other cell types such as endothelial cells can provide important insights for the design of a material that evokes the required wound healing and tissue responses. The ultimate goal is to improve the quality of life of patients by creating implants that are rapidly integrated and successfully remodeled. To achieve this, further development of the biomaterial surface in order to direct protein adsorption is required.

6.4 Conclusion

The use of ATMPs for therapeutic purposes is an increasingly attractive alternative to traditional treatments as it offers great potential in terms of new therapeutic options, personalized medicine and the possibility of a one-time cure. However, ATMPs are still facing economic, regulatory and scientific challenges. This work

presents perspectives for addressing these hurdles. Monitoring the biological complexity in a non-destructive and non-invasive way to allow quality assessment of ATMPs is an important component to ensure their safety and functionality. In this thesis, a possibility for a non-invasive quality control of stem cells is presented, which is based on epigenetic patterns, more precisely DNA methylation states. We successfully demonstrated that Raman microspectroscopy in combination with multivariate data analysis is capable to distinguish between lower and higher global DNA methylation states indicating the pluripotency of the cell [150,227]. Further optimisation of the methodology could enable the rapid and accurate quality assessment of ATMPs, thereby facilitating their transition towards industrialization. Another challenge for ATMPs, especially TEPs, are their biological complexity and the high costs of development, production and storage, which make them very expensive [228]. To this end, an electrospun vascular graft was fabricated, on which primary-isolated vascular endothelial cells were cultured using an in-house designed simplified bioreactor system. Using this system to produce TEVGs could enable a more cost-effective production of vascular TEPs. In addition, the designed electrospun vascular graft, which possesses mechanical properties comparable to those of a native vascular graft and a surface biofunctionalization with two different ECM proteins, has been shown to promote the adherence and proliferation of endothelial progenitor cells in vitro. These properties have the potential to make the graft suitable for in situ tissue engineering. Following this approach in the future enables the fabrication of a cell-free construct, which reduces the biological complexity and simplifies the production and storage of the vascular graft, thus saving costs.

Finally, the influence of PU surfaces with different chemical and topographic properties on the bioactivity of adsorbed FN was investigated. We successfully demonstrated that surface roughness and chemistry influences the orientation and conformation of the adsorbed protein and thus its bioactivity. In addition, we showed that the adsorbed FN on the different surfaces altered the cell response of two different endothelial cell phenotypes regarding cell-cell and cell-material interaction. The findings can help design surfaces that control cell response by modulating protein adsorption and thus improve endothelialization.

References

1. Walsh, G. Biopharmaceuticals, an overview. in *Biopharmaceuticals, an Industrial Perspective* (eds. Walsh, G. & Murphy, B.) **34,** 1–19 (Springer Netherlands, 2010).
2. *Regulation (EC) No 1394/2007 of the European Parliament and of the Council of 13 November 2007 on advanced therapy medicinal products and amending Directive 20o1/83/EC and Regulation (EC) No 726/2004 OJ L 324.* (2007).
3. Schneider, C. K. *et al.* Challenges with advanced therapy medicinal products and how to meet them. *Nature Reviews Drug Discovery* **9,** 195–201 (2010).
4. Miliotou, A. N. & Papadopoulou, L. C. CAR T-cell Therapy: A New Era in Cancer Immunotherapy. *Curr. Pharm. Biotechnol.* **19,** 5–18 (2018).
5. Song, H. H. G., Rumma, R. T., Ozaki, C. K., Edelman, E. R. & Chen, C. S. Vascular Tissue Engineering: Progress, Challenges, and Clinical Promise. *Cell Stem Cell* **22,** 340–354 (2018).
6. Shinoka, T. Development of a tissue-engineering vascular graft for use in wcongenital heart surgery. *EBioMedicine* **1,** 12–13 (2014).
7. Ong, C. S. *et al.* Tissue engineered vascular grafts: current state of the field. *Expert Review of Medical Devices* **14,** 383–392 (2017).
8. Drews, J. D. *et al.* Spontaneous reversal of stenosis in tissue-engineered vascular grafts. *Sci. Transl. Med.* **12,** (2020).
9. Waddington, C. H. The epigenotype. 1942. *Int. J. Epidemiol.* **41,** 10–13 (2012).
10. Dupont, C., Armant, D. R. & Brenner, C. A. Epigenetics: Definition, mechanisms and clinical perspective. *Semin. Reprod. Med.* **27,** 351–357 (2009).
11. Armstrong, L. *Epigenetics.* (2014).
12. Newell-Price, J., Clark, A. J. L. & King, P. DNA methylation and silencing of gene expression. *Trends Endocrinol. Metab.* **11,** 142–148 (2000).
13. Urieli-Shoval, S., Gruenbaum, Y., Sedat, J. & Razin, A. The absence of detectable methylated bases in Drosophila melanogaster DNA. *FEBS Lett.* **146,** 148–152 (1982).
14. Zeng, Y. & Chen, T. DNA methylation reprogramming during mammalian development. *Genes* **10,** (2019).
15. Auclair, G., Guibert, S., Bender, A. & Weber, M. Ontogeny of CpG island methylation and specificity of DNMT3 methyltransferases during embryonic development in the mouse. *Genome Biol.* **15,** 545 (2014).
16. Meissner, A. *et al.* Genome-scale DNA methylation maps of pluripotent and differentiated cells. *Nature* **454,** 766–70 (2008).
17. Deng, J. *et al.* Targeted bisulfite sequencing reveals changes in DNA methylation associated with nuclear reprogramming. *Nat Biotechnol* **27,** 353–360 (2009).
18. Biniszkiewicz, D. *et al.* Dnmt1 overexpression causes genomic hypermethylation, loss of imprinting, and embryonic lethality. *Mol. Cell. Biol.* **22,** 2124–35 (2002).
19. Bibikova, M., Laurent, L. C., Ren, B., Loring, J. F. & Fan, J. B. Unraveling Epigenetic Regulation in Embryonic Stem Cells. *Cell Stem Cell* **2,** 123–134 (2008).
20. Alegría-Torres, J. A., Baccarelli, A. & Bollati, V. Epigenetics and lifestyle. *Epigenomics* **3,** 267–277 (2011).
21. Egger, G., Liang, G., Aparicio, A. & Jones, P. a. Epigenetics in human disease and prospects for epigenetic therapy. *Nature* **429,** 457–463 (2004).
22. Hon, G. C. *et al.* Global DNA hypomethylation coupled to repressive chromatin domain formation and gene silencing in breast cancer. *Genome Res.* **22,** 246–258 (2012).
23. Ehrlich, M. DNA hypomethylation in cancer cells. *Epigenomics* **1,** 239–59 (2009).
24. Toraño, E. G., Petrus, S., Fernandez, A. F. & Fraga, M. F. Global DNA hypomethylation in cancer: Review of validated methods and clinical significance. *Clin. Chem. Lab. Med.* **50,** 1733–1742 (2012).

25.   Valencia-Morales, M. D. P. *et al.* The DNA methylation drift of the atherosclerotic aorta increases with lesion progression. *BMC Med. Genomics* **8,** 7 (2015).

26.   Bradbury, J. Human epigenome project - Up and running. *PLoS Biol.* **1,** e82 (2003).

27.   Feinberg, A. P. The epigenetics of cancer etiology. *Semin. Cancer Biol.* **14,** 427–432 (2004).

28.   Chik, F., Szyf, M. & Rabbani, S. A. Role of epigenetics in cancer initiation and progression. *Adv. Exp. Med. Biol.* **720,** 91–104 (2011).

29.   Ehrlich, M. DNA hypermethylation in disease: mechanisms and clinical relevance. *Epigenetics* **14,** 1141–1163 (2019).

30.   Laukkanen, M. O. *et al.* Local hypomethylation in atherosclerosis found in rabbit ec-sod gene. *Arterioscler. Thromb. Vasc. Biol.* **19,** 2171–2178 (1999).

31.   Tabaei, S. & Tabaee, S. S. DNA methylation abnormalities in atherosclerosis. *Artif. Cells, Nanomedicine, Biotechnol.* **47,** 2031–2041 (2019).

32.   Unnikrishnan, A. *et al.* Revisiting the genomic hypomethylation hypothesis of aging. *Ann. N. Y. Acad. Sci.* **1418,** 69–79 (2018).

33.   Horvath, S. DNA methylation age of human tissues and cell types. *Genome Biol.* **14,** R115 (2013).

34.   Unnikrishnan, A. *et al.* The role of DNA methylation in epigenetics of aging. *Pharmacology and Therapeutics* **195,** 172–185 (2019).

35.   Huan, T. *et al.* Genome-wide identification of DNA methylation QTLs in whole blood highlights pathways for cardiovascular disease. *Nat. Commun.* **10,** 1–14 (2019).

36.   Brauchle, E. & Schenke-Layland, K. Raman spectroscopy in biomedicine - non-invasive in vitro analysis of cells and extracellular matrix components in tissues. *Biotechnol. J.* **8,** 288–297 (2013).

37.   Mariani, M. M. & Deckert, V. Raman Spectroscopy: Principles, Benefits, and Applications. in *Methods in Physical Chemistry* **1,** 419–444 (Wiley-VCH Verlag GmbH & Co. KGaA, 2012).

38.   Long, D. A. *The Raman Effect: A Unified Treatment of the Theory of Raman Scattering by Molecules. John Wiley & Sons Ltd* **8,** (John Wiley & Sons, Ltd, 2002).

39.   Ellis, D. I. & Goodacre, R. Metabolic fingerprinting in disease diagnosis: Biomedical applications of infrared and Raman spectroscopy. *Analyst* **131,** 875–885 (2006).

40.   Boyaci, I. H. *et al.* Dispersive and FT-Raman spectroscopic methods in food analysis. *RSC Advances* **5,** 56606–56624 (2015).

41.   Tipping, W. J., Lee, M., Serrels, A., Brunton, V. G. & Hulme, A. N. Stimulated Raman scattering microscopy: an emerging tool for drug discovery. *Chem. Soc. Rev.* **45,** 2075–89 (2016).

42.   Hehl, G. *et al.* Coherent Raman Scattering Microscopy: New Quantitative and Non-Invasive Tools for Biomedical Research. *Biophys. J.* **102,** 617a (2012).

43.   Swain, R. J. & Stevens, M. M. Raman microspectroscopy for non-invasive biochemical analysis of single cells. *Biochem. Soc. Trans.* **35,** 544–549 (2007).

44.   Brauchle, E. *et al.* Biomechanical and biomolecular characterization of extracellular matrix structures in human colon carcinomas. *Matrix Biol.* **68–69,** 180–193 (2018).

45.   Brauchle, E. *et al.* Raman microspectroscopy as a diagnostic tool for the non-invasive analysis of fibrillin-1 deficiency in the skin and in the in vitro skin models. *Acta Biomater.* **52,** 41–48 (2017).

46.   Picardi, G. *et al.* Tissue degeneration in ALS affected spinal cord evaluated by Raman spectroscopy. *Sci. Rep.* **8,** 13110 (2018).

47.   Rowe, P. I. *et al.* Thermal stability of intralipid optical phantoms. *Appl. Spectrosc.* **67,** 993–996 (2013).

48.   Marzi, J., Brauchle, E. M., Schenke-Layland, K. & Rolle, M. W. Non-invasive

functional molecular phenotyping of human smooth muscle cells utilized in cardiovascular tissue engineering. *Acta Biomater.* **89,** 193–205 (2019).

49. Dunteman H., G. & Dunteman H., G. *Principal Component Analysis. Ser. Newbury Park SAGE, Quant. Appl. Soc. Sci.* (Springer-Verlag, 1989).

50. Fouse, S. D. *et al.* Promoter CpG Methylation Contributes to ES Cell Gene Regulation in Parallel with Oct4/Nanog, PcG Complex, and Histone H3 K4/K27 Trimethylation. *Cell Stem Cell* **2,** 160–169 (2008).

51. Kessler, R. W. *Prozessanalytik: Strategien und Fallbeispiele aus der industriellen Praxis.* (Wiley-VCH, 2012).

52. Catto, V., Farè, S., Freddi, G. & Tanzi, M. C. Vascular Tissue Engineering: Recent Advances in Small Diameter Blood Vessel Regeneration. *ISRN Vasc. Med.* **2014,** 1–27 (2014).

53. Wang, H. *et al.* Global, regional, and national life expectancy, all-cause mortality, and cause-specific mortality for 249 causes of death, 1980–2015: a systematic analysis for the Global Burden of Disease Study 2015. *Lancet* **388,** 1459–1544 (2016).

54. Mathur, R. Role of diabetes, hypertension, and cigarette smoking on atherosclerosis. *J. Cardiovasc. Dis. Res.* **1,** 64–68 (2010).

55. Carnall, D. Angioplasty. *BMJ* **321,** 122 (2000).

56. Koneru, S. *et al.* Long-term clinical outcome of rescue balloon angioplasty compared with rescue stenting after failed thrombolysis. *Hear. Dis.* **3,** 217–220 (2001).

57. Chlupáč, J., Filová, E., Bačáková, L. & Bačáková, L. Blood Vessel Replacement: 50 years of Development and Tissue Engineering Paradigms in Vascular Surgery. *Physiol. Res* **58,** 119–139 (2009).

58. Sánchez, P. F., Brey, E. M. & Carlos Briceño, J. Endothelialization mechanisms in vascular grafts. *J. Tissue Eng. Regen. Med.* **12,** 2164–2178 (2018).

59. Chang, W. G. & Niklason, L. E. A short discourse on vascular tissue engineering. *npj Regen. Med.* **2,** 1–8 (2017).

60. Ercolani, E., Del Gaudio, C. & Bianco, A. Vascular tissue engineering of small-diameter blood vessels: Reviewing the electrospinning approach. *Journal of Tissue Engineering and Regenerative Medicine* **9,** 861–888 (2015).

61. Seifu, D. G., Purnama, A., Mequanint, K. & Mantovani, D. Small-diameter vascular tissue engineering. *Nature Reviews Cardiology* **10,** 410–421 (2013).

62. Ravi, S., Qu, Z. & Chaikof, E. L. Polymeric materials for tissue engineering of arterial substitutes. *Vascular* **17,** (2009).

63. Félétou, M. Multiple Functions of the Endothelial Cells. (2011).

64. Davis, G. E. & Senger, D. R. Endothelial extracellular matrix: Biosynthesis, remodeling, and functions during vascular morphogenesis and neovessel stabilization. *Circulation Research* **97,** 1093–1107 (2005).

65. Sanes, J. R. The basement membrane/basal lamina of skeletal muscle. *Journal of Biological Chemistry* **278,** 12601–12604 (2003).

66. Mouw, J. K., Ou, G. & Weaver, V. M. Extracellular matrix assembly: A multiscale deconstruction. *Nature Reviews Molecular Cell Biology* **15,** 771–785 (2014).

67. Jayadev, R. & Sherwood, D. R. Basement membranes. *Current Biology* **27,** R207–R211 (2017).

68. Järveläinen, H., Sainio, A. & Wight, T. N. Pivotal role for decorin in angiogenesis. *Matrix Biol.* **43,** 15–26 (2015).

69. Riessen, R. *et al.* Regional differences in the distribution of the proteoglycans biglycan and decorin in the extracellular matrix of atherosclerotic and restenotic human coronary arteries. *Am. J. Pathol.* **144,** 962–74 (1994).

70. Salisbury, B. G. & Wagner, W. D. Isolation and preliminary characterization of proteoglycans dissociatively extracted from human aorta. *J. Biol. Chem.* **256,** 8050–7 (1981).

71. Pozzi, A. & Zent, R. Regulation of endothelial cell functions by basement

membrane- and arachidonic acid-derived products. *Wiley Interdiscip. Rev. Syst. Biol. Med.* **1,** 254–272 (2009).

72. LeBleu, V. S., MacDonald, B. & Kalluri, R. Structure and function of basement membranes. *Experimental Biology and Medicine* **232,** 1121–1129 (2007).

73. Bacakova, L. *et al.* The Role of Vascular Smooth Muscle Cells in the Physiology and Pathophysiology of Blood Vessels. in *Muscle Cell and Tissue - Current Status of Research Field* 229 (IntechOpen, 2018).

74. Stenmark, K. R. *et al.* The Adventitia: Essential Regulator of Vascular Wall Structure and Function. *Annu. Rev. Physiol.* **75,** 23–47 (2013).

75. Witter, K., Tonar, Z. & Schöpper, H. How many Layers has the Adventitia? - Structure of the Arterial Tunica Externa Revisited. *Anat. Histol. Embryol.* **46,** 110–120 (2017).

76. Baikoussis, N. G. *et al.* The implication of vasa vasorum in surgical diseases of the aorta. *Eur. J. Cardio-Thoracic Surg.* **40,** 412–417 (2011).

77. Marieb, E. N. & Hoehn, K. *Human anatomy & physiology*.

78. Hoerstrup, S. P. *et al.* Tissue engineering of small caliber vascular grafts. *Eur. J. Cardio-thoracic Surg.* **20,** 164–169 (2001).

79. Serbo, J. V. & Gerecht, S. Vascular tissue engineering: Biodegradable scaffold platforms to promote angiogenesis. *Stem Cell Res. Ther.* **4,** 8 (2013).

80. Zhang, W. J., Liu, W., Cui, L. & Cao, Y. Tissue engineering of blood vessel: Tissue Engineering Review Series. *J. Cell. Mol. Med.* **11,** 945–957 (2007).

81. Bajpai, V. K. & Andreadis, S. T. Stem cell sources for vascular tissue engineering and regeneration. *Tissue Eng. - Part B Rev.* **18,** 405–425 (2012).

82. Hur, J. *et al.* Characterization of Two Types of Endothelial Progenitor Cells and Their Different Contributions to Neovasculogenesis. *Arterioscler. Thromb. Vasc. Biol.* **24,** 288–293 (2004).

83. Yoder, M. C. *et al.* Redefining endothelial progenitor cells via clonal analysis and hematopoietic stem/progenitor cell principals. in *Blood* **109,** 1801–1809 (The American Society of Hematology, 2007).

84. Allan, D. S. & Strunk, D. *Regenerative therapy using blood-derived stem cells*. (Humana Press, 2012).

85. Wobus, A. M. & Boheler, K. R. Embryonic stem cells: Prospects for developmental biology and cell therapy. *Physiological Reviews* **85,** 635–678 (2005).

86. Cong, X., Zhang, S.-M., Batty, L. & Luo, J. Application of Human Induced Pluripotent Stem Cells in Generating Tissue-Engineered Blood Vessels as Vascular Grafts. *Stem Cells Dev.* **28,** 1581–1594 (2019).

87. Takahashi, K. & Yamanaka, S. Induction of Pluripotent Stem Cells from Mouse Embryonic and Adult Fibroblast Cultures by Defined Factors. *Cell* **126,** 663–676 (2006).

88. Wang, Z., Mithieux, S. M. & Weiss, A. S. Fabrication Techniques for Vascular and Vascularized Tissue Engineering. *Adv. Healthc. Mater.* **8,** 1900742 (2019).

89. Xu, W. *et al.* Mechanical properties of small-diameter polyurethane vascular grafts reinforced by weft-knitted tubular fabric. *J. Biomed. Mater. Res. - Part A* **92,** 1–8 (2010).

90. He, W. *et al.* The Preparation and Performance of a New Polyurethane Vascular Prosthesis. *Cell Biochem. Biophys.* **66,** 855–866 (2013).

91. Kanie, K. *et al.* Collagen type IV-specific tripeptides for selective adhesion of endothelial and smooth muscle cells. *Biotechnol. Bioeng.* **109,** 1808–1816 (2012).

92. Li, J. *et al.* A novel strategy to graft RGD peptide on biomaterials surfaces for endothelization of small-diamater vascular grafts and tissue engineering blood vessel. in *Journal of Materials Science: Materials in Medicine* **19,** 2595–2603 (2008).

93. Barron, V., Lyons, E., Stenson-Cox, C., McHugh, P. E. & Pandit, A. Bioreactors for Cardiovascular Cell and Tissue Growth: A Review. *Annals of Biomedical Engineering* **31,** 1017–1030 (2003).

94. Maschhoff, P. *et al.* An intelligent bioreactor system for the cultivation of a bioartificial vascular graft. *Eng. Life Sci.* **17,** 567–578 (2017).

95. Zhou, J., Li, Y. S. & Chien, S. Shear stress-initiated signaling and its regulation of endothelial function. *Arterioscler. Thromb. Vasc. Biol.* **34,** 2191–2198 (2014).

96. Pashneh-Tala, S., MacNeil, S. & Claeyssens, F. The tissue-engineered vascular graft - Past, present, and future. *Tissue Engineering - Part B: Reviews* **22,** 68–100 (2016).

97. Daum, R. *et al.* Fibronectin Adsorption on Electrospun Synthetic Vascular Grafts Attracts Endothelial Progenitor Cells and Promotes Endothelialization in Dynamic In Vitro Culture. *Cells* **9,** 778 (2020).

98. Melchiorri, A. J., Hibino, N. & Fisher, J. P. Strategies and techniques to enhance the in situ endothelialization of small-diameter biodegradable polymeric vascular grafts. *Tissue Eng. Part B. Rev.* **19,** 292–307 (2013).

99. Zhang, M. *et al.* Immobilization of anti-CD31 antibody on electrospun poly(e{open}-caprolactone) scaffolds through hydrophobins for specific adhesion of endothelial cells. *Colloids Surfaces B Biointerfaces* **85,** 32–39 (2011).

100. Edlund, U., Sauter, T. & Albertsson, A.-C. Covalent VEGF protein immobilization on resorbable polymeric surfaces. *Polym. Adv. Technol.* **22,** 166–171 (2011).

101. Strahm, Y. *et al.* Endothelial-cell-binding aptamer for coating of intracoronary stents. *J. Invasive Cardiol.* **22,** 481–487 (2010).

102. Tardif, K. *et al.* A phosphorylcholine-modified chitosan polymer as an endothelial progenitor cell supporting matrix. *Biomaterials* **32,** 5046–5055 (2011).

103. Sgarioto, M. *et al.* Collagen type I together with fibronectin provide a better support for endothelialization. *Comptes Rendus - Biol.* **335,** 520–528 (2012).

104. Wang, X. *et al.* Extracellular matrix inspired surface functionalization with heparin, fibronectin and VEGF provides an anticoagulant and endothelialization supporting microenvironment. *Appl. Surf. Sci.* **320,** 871–882 (2014).

105. Xue, J., Wu, T., Dai, Y. & Xia, Y. Electrospinning and electrospun nanofibers: Methods, materials, and applications. *Chemical Reviews* **119,** 5298–5415 (2019).

106. Gonzales, R. R. *et al.* Modification of nanofiber support layer for thin film composite forward osmosis membranes via layer-by-layer polyelectrolyte deposition. *Membranes (Basel).* **8,** (2018).

107. Vlachou, M., Siamidi, A. & Kyriakou, S. Electrospinning and Drug Delivery. in *Electrospinning and Electrospraying - Techniques and Applications* (IntechOpen, 2019).

108. Hinderer, S., Brauchle, E. & Schenke-Layland, K. Generation and Assessment of Functional Biomaterial Scaffolds for Applications in Cardiovascular Tissue Engineering and Regenerative Medicine. *Adv. Healthc. Mater.* **4,** 2326–2341 (2015).

109. Ndreu, A., Nikkola, L., Ylikauppilar, H., Ashammakhi, N. & Hasirci, V. Electrospun biodegradable nanofibrous mats for tissue engineering. *Nanomedicine* **3,** 45–60 (2008).

110. Li, M. *et al.* Electrospun protein fibers as matrices for tissue engineering. *Biomaterials* **26,** 5999–6008 (2005).

111. Boland, E. D. *et al.* Electrospinning collagen and elastin: Preliminary vascular tissue engineering. *Front. Biosci.* **9,** 1422–1432 (2004).

112. Matthews, J. A., Wnek, G. E., Simpson, D. G. & Bowlin, G. L. Electrospinning of collagen nanofibers. *Biomacromolecules* **3,** 232–238 (2002).

113. Piccirillo, G. *et al.* Non-invasive characterization of hybrid gelatin:poly-l-lactide electrospun scaffolds using second harmonic generation and multiphoton imaging. *J. Mater. Chem. B* **6,** 6399–6412 (2018).

114. Hinderer, S. *et al.* Engineering of a bio-functionalized hybrid off-the-shelf heart valve. *Biomaterials* **35,** 2130–2139 (2014).

115. Jaffer, I. H. & Weitz, J. I. The blood compatibility challenge. Part 1: Blood-contacting medical devices: The scope of the problem. *Acta Biomaterialia* **94,** 2–

10 (2019).

116. Hlady, V. & Buijs, J. Protein adsorption on solid surfaces. *Curr. Opin. Biotechnol.* **7,** 72–77 (1996).

117. Malmsten, M. Formation of adsorbed protein layers. *J. Colloid Interface Sci.* **207,** 186–199 (1998).

118. Schmidt, D. R., Waldeck, H. & Kao, W. J. Protein Adsorption to Biomaterials. in *Biological Interactions on Materials Surfaces* 1–18 (Springer US, 2009).

119. Andrew White - Research. Available at: http://andrew-white.com/research/rational. (Accessed: 19th November 2020)

120. Nakanishi, K., Sakiyama, T. & Imamura, K. On the adsorption of proteins on solid surfaces, a common but very complicated phenomenon. *Journal of Bioscience and Bioengineering* **91,** 233–244 (2001).

121. Bremer, M. G. E. G., Duval, J., Norde, W. & Lyklema, J. Electrostatic interactions between immunoglobulin (IgG) molecules and a charged sorbent. in *Colloids and Surfaces A: Physicochemical and Engineering Aspects* **250,** 29–42 (Elsevier B.V., 2004).

122. Jones, K. L. & O'Melia, C. R. Protein and humic acid adsorption onto hydrophilic membrane surfaces: Effects of pH and ionic strength. *J. Memb. Sci.* **165,** 31–46 (2000).

123. Andrade, J. D., Hlady, V. & Wei, A. P. Adsorption of complex proteins at interfaces. *Pure Appl. Chem.* **64,** 1777–1781 (1992).

124. Rabe, M., Verdes, D. & Seeger, S. Understanding protein adsorption phenomena at solid surfaces. *Advances in Colloid and Interface Science* **162,** 87–106 (2011).

125. Norde, W. My voyage of discovery to proteins in flatland ...and beyond. *Colloids and Surfaces B: Biointerfaces* **61,** 1–9 (2008).

126. ANDRADE, J. D. & HLADY, V. Plasma Protein Adsorption: The Big Twelve. *Ann. N. Y. Acad. Sci.* **516,** 158–172 (1987).

127. Vroman, L. Effect of adsorbed proteins on the wettability of hydrophilic and hydrophobic solids. *Nature* **196,** 476–477 (1962).

128. Wilson, C. J., Clegg, R. E., Leavesley, D. I. & Pearcy, M. J. Mediation of biomaterial-cell interactions by adsorbed proteins: A review. *Tissue Engineering* **11,** 1–18 (2005).

129. Curtis, A. S. G. & Forrester, J. V. The Competitive Effects of Serum Proteins on Cell Adhesion. *J. Cell Sci* **71,** 17–35 (1984).

130. Hlady, V., Buijs, J. & Jennissen, H. P. Methods for studying protein adsorption. *Methods Enzymol.* **309,** 402–429 (1999).

131. Song, K., Lee, J., Choi, S. O. & Kim, J. Interaction of surface energy components between solid and liquid on wettabilit. *Polymers (Basel).* **11,** (2019).

132. Vogler, E. A. Protein adsorption in three dimensions. *Biomaterials* **33,** 1201–1237 (2012).

133. Silva, R. A., Urzúa, M. D., Petri, D. F. S. & Dubin, P. L. Protein adsorption onto polyelectrolyte layers: Effects of protein hydrophobicity and charge anisotropy. *Langmuir* **26,** 14032–14038 (2010).

134. Jana, S. Endothelialization of cardiovascular devices. *Acta Biomaterialia* **99,** 53–71 (2019).

135. Caiado, F. & Dias, S. *Endothelial progenitor cells and integrins: adhesive needs. Fibrogenesis & Tissue Repair* **5,** (2012).

136. Verdanova, M., Sauerova, P., Hempel, U. & Kalbacova, M. H. Initial cell adhesion of three cell types in the presence and absence of serum proteins. *Histochem. Cell Biol.* **148,** 273–288 (2017).

137. Wu, C. Focal Adhesion: A Focal Point in Current Cell Biology and Molecular Medicine. *Cell Adh. Migr.* **1,** 13–18 (2007).

138. Kanchanawong, P. *et al.* Nanoscale architecture of integrin-based cell adhesions. *Nature* **468,** 580–584 (2010).

139. Zaidel-Bar, R., Cohen, M., Addadi, L. & Geiger, B. Hierarchical assembly of cell-

matrix adhesion complexes. in *Biochemical Society Transactions* **32,** 416–420 (Portland Press, 2004).

140. Geiman, T. M. & Muegge, K. DNA methylation in early development. *Mol. Reprod. Dev.* **77,** 105–113 (2010).

141. Kaneda, M. *et al.* Essential role for de novo DNA methyltransferase Dnmt3a in paternal and maternal imprinting. *Nature* **429,** 900–903 (2004).

142. Liu, J., B Hesson, L. & Ward, R. L. Liquid Chromatography Tandem Mass Spectrometry for the Measurement of Global DNA Methylation and Hydroxymethylation. *J. Proteomics Bioinform.* **01,** (2013).

143. Frommer, M. *et al.* A genomic sequencing protocol that yields a positive display of 5-methylcytosine residues in individual DNA strands. *Proc. Natl. Acad. Sci. U. S. A.* **89,** 1827–31 (1992).

144. Huang, Z. *et al.* Near-infrared Raman spectroscopy for optical diagnosis of lung cancer. *Int. J. Cancer* **107,** 1047–1052 (2003).

145. Stone, N., Kendall, C., Smith, J., Crow, P. & Barr, H. Raman Spectroscopy for Identification of Epithelial Cancers. *Faraday Discuss.* **126,** 141–157 (2004).

146. Ruiz-Chica, a. J., Medina, M. a., Sánchez-Jiménez, F. & Ramírez, F. J. Characterization by Raman spectroscopy of conformational changes on guanine– cytosine and adenine–thymine oligonucleotides induced by aminooxy analogues of spermidine. *J. Raman Spectrosc.* **35,** 93–100 (2004).

147. Katainen, E. *et al.* Quantification of the amphetamine content in seized street samples by Raman spectroscopy. *J. Forensic Sci.* **52,** 88–92 (2007).

148. Ying, Q.-L. *et al.* The ground state of embryonic stem cell self-renewal. *Nature* **453,** 519–523 (2008).

149. Silva, J. *et al.* Promotion of reprogramming to ground state pluripotency by signal inhibition. *PLoS Biol.* **6,** 2237–2247 (2008).

150. Leitch, H. G. *et al.* Naive pluripotency is associated with global DNA hypomethylation. *Nat. Struct. Mol. Biol.* **20,** 311–6 (2013).

151. Movasaghi, Z., Rehman, S. & Rehman, I. U. Raman Spectroscopy of Biological Tissues. *Appl. Spectrosc. Rev.* **42,** 493–541 (2007).

152. Carrabba, M. & Madeddu, P. Current strategies for the manufacture of small size tissue engineering vascular grafts. *Frontiers in Bioengineering and Biotechnology* **6,** (2018).

153. Hinderer, S. *et al.* Surface functionalization of electrospun scaffolds using recombinant human decorin attracts circulating endothelial progenitor cells. *Sci. Rep.* **8,** 110 (2018).

154. Lenselink, E. A. Role of fibronectin in normal wound healing. *Int. Wound J.* **12,** 313–316 (2015).

155. Grinnell, F. Fibronectin and wound healing. *Journal of Cellular Biochemistry* **26,** 107–116 (1984).

156. Kutuzova, L. *et al.* In vitro bio-stability screening of novel implantable polyurethane elastomers: Morphological design and mechanical aspects. *Curr. Dir. Biomed. Eng.* **4,** 535–538 (2018).

157. Athanasopulu, K., Kutuzova, L., Thiel, J., Lorenz, G. & Kemkemer, R. Enhancing the biocompatibility of siliconepolycarbonate urethane based implant materials. *Curr. Dir. Biomed. Eng.* **5,** 453–455 (2019).

158. Liliensiek, S. J., Nealey, P. & Murphy, C. J. Characterization of endothelial basement membrane nanotopography in rhesus macaque as a guide for vessel tissue engineering. *Tissue Eng. Part A* **15,** 2643–51 (2009).

159. Abrams, G. A., Murphy, C. J., Wang, Z. Y., Nealey, P. F. & Bjorling, D. E. Ultrastructural basement membrane topography of the bladder epithelium. *Urol. Res.* **31,** 341–346 (2003).

160. Hironaka, K., Makino, H., Yamasaki, Y. & Ota, Z. *Renal basement membranes by ultrahigh resolution scanning electron microscopy. Kidney International* **43,** (1993).

161. Takeuchi, T. & Gonda, T. Distribution of the pores of epithelial basement

membrane in the rat small intestine. *J. Vet. Med. Sci.* **66,** 695–700 (2004).

162. Yurchenco, P. D. & Ruben, G. C. Basement membrane structure in situ: Evidence for lateral associations in the type IV collagen network. *J. Cell Biol.* **105,** 2559–2568 (1987).

163. Howat, W. J., Holmes, J. A., Holgate, S. T. & Lackie, P. M. Basement membrane pores in human bronchial epithelium: A conduit for infiltrating cells? *Am. J. Pathol.* **158,** 673–680 (2001).

164. Salmerón-Sánchez, M. *et al.* Role of material-driven fibronectin fibrillogenesis in cell differentiation. *Biomaterials* **32,** 2099–2105 (2011).

165. Sevilla, C. A., Dalecki, D. & Hocking, D. C. Regional Fibronectin and Collagen Fibril Co-Assembly Directs Cell Proliferation and Microtissue Morphology. *PLoS One* **8,** e77316 (2013).

166. Laterreur, V. *et al.* Comparison of the direct burst pressure and the ring tensile test methods for mechanical characterization of tissue-engineered vascular substitutes. *J. Mech. Behav. Biomed. Mater.* **34,** 253–263 (2014).

167. Ishizaki, T., Saito, N. & Takai, O. Correlation of cell adhesive behaviors on superhydrophobic, superhydrophilic, and micropatterned superhydrophobic/superhydrophilic surfaces to their surface chemistry. *Langmuir* **26,** 8147–8154 (2010).

168. Dee, K. C., Puleo, D. A. & Bizios, R. Protein-Surface Interactions. in *An Introduction to Tissue-Biomaterial Interaction* 37–51 (Wiley, 2002).

169. Thyparambil, A. A., Wei, Y. & Latour, R. A. Experimental characterization of adsorbed protein orientation, conformation, and bioactivity. *Biointerphases* **10,** 019002 (2015).

170. Latour, R. A. Molecular Simulation of Protein-Surface Interactions. in *Biological Interactions on Material Surfaces* (eds. Puleo, D. A. & Bizios, R.) 73–74 (Springer US, 2009).

171. Lebaron, R. G. & Athanasiou, K. A. Extracellular matrix cell adhesion peptides: Functional applications in orthopedic materials. *Tissue Engineering* **6,** 85–103 (2000).

172. Dejana, E., Hirschi, K. K. & Simons, M. The molecular basis of endothelial cell plasticity. *Nature Communications* **8,** (2017).

173. Lacorre, D. A. *et al.* Plasticity of endothelial cells: Rapid dedifferentiation of freshly isolated high endothelial venule endothelial cells outside the lymphoid tissue microenvironment. *Blood* **103,** 4164–4172 (2004).

174. Adipurnama, I., Yang, M. C., Ciach, T. & Butruk-Raszeja, B. Surface modification and endothelialization of polyurethane for vascular tissue engineering applications: A review. *Biomaterials Science* **5,** 22–37 (2017).

175. Hoshi, R. A. *et al.* The blood and vascular cell compatibility of heparin-modified ePTFE vascular grafts. *Biomaterials* **34,** 30–41 (2013).

176. Sridharan, R., Cameron, A. R., Kelly, D. J., Kearney, C. J. & O'Brien, F. J. Biomaterial based modulation of macrophage polarization: A review and suggested design principles. *Materials Today* **18,** 313–325 (2015).

177. Parisi, L. *et al.* A glance on the role of fibronectin in controlling cell response at biomaterial interface. *Japanese Dental Science Review* **56,** 50–55 (2020).

178. Seeger, J. M. & Klingman, N. Improved in vivo endothelialization of prosthetic grafts by surface modification with fibronectin. *J. Vasc. Surg.* **8,** 476–482 (1988).

179. Choi, W. S. *et al.* Enhanced Patency and Endothelialization of Small-Caliber Vascular Grafts Fabricated by Coimmobilization of Heparin and Cell-Adhesive Peptides. *ACS Appl. Mater. Interfaces* **8,** 4336–4346 (2016).

180. To, W. S. & Midwood, K. S. Plasma and cellular fibronectin: Distinct and independent functions during tissue repair. *Fibrogenesis and Tissue Repair* **4,** 21 (2011).

181. Lai, C. S. *et al.* Solution structure of human plasma fibronectin under different solvent conditions: Fluorescence energy transfer, circular dichroism and light-

scattering studies. *J. Mol. Biol.* **230,** 625–640 (1993).

182. Tooney, N. M., Mosesson, M. W., Amrani, D. L., Hainfeld, J. F. & Wall, J. S. Solution and surface effects on plasma fibronectin structure. *J. Cell Biol.* **97,** 1686–1692 (1983).

183. Cantini, M., Rico, P., Moratal, D. & Salmerón-Sánchez, M. Controlled wettability, same chemistry: Biological activity of plasma-polymerized coatings. *Soft Matter* **8,** 5575–5584 (2012).

184. Thevenot, P., Hu, W. & Tang, L. Surface chemistry influences implant biocompatibility. *Curr. Top. Med. Chem.* **8,** 270–80 (2008).

185. Hovgaard, M. B., Rechendorff, K., Chevallier, J., Foss, M. & Besenbacher, F. Fibronectin adsorption on tantalum: The influence of nanoroughness. *J. Phys. Chem. B* **112,** 8241–8249 (2008).

186. García, A. J., Vega, M. D. & Boettiger, D. Modulation of cell proliferation and differentiation through substrate-dependent changes in fibronectin conformation. *Mol. Biol. Cell* **10,** 785–98 (1999).

187. Keselowsky, B. G., Collard, D. M. & García, A. J. Surface chemistry modulates fibronectin conformation and directs integrin binding and specificity to control cell adhesion. *J. Biomed. Mater. Res. - Part A* **66,** 247–259 (2003).

188. Campillo-Fernández, A. J. *et al.* Analysis of the Biological Response of Endothelial and Fibroblast Cells Cultured on Synthetic Scaffolds with Various Hydrophilic/Hydrophobic Ratios: Influence of Fibronectin Adsorption and Conformation. *Tissue Eng. Part A* **15,** 1331–1341 (2009).

189. Bowditch, R. *et al.* Integrin alpha IIb beta 3 (platelet GPIIb-IIIa) recognizes multiple sites in fibronectin. *J. Biol. Chem.* **266,** 23323–23328 (1991).

190. Ambesi, A., Klein, R. M., Pumiglia, K. M. & McKeown-Longo, P. J. Anastellin, a fragment of the first type III repeat of fibronectin, inhibits extracellular signal-regulated kinase and causes G(1) arrest in human microvessel endothelial cells. *Cancer Res.* **65,** 148–56 (2005).

191. Homandberg, G. A., Kramer-Bjerke, J., Grant, D., Christianson, G. & Eisenstein, R. Heparin-binding fragments of fibronectin are potent inhibitors of endothelial cell growth: structure-function correlations. *Biochim. Biophys. Acta (BBA)/Protein Struct. Mol.* **874,** 61–71 (1986).

192. Podestá, F., Roth, T., Ferrara, F., Cagliero, E. & Lorenzi, M. Cytoskeletal changes induced by excess extracellular matrix impair endothelial cell replication. *Diabetologia* **40,** 879–886 (1997).

193. Schnittler, H. *et al.* Actin filament dynamics and endothelial cell junctions: The Ying and Yang between stabilization and motion. *Cell and Tissue Research* **355,** 529–543 (2014).

194. Danen, E. H. J., Sonneveld, P., Brakebusch, C., Fässler, R. & Sonnenberg, A. The fibronectin-binding integrins α5β1 and αvβ3 differentially modulate RhoA-GTP loading, organization of cell matrix adhesions, and fibronectin fibrillogenesis. *J. Cell Biol.* **159,** 1071–1086 (2002).

195. Jahed, Z., Shams, H., Mehrbod, M. & Mofrad, M. R. K. Mechanotransduction pathways linking the extracellular matrix to the nucleus. in *International Review of Cell and Molecular Biology* **310,** 171–220 (Elsevier Inc., 2014).

196. Saunders, R. M. *et al.* Role of vinculin in regulating focal adhesion turnover. *Eur. J. Cell Biol.* **85,** 487–500 (2006).

197. Taha, A. A. & Schnittler, H. J. Dynamics between actin and the VE-cadherin/catenin complex: Novel aspects of the ARP2/3 complex in regulation of endothelial junctions. *Cell Adhesion and Migration* **8,** 125–135 (2014).

198. Sales, A. *et al.* Cell Type-Dependent Integrin Distribution in Adhesion and Migration Responses on Protein-Coated Microgrooved Substrates. *ACS Omega* **4,** 1791–1800 (2019).

199. Gilmore, A. P. & Romer, L. H. Inhibition of focal adhesion kinase (FAK) signaling in focal adhesions decreases cell motility and proliferation. *Mol. Biol. Cell* **7,** 1209–

1224 (1996).

200. Katoh, K. Activation of Rho-kinase and focal adhesion kinase regulates the organization of stress fibers and focal adhesions in the central part of fibroblasts. *PeerJ* **2017,** e4063 (2017).

201. Lawson, C. & Schlaepfer, D. D. Integrin adhesions: Who's on first? What's on second?: Connections between FAK and talin. *Cell Adhesion and Migration* **6,** 302–306 (2012).

202. Lampugnani, M. G. Endothelial cell-to-cell junctions: Adhesion and signaling in physiology and pathology. *Cold Spring Harb. Perspect. Med.* **2,** a006528 (2012).

203. Alliance for Regenerative Medicine. *Clinical Trials in Europe: Recent Trends in ATMP Development.* (2019).

204. Brauchle, E., Thude, S., Brucker, S. Y. & Schenke-Layland, K. Cell Death Stages in Single Apoptotic and Necrotic Cells Monitored by Raman Microspectroscopy. *Sci. Rep.* **4,** 4698 (2014).

205. Brauchle, E. *et al.* Non-invasive Chamber-Specific Identification of Cardiomyocytes in Differentiating Pluripotent Stem Cells. *Stem Cell Reports* **6,** 188–199 (2016).

206. Eder, C. & Wild, C. Technology forecast: advanced therapies in late clinical research, EMA approval or clinical application via hospital exemption. *J. Mark. Access Heal. Policy* **7,** 1600939 (2019).

207. Feng, X. *et al.* Raman biophysical markers in skin cancer diagnosis. *J. Biomed. Opt.* **23,** 1 (2018).

208. Zheng, Q. *et al.* Raman spectroscopy as a potential diagnostic tool to analyse biochemical alterations in lung cancer. *Analyst* **145,** 385–392 (2020).

209. Lombardini, A. *et al.* High-resolution multimodal flexible coherent Raman endoscope article. *Light Sci. Appl.* **7,** 2047–7538 (2018).

210. Zhong, J., Agha, G. & Baccarelli, A. A. The Role of DNA Methylation in Cardiovascular Risk and Disease: Methodological Aspects, Study Design, and Data Analysis for Epidemiological Studies. *Circulation Research* **118,** 119–131 (2016).

211. Nogueira, G. V. *et al.* Raman spectroscopy study of atherosclerosis in human carotid artery. *J. Biomed. Opt.* **10,** 031117 (2005).

212. You, A. Y. F. *et al.* Raman spectroscopy imaging reveals interplay between atherosclerosis and medial calcification in the human aorta. *Sci. Adv.* **3,** 1701156 (2017).

213. Barkholt, L., Voltz-Girolt, C., Raine, J., Salmonson, T. & Schüssler-Lenz, M. European regulatory experience with advanced therapy medicinal products. *Nature Reviews Drug Discovery* **18,** 8–9 (2018).

214. ATPM mit EU-Zulassung | Übersicht des vfa. Available at: https://www.vfa.de/de/arzneimittel-forschung/datenbanken-zu-arzneimitteln/atmp. (Accessed: 4th July 2020)

215. Yu, T. T. L., Gupta, P., Ronfard, V., Vertès, A. A. & Bayon, Y. Recent progress in European advanced therapy medicinal products and beyond. *Front. Bioeng. Biotechnol.* **6,** 130 (2018).

216. Support for advanced-therapy developers | European Medicines Agency. Available at: https://www.ema.europa.eu/en/human-regulatory/research-development/advanced-therapies/support-advanced-therapy-developers. (Accessed: 14th August 2020)

217. Jørgensen, J. & Kefalas, P. Reimbursement of licensed cell and gene therapies across the major European healthcare markets. *J. Mark. Access Heal. Policy* **3,** 29321 (2015).

218. Li, S., Sengupta, D. & Chien, S. Vascular tissue engineering: From in vitro to in situ. *Wiley Interdisciplinary Reviews: Systems Biology and Medicine* **6,** 61–76 (2014).

219. Rothuizen, T. C. *et al.* Development and evaluation of in vivo tissue engineered

blood vessels in a porcine model. *Biomaterials* **75,** 82–90 (2016).

220. Scott, R. A., Paderi, J. E., Sturek, M. & Panitch, A. Decorin Mimic Inhibits Vascular Smooth Muscle Proliferation and Migration. *PLoS One* **8,** e82456 (2013).

221. Nili, N. *et al.* Decorin inhibition of PDGF-stimulated vascular smooth muscle cell function: Potential mechanism for inhibition of intimal hyperplasia after balloon angioplasty. *Am. J. Pathol.* **163,** 869–878 (2003).

222. Sivaraman, B. & Latour, R. A. The Adherence of platelets to adsorbed albumin by receptor-mediated recognition of binding sites exposed by adsorption-induced unfolding. *Biomaterials* **31,** 1036–1044 (2010).

223. Horbett, T. A. Fibrinogen adsorption to biomaterials. *Journal of Biomedical Materials Research - Part A* **106,** 2777–2788 (2018).

224. Evans-Nguyen, K. M. & Schoenfisch, M. H. Fibrin proliferation at model surfaces: Influence of surface properties. *Langmuir* **21,** 1691–1694 (2005).

225. Harvey, A. G., Hill, E. W. & Bayat, A. Designing implant surface topography for improved biocompatibility. *Expert Review of Medical Devices* **10,** 257–267 (2013).

226. Llopis-Hernández, V. *et al.* Material-driven fibronectin assembly for high-efficiency presentation of growth factors. *Sci. Adv.* **2,** E1600188 (2016).

227. Theunissen, T. W. *et al.* Molecular Criteria for Defining the Naive Human Pluripotent State. *Cell Stem Cell* **19,** 502–515 (2016).

228. Bouchie, A. Tissue engineering firms go under. *Nature Biotechnology* **20,** 1178–1179 (2002).

Acknowledgements

Ein großer Dank gilt meiner Doktormutter Prof. Dr. Katja Schenke-Layland. Ihre fachliche Unterstützung, ihr Blick auf das Ziel, ihre Geduld und ihre Art mich zu motivieren haben mir sehr geholfen und mich vorangebracht.

Des Weiteren danke ich Prof. Dr. Ralf Kemkemer und Prof. Dr. Chassé für die Leitung und Organisation des Promotionskollegs IPMB der Universität Tübingen und der Hochschule Reutlingen. Bei Prof. Dr. Ralf Kemkemer bedanke ich mich zudem für seine Unterstützung als zweiter Berichterstatter.

Mein Dank gilt auch Prof. Dr. Martina Seifert sowie Constanze Wild für die gute Zusammenarbeit im DFG-Projekt.

Ich möchte mich besonders bei Dr. Eva Brauchle für ihre Unterstützung im ersten Jahr meiner Doktorarbeit, für ihre genialen Ideen und ihre große Hilfsbereitschaft bedanken.

Ebenfalls danken möchte ich Dr. Svenja Hinderer für die Betreuung meiner Doktorarbeit sowie ihrer fachlichen Unterstützung und Diskussionsbereitschaft.

Martin Weiss danke ich für seine fachliche Unterstützung sowie für die vielen unterhaltsamen Zeiten.

Ich möchte mich bei Shannon Lee Layland für das Korrekturlesen der Publikationen bedanken.

Ein großer Dank gilt Ivana Mrsic, Johanna Hutterer und Achim Junginger, von welchen ich im Rahmen unseres fachübergreifenden Projekts vieles lernen durfte. Ich danke ihnen für all die anregenden Diskussionen und Ideen.

Ganz besonders danken möchte ich meinen Freunden und Kollegen Dmitri Visser, Kathrin Stadelmann und Nora Feuerer für die geniale gemeinsame Zeit, die gemeinsamen Nachtschichten, die guten Unterhaltungen, die unvergesslichen Erlebnisse auch außerhalb der Arbeit und für all ihre fachliche Unterstützung, Motivation und Hilfsbereitschaft.

Allen Mitarbeitern der AG Schenke-Layland gilt mein herzliches Dankeschön für ihre Hilfsbereitschaft und Unterstützung. Ebenfalls danke ich den Mitarbeitern des NMI, insbesondere dem Bereich Biomedizin und Materialwissenschaften unter der Leitung von Dr. Hanna Hartmann für die freundschaftliche Arbeitsatmosphäre, die Hilfsbereitschaft sowie die Organisation der Labore.

Mein besonderer Dank gilt meinen Eltern und meinen Freunden, die mich in der gesamten Zeit begleitet, mich bestärkt und für mich gebetet haben.

Schließlich danke ich Gott, dem Schöpfer und Vater im Himmel, der mir in seiner Liebe und Treue immer wieder die Kraft, den Frieden und die Freude in alledem gegeben hat.

Declaration

Ich erkläre hiermit, dass ich die zur Promotion eingereichte Arbeit mit dem Titel "Development and Non-invasive Quality Assessment of Advanced Therapy Medicinal Products" selbstständig verfasst, nur die angegebenen Quellen und Hilfsmittel benutzt und wörtlich oder inhaltlich übernommene Zitate also solche gekennzeichnet habe. Ich erkläre, dass die Richtlinien zur Sicherung guter wissenschaftlicher Praxis der Universität Tübingen beachtet wurden. Ich versichere an Eides statt, dass diese Angaben wahr sind und dass ich nichts verschwiegen habe. Mir ist bekannt, dass die falsche Angabe einer Versicherung an Eides statt mit Freiheitsstrafe bis zu drei Jahren oder mit Geldstrafe bestraft wird.

Ruben Daum

Appendices

Appendix I: Daum, R., Brauchle, E., Berrio, D.A.C. et al. *Non-invasive detection of DNA methylation states in carcinoma and pluripotent stem cells using Raman microspectroscopy and imaging,* Scientific Reports, 2019, 9, 1

SCIENTIFIC REP⚙RTS

OPEN

Non-invasive detection of DNA methylation states in carcinoma and pluripotent stem cells using Raman microspectroscopy and imaging

Ruben Daum[1,2], Eva M. Brauchle[1,2], Daniel Alejandro Carvajal Berrio[1], Tomasz P. Jurkowski [3] & Katja Schenke-Layland [1,2,4]

DNA methylation plays a critical role in the regulation of gene expression. Global DNA methylation changes occur in carcinogenesis as well as early embryonic development. However, the current methods for studying global DNA methylation levels are invasive and require sample preparation. The present study was designed to investigate the potential of Raman microspectroscopy and Raman imaging as non-invasive, marker-independent and non-destructive tools for the detection of DNA methylation in living cells. To investigate global DNA methylation changes, human colon carcinoma HCT116 cells, which were hypomorphic for DNA methyltransferase 1, therefore showing a lower global DNA methylation (DNMT1^{−/−} cells), were compared to HCT116 wildtype cells. As a model system for early embryogenesis, murine embryonic stem cells were adapted to serum-free 2i medium, leading to a significant decrease in DNA methylation. Subsequently, 2i medium -adapted cells were compared to cells cultured in serum-containing medium. Raman microspectroscopy and imaging revealed significant differences between high- and low-methylated cell types. Higher methylated cells demonstrated higher relative intensities of Raman peaks, which can be assigned to the nucleobases and 5-methylcytosine. Principal component analysis detected distinguishable populations of high- and low-methylated samples. Based on the provided data we conclude that Raman microspectroscopy and imaging are suitable tools for the real-time, marker-independent and artefact-free investigation of the DNA methylation states in living cells.

DNA methylation and de-methylation are involved in gene expression, disease mechanisms and reactions to environmental substances. It is assumed that the cellular memory is mainly inherited by DNA methylation[1]. In the DNA methylation process, methyl groups are added to cytosine within CpG dinucleotides. The reaction is catalyzed by DNA methyltransferases (DNMT)[2,3]. There are three catalytically active DNMTs in mammalians. DNMT1 maintains methylation patterns by methylating the newly synthesized DNA strand. DNMT3a and DNMT3b are required for *de novo* DNA methylation[4–6]. As methylation of promotor regions typically represses gene transcription, most of the DNA methylation-related consequences are genomic imprinting and inactivation of the X chromosome in female mammals[7]. Early embryogenesis is marked by dramatic changes in DNA methylation. After fertilization, DNA methylation in the genome becomes erased over several DNA replication cycles involving both active and passive demethylation[8]. Around implantation, DNMT3a and DNMT3b are expressed at high levels to form the normal embryonic methylation patterns[9]. In the blastocyst stage, high global levels of

[1]Department of Women's Health, Research Institute for Women's Health, Eberhard-Karls-University Tübingen, Silcherstr. 7/1, 72076, Tübingen, Germany. [2]The Natural and Medical Sciences Institute (NMI) at the University of Tübingen, Markwiesenstr. 55, 72770, Reutlingen, Germany. [3]Department of Biochemistry, Institute of Biochemistry and Technical Biochemistry, University of Stuttgart, Allmandring 31, 70569, Stuttgart, Germany. [4]Department of Medicine/Cardiology, Cardiovascular Research Laboratories, David Geffen School of Medicine at UCLA, 675 Charles E. Young Drive South, MRL 3645, Los Angeles, CA, USA. Correspondence and requests for materials should be addressed to K.S.-L. (email: katja.schenke-layland@med.uni-tuebingen.de)

73

DNA methylation are detected[10]. Tracking of these massive changes in global DNA methylation could provide new insights about early embryogenesis. After the blastocyst status, the global DNA methylation levels do not dramatically change any more during differentiation[11–13]. However, it was shown that during carcinogenesis, in most cancers, a site-specific DNA hypermethylation and a global DNA hypomethylation takes place[14–16]. In the case when promotors of tumor suppressor genes get hypermethylated, the genes are switched off[17,18]. Global hypomethylation in turn leads to genome instability and activation of transposable elements and oncogenes[17]. It has been estimated that 70% of all cancers lead to a reduced global DNA methylation, 18% with no change, and 12% with an increased DNA methylation relative to the adjacent normal tissue[19]. This overall change of DNA methylation could serve as a valid biomarker for cancer.

There are various approaches to detect and analyze global DNA methylation. A well-established method is immunofluorescence (IF) staining based on the use of an anti-5-methylcytosine (5mC) antibody and a secondary antibody labeled with a fluorescent dye. The method offers a straightforward visualization of methylated DNA[20]. Furthermore, to study global DNA methylation, an enzyme-linked immunosorbent assay (ELISA) based on anti-5mC can be performed. Liquid chromatography-mass spectrometry is also commonly used, yet it requires sample preparation and expensive machines to measure the DNA methylation level[21]. One of the currently most widely used techniques to assess DNA methylation is the bisulfite conversion. The DNA is treated with sodium bisulfite, which deaminates non-methylated cytosines, converting them into uracils, whereas the treatment does not change methylated cytosine[22]. By comparing the sequences of converted and unconverted DNA, it is possible to identify methylated sites. However, all these methods are invasive and potentially create artifacts as they require fixation and staining procedures, cell lysis or DNA isolation. So far, there is no appropriate method established that allows the online monitoring of global DNA methylation changes in living cells.

A promising tool for online monitoring of living cells and tissues is Raman microspectroscopy as it is a non-invasive and marker-independent technique based on light scattering of the illuminated material[23]. In the last decade, Raman spectroscopy has become a method of interest for the field of biomedical research[24,25]. It is a time-saving alternative to other methods investigating biological systems such as fluorescence imaging[26]. Moreover, it allows the analysis of biological processes within living cells. The Raman measurement obtains signals from proteins, lipids, nucleic acids, carbohydrates and inorganic crystals, which enables to identify and distinguish cell phenotypes and tissues based on their individual biochemical signature[23]. The detection of DNA methylation using Raman microspectroscopy is not yet established. Some studies investigating DNA methylation were performed using surface-enhanced Raman spectroscopy (SERS)[27–29]. However, no investigations on living cells have been performed to date.

In the present study, we used Raman microspectroscopy and principle component analysis (PCA) to identify Raman shifts that can indicate global DNA methylation changes in living cells. Two cell types that differ in their global DNA methylation level were measured and compared with each other. Genetic modified human colon cancer cells that are DNMT1 hypomorph (DNMT1$^{-/-}$ cells) were compared to HCT116 wildtype (WT) cells[30]. The DNMT1$^{-/-}$ cells still retain some DNMT1 activity, yet much reduced, leading to a decreased genome wide methylation level. As a model system to investigate global DNA methylation changes in early embryogenesis, murine embryonic stem cells (mESC) were utilized. mESCs were cultured in serum-containing medium or they were adapted to serum-free 2i medium, leading to a significant decrease in DNA methylation[31]. The aim of the study was to investigate if Raman microspectroscopy and imaging are capable to detect the different global DNA methylation levels in both cell types. IF staining and 5mC ELISA were used to quantify the global DNA methylation in the cells. These routine methods served as reference in order to verify the results from the Raman measurements.

Results

5mC and methylated DNA show significantly increased Raman bands.   Before measuring DNA methylation within cells, cytidine and 5mC as well as methylated and non-methylated DNA standards were investigated with Raman microspectroscopy (Suppl. Fig. 1). The Raman spectra of 5mC and methylated DNA revealed increased signals in the region of 1331–1335 cm^{-1} (Suppl. Fig. 1a, b). Furthermore, methylated DNA showed significantly increased Raman bands at 1335 cm^{-1} (p < 0.05), 1379 cm^{-1} (p < 0.05) and 1579 cm^{-1} (p < 0.01) (Suppl. Fig. 1c).

DNMT1-deficient cells reveal a decreased global DNA methylation.   Global DNA methylation of the human colon cancer cell line HCT116 was studied. Wildtype (WT) cells and DNMT1$^{-/-}$ cells were utilized. DNA methylation was examined using 5mC fluorescence staining and a 5mC ELISA (Fig. 1). Qualitative differences between WT and DNMT1$^{-/-}$ cells were identified within the nuclei, showing various 5mC-expressing foci in the WT cells (Fig. 1a; white arrows). When focusing on the overall fluorescence intensity of the entire cell nucleus, no significant difference in gray value intensity (GVI) per cell was detected (p = 0.914) (Fig. 1b). However, analysis of the subnuclear localization patterns showed a significant increase of 5mC-foci within the cell nuclei of WT cells when compared with DNMT1$^{-/-}$ cells (p < 0.05) (Fig. 1c). 5mC ELISA analysis exhibited a statistically significant 0.6% decrease in global DNA methylation in the DNMT1$^{-/-}$ cells when compared to WT cells (Fig. 1d; p < 0.05). In the WT cells, 1.4% of all cytosines were methylated, whereas the DNMT1$^{-/-}$ cells contained only 0.8% methylated cytosines (Fig. 1d).

Raman analysis of WT and DNMT1$^{-/-}$ cells shows differences in nucleic acid bands.   The Raman spectral signature of the HCT116 WT cells displayed a cellular peak pattern consisting of complex overlapping signals from the biochemical cellular components (Fig. 2a,i). DNMT1$^{-/-}$ cells revealed an increased relative Raman signal at 830 cm^{-1} and decreased relative spectral intensities at the Raman bands 786 cm^{-1}, 1257 cm^{-1}, 1330 cm^{-1}, 1342 cm^{-1}, 1579 cm^{-1}, 1610 cm^{-1} and 1662 cm^{-1} (Fig. 2a,ii). Statistical analysis showed a significant change in intensity at 1257 cm^{-1} (p < 0.001), 1330 cm^{-1} (p < 0.01) and 1579 cm^{-1} (p < 0.001) (Fig. 2b).
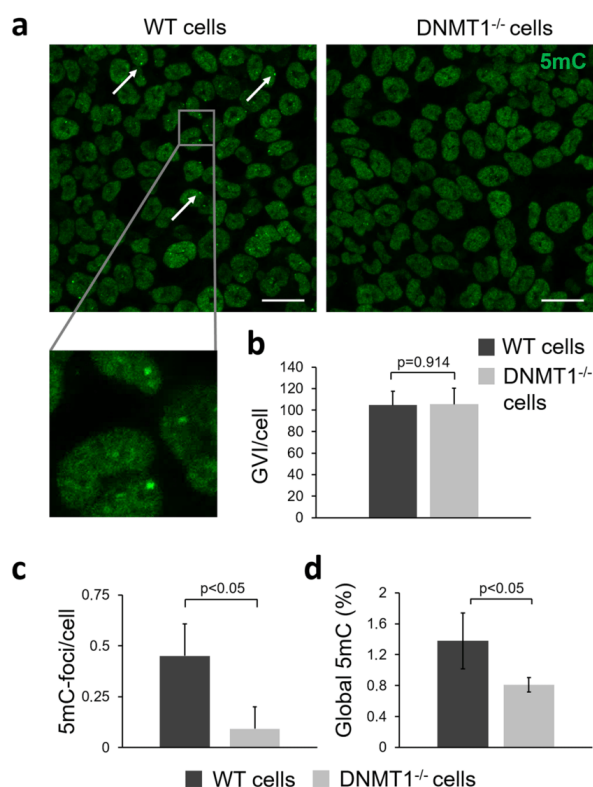
74

Figure 1. Investigation of global DNA methylation in HCT116 WT and DNMT1$^{-/-}$ cells. (**a**) Immunofluorescence staining of 5-methylcytosine (5mC) in WT and DNMT1$^{-/-}$ cells. WT cells show various dense 5mC-foci within the nucleus indicated by white arrows. Scale bars equal 20 μm. (**b,c**) Semi-quantitative fluorescence intensity analysis of 5mC-stained cells. WT cells show significant more 5mC-foci/cell than DNMT1$^{-/-}$ cells. Two-tailed t-test, n = 3. (**d**) Global 5mC level in WT cells are significantly higher than in DNMT1$^{-/-}$ cells. Two-tailed t-test, n = 3.

For further analysis of the spectral data, PCA was performed. PCA is commonly used to resolve complex spectral peak shifts and to reveal spectroscopic variations and peak correlations by calculating principal components (PCs), which dissolve the variances within the spectra data set[32,33]. In the score plot (Fig. 2c), every data point represents a Raman spectrum of a single cell. The score values were used to validate significant differences in the Raman spectra of WT cells and DNMT1$^{-/-}$ cells. In the PC 4 scores plot, which describes 3% of the total spectral variances, WT cells and DNMT1$^{-/-}$ cells showed a separation tendency. Statistical analysis revealed significant differences of the PC 4 score value between WT and DNMT1$^{-/-}$ cells (p < 0.001) (Fig. 2c). Other PC scores did not show significant differences (Suppl. Fig. 3). In general, loadings of each PC demonstrate the spectral changes, which determine the position of the PC score values[33]. Positive peaks in the loadings indicate increased Raman signals in the original spectra of the positive score values. In contrast, negative loading values represent increased Raman signals in the spectra of the negative score values[33]. Based on the PC 4 loading, increased bands at 786 cm^{-1}, 1257 cm^{-1}, 1330 cm^{-1} and 1579 cm^{-1} were identified in the spectra of WT cells (Fig. 2d, arrows). DNMT1$^{-/-}$ cells showed an increased Raman signal at 1445 cm^{-1}. However, the loading was quite noisy, which indicates that only slight differences of the Raman signals characterize the PC 4. Loadings of PC 1, 2 and 3 showed mostly the spectral baseline (Suppl. Fig. 3).

2i medium-adapted mESCs retain their pluripotency and show a significant global demethylation of genomic DNA. In order to reduce global DNA methylation, mESCs were adapted to serum-free 2i medium (2i mESCs) as previously described[31]. Before DNA methylation analysis, the pluripotency of the
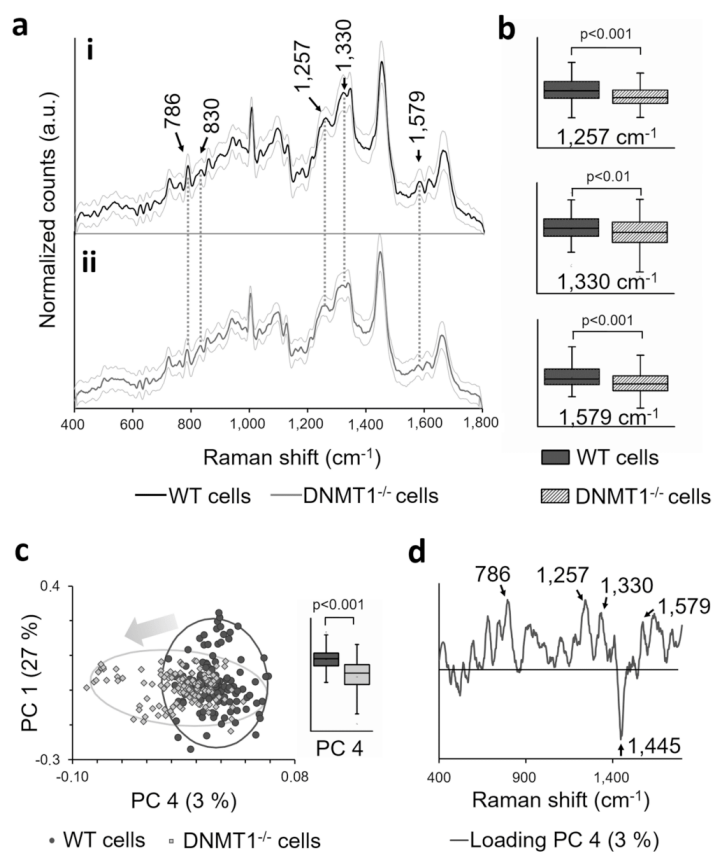
75

Figure 2. Identification of DNA methylation Raman signatures in WT and DNMT1$^{-/-}$ cells. (**a**) Raman spectra of (i) HCT116 WT and (ii) DNMT1$^{-/-}$ cells. Raman signatures that can be assigned to DNA bands are indicated by arrows. Standard deviations are indicated by the gray lines. n = 125. (**b**) Statistical analysis of significantly increased Raman bands, which can be assigned to DNA methylation. (**c**) Score plot of PC 1 and PC 4 shows a grouping tendency between WT and DNMT1$^{-/-}$ cells illustrated by a gray arrow. The score mean value of both groups for PC 4 differs significantly from each other. Two-tailed *t*-test, n = 125 (**d**) PC 4 Loading describes the Raman shifts that vary in WT cells compared to DNMT1$^{-/-}$ cells. Noticeable DNA peaks are indicated by arrows.

control and 2i mESCs was verified via Nanog and Oct4 protein expression by IF staining (Suppl. Fig. 2). As expected, both control and 2i mESCs showed Nanog and Oct4 protein expression (Suppl. Fig. 2a and b); however, semi-quantitative analysis of fluorescence intensities revealed a significantly higher Nanog expression in mESCs cultured in 2i medium when compared with the ESCs that were cultured in serum-containing control medium (Suppl. Fig. 2a). In addition, *Nanog* gene expression of 2i mESCs was 3-fold higher (p < 0.05) compared to the control mESCs, and *Oct4* gene expression of 2i mESCs was 2-fold higher compared to control mESCs (Suppl. Fig. 2c).

mESC adaption to serum-free 2i medium results in a massive global demethylation of the genomic DNA[34,35]. For the determination of global DNA methylation levels in control versus 2i mESCs, a 5mC ELISA was performed revealing a significantly decreased relative cytosine 5mC of 4% (4.7% in control mESCs before adaption and 0.7% in 2i mESCs after adaption) (Fig. 3a; p < 0.001). This result was confirmed by 5mC IF staining (Fig. 3b). The semi-quantitative fluorescence intensity analysis of the whole nucleus exhibited significantly lower GVI per colony in the 2i mESCs when compared with the control mESCs (Fig. 3c). By comparing subnuclear localization patterns of 5mC, we further identified that the control mESCs exhibited significantly more 5mC-foci within each cell nucleus (Fig. 3b, white arrows, and Fig. 3d).
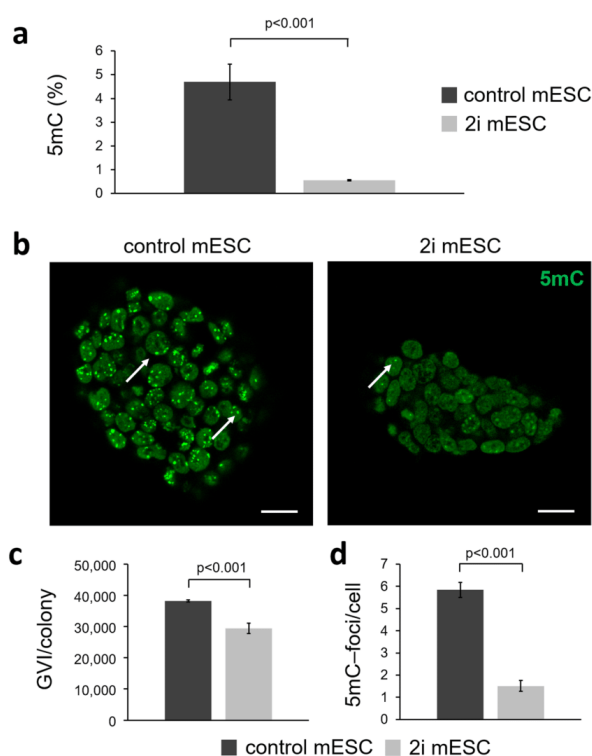
Figure 3. Investigation of global DNA methylation changes. (**a**) 5mC expression in mESCs cultured under control conditions or in 2i medium. 2i medium-adapted cells show a significantly lower DNA methylation. Two-tailed *t*-test, n = 3. (**b**) Immunofluorescence staining of 5mC. Scale bars equal 20 μm. (**c** + **d**) Quantitative fluorescence intensity analysis of 5mC-stained mESCs. 2i medium-cultured mESCs show a significant lower mean intensity and less 5mC-foci/cell (indicated by white arrows in **b**) when compared with cells cultured in the presence of serum (control). Two-tailed *t*-test, n = 3.

Raman microspectroscopy revealed altered nucleic acid signals in 2i medium-adapted mESCs. Control mESCs and 2i mESCs were investigated with Raman microspectroscopy. Non-stained control and 2i mESCs showed defined peak patterns containing complex overlapping signals from lipids, proteins, carbohydrates and nucleic acids[36]. Several differences in relative intensities between control mESCs (Fig. 4a,i) and 2i mESCs (Fig. 4a,ii) were identified. The most prominent ones, which can be assigned to nucleic acid bands, are highlighted with black arrows (Fig. 4a). Most prominent increased Raman bands in control mESCs were detected at $1257\,cm^{-1}$, $1331\,cm^{-1}$, $1379\,cm^{-1}$ and $1575\,cm^{-1}$. 2i mESCs exhibited an increasing relative intensity at $818\,cm^{-1}$. Statistical significant decreased Raman shifts were identified at $1257\,cm^{-1}$ ($p < 0.01$), $1331\,cm^{-1}$ ($p < 0.001$) and $1575\,cm^{-1}$ ($p < 0.001$) (Fig. 4b). The corresponding PCA analysis showed separated clusters for control and 2i mESCs in PC 4, which explained 3% of the total spectral variance. The PC 4 score values of control and 2i mESCs differed significantly ($p < 0.001$) (Fig. 4c). The corresponding loading of PC 4 showed decreased Raman bands ($786\,cm^{-1}$, $896\,cm^{-1}$, $1257\,cm^{-1}$, $1331\,cm^{-1}$) and increased signals ($481\,cm^{-1}$, $1441\,cm^{-1}$) for 2i mESCs when compared to control mESCs. In general, we noted that the loadings were quite noisy, which indicates that only slight differences of the Raman signals characterize the PC 4 (Fig. 4d). For the other PC scores, no separation tendency was detected. Scores and loadings of PC 1–3 are shown in Suppl. Fig. 4.

Raman spectra differentiate between low and high methylation status independent of the cell type. To further investigate whether the differences in Raman spectra of the low and high global DNA methylation status are independent of species and cell types, PCA were performed on the whole data sets consisting of the spectra from all, the mESCs (control and 2i mESCs) and human colon cancer (HCT116 WT and DNMT1$^{-/-}$) cells. A 3D score plot of PC 2 (12%), PC 4 (3%) and PC 5 (2%) revealed separations between the samples (Fig. 5a).
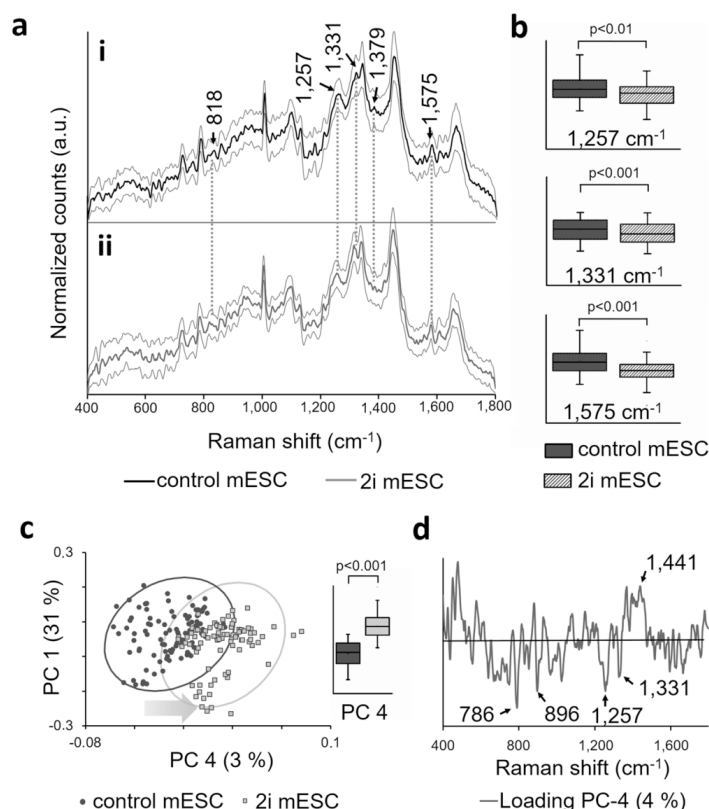
Figure 4. Identification of mESC Raman signatures due to an altered global DNA methylation. (**a**) Raman spectra of mESCs cultured in (i) control and (ii) 2i medium. Raman signatures that can be assigned to DNA bands are indicated by black arrows. The standard deviation is indicated by the gray lines. (**b**) Statistical analysis of significantly increased Raman bands, which can be assigned to DNA methylation. Two-tailed t-test, n = 85. (**c**) Score plot of PC 1 and PC 3 shows a grouping tendency of mESCs cultured in control and 2i media. The direction of the gray arrow indicates the loss of DNA methylation. The score mean value of both groups for PC 4 differs significantly from each other. Two-tailed t-test, n = 85 (**d**) PC 4 loading describes the Raman shifts that vary in 2i-adapted mESCs compared with mESCs cultured in the control medium. Peaks of interest are indicated by black arrows.

PC 2 reflects differences between cell types and separates between mESC as well as the WT and DNMT1$^{-/-}$ cells. In addition, PC 5 revealed a separation tendency between the high-methylated mESC control and the HCT116 WT cells, and the low-methylated 2i mESC and DNMT1$^{-/-}$ cells. This separation is also illustrated in Fig. 5b, showing the mean score values of PC 5. The score values of the control mESCs differed significantly from the score values of the 2i mESCs (p < 0.001), and the score values of the HCT116 WT cells differed significantly from the score values of the DNMT1$^{-/-}$ (p < 0.01).

The most prominent Raman peaks that revealed altered relative intensities in Raman spectra of the high- and low-methylated mESCs and the high- and low-methylated human colon cancer WT and DNMT1$^{-/-}$ cells are summarized in Table 1. Most of them show increased signals for high level of DNA methylation (786 cm^{-1}, 1257 cm^{-1}, 1317–1323 cm^{-1}, 1335 cm^{-1}, 1342 cm^{-1}, 1379 cm^{-1}, 1579 cm^{-1}, 1605–1610 cm^{-1} and 1662 cm^{-1}). The Raman band at 815–830 cm^{-1} revealed a decreased relative intensity in the high-methylated cells.

Raman imaging identifies 5mC-foci on a subnuclear level. Since the differences in the Raman spectra between the investigated groups were rather subtle, high-resolution Raman imaging was additionally performed to obtain laterally-resolved spectral information of the 5mC–foci within the cell nuclei. HCT16 WT
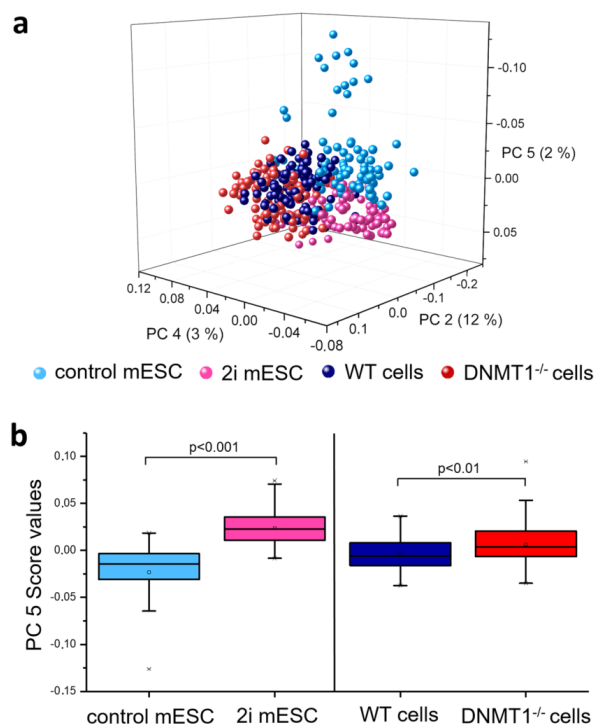
Figure 5. Comparison of Raman spectra from mouse pluripotent stem cells cultured in either control or 2i medium with human colon cancer WT and DNMT$^{-/-}$ cells. (**a**) 3D score plot of Raman spectra from control mESCs, 2i mESCs as well as human colon cancer WT and DNMT1$^{-/-}$ cells showing PC 2, PC 4 and PC 5. There is a grouping tendency between control mESCs and WT cells (blue shades), as well as 2i mESCs, DNMT1$^{-/-}$ cells (green shades). (**b**) The grouping tendency is visualized by a box plot of PC 5 score values. It shows significantly lower scores for control mESCs and WT cells when compared with 2i mESC and DNMT1$^{-/-}$ cells. One-way ANOVA, n = 30.

Raman Shift (cm^{-1})	Assignment	↑↓ relative Raman intensity for high-methylated cells
786	5-Methylcytosine[52], Cytosine, Thymine, Phosphate backbone of DNA/RNA[39,47–49]	↑
815–830	Phosphate backbone of DNA/RNA[54]	↓
1257	Cytosine, Adenine[38,41]	↑
1317–1323	Guanine[41,47]	↑
1335	CH$_2$CH$_3$ wagging[37]	↑
1342	Guanine[47]	↑
1379/1386	CH$_3$[39,53]	↑
1579	Pyrimidine ring[39]	↑
1605–1610	Cytosine[41]	↑
1662	DNA[58,59]	↑

Table 1. Identified Raman peaks that are altered due to global DNA methylation in mESCs and human colon cancer cells.

and DNMT1$^{-/-}$ cells (Fig. 6a–d) as well as control and 2i mESCs (Fig. 6e–h) were scanned with a resolution of $0.2 \times 0.2\,\mu m$. A heat map of both cell types was created using the sum of the intensities at $1257\,cm^{-1}$, $1331\,cm^{-1}$ and $1579\,cm^{-1}$. The heat maps of the resulting Raman images showed specific structures within the nucleus that were comparable to the structures seen when performing 5mC IF staining (Fig. 6a,b,e,f). In the average spectra from high-intensity (highly methylated) regions and low-intensity (background) regions of the heat maps, increased Raman peaks in the spectral region of $1250–1390\,cm^{-1}$ were observed for both cell types (Fig. 6c,g). The semi-quantitative pixel intensity analysis of the heat maps exhibited significantly lower values for the HCT116 DNMT1$^{-/-}$ cells and 2i mESCs when compared with the HCT116 WT cells and control mESCs (Fig. 6d,h; $p < 0.05$).

Discussion

It this study, we demonstrated that Raman microspectroscopy and Raman imaging have the potential to detect DNA methylation states in living cells. We utilized different cell types from human and mouse origin that differ in their global DNA methylation level, and identified specific Raman signals that can be employed to monitor methylated DNA *in situ*.

In a first step, by measuring 5mC and methylated DNA, we identified specific Raman bands at $1257\,cm^{-1}$, $1335\,cm^{-1}$, $1379\,cm^{-1}$ and $1579\,cm^{-1}$ that can be assigned to nucleobases or CH$_3$ (Table 1)[37–41]. These results demonstrate that differences between methylated and non-methylated DNA can be detected by Raman microspectroscopy.

Next, we used WT cells of the human colon cancer cell line HCT116 and their DNMT1-hypomorph progeny showing a lower global DNA methylation. We confirmed the decreased global DNA methylation in DNMT1$^{-/-}$ cells by anti-5mC IF staining and 5mC ELISA. Interestingly, in our study, in both the WT and DNMT1$^{-/-}$ cells, the 5mC ELISA revealed a lower global DNA methylation level when compared to previous studies[30]. Literature determined 4.0% methylated cytosines for WT cells, and our results revealed 1.3%. For DNMT1$^{-/-}$ cells, 3.2% of all cytosines were reported to be methylated[30]. In our study, we quantified 0.7% methylated cytosines. Nevertheless, the relative global DNA methylation difference of 0.6% between the samples is similar to what had been previously reported[30].

Our Raman microspectroscopy measurements showed differences in the Raman signatures of WT and DNMT1$^{-/-}$ cells. PCA revealed a grouping tendency for PC 4 (Fig. 2). Although some overlapping of the populations was seen that might be due to biological variances within the samples, the mean score values revealed a significant difference between the two samples. Most differences in Raman spectra as well as striking peaks in the loading plot could be assigned to nucleic acid bands (Table 1).

The second cell type in this study were mESCs that were either maintained in routine serum-containing control medium, or they were adapted to serum-free 2i medium. As expected, exposure to 2i medium led to massive global DNA demethylation as described before[31,34,35], which was successfully confirmed by anti-5mC IF staining and 5mC ELISA. Accordingly, the control mESCs revealed a global DNA methylation of 4%[34,35], and only 1% of all cytosines were methylated in the 2i medium-adapted mESCs[34]. We confirmed that the mESCs maintained their pluripotency after 2i adaption by gene and protein expression profiling focusing on the pluripotency markers Nanog and Oct4, which were increased after two weeks of 2i medium adaption. This observation is conform with a report by Ying *et al.* who postulated that 2i ESCs represent the ground state of pluripotency[31]. Therefore, we hypothesize that the 2i mESCs used in our study were actually closer to the "naïve pluripotent ground state" than mESCs cultured in standard serum-containing medium[31,42]. However, the adaption process of mESCs to serum-free 2i medium seems to be not homogenous and may require modified culture protocols. The gene expression of the pluripotency markers *Nanog* and *Oct4* (Suppl. Fig. 2) as well as the 5mC fluorescence signal (Fig. 3) revealed high variances within the 2i mESC population. Interestingly, Abranches *et al.* made similar observations showing higher Nanog fluctuations in cells that were exposed to 2i medium[43]. One explanation for this could be that some of the cells in our population were already differentiated prior exposure to the 2i medium. Tamm *et al.* examined the capacity of 2i medium to rescue partially-differentiated mESCs by culturing spontaneously-differentiated cells in 2i medium[44]. They found that the cells were not able to return to the ground state anymore[44].

Employing Raman microspectroscopy, we were able to distinguish between 2i medium-adapted and control mESCs. Overlapping populations in PC 4 can be explained by biological variances within the samples due to the heterogeneity of the 2i mESC population as described above. The most prominent Raman bands, which revealed the major differences, were assigned to nucleic acid bands and methyl groups (Table 1). DNA methylation and remodeling of chromatin are the most striking changes during early embryogenesis[8–10,45]. It can therefore be assumed that the DNA methylation level represents a potential biomarker that can be tracked during early embryonic development. Nevertheless, it must be taken into account that the 2i medium-treated mESCs used in our model system may also show other epigenetic changes, e.g. a reduction of H3K27me3[46].

In all experiments of this study, we detected altered relative peak intensities in the Raman spectra of cells with different DNA methylation levels. Most of the Raman shifts were assignable to DNA components, nucleobases, phosphate and ribose. We identified marker peaks, which can be assigned to 5mC, such as the Raman shift at $786\,cm^{-1}$. This peak is also associated with cytosine, thymine or phosphate[41,47–51]. However, Barhoumi *et al.* described the appearance of a peak in case of 5mC at the same position[52]. The comparison of the loadings from both cell types in our study revealed a higher relative intensity at $786\,cm^{-1}$ for the cells with a higher DNA methylation (human colon cancer WT cells and control mESCs). A further peak at $1330–1331\,cm^{-1}$, which can be assigned to CH$_3$ and CH$_3$CH$_2$ twisting and wagging modes in nucleic acids, was observed for all highly methylated cells as well as for 5mC and methylated DNA[39,53,54]. In addition, an increased peak between the wavenumbers $1379\,cm^{-1}$ and $1386\,cm^{-1}$, also shown in the Raman spectra of methylated DNA, was detected in the spectra of control mESCs. In this region, previous studies described symmetric CH$_3$ bending[39,53].
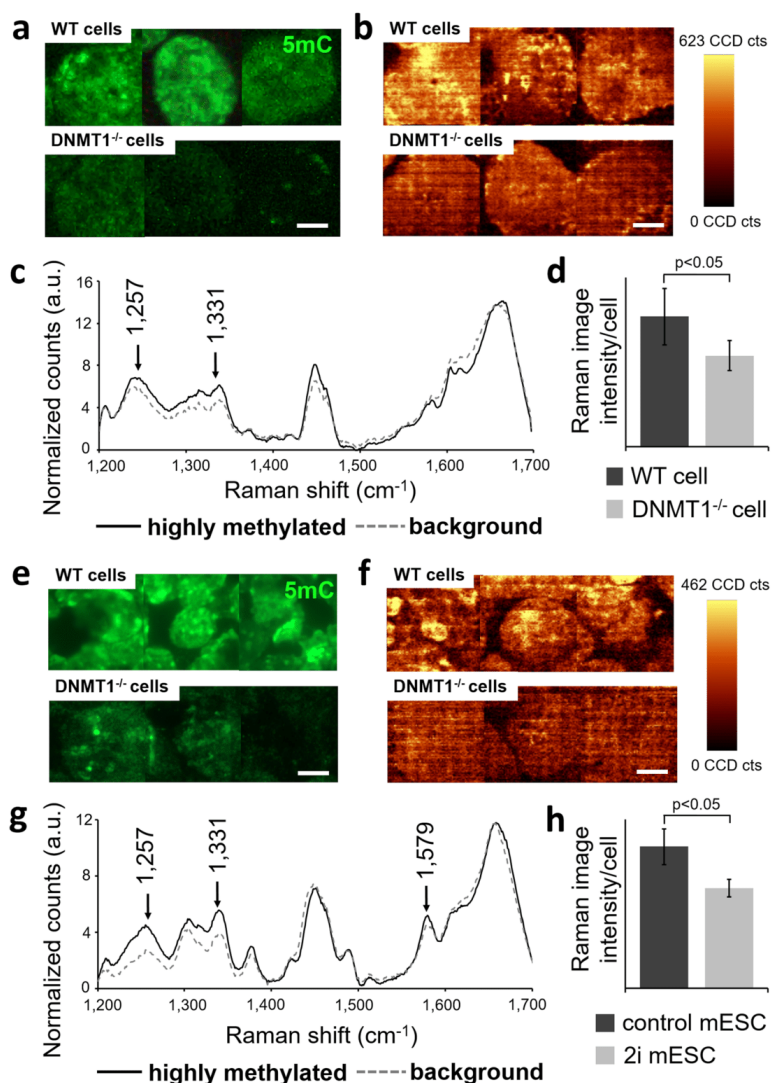
Figure 6. Detection of 5mC-foci with high-resolution Raman imaging of HCT116 cells and mESCs. (**a**) Anti-5mC immunofluorescence staining of HCT116 WT and DNMT1$^{-/-}$ cells. (**b**) Heat maps of the Raman images obtained from HCT116 WT and DNMT1$^{-/-}$ cells using the sum intensities of 1257 cm^{-1}, 1379 cm^{-1} and 1579 cm^{-1}. (**c**) Average spectra from high-intensity regions and low-intensity regions of the heat maps from panel (b). (**d,h**) Statistical analysis of the Raman images from panels b and f. Two-tailed t-test, n = 3. (**e**) Anti-5mC immunofluorescence staining of mESC control and 2i mESCs. (**f**) Heat maps of the Raman images from mESC control and 2i mESCs using the sum intensities described in panel b. (**g**) Average spectra from high-intensity regions and low-intensity regions of the heat maps from panel f. Scale bars in all images equal 5 μm.

In addition to 5mC markers, we observed changes in DNA signals which might be an indirect effect of 5mC. Most predominant peaks that cannot directly be assigned to 5mC but to other nucleobases and potential chromatin changes were observed at 1257 cm^{-1} (thymine, cytosine, adenine)[41,48,49,55], 1304 cm^{-1}[28,39] (cytosine, adenine)[56],

$1323\,\text{cm}^{-1}$ (guanine)[57], $1579\,\text{cm}^{-1}$ (pyrimidine ring)[39] and $1662\,\text{cm}^{-1}$ (amide I, nucleic acid modes)[58,59]. These peaks were also detected in the loadings of the corresponding PCs for the compared cell types. In addition, the Raman peaks at $1257\,\text{cm}^{-1}$ and $1579\,\text{cm}^{-1}$ were also observed in the spectra of methylated DNA. It is still unclear why methylated DNA seems to enhance nucleobase-assigned Raman shifts. A possible explanation for the enhanced Raman shift of thymine could be that it is, similar to cytosine, a pyrimidine ring[39,47,60]. Due to the additional methyl group at C5, the 5mC has a very similar chemical structure when compared to the thymine[61]. Raman signals for 5mC might therefore appear at the same positions as those described previously for thymine.

We analyzed the Raman images of the HCT116 cells and mESCs. Using the sum of the intensities at $1257\,\text{cm}^{-1}$, $1331\,\text{cm}^{-1}$ and $1579\,\text{cm}^{-1}$, a heat map of the Raman images from both cell types was generated. We were able to show a significant intensity increase in the heat maps of the mESC control and HCT116 WT cells when compared with the mESC 2i and HCT116 DNMT1$^{-/-}$ cells (Fig. 6d,h). In addition, the heat maps revealed structures within the nuclei that were similar to the 5mC-foci identified by the anti-5mC IF staining (Fig. 6b,f). These regions are likely to be composed of heterochromatin, since the DNA is densely packed here and thus generates a stronger Raman signal[62]. Since most of the DNA methylation-related consequences are genomic imprinting, DNA methylation is more strongly present in heterochromatic regions[63], suggesting that the structures can be associated with DNA methylation. Based on our results, we hypothesize that the Raman bands at $1257\,\text{cm}^{-1}$, $1331\,\text{cm}^{-1}$ and $1579\,\text{cm}^{-1}$ are potential markers for DNA methylation.

The overall challenge of this study was to assess DNA methylation changes *in situ*, which represent only a small fraction of all the processes that take place at a certain time in a living cell. Not only the epigenome, but also the genome, transcriptome and proteome of a cell is subject to complex dynamic processes[46]. This might be one of the reasons why some of the detected changes were only minor. In order to obtain statistically even more valid data, more cell types could be included in further investigations, and direct methods for the elimination of DNA methylation such as DNMT 1/3a/3b trible KO could be used.

Conclusion

Our data demonstrate that Raman microspectroscopy and Raman imaging in combination with PCA possess the required fidelity to detect little but significant changes in DNA methylation status on a single cell level. Here, we employed these technologies to track epigenetic changes in mouse pluripotent stem and human colon cancer cells *in situ*. We also showed that high-resolution Raman imaging can resolve structures on a nano- and microscale within the nucleus of living cells enabling the monitoring of epigenetic processes. Raman microspectroscopy and Raman imaging may ultimately allow scientists to further decipher crucial connections between epigenetics and early human embryogenesis, aging or diseases.

Methods

Cell culture.   Rhee *et al.* previously generated a HCT116 DNMT1 knockout construct in which exons 3, 4, and 5 of human DNMT1 were replaced with a hygromycin resistance gene. The disruption of DNMT1 led to a reduced global DNA methylation[30]. Human colon cancer HCT116 wildtype cells (ATCC® CCL-247™) and DNMT1$^{-/-}$ cells were cultured in RPMI medium 1640 (Thermo Fisher Scientific, Waltham, USA) with 10% FBS and 1% P/S.

CCE mESCs (ATCC® SCRC-1023™) were cultured in KO-DMEM (Thermo Fisher Scientific), supplemented with 15% fetal bovine serum, 1% Penicillin-Streptomycin, 1% MEM non-essential amino acids, 1% L-Glutamine, 0.2% HEPES, 0.1% 2-Mercaptoethanol (all Thermo Fisher Scientific) and 0.1% Leukemia inhibitory factor (Merck, Darmstadt, Germany). Cells were split every second day. To obtain naïve mESCs, the cells were adapted to a serum-free culture condition using ESGRO®-2i Medium (Merck) according to the manufacturer's protocol. The adaption took 14 days. Every second day, cells were split.

Immunofluorescence (IF) staining.   IF staining was performed using a 5mC mouse monoclonal IgG antibody (Merck, MABE146) according to a previously described protocol[64] with slight modifications. Cells were washed with PBS and fixed with 0.25% paraformaldehyde (Sigma-Aldrich, St. Louis, USA) in PBS$^-$ for 10 minutes at 37 °C, and 88% methanol at −20 °C for 30 minutes. After washing, the cells were treated with 1 M HCl at 30 °C for 30 minutes and were neutralized with 0.1 M sodium borate (pH 8.5). In order to reduce nonspecific binding, the cells were incubated with 2% goat block solution for 20 minutes at 37 °C. Afterwards, the cells were incubated with the 5mC antibody (1:2000, stock 2 mg/ml) overnight at 4 °C. Finally, the cells were stained with goat anti-mouse IgG Alexa Fluor 488 (1:250, Thermo Fisher Scientific) for 30 minutes at room temperature in the dark. IF staining against Nanog and Oct4 (also known as POU5F1) was done as previously described[65]. As primary antibodies served Oct4 rabbit polyclonal IgG (1:200; ab19857, abcam, Cambridge, UK) and Nanog rabbit polyclonal IgG (1:100, NB100–588, Novus Biologicals, Littleton, USA). Goat anti-rabbit IgG-Alexa Fluor 488 (1:250, Thermo Fisher Scientific) was used as secondary antibody. DAPI (1:1, in DPBS, Roche Diagnostics, Mannheim, Germany) was used for nuclear staining. Imaging was done with an LSM 710 confocal microscope (Carl Zeiss AG, Oberkochen, Germany). ImageJ (NIH) was used for semi-quantitative fluorescence analyses.

Detection of global DNA methylation using 5mC ELISA.   DNA was isolated using the FlexiGene® DNA Kit (Qiagen, Hilden, Germany) as instructed by the manufacturer. The 5mC DNA ELISA Kit (D5325, ZymoResearch, Irvine, USA) was used to quantify global DNA methylation. It is based on the colorimetric detection of 5mC using an anti-5mC antibody. The procedure was done according to the manufacturer's protocol. The wells were loaded with 100 ng DNA. Absorbance was detected at 405 nm using an Infinite® 200 Pro microplate reader (Tecan Group AG, Männedorf, Switzerland). Levels of 5mC were calculated as the percentage of methylated cytosines in total DNA content based on a standard curve generated using the kit controls.

Quantitative reverse transcription polymerase chain reaction (RT-qPCR). RNA was extracted from control and 2i mESC as well as primary-isolated mouse embryonic fibroblasts using RNeasy® Plus Mini Kit (Qiagen) following manufacturer's protocol and stored at −80 °C prior further use. The amount and purity of the RNA were determined by NanoDrop 2000 spectral photometer analysis (Thermo Scientific). A total amount of 1 μg RNA was used to synthesize cDNA utilizing a transcriptor first strand cDNA synthesis kit (Roche). RT-qPCR was carried out using a QuantiTect SYBR Green PCR kit for mESCs (Qiagen). cDNA was used in qPCR reactions with *Nanog* and *Oct4* primers (Qiagen). The samples were normalized to the housekeeping gene *Gapdh* (Qiagen). All procedures were performed as instructed by the manufacturer. For the quantification of the qPCR data, the ΔΔCt was used to determine fold change in RNA expression patterns.

Raman microspectroscopy of cytidine, 5mC, methylated and non-methylated DNA standard. Cytidine, 5mC (Sigma Aldrich, St. Louis, USA) as well as methylated and non-methylated DNA standards (D5325-5-1, D5325-5-2, ZymoResearch, Irvine, USA) were measured with a confocal Raman microspectroscope (alpha300R, WiTEC GmbH, Ulm, Germany). Raman spectra were acquired with a 50x air objective (N.A. 0.55; Carl Zeiss GmbH, Jena, Germany), using an excitation wavelength of 532 nm, a laser power of 60 mW and an acquisition time of one second.

Raman microspectroscopy of single living cells. A custom-built Raman microscope as previously described[65–67] was employed for measuring single living cells. The device consists of a near-infrared 784 nm diode laser with a maximum output power of 85 mW, which was integrated into a standard fluorescence microscope (IX71, Olympus, Japan). A 60x water immersion objective (Olympus®) with a 1.2 numerical aperture (NA) was used for the Raman measurements, resulting in a laser spot in approximately 1 μm diameter[68]. Spectra were detected using an air-cooled charge couple device camera (Andor, Belfast, UK). All cells were trypsinized using 0.25% Trypsin-EDTA (Thermo Fisher Scientific), centrifuged and resuspended in PBS, and transferred to a glas bottom petri dish (Ibidi, Martinsried, Germany). For each sample, 90 single living cells were measured using 10 accumulations, each 10 seconds. The laser was focused on the center of each cell due to an optical trapping effect[69]. The laser focus targets automatically the densest organelle of each cell, which was previously shown to be the cell nucleus[70]. A reference spectrum of the background (glass bottom petri dish covered with PBS) was taken after every ten cells.

Analysis of Raman spectra. Details on the pre-processing steps were published previously in detail[65,68]. Pre-treatment of the Raman spectra (background subtraction and baseline correction) was performed using the OPUS 4.2 software (Bruker, Ettlingen, Germany). The spectra were cut from the range of 0–1,935 cm⁻¹ to 400–1,800 cm⁻¹. In order to perform a PCA, the pre-treated data was imported to the Unscrambler X 14.0 software (Camo Software, Oslo, Norway). Vector normalization (normalized to length 1) was applied on the spectra. Afterwards, a PCA analysis with up to 7 principal components (PCs) was performed. The PCA results were presented in a scores plot and loading plots. To compare cells with high versus low methylation levels, confidence ellipses were calculated using the software Origin Pro 9.1 (OriginLab, Northampton, USA).

Raman imaging of mESCs and HCT116 cells. For Raman imaging of cells, the confocal Raman microspectroscope alpha300R (WITec GmbH, Ulm, Germany) was employed. mESCs and HCT116 cells were trypsinized using 0.25% Trypsin-EDTA (Thermo Fisher Scientific), centrifuged and resuspended in PBS. Cells were immobilized on a glass slide using the Shandon Cytospin 3 (Thermo Fisher Scientific). The cytospots were dried for 20 min and stored at −20 °C. Prior to Raman imaging, the cells were IF-stained using an antibody against 5mC as described above. Raman images were acquired with a 63x Apochromat water dipping objective (N.A. 1.0; Carl Zeiss GmbH, Jena, Germany). Cells were located and an area of $15 \times 15\,\mu m$ was imaged using a step size of 0.2 μm. A green laser with an excitation wavelength of 532 nm was used. The laser power was set on 60 mW and the acquisition time was 0.5 seconds. mESCs obtained from the control and 2i cultures and HTC WT and DNMT1⁻/⁻ cells were imaged and compared. Raman images were analyzed using the Project Five 5.1 Plus software (WITec GmbH). A cosmic ray removal and a baseline correction was employed prior to analysis. In order to generate a heat map of selected Raman signals, intensity sum filters for the respective Raman bands were created and summed up. Semi-quantitative analysis of the heat maps was performed with ImageJ.

Statistical analysis. Except stated otherwise, data are shown in mean ± standard deviation (SD). One-way analysis of variance (ANOVA) was performed to compare data groups. Student's t-test was performed to compare between two data groups using OriginPro (OriginLab®). Probability values of 95%, 99% and 99.9% ($p < 0.05$, 0.01, 0.001) were used to determine significance.

References
1. Zhou, Y., Kim, J., Yuan, X. & Braun, T. Epigenetic modifications of stem cells: A paradigm for the control of cardiac progenitor cells. *Circ. Res.* **109**, 1067–1081 (2011).
2. Cheng, X. & Roberts, R. J. AdoMet-dependent methylation, DNA methyltransferases and base flipping. *Nucleic Acids Res.* **29**, 3784–95 (2001).
3. Jurkowska, R. Z., Jurkowski, T. P. & Jeltsch, A. Structure and Function of Mammalian DNA Methyltransferases. *Chem Bio Chem* **12**, 206–222 (2011).
4. Knippers, R. *Molekulare Genetik: 68 Tabellen.* (Thieme, 2006).
5. Sen, G. L., Reuter, J. A., Webster, D. E., Zhu, L. & Khavari, P. A. DNMT1 maintains progenitor function in self-renewing somatic tissue. *Nature* **463**, 563–567 (2010).
6. Ravichandran, M., Jurkowska, R. Z. & Jurkowski, T. P. Target specificity of mammalian DNA methylation and demethylation machinery. *Org. Biomol. Chem.* **16**, 1419–1435 (2018).

7. Sadikovic, B., Al-Romaih, K., Squire, J. A. & Zielenska, M. Cause and consequences of genetic and epigenetic alterations in human cancer. *Curr. Genomics* **9**, 394–408 (2008).

8. Geiman, T. M. & Muegge, K. DNA methylation in early development. *Mol. Reprod. Dev.* **77**, 105–113 (2010).

9. Kaneda, M. *et al.* Essential role for de novo DNA methyltransferase Dnmt3a in paternal and maternal imprinting. *Nature* **429**, 900–903 (2004).

10. Ito, S. *et al.* Role of Tet proteins in 5mC to 5hmC conversion, ES-cell self-renewal and inner cell mass specification. *Nature* **466**, 1129–1133 (2010).

11. Meissner, A. *et al.* Genome-scale DNA methylation maps of pluripotent and differentiated cells. *Nature* **454**, 766–70 (2008).

12. Deng, J. *et al.* Targeted bisulfite sequencing reveals changes in DNA methylation associated with nuclear reprogramming. *Nat Biotechnol* **27**, 353–360 (2009).

13. Biniszkiewicz, D. *et al.* Dnmt1 overexpression causes genomic hypermethylation, loss of imprinting, and embryonic lethality. *Mol. Cell. Biol.* **22**, 2124–35 (2002).

14. Hon, G. C. *et al.* Global DNA hypomethylation coupled to repressive chromatin domain formation and gene silencing in breast cancer. *Genome Res.* **22**, 246–258 (2012).

15. Ehrlich, M. DNA hypomethylation in cancer cells. *Epigenomics* **1**, 239–59 (2009).

16. Toraño, E. G., Petrus, S., Fernandez, A. F. & Fraga, M. F. Global DNA hypomethylation in cancer: Review of validated methods and clinical significance. *Clin. Chem. Lab. Med.* **50**, 1733–1742 (2012).

17. Egger, G., Liang, G., Aparicio, A. & Jones, P. A. Epigenetics in human disease and prospects for epigenetic therapy. *Nature* **429**, 457–463 (2004).

18. Saunderson, E. A. *et al.* Hit-and-run epigenetic editing prevents senescence entry in primary breast cells from healthy donors. *Nat. Commun.* **8**, 1450 (2017).

19. Paz, M. F. *et al.* Germ-line variants in methyl-group metabolism genes and susceptibility to DNA methylation in normal tissues and human primary tumors. *Cancer Res.* **62**, 4519–4524 (2002).

20. Barton, S. C. *et al.* Genome-wide methylation patterns in normal and uniparental early mouse embryos. *Hum. Mol. Genet.* **10**, 2983–7 (2001).

21. Liu, J., Hesson, L. B. & Ward, R. L. Liquid Chromatography Tandem Mass Spectrometry for the Measurement of Global DNA Methylation and Hydroxymethylation. *J. Proteomics Bioinform.* **01** (2013).

22. Frommer, M. *et al.* A genomic sequencing protocol that yields a positive display of 5-methylcytosine residues in individual DNA strands. *Proc. Natl. Acad. Sci. USA* **89**, 1827–31 (1992).

23. Brauchle, E. & Schenke-Layland, K. Raman spectroscopy in biomedicine - non-invasive *in vitro* analysis of cells and extracellular matrix components in tissues. *Biotechnol. J.* **8**, 288–297 (2013).

24. Tipping, W. J., Lee, M., Serrels, A., Brunton, V. G. & Hulme, A. N. Stimulated Raman scattering microscopy: an emerging tool for drug discovery. *Chem. Soc. Rev.* **45**, 2075–89 (2016).

25. Hehl, G. *et al.* Coherent Raman Scattering Microscopy: New Quantitative and Non-Invasive Tools for Biomedical Research. *Biophys. J.* **102**, 617a (2012).

26. Downes, A. & Elfick, A. Raman spectroscopy and related techniques in biomedicine. *Sensors* **10**, 1871–1889 (2010).

27. Barhoumi, A., Zhang, D., Tam, F. & Halas, N. J. Surface-enhanced raman spectroscopy of DNA. *J. Am. Chem. Soc.* **130**, 5523–5529 (2008).

28. Camafeita, L. E., Sánchez-Cortés, S. & García-Ramos, J. V. SERS of guanine and its alkyl derivatives on gold sols. *J. Raman Spectrosc.* **27**, 533–537 (1996).

29. Guerrini, L., Krpetić, Ž., Van Lierop, D., Alvarez-Puebla, R. A. & Graham, D. Direct surface-enhanced Raman scattering analysis of DNA duplexes. *Angew. Chemie - Int. Ed.* **54**, 1144–1148 (2015).

30. Rhee, I. *et al.* DNMT1 and DNMT3b cooperate to silence genes in human cancer cells. *Nature* **416**, 552–556 (2002).

31. Ying, Q.-L. *et al.* The ground state of embryonic stem cell self-renewal. *Nature* **453**, 519–523 (2008).

32. Bonnier, F. & Byrne, H. J. Understanding the molecular information contained in principal component analysis of vibrational spectra of biological systems. *Analyst* **137**, 322–332 (2012).

33. Lavine, B. A user-friendly guide to multivariate calibration and classification, Tomas Naes, Tomas Isakson, Tom Fearn & Tony Davies, NIR Publications, Chichester, 2002, ISBN 0-9528666-2-5, £45.00. *J. Chemom.* **17**, 571–572 (2003).

34. Leitch, H. G. *et al.* Naive pluripotency is associated with global DNA hypomethylation. *Nat. Struct. Mol. Biol.* **20**, 311–6 (2013).

35. Stadler, M. B. *et al.* DNA-binding factors shape the mouse methylome at distal regulatory regions. *Nature* **480**, 490–5 (2011).

36. Movasaghi, Z., Rehman, S. & Rehman, I. U. Raman Spectroscopy of Biological Tissues. *Appl. Spectrosc. Rev.* **42**, 493–541 (2007).

37. Huang, Z. *et al.* Near-infrared Raman spectroscopy for optical diagnosis of lung cancer. *Int. J. Cancer* **107**, 1047–1052 (2003).

38. Chan, J. W. *et al.* Micro-Raman Spectroscopy Detects Individual Neoplastic and Normal Hematopoietic Cells. *Biophys. J.* **90**, 648–56 (2006).

39. Stone, N., Kendall, C., Smith, J., Crow, P. & Barr, H. Raman Spectroscopy for Identification of Epithelial Cancers. *Faraday Discuss.* **126**, 141–157 (2004).

40. Katainen, E. *et al.* Quantification of the Amphetamine Content in Seized Street Samples by Raman Spectroscopy. *J. Forensic Sci.* **52**, 88–92 (2007).

41. Ruiz-Chica, A. J., Medina, M. A., Sánchez-Jiménez, F. & Ramírez, F. J. Characterization by Raman spectroscopy of conformational changes on guanine–cytosine and adenine–thymine oligonucleotides induced by aminooxy analogues of spermidine. *J. Raman Spectrosc.* **35**, 93–100 (2004).

42. Guo, G. *et al.* Resolution of cell fate decisions revealed by single-cell gene expression analysis from zygote to blastocyst. *Dev. Cell* **18**, 675–85 (2010).

43. Abranches, E. *et al.* Stochastic NANOG fluctuations allow mouse embryonic stem cells to explore pluripotency. *Development* **141**, 2770–9 (2014).

44. Tamm, C., Pijuan Galitó, S. & Annerén, C. A comparative study of protocols for mouse embryonic stem cell culturing. *PLoS One* **8**, e81156 (2013).

45. Kafri, T. *et al.* Developmental pattern of gene-specific DNA methylation in the mouse embryo and germ line. *Genes Dev.* **6**, 705–14 (1992).

46. Marks, H. *et al.* The transcriptional and epigenomic foundations of ground state pluripotency. *Cell* **149**, 590–604 (2012).

47. Notingher, I. *et al.* Discrimination between ricin and sulphur mustard toxicity *in vitro* using Raman spectroscopy. *J. R. Soc. Interface* **1**, 79–90 (2004).

48. Puppels, G. J., Garritsen, H. S., Segers-Nolten, G. M., de Mul, F. F. & Greve, J. Raman microspectroscopic approach to the study of human granulocytes. *Biophys. J.* **60**, 1046–56 (1991).

49. Overman, S. A. *et al.* Conformation and interactions of the packaged double-stranded DNA genome of bacteriophage T7. *Biospectroscopy* **4**, S47–S56 (1998).

50. Notingher, I. & Hench, L. L. Raman microspectroscopy: a noninvasive tool for studies of individual living cells *in vitro*. *Expert Rev. Med. Devices* **3**, 215–234 (2006).

51. Sathuluri, R. R., Yoshikawa, H., Shimizu, E., Saito, M. & Tamiya, E. Gold Nanoparticle-Based Surface-Enhanced Raman Scattering for Noninvasive Molecular Probing of Embryonic Stem Cell Differentiation. *PLoS One* **6**, e22802 (2011).

52. Barhoumi, A. & Halas, N. J. Detecting chemically modified DNA bases using surface-enhanced raman spectroscopy. *J. Phys. Chem. Lett.* **2**, 3118–3123 (2011).
53. Katainen, E. *et al.* Quantification of the amphetamine content in seized street samples by Raman spectroscopy. *J. Forensic Sci.* **52**, 88–92 (2007).
54. Cheng, W. T., Liu, M. T., Liu, H. N. & Lin, S. Y. Micro-Raman spectroscopy used to identify and grade human skin pilomatrixoma. *Microsc. Res. Tech.* **68**, 75–79 (2005).
55. Notingher, I. *et al. In situ* characterisation of living cells by Raman spectroscopy. *Spectroscopy* **16**, 43–51 (2002).
56. Binoy, J. *et al.* NIR-FT Raman and FT-IR spectral studies and ab initio calculations of the anti-cancer drug combretastatin-A4. *J. Raman Spectrosc.* **35**, 939–946 (2004).
57. Coluccio, M. L. *et al.* From nucleotides to DNA analysis by a SERS substrate of a self similar chain of silver nanospheres. *J. Opt.* **17**, 114021 (2015).
58. Mahadevan-Jansen, A. & Richards-Kortum, R. R. Raman spectroscopy for the detection of cancers and precancers. *J. Biomed. Opt.* **1**, 31 (1996).
59. Barr, H., Dix, T. & Stone, N. Optical spectroscopy for the early diagnosis of gastrointestinal malignancy. *Lasers Med. Sci.* **13**, 3–13 (1998).
60. Farquharson, S., Shende, C., Inscore, F. E., Maksymiuk, P. & Gift, A. Analysis of 5-fluorouracil in saliva using surface-enhanced Raman spectroscopy. *J. Raman Spectrosc.* **36**, 208–212 (2005).
61. Johnson, T. B. & Coghill, R. D. Researches on pyrimidines. C111. The discovery of 5-methyl-cytosine in tuberculinic acid, the nucleic acid of the tubercle bacillus. *J. Am. Chem. Soc.* **47**, 2838–2844 (1925).
62. Zhang, X. *et al.* Label-free live-cell imaging of nucleic acids using stimulated raman scattering microscopy. *Chem Phys Chem* **13**, 1054–1059 (2012).
63. Mathieu, O., Picard, G. & Tourmente, S. Methylation of a euchromatin-heterochromatin transition region in Arabidopsis thaliana chromosome 5 left arm. *Chromosome Res.* **10**, 455–66 (2002).
64. Milutinovic, S., Zhuang, Q., Niveleau, A. & Szyf, M. Knockdown of DNA methyltransferase 1 triggers an intra-S-phase arrest of DNA replication and induction of stress response genes. *J. Biol. Chem.* **278**, 14985–14995 (2003).
65. Brauchle, E. *et al.* Non-invasive Chamber-Specific Identification of Cardiomyocytes in Differentiating Pluripotent Stem Cells. *Stem Cell Reports* **6**, 188–199 (2016).
66. Pudlas, M. *et al.* Raman Spectroscopy: A Noninvasive Analysis Tool for the Discrimination of Human Skin Cells. *Tissue Eng. Part C Methods* **17**, 1027–1040 (2011).
67. Votteler, M. *et al.* Raman spectroscopy for the non-contact and non-destructive monitoring of collagen damage within tissues. *J. Biophotonics* **5**, 47–56 (2012).
68. Brauchle, E., Thude, S., Brucker, S. Y. & Schenke-Layland, K. Cell Death Stages in Single Apoptotic and Necrotic Cells Monitored by Raman Microspectroscopy. *Sci. Rep.* **4**, 4698 (2014).
69. Ashkin, A. Acceleration and Trapping of Particles by Radiation Pressure. *Phys. Rev. Lett.* **24**, 156–159 (1970).
70. Perney, N. M. B., Horak, P., Hanley, N. A. & Melvin, T. The self-orientation of mammalian cells in optical tweezers—the importance of the nucleus. *Phys. Biol.* **9**, 024001 (2012).

Acknowledgements

Author Contributions

R.D. and D.A.C.B. performed the Raman imaging experiments and analyses. R.D. performed all other experiments. E.M.B., T.P.J. and K.S.-L. provided scientific advice. T.P.J. provided the HCT116 cells. R.D., E.M.B., T.P.J. and K.S.-L. wrote the manuscript.

Additional Information

Supplementary information accompanies this paper at https://doi.org/10.1038/s41598-019-43520-z.

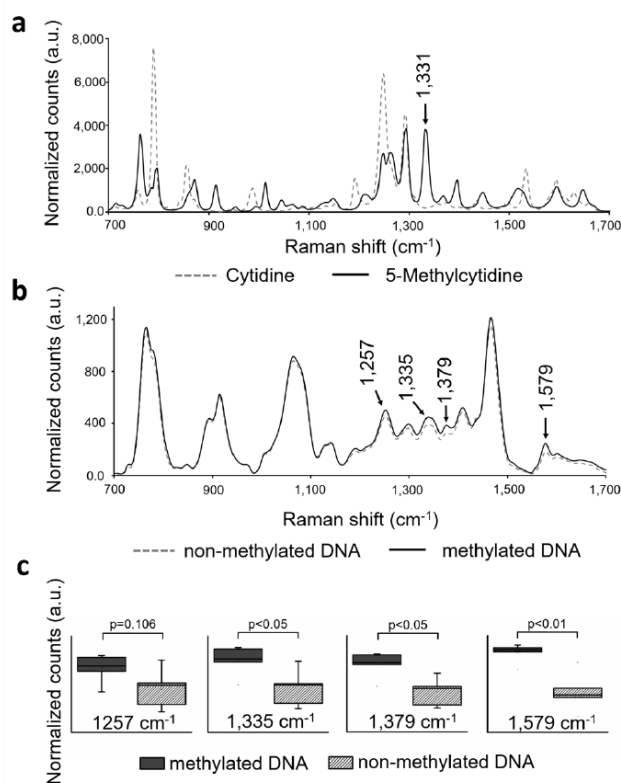**Competing Interests:** The authors declare no competing interests.

Publisher's note: Springer Nature remains neutral with regard to jurisdictional claims in published maps and institutional affiliations.

24 **Supplemental Figures**

25

26 **Suppl. Fig. 1. Raman spectra of cytidine, 5mC, methylated and non-methylated DNA**

27 (**a**) Raman spectra of cytidine and 5mC show various different intensities with a distinct

28 increased Raman band for 5mC at 1331 cm^{-1}. (**b**) Raman spectra of methylated and non-

29 methylated DNA. Increased Raman bands for methylated DNA are indicated by arrows.

30 (**c**) The methylated DNA shows significant increased Raman bands at 1335 cm^{-1}, 1379

31 cm^{-1} and 1579 cm^{-1}. Two-tailed *t*-test, n=5.

32

33
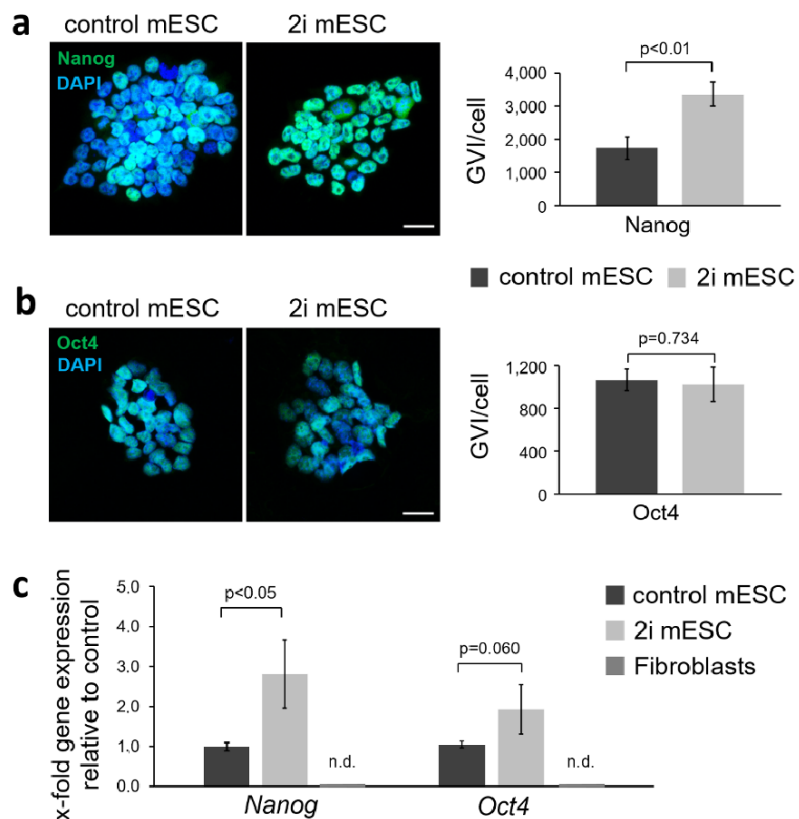
Suppl. Fig. 2. Verification of the pluripotency of mESCs adapted to 2i medium

(**a**) Nanog and (**b**) Oct4 IF staining (green) of mESCs cells cultured in either control (control mESC) or 2i medium (2i mESC). Nanog staining shows significantly higher GVI/cell values in 2i medium-adapted mESCs. Two-tailed *t*-test, n=3. Scale bars equal 20 µm. (**c**) Relative expression of *Nanog* and *Oct4* in control mESC or 2i mESC. Two-tailed *t*-test, n=3

a

PCA Score values				
PC	Mean		SD		p-value*
	WT	DNMT⁻/⁻	WT	DNMT⁻/⁻	
1	-0.0081	-0.0078	0.1022	0.0645	**0.1837**
2	-0.0077	0.0076	0.0466	0.0513	**0.0234**
3	0.0008	-0.0006	0.0261	0.0334	**0.7397**
4	-0.0099	0.0101	0.0184	0.0267	$4.24*10^{-10}$

*Two-tailed t-test, n=125

b
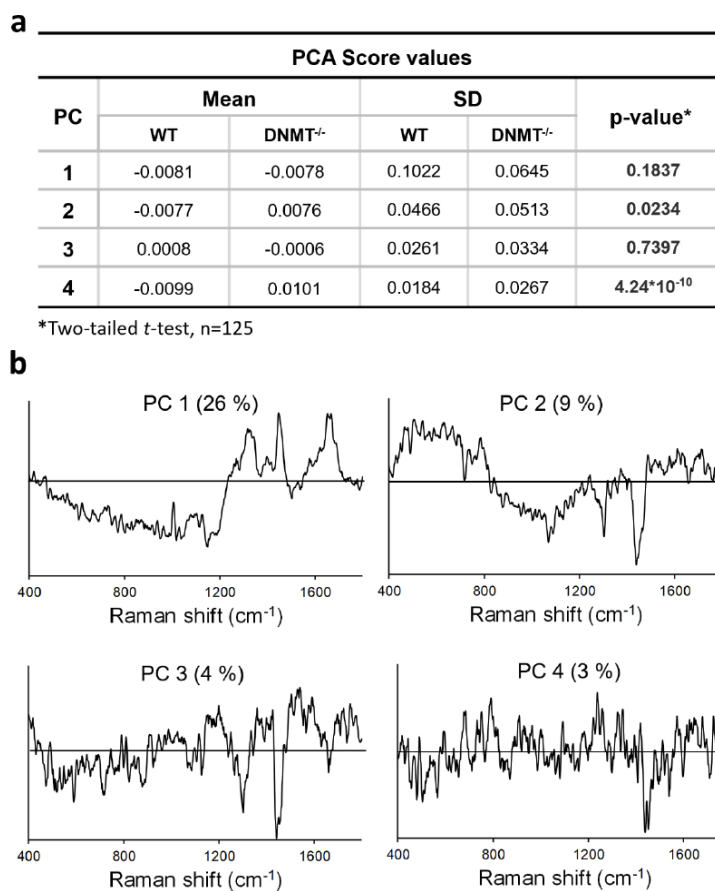
40

41 **Suppl. Fig. 3. PCA score values and loadings of the human colon cancer cell**

42 **experiments**

43 (**a**) Mean values, standard deviations and p-values of the PC score values from WT versus

44 DNMT1⁻/⁻ cells. Two-tailed t-test, n=125. (**b**) PC 1 – PC 3 loadings of the WT versus

45 DNMT1⁻/⁻ cells.

a

	Mean		SD		
PC	control mESC	2i mESC	control mESC	2i mESC	**p-value***
1	0.0171	-0.0196	0.0782	0.0857	**0.0141**
2	0.0077	-0.0088	0.0669	0.0555	**0.0880**
3	0.0106	-0.0122	0.0589	0.0300	**0.0027**
4	-0.0183	0.0209	0.0190	0.0181	**$2.59*10^{-25}$**

PCA Score values

*Two-tailed t-test, n=85

b

46
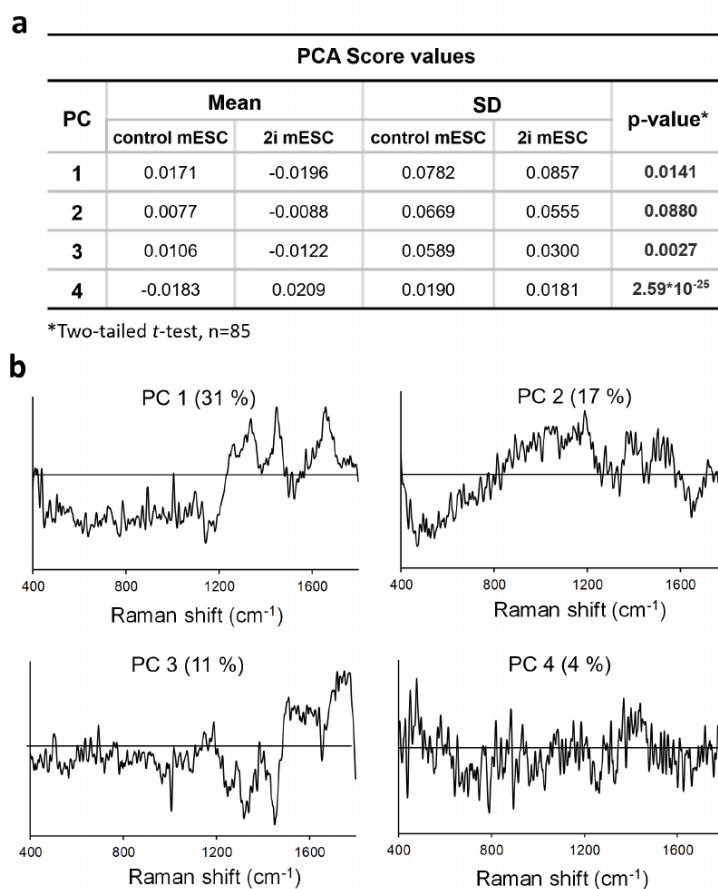
Suppl. Fig. 4. PCA scores and loadings of the mESC experiments

(**a**) Mean values, standard deviations and p-values of the PC score values from mESCs cultured in control (control mESC) or 2i medium (2i mESC). Two-tailed t-test, n=85. (**b**) PC 1 – PC 3 loadings of the control mESCs or 2i mESCs.

89

Appendix II: Daum, R., Visser, D., Wild, C. et al. *Fibronectin Adsorption on Electrospun Synthetic Vascular Grafts Attracts Endothelial Progenitor Cells and Promotes Endothelialization in Dynamic In Vitro Culture*, Cells, 2020; **9**, 3

cells | MDPI

Article

Fibronectin Adsorption on Electrospun Synthetic Vascular Grafts Attracts Endothelial Progenitor Cells and Promotes Endothelialization in Dynamic In Vitro Culture

Ruben Daum [1], Dmitri Visser [1], Constanze Wild [2], Larysa Kutuzova [3], Maria Schneider [2], Günter Lorenz [3], Martin Weiss [1,4], Svenja Hinderer [1], Ulrich A. Stock [5], Martina Seifert [2] and Katja Schenke-Layland [1,4,6,7,*]

[1] NMI Natural and Medical Sciences Institute at the University of Tübingen, 72770 Reutlingen, Germany; ruben.daum@nmi.de (R.D.); dmitri.visser@nmi.de (D.V.); martin.weiss@med.uni-tuebingen.de (M.W.); hinderer@polymedics.de (S.H.)
[2] Institute of Medical Immunology and BIH Center for Regenerative Therapies (BCRT), Charité-Universitätsmedizin Berlin, Corporate Member of Freie Universität Berlin, Humboldt-Universität zu Berlin, and Berlin Institute of Health, 13353 Berlin, Germany; constanze.wild@charite.de (C.W.); maria.schneider@charite.de (M.S.); martina.seifert@charite.de (M.S.)
[3] Applied Chemistry, University of Reutlingen, 72762 Reutlingen, Germany; larysa.kutuzova@reutlingen-univeristy.de (L.K.); guenter.lorenz@reutlingen-university.de (G.L.)
[4] Department of Women's Health, Research Institute for Women's Health, Eberhard-Karls-University Tübingen, 72076 Tübingen, Germany
[5] Department of Cardiothoracic Surgery, Royal Brompton and Harefield Foundation Trust, Harefield Hospital Hill End Rd, Harefiled UB9 6JH, UK; u.stock@rbht.nhs.uk
[6] Cluster of Excellence iFIT (EXC 2180) "Image-Guided and Functionally Instructed Tumor Therapies", Eberhard-Karls-University Tübingen, 72076 Tübingen, Germany
[7] Department of Medicine/Cardiology, Cardiovascular Research Laboratories, David Geffen School of Medicine at UCLA, Los Angeles, CA 90095, USA
*   Correspondence: katja.schenke-layland@med.uni-tuebingen.de; Tel.: +49-707-1298-5205

check for updates

Abstract: Appropriate mechanical properties and fast endothelialization of synthetic grafts are key to ensure long-term functionality of implants. We used a newly developed biostable polyurethane elastomer (TPCU) to engineer electrospun vascular scaffolds with promising mechanical properties (E-modulus: 4.8 ± 0.6 MPa, burst pressure: 3326 ± 78 mmHg), which were biofunctionalized with fibronectin (FN) and decorin (DCN). Neither uncoated nor biofunctionalized TPCU scaffolds induced major adverse immune responses except for minor signs of polymorph nuclear cell activation. The in vivo endothelial progenitor cell homing potential of the biofunctionalized scaffolds was simulated in vitro by attracting endothelial colony-forming cells (ECFCs). Although DCN coating did attract ECFCs in combination with FN (FN + DCN), DCN-coated TPCU scaffolds showed a cell-repellent effect in the absence of FN. In a tissue-engineering approach, the electrospun and biofunctionalized tubular grafts were cultured with primary-isolated vascular endothelial cells in a custom-made bioreactor under dynamic conditions with the aim to engineer an advanced therapy medicinal product. Both FN and FN + DCN functionalization supported the formation of a confluent and functional endothelial layer.

Keywords: vascular graft; endothelialization; tissue engineering; decorin; fibronectin; electrospinning; endothelial progenitor cells; bioreactor; biostable polyurethane

1. Introduction

Atherosclerotic cardiovascular disease is one of the leading causes of death worldwide [1,2]. It includes all medical conditions, where blood flow to organs and limbs is reduced due to plaque deposition. Surgical intervention is required to reopen or replace the defective vessel. The use of autografts, like the saphenous vein or mammary artery, are still the standard clinical approach for the replacement of small diameter blood vessels [3]. However, mechanical or size mismatches, and mainly the scarce availability make alternative grafts necessary [4,5]. In this context, two strategies have emerged in recent years: synthetic substitutes and biological grafts [4]. Although large-diameter synthetic substitutes (>6 mm) are successfully used, small diameter grafts (<6 mm) show low patency rates due to their tendency to elicit thrombosis and the formation of intimal hyperplasia [6–8]. Appropriate mechanical properties and biocompatibility of the synthetic graft as well as a fast endothelialization after implantation are key properties to ensure a long-term functional implant. In addition, the graft should evoke a balanced immune reaction. On the one hand, a moderate immune response is beneficial in order to promote tissue regeneration. On the other hand, chronic immune responses can lead to inflammation, fibrosis, or calcification and should be avoided to ensure long-term function of the vascular graft [9].

Electrospinning has proven to be a suitable method for the fabrication of fibrous scaffolds and vascular constructs as it mimics the highly porous structure and physical properties of the extracellular matrix (ECM) of the native tissue. Due to their high porosity, pore interconnectivity, and large surface area, the fibrous scaffolds are able to promote cell adhesion, cell alignment, and cell proliferation [10–13]. In addition, in order to elicit in situ endothelialization in the body, the material surface can be functionalized with bioactive molecules. A central challenge in this context is the attraction, adhesion, and proliferation of endothelial progenitor cells (EPCs) or endothelial cells (ECs) to form a complete endothelium. Several strategies to address this issue have been described: immobilization of antibodies targeting markers for EPCs such as vascular endothelial growth factor receptor 2 (VEGFR2) and platelet endothelial cell adhesion molecule (PECAM-1) [14,15]; modification of the surface with peptides such as the Arg-Gly-Asp (RGD) or Cys-Ala-Gly (CAG) sequence [16,17]; immobilization of growth factors such as the vascular endothelial growth factor (VEGF) or stromal cell-derived factor-1 (SDF-1) [18,19]; immobilization of oligonucleotides and aptamers [20,21]; and surface modification with oligosaccharides and phospholipids [22,23]. However, it is necessary to develop surfaces with improved biocompatible, bioactive, targeted, and stable biofunctionalization [24].

A recent study described the attraction of EPCs by immobilized recombinant human decorin (DCN) [25]. The small leucine-rich proteoglycan plays a pivotal role in the ECM [26]. It is named after its first known function as a modulator of collagen fibrillogenesis [27]. In recent years, it has been shown that DCN influences a variety of biological processes in addition to its structural function. It is involved in cell attachment [28–30], proliferation [31,32], and migration [28,29,31,33]. Furthermore, it has been described that DCN inhibits the proliferation and migration of vascular smooth muscle cells but does not affect ECs [28,31]. With a proportion of 22% of all proteoglycans in the vessel wall, it also influences many biological processes in vascular homeostasis and angiogenesis [34–36]. Depending on the molecular environment, it can act pro-angiogenic or antiangiogenic [26,34]. For instance, DCN was shown to interact antagonistically with the mesenchymal epithelial transition factor (c-MET) and the VEGFR2, which significantly influences angiogenesis [26,34,37,38]. In addition, DCN binds to the transforming growth factor β (TGF-β), which in turn has an inhibiting effect on the endothelial-mesenchymal transition and fibrosis [26,39,40]. These properties make the protein a promising candidate for improving the endothelialization of a vascular graft. Another highly relevant ECM protein is fibronectin (FN). Since FN interacts with cells via the integrins $\alpha_5\beta_1$ or $\alpha_v\beta_3$, it is a suitable protein for bioactivating a material surface [41–44]. It is of interest with regard to endothelialization, as it plays a pivotal role in wound healing [45,46]. Several studies described the coating of FN in combination with collagens type I [47] and type IV [48], with fibrinogen and tropoelastin [49], hepatocyte growth factor [50], heparin,

91

and VEGF [51] and with SDF-1α [19] to improve reendothelialization. However, it has never been used in combination with DCN before.

Tissue engineering can be used as an alternative strategy to obtain a functional endothelium in a synthetic graft utilizing a patient's own cells [52]. After implantation, the tissue-engineered vascular graft (TEVG) is replaced by the host's cells and ECM and is thereby degraded [4]. However, the loss of mechanical properties due to a too rapid degradation and unfavorable biological reactions to the degradation products remain a major challenge [1,53]. A recent study addressed this problem by producing a TEGV that consists of a combination of a biodegradable and biostable polymer [54].

In our study, a newly developed biostable polyurethane elastomer was used to develop an electrospun scaffold with mechanical properties that are comparable to native vascular tissues, and a bioactive surface that attracts endothelial progenitor cells or promotes endothelialization [55]. For this purpose, planar and tubular electrospun scaffolds (Figure 1a) were biofunctionalized with FN, DCN, or FN and DCN in combination (FN + DCN; Figure 1b,c). The influence of the FN- and DCN-coated scaffolds on human immune cell features was examined (Figure 1d). Subsequently, the functionality of the electrospun scaffolds was further investigated. First, endothelial progenitor cell homing was simulated in vitro by attracting endothelial colony forming cells (ECFCs) with a potent angiogenic capacity and the capability to support vascular repair (Figure 1e,f). Secondly, in a classical TEVG approach primary-isolated vascular endothelial cells (vECs) were cultured in a custom-made bioreactor to create an advanced therapy medicinal product (ATMP) (Figure 1g).
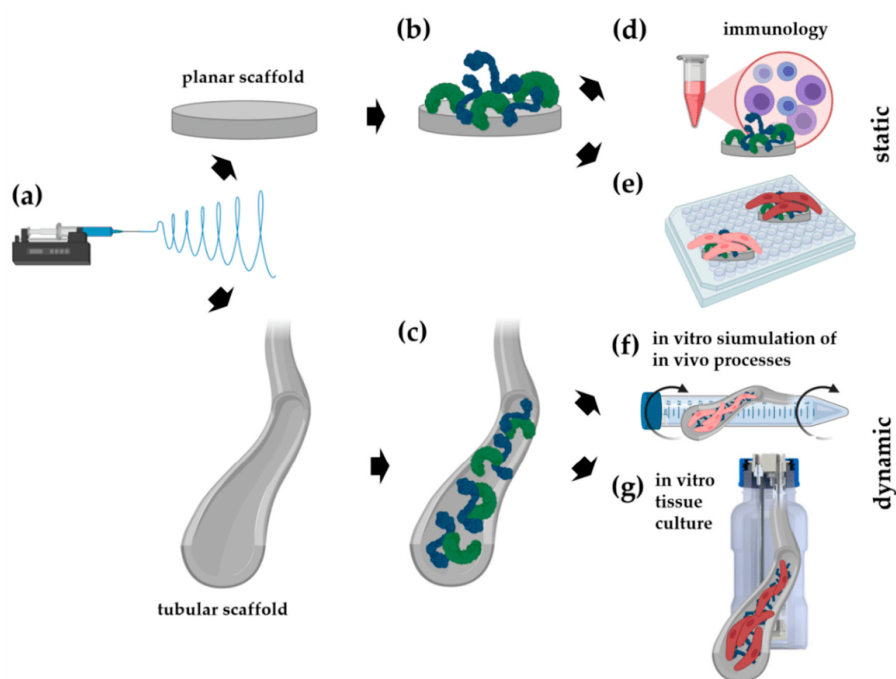
Figure 1. A newly developed polyurethane is used to produce planar and tubular electrospun scaffolds (**a**), which are biofunctionalized with either fibronectin (FN) or decorin (DCN) or with both extracellular matrix (ECM) proteins in combination (**b**,**c**). Besides investigating the immunology (**d**) and endothelial colony forming cell (ECFC) behavior on either planar (**e**) or in tubular scaffolds (**f**), the tubular scaffolds were also cultured with primary-isolated vascular endothelial cells (vECs) in an tissue-engineered vascular graft (TEVG) approach (**g**) in order to assess an ECM protein-improved endothelialization.

2. Materials and Methods

2.1. Electrospun Scaffold Fabrication

Planar and tubular scaffolds were produced by electrospinning of soft thermoplastic polycarbonate-urethane (TPCU). This elastomeric material was synthesized in our laboratory for special medical applications using the multistep one-pot approach [56], which gives good control of the polymer architecture in catalyst-free systems. In more detail, a long-chain aliphatic polycarbonate with more than 72% (*w/w*) in the TPCU formulation provides an additional crystallization of the soft segment, which enhances biostability of the implantable material as well as improves its mechanical properties. In vitro biostability of the TPCU was studied previously from a mechanical point of view under long-term oxidative treatment [55]. Cytocompatibility of the TPCU material was also demonstrated [57]. By adjusting the respective parameters to achieve a stable process and appropriate mechanical properties of the scaffold (Figure S1a), 0.1 g/mL of the polymer was dissolved in 1,1,1,3,3,3 hexafluoro-2-propanol (804515, Merck, Darmstadt, Germany) and electrospun with the process conditions summarized in Table 1. The electrospinning process was carried out in a temperature- and humidity-controlled electrospinning apparatus (EC-CLI, IME Technologies, Eindhoven, Netherlands).

Table 1. Process conditions for electrospinning planar and tubular scaffolds.

Description	Value
Distance	25 cm
Needle i.d.	0.4 mm
Voltage	18 kV/−0.2 kV (needle/collector)
Temperature	23 °C
Humidity	40%
Mandrel diameter [1]	6 mm
Mandrel rotation speed [1]	2000 rpm
Needle translation distance [1]	80 mm
Volume	6 mL
Flow rate	4 mL/h

i.d.= inner diameter; [1] tubular scaffolds.

2.2. Biofunctionalization of the Scaffolds

Before biofunctionalization, the appropriate disinfection method was investigated. Since ethanol did not affect the scaffold in terms of its mechanical properties (Figure S1b), the constructs were disinfected with 70% ethanol for 20 min and afterwards washed three times for 10 min with phosphate-buffered saline (PBS). Microbiological studies were carried out on the scaffolds to investigate the effectiveness of the disinfection method (Figure S3). The scaffolds were functionalized by protein adsorption. They were incubated for 2 h at 37 °C with 20 µg/mL human plasma FN (F1056, Sigma-Aldrich, St. Louis, USA) or 20 µg/mL recombinant full-length human DCN [25], individually or in combination. Excess protein was removed by washing the scaffolds with PBS.

2.3. Morphological and Mechanical Characterization of the Electrospun Scaffolds

For the morphological characterization, punches from the electrospun scaffolds were examined by scanning electron microscopy (SU8030, Hitachi, Tokyo, Japan) followed by the analysis using ImageJ and the DiameterJ package [58] to assess the pore and fiber sizes. For the investigation of the mechanical properties, a ring tensile test was performed based on the methods described by Laterreur et al. [59] in order to determine the circumferential tensile strength and burst pressure. Briefly, the tubular scaffolds were cut into pieces with the length $L_0 = 7$ mm, clamped into a uniaxial tensile testing device (Zwick Roell, Ulm, Germany), and stretched over a distance s with a velocity of 50 mm/min until rupture.

On the basis of the stress–strain curves (Figure S1c), the burst pressure P_b was then calculated by relating the registered force at rupture F_b to the elongation s_b as follows:

$$P_b = \frac{F_b \pi}{L_0 d_{pin}(\pi + 2) + 2L_0 s_b} \tag{1}$$

where d_{pin} represents the diameter of the pins that were used in the ring tensile test. A derivation of Equation (1) is provided by Lattereur et al. [59]. Using an OCA40 (DataPhysics Instruments GmbH, Filderstadt, Germany), the wettability of the scaffolds was analyzed as previously described [60]. A waterdrop with a volume of 2 μL was placed onto the scaffold and measured using the SCA20 software (DataPhysics Instruments, Filderstadt, Germany). The water absorption ability was determined by weighing the specimens in their dry and wet states after submerging the specimens in water for 1 h. The relative weight increase is referred to as the swelling ratio.

2.4. Immune Cell/Scaffold Co-Culture Assays

Polymorph nuclear cells (PMNs) were isolated from freshly donated human blood and peripheral blood mononuclear cells (PBMCs) from buffy coats according to the ethical approval by the local ethics committee at the Charité Berlin (EA2/139/10 approved on 10th December 2010; EA1/226/14 approved on 24th July 2014) and as recently described [61]. Monocytes were magnetically sorted via CD14 beads (130-050-201, Miltenyi Biotec, Bergisch Gladbach, Germany) from PBMCs as previously described [62]. Monocytes were differentiated into M0 macrophages by adding 50 ng/mL of macrophage colony-stimulating factor (M-CSF) (130-096-491, Miltenyi Biotec) to the culture medium for 7 days. All immune cell co-cultures were performed in Roswell Park Memorial Institute (RPMI) 1640 medium (F1415, Biochrom GmbH, Berlin, Germany) with 10% human serum type AB (H4522, Sigma-Aldrich), 1% L-glutamine (25030-024, Thermo Fisher Scientific, Waltham, MA, USA), and 1% penicillin/streptomycin (15140-122, Thermo Fisher Scientific).

First, the scaffold punches were incubated with 100 μg/mL of recombinant full-length human DCN [25] or 20 μg/mL of FN (F1056, Sigma-Aldrich) at 37 °C for 4 h. Next, punches were washed with PBS (L1825, Biochrom GmbH), placed into a well of a 48-well plate, and kept in place with a silicon ring (Ismatec, Wertheim, Germany). Thereafter, the different immune cell types were applied as follows:

Human PMNs were cultured on the uncoated, DCN- or FN-coated scaffolds; 0.2×10^6 PMNs in 200 μL of complete RPMI were seeded directly on the scaffold punches. Unstimulated cells were used as a negative control, and PMNs that were stimulated with 500 ng/mL of lipopolysaccharide (LPS; 297-473-0, Sigma-Aldrich) served as a positive control. LPS is a component of the bacterial cell membrane that triggers the activation of immune cells. After 4 h of culture, cells were harvested only by careful resuspension, stained with human-specific antibodies for CD11b (1:100; 557701, BD Bioscience, San Jose, CA, USA) and CD66b (1:200; 305107, BioLegend, Fell, Germany), and measured by flow cytometry (CytoFLEX LX, Beckman Coulter, Inc., Brea, CA, USA) as described recently [61]. The determined mean fluorescence intensities (MFIs) of marker expression were normalized to the MFI of unstimulated PMNs directly after isolation.

Human monocytes or M0 macrophages were cultured on the uncoated, DCN- or FN-coated scaffolds; 0.2×10^6 cells in 350 μL of complete RPMI were seeded directly on the scaffold punches. Monocytes that were stimulated with 100 ng/mL of LPS served as a positive control, and unstimulated monocytes served as a negative control. Macrophages cultured without any stimulus were used as negative control. To induce the polarization into the M1 phenotype, 20 ng/mL of IFNγ (130-096-486, Miltenyi Biotec) and 100 ng/mL of LPS were added to the medium of M0 macrophages. After two days of culture, monocytes/macrophages were harvested, stained with human-specific antibodies for CD80 (1:20; 305208, BioLegend) and human leukocyte antigen DR isotype (HLA-DR) (1:200; 307616, BioLegend), and measured by flow cytometry. Cells were detached by adding 100 μL of Accutase (A11105-01, Thermo Fisher Scientific) and incubating the cells at 37 °C for 30 min. The determined MFIs of the marker expression were normalized to the MFI of the unstimulated cells.

PBMCs were cultured on the uncoated, DCN- or FN-coated scaffolds; 0.3×10^6 cells were seeded in 400 μL of complete RPMI directly on the scaffold punches. Unstimulated PBMCs served as a negative control. For the positive controls, PBMCs were stimulated with anti-CD28 (556620, BD Bioscience)/anti-CD3 (OKT3, Janssen-Cilag, Neuss, Germany) antibodies. After three days of culture, PBMCs were harvested, stained with human-specific antibodies for CD69 (1:50; 310926 BioLegend), CD25 (1:50; 302605, BioLegend) and HLA-DR (1:100; 307640, BioLegend), and measured by flow cytometry. PBMCs were detached by adding 100 μL of Accutase and by incubating the cells at 37 °C for 30 min. After gating for single and living cells the CD14− and CD14+ populations were defined. For CD3+ cells, the MFI of the activation markers CD25, CD69, and HLA-DR was determined. The determined MFIs of the marker expression were normalized to the MFI of unstimulated PBMCs.

Co-culture supernatants of monocytes and macrophages were collected and the tumor necrosis factor alpha (TNFα) concentration was analyzed by ELISA (430205, BioLegend) according to the manufacturer's instructions.

2.5. Cell Culture of Primary Endothelial Cells and Endothelial Colony Forming Cells

Human primary-isolated vECs were isolated from foreskin biopsies under the ethics approval no 495/2018BO2 by enzymatic digestion with dispase and trypsin as previously described [63]. The vECs were cultured in endothelial cell growth medium and SupplementMix (C-22020, PromoCell, Heidelberg, Germany), supplemented with 1% penicillin-streptomycin (15140122, Thermo Fisher Scientific).

Human ECFCs (00189423, Lonza, Basel, Switzerland) were cultured in endothelial cell growth medium-2 with supplements (CC-3162, Lonza). Instead of the supplied fetal bovine serum, 5% of human serum (H4522, Sigma-Aldrich) was used. In addition, 1% L-Glutamine (21051024, Thermo Fisher Scientific) and 1% penicillin-streptomycin (15140122, Thermo Fisher Scientific) were added to the cell culture medium.

Both cell types were cultured at 37 °C and 5% CO_2 and passaged at approximately 80% confluence. The vECs were used for the experiment after 2–4 passages.

2.6. Cell Seeding and Culture on Planar Scaffolds

Prior to cell culture experiments, general biocompatibility of the electrospun scaffolds was examined with a cytotoxicity test based on EN ISO 10993-5 [64]. Briefly, the scaffolds were incubated for 72 h at 37 °C and 5% CO_2 in 1 mL endothelial cell growth medium supplemented with 1% penicillin-streptomycin at an extraction ratio of 0.1 mg/mL; 2×10^4 vECs seeded in a 96-well plate were then exposed for 24 h to the extracts supplied with the cell culture medium supplements. Endothelial cell growth medium without the scaffolds served as a negative control. Cells exposed to 1% SDS served as positive control. The extraction and control medium were removed, and an MTS (3-(4,5-dimethylthiazol-2-yl)-5-(3-carboxymethoxyphenyl)-2-(4-sulfophenyl)-2H-tetrazolium) assay (CellTiter 96Aqueous One Solution Cell Proliferation Assay, Promega, Madison, WI, USA) was performed according to the manufacturer's protocol; 20 μL MTS solution and 100 μL cell culture medium were added to each well. After 30 min of incubation at 37 °C, the absorbance of each well was measured at 450 nm using a microplate reader (PHERAstar, BMG Labtech, Ortenberg, Germany). Cell viability was determined by the absorbance of the samples relative to the negative control. No toxic effect of the material was observed (Figure S2a). Biofunctionalization of the scaffolds was then carried out as described above. Cells were seeded afterwards onto the biofunctionalized scaffolds with a diameter of 6 mm, which were placed in a 96-well plate. For the vECs, 5×10^3 cells/well and, for the ECFCs, 1×10^4 cells/well were seeded in 150 μL of the appropriate medium. If required, media change was carried out every 3 days.

2.7. Endothelial Colony Forming Cells (ECFC) Seeding Under Dynamic Conditions

The tubular electrospun scaffolds were cut to 6 cm length and biofunctionalized with FN and DCN alone or in combination as described above. A cell suspension of 4×10^5 ECFCs/mL was pipetted

into the tubular constructs. Afterwards, the constructs were closed at both ends and put in 15-mL centrifuge tubes filled with the corresponding cell culture medium. Placed on a roller mixer (RM5, CAT, Ballrechten-Dottingen, Germany), the tubes were rotated with 60 rpm for 24 h at 37 °C and 5% CO_2. For cell number analysis, the attached cells were stained with 4′,6-diamidino-2-phenylindole (DAPI) (1:50, 10236276001, Roche Diagnostics, Mannheim, Germany) and counted.

2.8. Development of a Bioreactor System for Tissue-Engineered Vascular Graft (TEVG) Culture

The TEVG approach was performed with a custom-made bioreactor setup. The culture chamber consists of a 250-mL glass bottle (Schott Duran, Wertheim, Germany) and encloses a removable custom-designed graft frame that holds the vascular graft. A computer-aided design (CAD) model for the graft frame was created in Solidworks (Dassault Systèmes, Vélizy-Villacoublay, France) and milled out of polyether ether ketone (PEEK; ADS Kunststofftechnik, Ahaus, Germany) using a 2.5-axis flatbed milling setup (Isel, Eichenzell, Germany) with computer numerical control (CNC). The constructed parts were subjected to the aforementioned cytotoxicity test to ensure no toxic leachables are released into the medium under culture (Figure S2b). The modular design of the culture chamber allows for a toolless assembly of the bioreactor system under a sterile bench.

The graft frame—once inserted into the culture chamber—is connected to medium reservoirs and a bubble trap with flexible silicone tubing. Sterile gas exchange is facilitated by sterile filters connected to the medium reservoirs. The entire setup is driven by a multichannel roller pump (Ismatec) (Figure 2).

The flow rates Q for dynamic culture were determined with a derived formulation of the Hagen–Poiseuille equation for laminar flow in straight circular pipes with internal radius r:

$$\tau = \frac{4\mu Q}{\pi r^3} \tag{2}$$

where μ denotes the dynamic viscosity. This gave an analytical approximation of the achieved wall shear stress (τ) within the cultured vascular graft. To validate this approximation and the assumption of a laminar regime within the vascular graft, in silico simulations were used to assess the local fluid dynamics within the vascular graft and graft frame interior. Briefly, the CAD model of the graft frame was meshed and exported to a computational fluid dynamics (CFD) solver (ANSYS Fluent). Dynamic culture with a wide range of flow rates was simulated under steady-state flow and Newtonian rheological conditions, after which the calculated wall shear stress on the interior graft wall was analyzed and compared to the aforementioned analytical solution (Figures S4 and S5).

2.9. Tissue Culture of Vascular Endothelial Cells Under Dynamic Conditions

Tubular electrospun scaffolds were cut to 7.5 cm length and biofunctionalized with 20 μg/mL FN as described previously. After inserting the graft frame into the culture chamber, 2×10^6 vECs/mL were seeded into the tubular scaffold. In order to achieve homogeneous cell adhesion across the entire tube, the culture chamber was placed horizontally and rotated every 15 minutes over 45 ° for 3 h at 37 °C and 5% CO_2. The culture chamber was consecutively connected to the rest of the bioreactor setup and filled with 70 mL culture medium, supplemented with 1% penicillin-streptomycin and 1% PrimocinTM (ant-pm-1, InvivoGen, San Diego, CA, USA). The seeded cells were allowed to proliferate under static conditions during the first three days, after which the flow rate was slowly increased over the course of two days, as shown in Figure 2e. Subsequently, the tubular construct was cultured under constant flow for seven days.
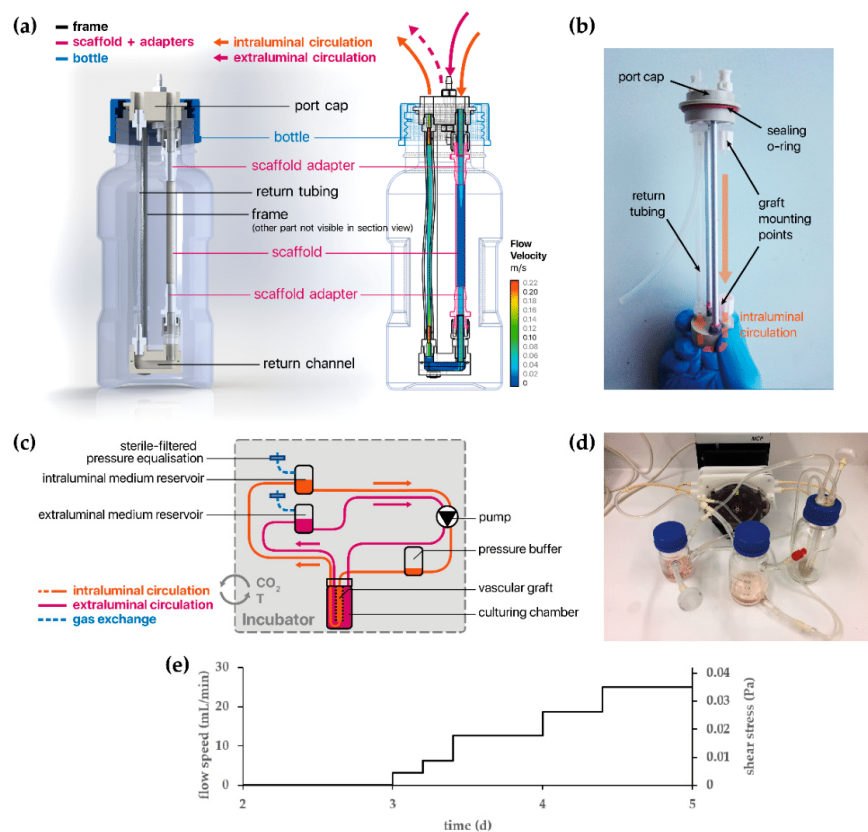
Figure 2. (**a**) A cross-sectional schematic representation of the culturing chamber and its parts. The wireframe model on the right is overlaid by the results of an in silico simulation and shows the flow velocity when the system is perfused with a flow rate of $Q = 20$ mL/min. (**b**) This photograph shows the graft frame (without scaffold), once it is taken out of the culturing chamber. (**c**) A schematic representation of the entire bioreactor setup, showing the circulation and connections to the medium reservoirs and pressure buffer/bubble trap. (**d**) A photograph showing the assembled bioreactor setup with all the components for the intraluminal circulation. (**e**) Applied perfusion flow speed as function of time with the corresponding wall shear stress.

2.10. Immunofluorescence Staining

In order to examine the protein coating, the biofunctionalized scaffolds were stained using DCN mouse monoclonal IgG_1 (1:200; sc-73896, Santa Cruz Biotechnology, Dallas, TX, USA) and FN polyclonal rabbit IgG (1:500; F3648, Sigma-Aldrich) antibodies. For fluorescence labeling, AlexaFluor 488 anti-mouse IgG (1:250; A-11001, Thermo Fisher Scientific) and AlexaFluor 546 anti-rabbit IgG (1:250; A-11035, Thermo Fisher Scientific) were used as secondary antibodies.

Cells cultured on the scaffolds were stained as follows: after washing once with PBS, the cell-seeded scaffolds were fixed with 4% paraformaldehyde (P6148, Sigma-Aldrich). In order to reduce nonspecific binding, the samples were incubated with 2% goat serum-containing block solution for 30 min. Afterwards, the cells were incubated over night at 4 °C with the following antibodies: Vascular endothelial cadherin (VE-cadherin) monoclonal mouse IgG_{2B} (1:500, MAB9381, R&D systems, Minneapolis, MN, USA), VEGFR2 polyclonal rabbit IgG (1:75, ab2349, Abcam, Cambridge, UK), PECAM-1 monoclonal mouse IgG_1 (1:100, sc-71872, Santa Cruz), von Willebrand factor (vWF)

97

polyclonal rabbit IgG (1:200, A0082, Dako, Glostrup, Denmark), and vinculin monoclonal mouse IgG_1 (1:500, MAP3574, Millipore, Burlington, MA, USA). F-actin was stained for 45 min in the dark with Alexa Fluor 647 Phalloidin (1:500, A22287, Thermo Fisher Scientific). Subsequently, samples were incubated with the appropriate secondary antibodies (AlexaFluor 488 anti-mouse IgG, AlexaFluor 546 anti-rabbit IgG, and AlexaFluor 488 anti-mouse IgG2b (all 1:250; Thermo Fisher Scientific)).

Finally, nuclei were stained with DAPI (1:50) for 15 min in the dark. Images were obtained by using a fluorescence microscope (Cell Observer, Carl Zeiss AG, Oberkochen, Germany).

2.11. Examination of the Cell Coverage on the Tubular Scaffolds

The cell coverage of the inner wall of the tubular constructs was investigated using MTT (3-(4,5-dimethylthiazol-2-yl)-2,5-diphenyltetrazolium bromide) (M2128-1G, Sigma-Aldrich). After culturing with vECs, the constructs were incubated for 20 min with 1 mg/mL MTT at 37 °C and 5% CO_2. The insoluble purple formazan produced by the cellular reduction of MTT was then examined macroscopically.

2.12. Image Analysis

FN and DCN coating were quantified by measuring the relative pixel intensity (RPI) of the immunofluorescence images. To assess protein expression in the experiments, the area within a defined fluorescence intensity threshold was measured and normalized to the cell number. The cell count in the static experiments was quantified by counting the DAPI-stained cell nuclei per area. The quantification of the adherent ECFCs in the dynamic experiment was performed by measuring the DAPI-stained area normalized to the total area. All images were analyzed using ImageJ [58].

2.13. Scanning Electron Microscopy of Cells

Prior to SEM imaging of the scaffolds with cells, a critical point drying step was performed. First, cells were fixed for 60 min with 4% paraformaldehyde (PFA)/ 25% glutaraldehyde in PBS. Subsequently, a series of ethanol solutions in ascending concentration up to 100% was carried out to remove water. Critical point drying was done with a CPD 030 (Bal-Tec AG, Balzers, Liechtenstein) according to the manufacturer's protocol. Prior to imaging, the specimens were platina-coated (SCD050, Bal-Tec AG) for one minute at 0.05 mbar and rinsed with Argon after the coating process. SEM imaging was performed with a SU8030 (Hitachi, Tokyo, Japan) and an Auriga® 40 (Zeiss, Oberkochen, Germany).

For SEM imaging of the monocytes and macrophages, the cells were cultured for two days on uncoated (w/o), DCN- or FN-coated scaffolds, followed by preparation (as described in Reference [62]) and imaging with a JCM 6000 Benchtop (JEOL, Freising, Germany).

2.14. Statistical Analysis

Except stated otherwise, data are presented as mean ± standard deviation. For the immune data, GraphPad Prism (GraphPad Software, San Diego, CA, USA) was used to determine statistical significance between two groups using a one-way ANOVA/Kruskal–Wallis test. For the other data, a one-way ANOVA/Fisher's Least Significant Difference test was performed. A Welch's t-test was performed to compare between two data groups using OriginPro (OriginLab, Northampton, MA, USA). Probability values of 95%, 99%, 99.9%, and 99.99% were used to determine significance.

3. Results

3.1. Biofunctionalization Does Not Impact the Mechanical Properties of Electrospun Tubular Constructs

Electrospinning was used to fabricate 110-mm long tubular scaffolds with an inner diameter of 5 mm and a thickness of 0.40 ± 0.06 mm (Figure 3a). In order to modulate the cell–material interaction, the surface was biofunctionalized with FN, DCN, or FN + DCN. The impact of the biofunctionalization on the morphological and mechanical properties of the material was investigated (Figure 3). Fiber and

pore size analysis of the SEM images revealed no significant alteration due to protein adsorption (Figure 3e). Higher magnifications of the SEM images showed distribution of the proteins on the fibers. While DCN formed randomly distributed aggregates on the TPCU scaffolds, FN coating showed a network-like deposition in the nanometer range, which was also seen in the FN + DCN-coated samples, in which clearly recognizable aggregates were deposited on the protein network (Figure 3b, white arrows). Biofunctionalization utilizing both proteins individually and in combination was confirmed by IF staining. DCN IF staining revealed a more heterogeneous distribution of DCN in combination with FN than alone (Figure 3c, white arrows). The contact angle of the scaffolds was not significantly changed by the adsorption of either FN or DCN in comparison with the uncoated scaffolds. A significantly higher swelling ratio was observed of scaffolds that had been coated with FN + DCN (Figure 3e; control: 93.7% ± 7.7% versus FN + DCN: 117.1% ± 8.7%, $p < 0.05$). Overall, biofunctionalization had no significant influence on the mechanical properties (Figure 3e). The ultimate tensile strength ranged from 21.1 ± 3.5 MPa (DCN) to 22.1 ± 3.7 MPa (FN). Burst pressures were in the range between 3124 ± 466 mmHg (FN + DCN) to 3326 ± 78 mmHg (controls). Interestingly, the elastic modulus of the samples coated with FN + DCN showed a lower value compared to the controls, although this was not statistically significant (3.7 ± 0.5 MPa FN + DCN versus 4.8 ± 0.6 MPa controls, $p = 0.125$).

We compared the mechanical properties (elastic modulus and burst pressure) of our electrospun scaffolds with autologous grafts, which are today's gold standard for vascular bypass surgeries, using data obtained from literature (Table 2) [65]. The elastic modulus of our constructs (4.8 ± 0.6 MPa) was slightly higher than that of saphenous veins (2.25–4.2 MPa) [66,67] and of iliofemoral arteries (1.54 MPa) and veins (3.11 MPa) [68]. However, compared with an internal mammary artery (8 MPa) and a femoral artery (FA, 10.5 MPa)—used for popliteal bypass surgery—our engineered scaffolds showed a lower elastic modulus [66,69,70]. Regarding the burst pressure, engineered scaffolds (3326 ± 78 mmHg) lied within the range of a saphenous vein (1250–3900 mmHg) [66,67,71,72] and an internal mammary artery (2000–3196 mmHg) [66,71]. Konig et al. recommends for a TEGV a minimum burst pressure of 1700 mmHg [71]. We can therefore argue that our constructs have suitable mechanical properties to serve as a vascular graft or TEGV.

Table 2. Mechanical properties of the electrospun constructs and native blood vessels.

| Graft Type	Elastic Modulus (MPa)	Burst Pressure (mmHg)	Ref.
Electrospun vascular graft	4.8 ± 0.6	3326 ± 78	-
Saphenous vein	4.2	1680–3900	[66]
Saphenous vein	2.25	1250	[67]
Saphenous vein	NA	1680	[73]
Saphenous vein	NA	2200	[72]
Saphenous vein	NA	1599	[71]
Internal mammary artery	NA	3196	[71]
Internal mammary artery	8	2000	[66]
Femoral artery	9–12	NA	[69]
Iliofemoral artery	1.54	NA	[68]
Iliofemoral vein	3.11	NA	[68]
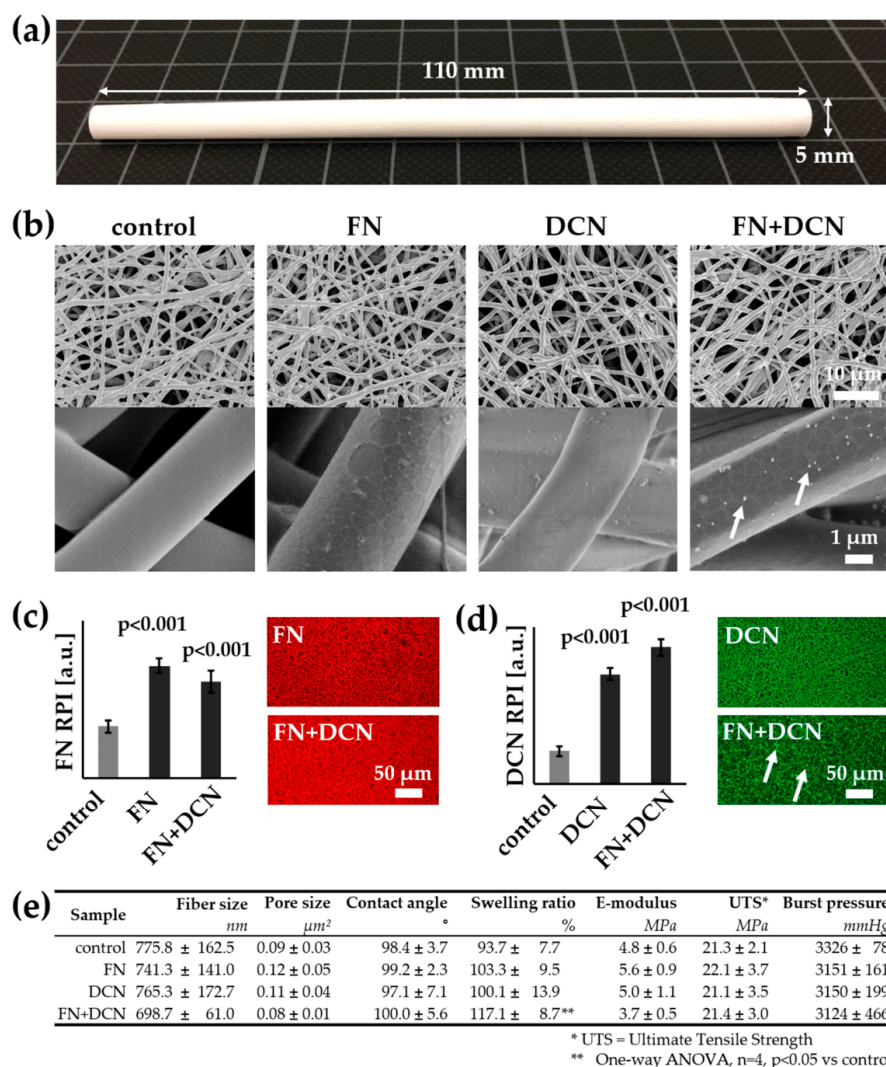
Figure 3. Morphological and mechanical characterization of the tubular biofunctionalized scaffolds: (**a**) Electrospun tubular scaffolds were fabricated with a length of 110 mm, an inner diameter of 5 mm, and a thickness of 0.40 ± 0.06 mm. (**b**) SEM images of control and biofunctionalized scaffolds: Scaffolds coated with FN show a network-like structure on the fibers. Aggregates deposited on the FN + DCN-coated samples are indicated by white arrows. (**c**,**d**) The coating of FN, DCN, or FN + DCN in combination was confirmed with IF staining: FN (red) and DCN (green). The white arrows indicate aggregates deposited on the FN + DCN-coated samples. Two-tailed *t*-test vs. control, n = 3, RPI = relative pixel intensity. (**e**) Fiber and pore size analysis shows no significant difference between the biofunctionalized scaffolds and the controls. Mechanical properties are not influenced by the protein coating. One-way ANOVA, n = 4, $p < 0.05$ vs. control.

3.2. Decorin and Fibronectin Coating of the Scaffolds Does Not Induce a Disadvantageous Immune Response

The effect of DCN- or FN-coated TPCU scaffolds on immune cells was investigated in order to estimate their suitability as vascular graft material. The immune response of a combination coating

was not required as the immune system would not react differently to the presence of both proteins in one coating. The performed immunological evaluation followed the normal sequence of immune activation [9], starting with PMNs that are followed by monocytes, which differentiate into macrophages at the site of injury, and finally T cells that become activated (Figure 4a).
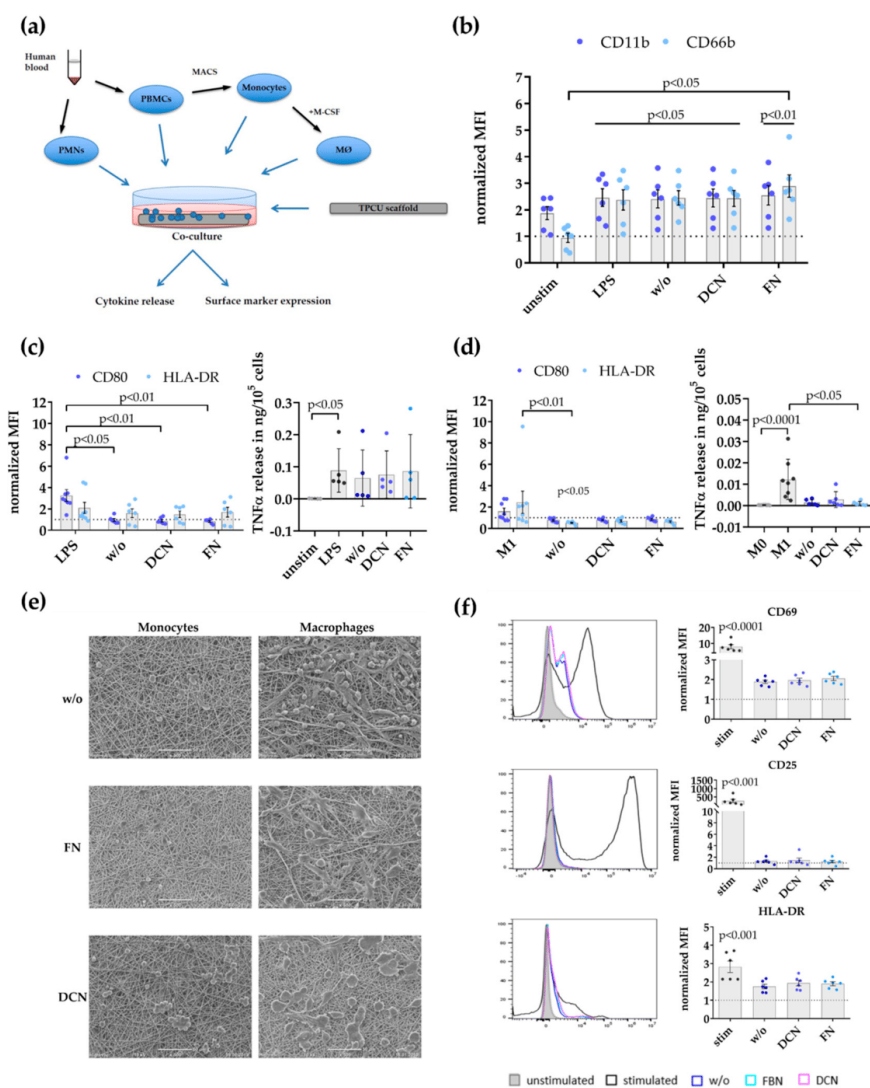
Figure 4. Immune response profile of FN- and DCN-coated planar scaffolds: (**a**) Schematic overview of the analysis steps and used immune cell assays. Polymorph nuclear cells (PMNs) and peripheral blood mononuclear cells (PBMCs) were isolated from human blood. Monocytes were acquired from PBMCs by magnetic separation via CD14 beads. Monocytes were differentiated into M0 macrophages (MØ) by stimulation with 50 ng/mL of macrophage colony-stimulating factor (M-CSF) for 7 days. (**b**) Surface expression of activation markers CD11b and CD66b by PMNs after 4 h: Displayed are the mean fluorescence intensities (MFI) normalized to unstimulated PMNs after isolation as mean ± SEM

(standard error of the mean) for unstimulated (unstim) and lipopolysaccharide (LPS)-stimulated cells, as well as PMNs cultured on the uncoated (w/o), DCN-coated (DCN), and FN-coated (FN) scaffolds determined with flow cytometry. Kruskal–Wallis test, n = 6. (**c**) Surface expression of activation markers CD80 and human leukocyte antigen DR isotype (HLA-DR), and tumor necrosis factor alpha (TNFα) release by monocytes. Shown are the MFI normalized to unstimulated monocytes as mean ± SEM for LPS-stimulated cells as well as monocytes cultured on uncoated (w/o), DCN-coated (DCN), and FN-coated (FN) scaffolds. Kruskal–Wallis test, n = 6–8. The TNF release is depicted in ng/10^5 cells as mean ± SEM for unstimulated (unstim) and LPS-stimulated cells as well as monocytes cultured on the uncoated (w/o), DCN-coated (DCN), and FN-coated (FN) scaffolds. Kruskal–Wallis test, n = 5. (**d**) Surface expression of activation markers CD80 and HLA-DR, and TNFα release by macrophage: Displayed is the MFI normalized to unstimulated M0 macrophages as mean ± SEM for macrophages differentiated to M1 and as well as cells cultured on uncoated (w/o), DCN-coated (DCN), and FN-coated (FN) scaffolds. Kruskal–Wallis test, n = 6–8. The TNFα release is shown in ng/10^5 cells as mean ± SEM for unstimulated M0 macrophages; macrophages differentiated to M1; and as well as cells cultured on the uncoated (w/o), DCN-coated (DCN), and FN-coated (FN) scaffolds. Kruskal–Wallis test, n = 6–9. (**e**) Representative SEM images of monocytes (left) and macrophages (right) on uncoated (w/o) and with biofunctionalized scaffolds (DCN and FN). Scale bars represent 50 μm. (**f**) Expression of activation markers CD69, CD25, and HLA-DR on CD3+ T cells in whole PBMC co-cultures: Shown are representative histograms (left) and the surface expression levels as MFI normalized to unstimulated T cells as mean ± SEM (right) for αCD3/αCD28-stimulated T cells (stim) as well as T cells cultured on uncoated (w/o), DCN-coated, and FN-coated scaffold. Kruskal–Wallis test, n = 6.

Initially, the expression of known PMN activation markers, the integrin CD11b, and the adhesion molecule CD66b was analyzed (Figure 4b). The normalized mean fluorescence intensity (MFI) for CD11b (stim 2.461 ± 0.3323, *p* = 0.0179; w/o 2.406 ± 0.3393, *p* = 0.0378; DCN 2.442 ± 0.3361, *p* = 0.0217; FN 2.549 ± 0.3644, *p* < 0.0090; all versus unstim 0 hours 1 ± 0) and CD66b (stim 2.372 ± 0.3875, *p* = 0.0453; w/o 2.448 ± 0.2728, *p* = 0.0414; DCN 2.431 ± 0.3041, *p* = 0.0453; FN: 2.893 ± 0.4239, *p* = 0.0073; all versus unstim 0 h 1 ± 0) was significantly increased on PMNs after LPS stimulation (positive control) and, after culture on the uncoated/coated scaffolds, compared to the level of PMNs directly after isolation (dotted line, set to 1). Additionally, PMNs on FN-coated TPCU scaffolds displayed a significantly higher CD66b expression compared with the unstimulated controls (FN 2.893 ± 0.4239 versus unstim 4 h 0.9438 ± 0.1723, *p* < 0.0345).

In a next step, monocyte responses were studied by flow cytometry analysis of the activation markers CD80 and HLA-DR (Figure 4c). The expression level for the co-stimulatory molecule CD80 was significantly upregulated only on LPS-stimulated monocytes compared with all other experimental groups (LPS 3.254 ± 0.5533 versus w/o 0.9592 ± 0.1342, *p* = 0.0143; versus DCN 0.8888 ± 0.1209, *p* = 0.0046; versus FN 0.8325 ± 0.08414, *p* = 0.0018). No significant differences in HLA-DR expression were detectable between the tested conditions. Additionally, no enhanced TNFα release of monocytes cultured on the uncoated/coated scaffolds was measured in contrast to a significantly elevated secretion in the LPS-stimulated controls compared to the unstimulated controls (LPS 0.08859 ± 0.03039 versus unstim 0.0005580 ± 0.0002111, *p* = 0.0228).

Then, macrophages (M0 type) generated in vitro by M-CSF were screened for signs of activation or polarization (Figure 4d). M0 (unstimulated) and M1 macrophages (IFNγ/LPS-stimulated) were used as control groups. Enhanced CD80 and HLA-DR expression and increase of TNFα secretion are hallmarks of pro-inflammatory M1 macrophages. There was no difference in the CD80 expression level between M0 macrophages (dotted line, set to 1) and all other experimental groups. The expression of HLA-DR by macrophages on uncoated scaffolds was significantly decreased compared with the M0 and M1 control settings (w/o 0.5220 ± 0.05753 versus M0 1 ± 0, *p* = 0.0106; versus M1 2.453 ± 1.040, *p* = 0.0049). Whereas M1 macrophages significantly elevated their TNFα release compared with M0 macrophages (M1 0.01229 ± 0.003333 versus M0 0.0002707 ± 0.00004142, *p* < 0.0001), no enhancement in pro-inflammatory cytokine release was measurable in all other experimental groups. Macrophages on the FN-coated scaffolds actually decreased their TNFα release compared with the M1 controls

(FN 0.0009826 ± 0.0004063 versus M1 0.01229 ± 0.003333, *p* = 0.0432). Complementary to the analysis of changes in surface marker and pro-inflammatory cytokine release by monocytes and macrophages, scanning electron microscopy was applied to assess the effects of co-culture on their morphology (Figure 4e). Scanning electron microscopy images were taken after the cells were cultured for two days on the different scaffold groups. Monocytes and macrophages on the DCN-coated scaffolds formed clusters of preferentially rounded cells. Macrophages cultured on uncoated or FN-coated scaffolds displayed more diverse shapes in contrast with cells grown on the DCN-coated TPCU scaffolds.

The potential activation of T cells was determined by flow cytometry analysis of known activation markers CD69, CD25, and HLA-DR [74] after culturing complete human PBMCs on either uncoated or coated scaffolds (Figure 4f). However, only anti-CD3/anti-CD28 stimulated T cells (stim; positive control) significantly elevated the expression level for CD69 (stim 7.956 ± 1.319 versus unstim 1 ± 0, *p* < 0.0001), CD25 (stim 265.6 ± 101.5 versus unstim 1 ± 0, *p* = 0.0008), and HLA-DR (stim 2.824 ± 0.3099 versus unstim 1 ± 0, *p* = 0.0001) compared with the level of the unstimulated controls (dotted line, set to 1). No significant increase in T cell activation marker expression was observed in any other experimental group.

3.3. Simulation of Endothelial Progenitor Cell Homing Using Endothelial Colony Forming Cells

3.3.1. ECFCs Show Altered VEGFR2 and PECAM-1 Expression Patterns on FN + DCN-Coated TPCU Scaffolds Under Static Culture Conditions

ECFCs were seeded on the biofunctionalized planar scaffolds and cultured under static conditions for 24 and 48 h. The amount of adherent ECFCs was significantly higher on samples coated with FN (24 h: 257 ± 57 cells/mm^2 versus control with 137 ± 46 cells/mm^2, *p* < 0.01; 48 h: 301 v 64 cells/mm^2 versus control with 52 ± 32 cells/mm^2, *p* < 0.001) and FN + DCN (24 h: 243 ± 63 cells/mm^2 versus control with 137 ± 46 cells/mm^2, *p* < 0.01; 48 h: 292 ± 54 cells/mm^2 versus control with 52 ± 32 cells/mm^2, *p* < 0.001) when compared with the uncoated samples (controls) throughout the entire culture period (Figure 5a). No significant difference of adherent cells was observed between FN coating and FN + DCN coating (24 h: *p* = 0.656; 48 h: *p* = 756). DCN coating did not show any significant difference in cell density in comparison with the uncoated controls (24 h: 105 ± 40 cells/mm^2 versus control with 137 ± 46 cells/mm^2, *p* = 0.340; 48 h: 30 ± 11 cells/mm^2 versus control with 52 ± 32 cells/mm^2, *p* = 0.460).

SEM analyses revealed that the ECFCs on the control and DCN-coated TPCU scaffolds had attained a spherical shape after 24 h whereas those on TPCU scaffolds that were coated with FN and FN + DCN showed a stretched morphology (Figure 5b). Immunofluorescence staining of samples 24 h after seeding (Figure 5c,d) identified a significantly lower PECAM-1 expression in ECFCs on FN + DCN-coated samples in comparison with FN coating (0.64 ± 0.30 versus 0.90 ± 0.25, *p* < 0.05). After 48 h, this effect tended to reverse, although the difference was not significant (0.70 ± 0.15 versus 0.54 ± 0.23, *p* = 0.073). A similar and statistically not significant tendency was detected for the fluorescence intensity of vWF. No significant changes were observed in VE-cadherin or vinculin expression. VEGFR2 expression was significantly decreased in cells cultured on FN-coated scaffolds when compared with cells grown on FN + DCN-coated scaffolds after 24 h (0.64 ± 0.11 versus 0.29 ± 0.16, *p* < 0.01). After 48 h, this effect vanished (0.28 ± 0.17 versus 0.28 ± 0.15, *p* = 0.942).
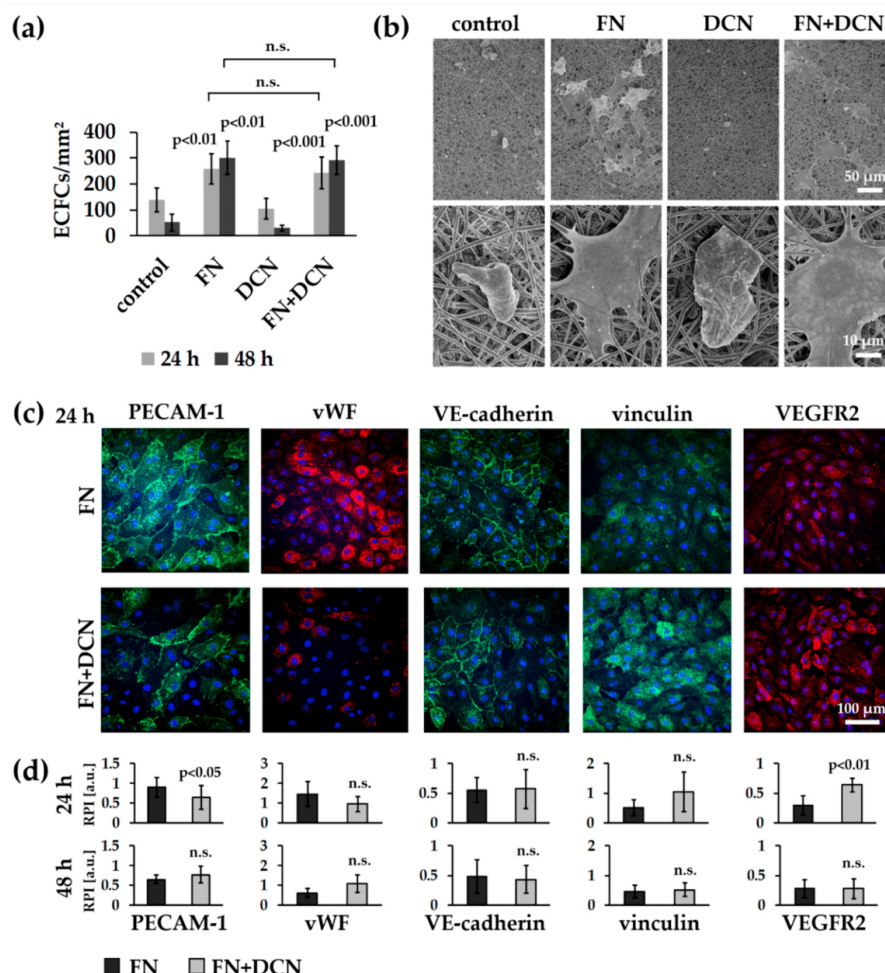
Figure 5. Static experiments of human ECFCs on FN-, DCN-, or FN + DCN-coated scaffolds: (**a**) Attachment and proliferation of the human ECFCs after 24 h and 48 h. Cells on FN and FN + DCN coating show a significantly higher proliferation when compared with cells gown on DCN and controls. Two-tailed *t*-test, compared to controls, n = 5, n.s. = not significant. (**b**) SEM images and (**c**) Immunofluorescence staining of ECFCs 24 h after seeding on ECM protein-coated scaffolds: Cells on FN and FN + DCN show a spread morphology in contrast to DCN coating and controls. (**d**) Semiquantitative fluorescence intensity analysis (relative pixel intensity (arbitrary units)) of cells on FN and FN + DCN shows no significant difference for the endothelial cell type marker von Willebrand factor (vWF) as well as vinculin and vascular endothelial cadherin (VE-cadherin). Platelet endothelial cell adhesion molecule (PECAM-1) expression is significantly decreased and VEGFR2 expression is significantly increased on FN + DCN-coated scaffolds after 24 h. Two-tailed *t*-test, n = 6, n.s. = not significant.

3.3.2. FN + DCN-Coating Attracts ECFCs Under Dynamic Culture Conditions

After ECFC seeding under static conditions, the cell-seeded scaffolds were dynamically cultured on a roller mixer for 24 h (Figure 6a). This approach was performed to reflect more closely the in vivo conditions. The analysis of the adherent cells showed a significantly increased cell number on the

FN + DCN-coated samples when compared with the controls and DCN-coated samples (5.7% ± 4.4% versus DCN coating with 1.0% ± 0.8%, $p < 0.05$ and versus control with 0.6% ± 0.7%, $p < 0.05$). The FN coating led to a nonsignificant decrease of adherent cells compared to FN + DCN coating (Figure 6b; 3.4% ± 1.5% versus 5.7% ± 4.4%, $p = 0.226$). Cells on all samples showed comparable PECAM-1 and vWF expression levels (Figure 6c). Distinct differences were observed in the cell morphology. F-actin staining helped visualizing the spread cells on the FN- and FN + DCN-coated scaffolds and cells with a more rounded morphology on the control samples and DCN-coated scaffolds (Figure 6c).
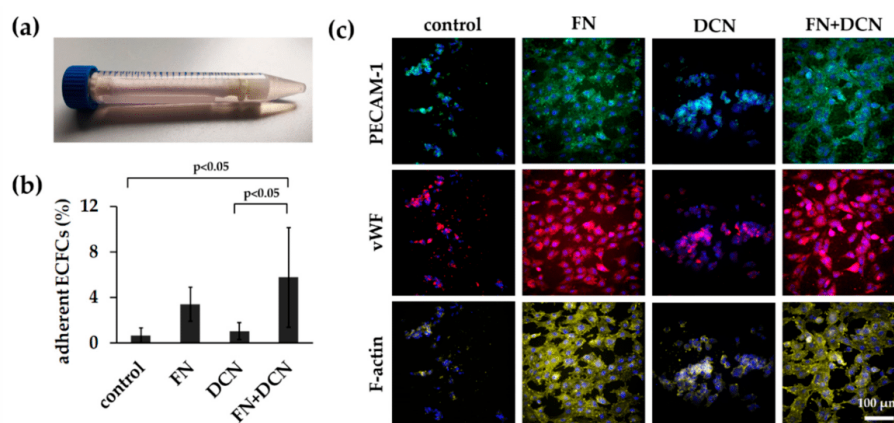
Figure 6. In vitro simulation of in vivo processes: ECFC attraction under dynamic conditions. (**a**) ECFCs were seeded into tubular constructs and cultured for 24 h on a roller mixer. (**b**) Adherent cells after 24 h on control scaffolds and on DCN-, FN-, and FN + DCN-coated scaffolds. FN + DCN coating shows a significantly higher cell number when compared with DCN coating and controls. One-way ANOVA, n = 4. (**c**) PECAM-1 (green), vWF (red), and F-actin (yellow) expression in ECFCs. Cells on FN and FN + DCN show a more spread morphology in contrast to the DCN and control samples.

3.4. In Vitro Tissue Engineering Approach Using Vascular Endothelial Cells

3.4.1. vECs Form an Endothelial Layer on FN- and FN + DCN-Coated Scaffolds Under Static Culture Conditions

vECs were seeded on the biofunctionalized planar constructs and cultured for 1, 4, and 7 days in order to investigate endothelialization (Figure 7a). One day after seeding, the cell number for all conditions was not significantly different. On day 4, vECs significantly increased proliferation on FN coating (78 ± 26 cells/mm^2 versus control with 8 ± 7 cells/mm^2, $p < 0.01$) and FN + DCN coating (55 ± 27 cells/mm^2 versus control with 8 ± 7 cells/mm^2, $p < 0.05$), while the VEC count on the DCN-coated samples had slightly decreased (7 ± 5 cells/mm^2 versus control with 8 ± 7 cells/mm^2, $p < 0.931$). This trend continued until day 7, on which a significantly increased cell count was detected for FN coating (186 ± 47 cells/mm^2 versus control with 16 ± 16 cells/mm^2, $p < 0.001$) and FN + DCN coating (135 ± 50 cells/mm^2 versus control with 16 ± 16 cells/mm^2, $p < 0.01$) in comparison with the uncoated controls. DCN coating of the TPCU scaffolds showed no improvement when compared with the control samples. Over the entire period of the experiment, the cell count was not significantly different between FN and FN + DCN coating.
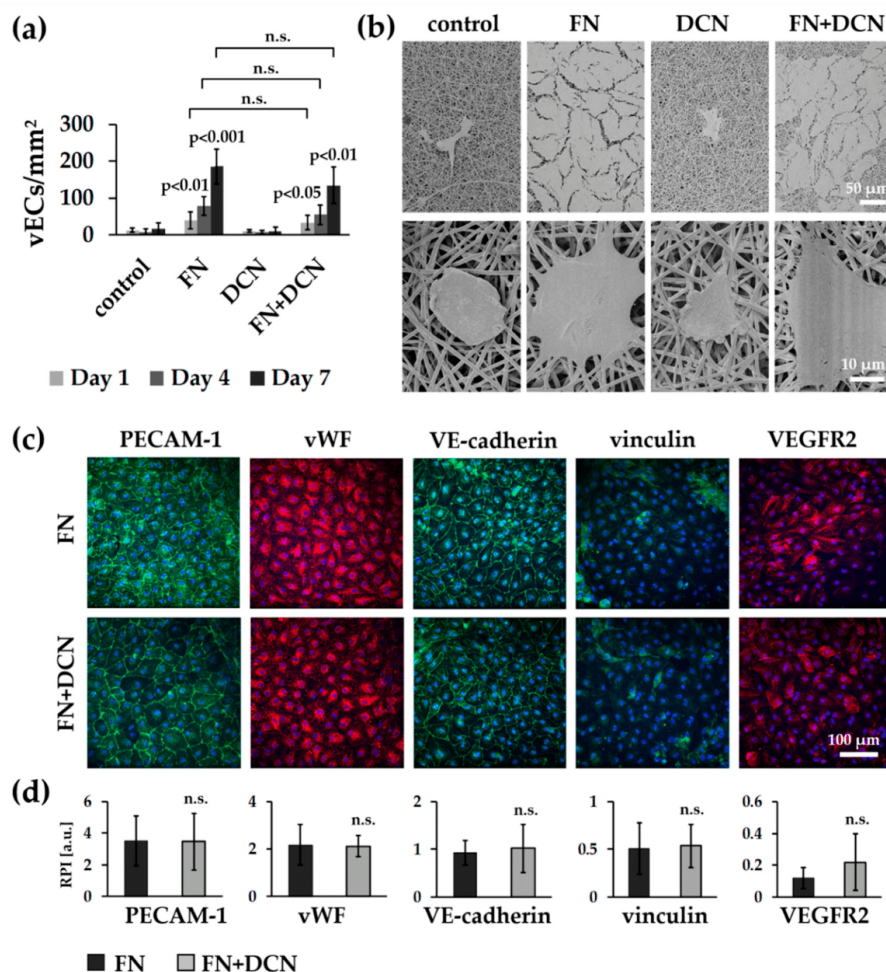
Figure 7. Static cell culture experiments of vECs on FN- and DCN-coated scaffolds: (**a**) Attachment and proliferation of vECs after 1, 4, and 7 days. vECs on FN and FN + DCN coating show a significantly higher proliferation rate compared with cells gown on DCN coating or control scaffolds. Two-tailed *t*-test, compared with control samples, n = 3, n.s. = not significant. (**b**) SEM images and (**c**) IF staining of vECs 7 days after seeding on ECM-coated scaffolds. Cells on FN and FN + DCN coating show a spread morphology in contrast with cells on DCN coating and control samples. (**d**) Semiquantitative fluorescence intensity analysis (relative pixel intensity (a.u.)) of cells on FN and FN + DCN coating shows no significant difference for PECAM-1, vWF, vinculin, or VE-cadherin expression. Two-tailed *t*-test, n = 5, n.s. = not significant.

While vECs on the control and DCN-coated scaffolds showed a spherical shape after 7 days as assessed using SEM, on FN and FN + DCN-coated scaffolds, vECs were stretched out and formed an almost confluent endothelial cell layer (Figure 7b). IF staining confirmed the expression of the endothelial cell type-specific markers PECAM-1, vWF, and VE-cadherin in the vECs on both FN and FN + DCN coating (Figure 7c). Semiquantitative analysis of fluorescence intensities revealed no significant differences of marker expression between FN and FN + DCN coating (Figure 7d). Vinculin expression was comparable in vECs on both coatings. With regard to VEGFR2, an increased fluorescence intensity

in cells grown on the FN + DCN-coated samples was observed. However, due to a high variation in expression levels of individual experiments, no statistical significance between cells grown on FN or FN + DCN coating could be determined.

In summary, our data showed that DCN coating of the TPCU scaffolds did not have a substantial advantage when aiming for an increased VEC proliferation or an improved cell–cell or cell–material interaction. For this reason, only FN biofunctionalized TPCU scaffolds were used for the following in vitro tissue engineering experiments.

3.4.2. vECs Cultured in a Custom-Made Bioreactor Under Flow Form a Confluent and Aligned Cell Layer on FN-Biofunctionalized TPCU

After successful implementation of the developed bioreactor system, we aimed to test whether the FN-biofunctionalized TPCU scaffolds can be endothelialized under dynamic conditions. vECs were seeded into the tubular TPCU scaffolds, and after an initial culture for three days under static conditions to allow cell attachment, a flow was employed that was stepwise increased to 25 mL/min within 1.5 days (Figure 2e). Under this flow, which causes a shear stress of about 0.03 Pa, the vEC-seeded FN-biofunctionalized scaffolds were cultured for seven days. Metabolic activity assessment using an MTT assay showed that a large part of the inner wall of our construct was covered with living cells, as indicated by the purple formazan stain (Figure 8a). IF staining and SEM further revealed a layer of confluent vECs that were aligned in the direction of flow (Figure 8b,c).
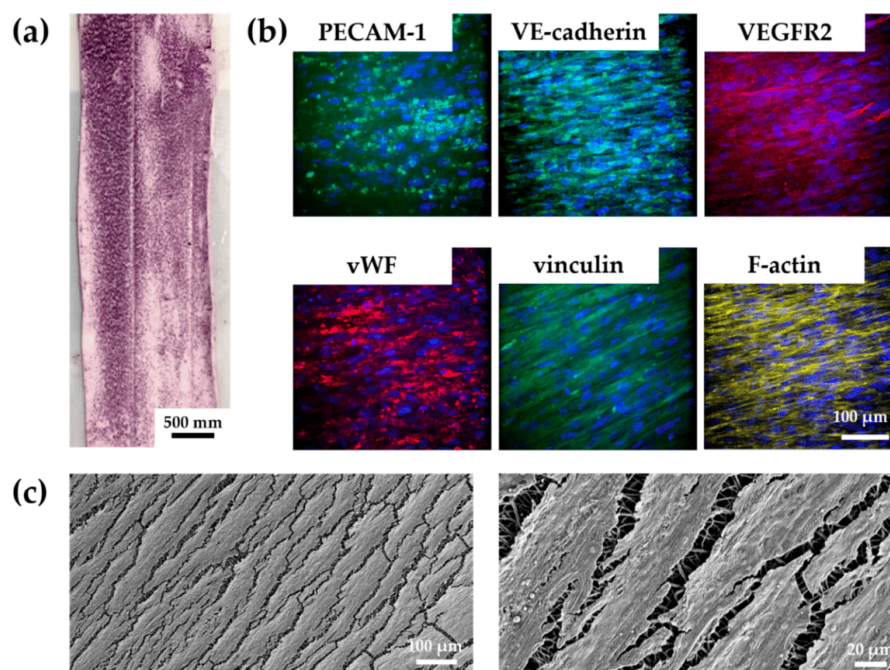
Figure 8. Tissue-engineering approach with vascular endothelial cells cultured for 7 days on FN-biofunctionalized electrospun tubular TPCU scaffolds under dynamic conditions: (**a**) Inner wall of the tubular construct shows living vECs indicated by the purple formazan stain. (**b**) PECAM-1, vWF, VE-cadherin, vinculin, VEGFR2, and F-actin expression were detected. vECs show an aligned morphology. (**c**) SEM confirms vECs that had aligned with the flow to which they were exposed to during the dynamic culture in the bioreactor.

Appendices

We confirmed the expression of the endothelial cell markers PECAM-1, vWF, and VE-cadherin. However, PECAM-1 and VE-cadherin did not appear to be located on the cell membrane as usual. Vinculin and VEGFR2 were also detected in the cells. Nevertheless, the staining of VEGFR2 showed only a weak signal.

4. Discussion

Due to a proven biocompatibility and biostability at body temperature [55,57], we selected for this study a novel thermoplastic polycarbonate urethane for the fabrication of a TEVG. At first, scaffolds were produced by electrospinning of the TPCU and were disinfected with 70% ethanol. Microbiological studies showed that ethanol treatment did not achieved 100% sterility (Figure S3; 2 out of 9 plates showed germ growth). We are aware that disinfection with ethanol does not necessarily inactivate all forms of microorganisms [75]; therefore, for the clinical translation, a more efficient sterilization method should be considered.

After disinfection, scaffolds were then biofunctionalized by adsorption of FN and DCN, either alone or in combination. The adsorbed proteins did not impact elastic modulus or burst pressure of the tubular constructs (Figure 3). We demonstrated that the biomechanical properties of our constructs were comparable to native vascular tissue (Table 2).

The ability to mimic the nanofibrous topography of the ECM makes electrospinning a powerful method for cardiovascular tissue-engineering applications. Several studies have already described the influence of fiber and pore size on cell adhesion, cell migration, proliferation, and differentiation, as well as cell–cell interaction [76–78]. In native blood vessels, the ECs are located on the basal lamina, a mixture of defined ECM proteins that form a network and bind cells [79]. The literature describes a wide range of pore and fiber diameters (1–1000 nm) from different vessels, depending on the position and physical properties of the vessel [80]. The main collagen component of the basal lamina is collagen type IV. It forms fibers that range from 20 to 52 nm [80–82]. In our study, the fiber diameters were between 699 ± 61 nm and 776 ± 163 nm, which is much higher compared to the collagen type IV fibers in native vessels. However, other studies developing electrospun vascular grafts reported comparable [83] or even larger fiber sizes [84,85] on which a functional endothelium was formed [84]. The pore size strongly depends on the vessel type and ranges between 5 nm and 8 μm [80,82,86–89]. Our constructs showed pore sizes between 0.08 ± 0.01 μm^2 and 0.12 ± 0.05 μm^2, which lies in the range of a native vessel.

Several studies have already described that FN improves the endothelialization of vascular grafts [19,48,49,51]. In our study, we observed a fibrous-like structure of the coated FN (Figure 3b). This phenomenon can be interpreted as material-driven fibrillogenesis, first described by Salmeron-Sanchez et al. [3]. In the human body, FN matrix assembly is a cell-mediated process [90] that influences cell growth, cell differentiation, and cell–cell interaction [76–78,90,91]. It has been shown that the adhesion of FN on poly (ethyl acrylate) (PEA) can lead to a spontaneous organization of FN into protein networks. It has also been shown that cell-free material-induced FN fibrillogenesis influences the maintenance and differentiation of stem cells [3,92]. Furthermore, it was described that the FN network has an increased ability to store growth factors [93]. To the best of our knowledge, our study is the first to show that material-driven fibrillogenesis can be observed on electrospun TPCU fibers. We presume that the surface properties, such as hydrophobicity and polarity, are comparable to those of PEA. Whether the FN network has a significant advantage in terms of cell behavior or growth factor binding compared to dispersed, coated FN molecules would need further investigation.

In addition to FN coating, in this study, we also used DCN coating. We observed that, after coating on the TPCU, DCN was randomly distributed in aggregates on the fibers (Figure 3b). Since DCN does not form fibrils, this coating behavior was expected. Even larger, globular DCN aggregates were observed on the FN + DCN samples (Figure 3b,d). Interestingly, these aggregates were predominantly seen on the FN fibrils and not on the TPCU itself. It is known that DCN interacts with FN [94,95]. Furthermore, the interaction of proteins with materials is determined by the geometrical, chemical,

and electrical properties of the substrate [96]. In this respect, it can be hypothesized that the DCN prefers the FN surface more than the hydrophobic polyurethane surface. Interestingly, we observed a significantly increased swelling ratio for FN + DCN (Figure 3e). This was not the case with individually FN- or DCN-coated TPCU. Depending on the surface properties of the material and the interaction with other proteins, the conformation, orientation, and bioactivity of a protein can also be influenced [96–98]. With this in mind, one can assume that both DCN and FN in combination can have a different bioactivity [99].

In contrast to our previous findings using poly (ethylene glycol) dimethacrylate-poly (L-lactide) (PEGdma-PLA) or a blend of poly-ε-caprolacton and gelatin [25,100], we identified a cell-repellent effect of the DCN-coated TCPU electrospun scaffolds for both human ECFCs and human vECs. As already discussed, cells prefer to adhere to hydrophilic surfaces [101]. Since the TCPU itself is highly hydrophobic (control: 98.4 ± 3.7 °), it can cause a cell-repellent effect. DCN alone was not able to diminish this effect (Figure 5a,b). Cell adhesion is influenced by cell-adhesive peptides such as the RGD sequence. Since DCN does not contain these sequences, as it is the case with FN, we assume that at least this integrin-based cell–material interaction cannot be mediated by DCN. It has been described that DCN can even partially inhibit cell adhesion; however, this has only been observed with fibroblasts and not with endothelial cells [28,102]. Hinderer et al. observed an attraction of ECFCs to DCN-coated PEGdma-PLA [25]. A direct comparison with this study is therefore difficult, since this polymer has different surface properties, which influence the amount and orientation of the adsorbed DCN and thus may have an altered impact on cell behavior [96]. FN coating reversed the cell-repellent effect of the TCPU, both with and without DCN (Figure 5). We can therefore conclude that the cell attraction and proliferation is supported by FN but not affected by DCN [99,103].

Scaffolds should in general exhibit low immunogenicity and at the same time support tissue regenerative processes. The evaluation of the immune response profiles of the analyzed control and ECM-coated scaffolds excluded any major adverse effects, with only minor innate activation characteristics. Co-culturing PMNs, as the first cells of an innate immune response, induced an activated cell phenotype regarding the expression of CD11b and CD66b. Monocytes were incompletely activated after co-culturing with the scaffold as indicated by only a weak tendency to upregulate the HLA-DR expression and to increase their TNFα release. From the literature, it is well known that the upregulation of CD80 and HLA-DR would be a hallmark of M1 macrophages [62,104] and that the fiber and pore size of electrospun scaffolds could impact the macrophage polarization state [105]. When analyzing the potential impact of the TPCU scaffolds on macrophage polarization, no clear trend to drive the process into a specific macrophage subtype could be determined. Also, the coating by either DCN or FN did not trigger a specific type of macrophage polarization. In contrast, co-culture studies with soluble recombinant DCN demonstrated that macrophages responded with an upregulated CD80 expression as well an increased secretion of TNFα and IL-10 [25]. The absent responses in the present study may result from the far lower amount of protein present on the coated scaffolds in comparison with the high protein amounts available within solutions or even by conformational changes. Not surprisingly, adaptive T cell responses were also not detected. T cells on scaffolds simply showed a trend to upregulate CD69 and HLA-DR without significant changes.

A functional endothelium is mainly characterized by cell–cell junctions [106]. As PECAM-1 is the most abundant component of the EC junction, which contributes to the maintenance of the EC permeability barrier, its expression is essential for a functional EC layer [107]. In our study, the ECFCs on FN coating revealed a significantly increased PECAM-1 expression after 24 h compared with ECFCs cultured on FN + DCN-coated scaffolds. In contrast, the VEGFR2 expression was significantly decreased in the ECFCs on FN coating after 24 h compared with FN + DCN coating. It has been reported that VEGFR2 is highly expressed in early endothelial precursor cells but not in all mature ECs [108,109]. For example, PECAM-1 is less expressed in endothelial progenitor cells, as it is typically associated with a more mature EC phenotype [110]. Interestingly, DCN has been reported to stimulate the maintenance of undifferentiated progenitor cells [111], and FN promotes endothelial

Appendices

cell differentiation [112]. Therefore, we hypothesize that the FN + DCN coating in our experiments kept the ECFCs in a precursor cell state compared with the culture on only FN. It may also be possible that a direct interaction of DCN with VEGFR2 leads to its upregulation. A positive feedback loop between VEGF and VEGFR2 has been described [113]. Whether DCN has the same effect remains to be confirmed.

Since DCN exerts many other functions, an indirect regulation of VEGFR2 is also conceivable [34,114]. Mazor et al. showed that the matrix metalloproteinase-1 (MMP-1) promotes the expression of VEGFR2 [115]. The core protein of DCN in turn is able to stimulate the expression of MMP-1 [116,117]. Furthermore, Murakami et al. reported that increased concentrations of the fibroblast growth factor (FGF) led to an increase in VEGFR2 levels [118]. DCN, in turn, can bind to FGF and can increase its activity [119]. It was also described that VEGFR2 expression is regulated by the disruption of the c-MET receptor tyrosine kinase [120]. As an antagonistic ligand of c-MET, DCN is able to inhibit its activity and thus might indirectly promote VEGFR2 expression [38]. We have already discussed the hypothesis that DCN in interaction with FN may exhibit an altered bioactivity. This would explain why DCN, which was adsorbed on the TPCU scaffold surface, impacted ECs in combination with FN but did not without [96–98]. The reason for VEGFR2 upregulation can also be due to FN. It might be possible that, in combination with DCN, its conformation and function is also changed [96–98]. It has been shown that conformational remodeling of the FN matrix selectively regulates VEGF signaling [121]. VEGF in turn regulates VEGFR2 expression [113]. By binding to VEGF, FN can promote full phosphorylation and activation of VEGFR2 [122]. Interestingly, after 48 h, the difference between FN and FN + DCN coating for both the PECAM-1 and VEGFR2 expression had vanished (Figure 5d). With regard to VEGFR2, a short half-life of the receptor is described, which enables ECs to adapt quickly to changes in the extracellular environment [118,123]. This leads to the question of how long the biofunctionalized DCN coating was fully biologically active in our study. Due to its natural presence in the body, it can be easily degraded [124]. We showed that DCN acts on ECFCs for at least 24 h under static conditions. The culture of vECs over 7 days under static conditions revealed the same expression of PECAM-1 and VEGFR2 on FN and FN + DCN coating (Figure 7). This observation supports the assumption that the DCN was only active for a short period of time and that its effect had disappeared after 7 days. In addition, it is possible that the vECs are not as sensitive to DCN, as we have observed with the ECFCs. Several studies have described an increase in VEGFR2 expression during differentiation and expansion of endothelial progenitor cells [109,125]. At the same time, VEGFR2 expression was relatively low during the proliferation phase [126]. Since the vECs are mature cells, it can be assumed that the externally changed conditions do not affect the VEFGR2 expression significantly. Nevertheless, in this study, we successfully showed that vECs formed an endothelium on biofunctionalized FN-coated constructs after 7 days of culture whereas DCN-coated TPCU scaffolds did not show a significant effect on cell proliferation.

In our TEVG experiments using a custom-made bioreactor, we observed a unidirectional cell orientation in the direction of the flow. The response of ECs to shear stress is well studied [127–129]. It has been shown that, under flow, the morphology of vECs changes from a cobblestone (static) to an elongated form and that vECs align in the direction of the flow in only 24 h [127]. The hemodynamic forces can modulate not only the phenotype but also the gene expression of the cells. In this context, the correct flow is of great importance for a properly functioning endothelium [130]. In our study, IF staining revealed the expression of vWF, PECAM-1, and VE-cadherin. However, PECAM-1 and VE-cadherin were not located on the cell membrane as usually seen. VEGFR2 expression was quite weak, and the F-actin staining revealed a rather fibroblast-like cell morphology. We hypothesize that the vECs underwent endothelial-mesenchymal transition (EndMT). ECs, which undergo EndMT, lose the expression of the characteristic surface endothelial markers PECAM-1, VE-cadherin, and VEGFR2 [39,131,132]. Mahmoud et al. showed that the EndMT can be induced under low shear stress (0.4 Pa) [133]. In our approach, the cells experienced a wall shear stress of about 0.03 Pa, which is slightly lower than a venous wall shear stress (0.06 Pa) [134]. In silico simulations of our dynamic bioreactor culture

confirmed laminar flow conditions along a large part of the vascular wall using the applied parameters. Another reason for the fibroblast-like phenotype could be that ECs are highly plastic [135,136]. Therefore, culturing ECs in vitro in an artificial environment can lead to cell dedifferentiation [136,137]. This highlights the importance of fine-tuning the culture conditions to create a functional TEGV.

5. Conclusions

In the present study, we successfully engineered a TPCU electrospun vascular graft which combines appropriate mechanical properties with a highly bioactive surface for the attraction of ECs. The FN biofunctionalization was characterized by a material-driven fibrillogenesis, which might have a positive impact on FN functionality [3]. To imitate the physiological conditions of a blood vessel, a bioreactor for in vitro tissue culture was designed and manufactured. vECs seeded on the FN-functionalized constructs formed a confluent and functional endothelium under static and dynamic conditions. In contrast, DCN-biofunctionalized TPCU scaffolds had a cell-repellent effect on vECs and ECFCs, most likely due to the high hydrophobic properties of the TPCU. However, since DCN has been shown to inhibit the adhesion of fibroblasts, it remains a promising protein for the functionalization of vascular grafts [29].

The challenge for the future will be to combine the advantages of different proteins and to thus increase the selectivity, functionality, and stability of a biofunctionalized vascular graft while keeping the complexity of the coating as low as possible.

References

1. Catto, V.; Farè, S.; Freddi, G.; Tanzi, M.C. Vascular Tissue Engineering: Recent Advances in Small Diameter Blood Vessel Regeneration. *ISRN Vasc. Med.* **2014**, *2014*, 923030. [CrossRef]
2. Causes of Death. Available online: https://www.who.int/data/gho/data/themes/topics/causes-of-death/GHO/causes-of-death (accessed on 29 December 2019).
3. Salmerón-Sánchez, M.; Rico, P.; Moratal, D.; Lee, T.T.; Schwarzbauer, J.E.; García, A.J. Role of Material-Driven Fibronectin Fibrillogenesis in Cell Differentiation. *Biomaterials* **2011**, *32*, 2099–2105. [CrossRef] [PubMed]
4. Sánchez, P.F.; Brey, E.M.; Carlos Briceño, J.C. Endothelialization Mechanisms in Vascular Grafts. *J. Tissue Eng. Regen. Med.* **2018**, *12*, 2164–2178. [CrossRef] [PubMed]
5. L'Heureux, N.; Dusserre, N.; Marini, A.; Garrido, S.; De la Fuente, L.; McAllister, T. Technology Insight: The Evolution of Tissue-Engineered Vascular Grafts - From Research to Clinical Practice. *Nat. Clin. Pract. Cardiovasc. Med.* **2007**, *4*, 389–395. [CrossRef] [PubMed]

111

Appendices

6. Ercolani, E.; Del Gaudio, C.; Bianco, A. Vascular Tissue Engineering of Small-Diameter Blood Vessels: Reviewing the Electrospinning Approach. *J. Tissue Eng. Regen. Med.* **2015**, *9*, 861–888. [CrossRef] [PubMed]
7. Seifu, D.G.; Purnama, A.; Mequanint, K.; Mantovani, D. Small-Diameter Vascular Tissue Engineering. *Nat. Rev. Cardiol.* **2013**, *10*, 410–421. [CrossRef]
8. Ravi, S.; Qu, Z.; Chaikof, E.L. Polymeric Materials for Tissue Engineering of Arterial Substitutes. *Vascular* **2009**, *17*, S45–S54. [CrossRef]
9. Julier, Z.; Park, A.J.; Briquez, P.S.; Martino, M.M. Promoting Tissue Regeneration by Modulating the Immune System. *Acta Biomater.* **2017**, *53*, 13–28. [CrossRef]
10. Hinderer, S.; Brauchle, E.; Schenke-Layland, K. Generation and Assessment of Functional Biomaterial Scaffolds for Applications in Cardiovascular Tissue Engineering and Regenerative Medicine. *Adv. Healthc. Mater.* **2015**, *4*, 2326–2341. [CrossRef]
11. Ndreu, A.; Nikkola, L.; Ylikauppilar, H.; Ashammakhi, N.; Hasirci, V. Electrospun Biodegradable Nanofibrous Mats for Tissue Engineering. *Nanomedicine* **2008**, *3*, 45–60. [CrossRef]
12. Li, M.; Mondrinos, M.J.; Gandhi, M.R.; Ko, F.K.; Weiss, A.S.; Lelkes, P.I. Electrospun Protein Fibers as Matrices for Tissue Engineering. *Biomaterials* **2005**, *26*, 5999–6008. [CrossRef]
13. Boland, E.D.; Matthews, J.A.; Pawlowski, K.J.; Simpson, D.G.; Wnek, G.E.; Bowlin, G.L. Electrospinning Collagen and Elastin: Preliminary Vascular Tissue Engineering. *Front. Biosci.* **2004**, *9*, 1422–1432. [CrossRef] [PubMed]
14. Zhang, M.; Wang, Z.; Wang, Z.; Feng, S.; Xu, H.; Zhao, Q.; Wang, S.; Fang, J.; Qiao, M.; Kong, D. Immobilization of Anti-CD31 Antibody on Electrospun Poly(E{open}-Caprolactone) Scaffolds through Hydrophobins for Specific Adhesion of Endothelial Cells. *Colloids Surf. B Biointerfaces* **2011**, *85*, 32–39. [CrossRef]
15. Markway, B.D.; McCarty, O.J.T.; Marzec, U.M.; Courtman, D.W.; Hanson, S.R.; Hinds, M.T. Capture of Flowing Endothelial Cells Using Surface-Immobilized Anti-Kinase Insert Domain Receptor Antibody. *Tissue Eng.-Part C Methods* **2008**, *14*, 97–105. [CrossRef]
16. Kanie, K.; Narita, Y.; Zhao, Y.; Kuwabara, F.; Satake, M.; Honda, S.; Kaneko, H.; Yoshioka, T.; Okochi, M.; Honda, H.; et al. Collagen Type IV-Specific Tripeptides for Selective Adhesion of Endothelial and Smooth Muscle Cells. *Biotechnol. Bioeng.* **2012**, *109*, 1808–1816. [CrossRef]
17. Li, J.; Ding, M.; Fu, Q.; Tan, H.; Xie, X.; Zhong, Y. A Novel Strategy to Graft RGD Peptide on Biomaterials Surfaces for Endothelization of Small-Diamater Vascular Grafts and Tissue Engineering Blood Vessel. *J. Mater. Sci. Mater. Med.* **2008**, *19*, 2595–2603. [CrossRef]
18. Edlund, U.; Sauter, T.; Albertsson, A.-C. Covalent VEGF Protein Immobilization on Resorbable Polymeric Surfaces. *Polym. Adv. Technol.* **2011**, *22*, 166–171. [CrossRef]
19. De Visscher, G.; Mesure, L.; Meuris, B.; Ivanova, A.; Flameng, W. Improved Endothelialization and Reduced Thrombosis by Coating a Synthetic Vascular Graft with Fibronectin and Stem Cell Homing Factor SDF-1α. *Acta Biomater.* **2012**, *8*, 1330–1338. [CrossRef] [PubMed]
20. Schleicher, M.; Hansmann, J.; Elkin, B.; Kluger, P.J.; Liebscher, S.; Huber, A.J.T.; Fritze, O.; Schille, C.; Müller, M.; Schenke-Layland, K.; et al. Oligonucleotide and Parylene Surface Coating of Polystyrene and EPTFE for Improved Endothelial Cell Attachment and Hemocompatibility. *Int. J. Biomater.* **2012**, *2012*, 397813. [CrossRef] [PubMed]
21. Strahm, Y.; Flueckiger, A.; Billinger, M.; Meier, P.; Mettler, D.; Weisser, S.; Schaffner, T.; Hess, O. Endothelial-Cell-Binding Aptamer for Coating of Intracoronary Stents. *J. Invasive Cardiol.* **2010**, *22*, 481–487.
22. Suuronen, E.J.; Zhang, P.; Kuraitis, D.; Cao, X.; Melhuish, A.; McKee, D.; Li, F.; Mesana, T.G.; Veinot, J.P.; Ruel, M. An Acellular Matrix-Bound Ligand Enhances the Mobilization, Recruitment and Therapeutic Effects of Circulating Progenitor Cells in a Hindlimb Ischemia Model. *FASEB J.* **2009**, *23*, 1447–1458. [CrossRef] [PubMed]
23. Tardif, K.; Cloutier, I.; Miao, Z.; Lemieux, C.; St-Denis, C.; Winnik, F.M.; Tanguay, J.F. A Phosphorylcholine-Modified Chitosan Polymer as an Endothelial Progenitor Cell Supporting Matrix. *Biomaterials* **2011**, *32*, 5046–5055. [CrossRef] [PubMed]
24. Melchiorri, A.J.; Hibino, N.; Fisher, J.P. Strategies and Techniques to Enhance the in Situ Endothelialization of Small-Diameter Biodegradable Polymeric Vascular Grafts. *Tissue Eng. Part B. Rev.* **2013**, *19*, 292–307. [CrossRef] [PubMed]

25. Hinderer, S.; Sudrow, K.; Schneider, M.; Holeiter, M.; Layland, S.L.; Seifert, M.; Schenke-Layland, K. Surface Functionalization of Electrospun Scaffolds Using Recombinant Human Decorin Attracts Circulating Endothelial Progenitor Cells. *Sci. Rep.* **2018**, *8*, 110. [CrossRef]

26. Zhang, W.; Ge, Y.; Cheng, Q.; Zhang, Q.; Fang, L.; Zheng, J. Decorin Is a Pivotal Effector in the Extracellular Matrix and Tumour Microenvironment. *Oncotarget* **2018**, *9*, 5480–5491. [CrossRef]

27. Chen, S.; Young, M.F.; Chakravarti, S.; Birk, D.E. Interclass Small Leucine-Rich Repeat Proteoglycan Interactions Regulate Collagen Fibrillogenesis and Corneal Stromal Assembly. *Matrix Biol.* **2014**, *35*, 103–111. [CrossRef]

28. Fiedler, L.R.; Schönherr, E.; Waddington, R.; Niland, S.; Seidler, D.G.; Aeschlimann, D.; Eble, J.A. Decorin Regulates Endothelial Cell Motility on Collagen I through Activation of Insulin-like Growth Factor I Receptor and Modulation of A2β1 Integrin Activity. *J. Biol. Chem.* **2008**, *283*, 17406–17415. [CrossRef]

29. Fiedler, L.R.; Eble, J.A. Decorin Regulates Endothelial Cell-Matrix Interactions during Angiogenesis. *Cell Adh. Migr.* **2009**, *3*, 3–6. [CrossRef]

30. Zafiropoulos, A.; Nikitovic, D.; Katonis, P.; Tsatsakis, A.; Karamanos, N.K.; Tzanakakis, G.N. Decorin-Induced Growth Inhibition Is Overcome through Protracted Expression and Activation of Epidermal Growth Factor Receptors in Osteosarcoma Cells. *Mol. Cancer Res.* **2008**, *6*, 785–794. [CrossRef]

31. Nili, N.; Cheema, A.N.; Giordano, F.J.; Barolet, A.W.; Babaei, S.; Hickey, R.; Eskandarian, M.R.; Smeets, M.; Butany, J.; Pasterkamp, G.; et al. Decorin Inhibition of PDGF-Stimulated Vascular Smooth Muscle Cell Function: Potential Mechanism for Inhibition of Intimal Hyperplasia after Balloon Angioplasty. *Am. J. Pathol.* **2003**, *163*, 869–878. [CrossRef]

32. D'Antoni, M.L.; Risse, P.A.; Ferraro, P.; Martin, J.G.; Ludwig, M.S. Effects of Decorin and Biglycan on Human Airway Smooth Muscle Cell Adhesion. *Matrix Biol.* **2012**, *31*, 101–112. [CrossRef]

33. De Lange Davies, C.; Melder, R.J.; Munn, L.L.; Mouta-Carreira, C.; Jain, R.K.; Boucher, Y. Decorin Inhibits Endothelial Migration and Tube-like Structure Formation: Role of Thrombospondin-1. *Microvasc. Res.* **2001**, *62*, 26–42. [CrossRef]

34. Järveläinen, H.; Sainio, A.; Wight, T.N. Pivotal Role for Decorin in Angiogenesis. *Matrix Biol.* **2015**, *43*, 15–26. [CrossRef]

35. Riessen, R.; Isner, J.M.; Blessing, E.; Loushin, C.; Nikol, S.; Wight, T.N. Regional Differences in the Distribution of the Proteoglycans Biglycan and Decorin in the Extracellular Matrix of Atherosclerotic and Restenotic Human Coronary Arteries. *Am. J. Pathol.* **1994**, *144*, 962–974.

36. Salisbury, B.G.; Wagner, W.D. Isolation and Preliminary Characterization of Proteoglycans Dissociatively Extracted from Human Aorta. *J. Biol. Chem.* **1981**, *256*, 8050–8057.

37. Khan, G.A.; Girish, G.V.; Lala, N.; di Guglielmo, G.M.; Lala, P.K. Decorin Is a Novel VEGFR-2-Binding Antagonist for the Human Extravillous Trophoblast. *Mol. Endocrinol.* **2011**, *25*, 1431–1443. [CrossRef]

38. Goldoni, S.; Humphries, A.; Nyström, A.; Sattar, S.; Owens, R.T.; McQuillan, D.J.; Ireton, K.; Iozzo, R.V. Decorin Is a Novel Antagonistic Ligand of the Met Receptor. *J. Cell Biol.* **2009**, *185*, 743–754. [CrossRef]

39. Van Meeteren, L.A.; Ten Dijke, P. Regulation of Endothelial Cell Plasticity by TGF-β. *Cell Tissue Res.* **2012**, *347*, 177–186. [CrossRef]

40. Järvinen, T.A.H.; Ruoslahti, E. Target-Seeking Antifibrotic Compound Enhances Wound Healing and Suppresses Scar Formation in Mice. *Proc. Natl. Acad. Sci. USA* **2010**, *107*, 21671–21676. [CrossRef]

41. Liverani, L.; Killian, M.S.; Boccaccini, A.R. Fibronectin Functionalized Electrospun Fibers by Using Benign Solvents: Best Way to Achieve Effective Functionalization. *Front. Bioeng. Biotechnol.* **2019**, *7*, 68. [CrossRef]

42. Campos, D.M.; Gritsch, K.; Salles, V.; Attik, G.N.; Grosgogeat, B. Surface Entrapment of Fibronectin on Electrospun PLGA Scaffolds for Periodontal Tissue Engineering. *Biores. Open Access* **2014**, *3*, 117–126. [CrossRef]

43. Regis, S.; Youssefian, S.; Jassal, M.; Phaneuf, M.; Rahbar, N.; Bhowmick, S. Integrin A5β1-Mediated Attachment of NIH/3T3 Fibroblasts to Fibronectin Adsorbed onto Electrospun Polymer Scaffolds. *Polym. Eng. Sci.* **2014**, *54*, 2587–2594. [CrossRef]

44. Monchaux, E.; Vermette, P. Effects of Surface Properties and Bioactivation of Biomaterials on Endothelial Cells. *Front. Biosci.-Sch.* **2010**, *2*, 239–255.

45. Lenselink, E.A. Role of Fibronectin in Normal Wound Healing. *Int. Wound J.* **2015**, *12*, 313–316. [CrossRef]

46. Grinnell, F. Fibronectin and Wound Healing. *J. Cell. Biochem.* **1984**, *26*, 107–116. [CrossRef]

47. Sgarioto, M.; Vigneron, P.; Patterson, J.; Malherbe, F.; Nagel, M.D.; Egles, C. Collagen Type I Together with Fibronectin Provide a Better Support for Endothelialization. *Comptes Rendus-Biol.* **2012**, *335*, 520–528. [CrossRef]
48. Ardila, D.; Liou, J.-J.; Maestas, D.; Slepian, M.; Badowski, M.; Wagner, W.; Harris, D.; Vande Geest, J. Surface Modification of Electrospun Scaffolds for Endothelialization of Tissue-Engineered Vascular Grafts Using Human Cord Blood-Derived Endothelial Cells. *J. Clin. Med.* **2019**, *8*, 185. [CrossRef]
49. Tersteeg, C.; Roest, M.; Mak-Nienhuis, E.M.; Ligtenberg, E.; Hoefer, I.E.; de Groot, P.G.; Pasterkamp, G. A Fibronectin-Fibrinogen-Tropoelastin Coating Reduces Smooth Muscle Cell Growth but Improves Endothelial Cell Function. *J. Cell. Mol. Med.* **2012**, *16*, 2117–2126. [CrossRef]
50. Ota, T.; Sawa, Y.; Iwai, S.; Kitajima, T.; Ueda, Y.; Coppin, C.; Matsuda, H.; Okita, Y. Fibronectin-Hepatocyte Growth Factor Enhances Reendothelialization in Tissue-Engineered Heart Valve. *Ann. Thorac. Surg.* **2005**, *80*, 1794–1801. [CrossRef]
51. Wang, X.; Liu, T.; Chen, Y.; Zhang, K.; Maitz, M.F.; Pan, C.; Chen, J.; Huang, N. Extracellular Matrix Inspired Surface Functionalization with Heparin, Fibronectin and VEGF Provides an Anticoagulant and Endothelialization Supporting Microenvironment. *Appl. Surf. Sci.* **2014**, *320*, 871–882. [CrossRef]
52. Hoenig, M.R.; Campbell, G.R.; Campbell, J.H. Vascular Grafts and the Endothelium. *Endothel. J. Endothel. Cell Res.* **2006**, *13*, 385–401. [CrossRef]
53. Matsuzaki, Y.; John, K.; Shoji, T.; Shinoka, T. The Evolution of Tissue Engineered Vascular Graft Technologies: From Preclinical Trials to Advancing Patient Care. *Appl. Sci.* **2019**, *9*, 1274. [CrossRef]
54. Popov, G.; Vavilov, V.; Yukina, G.; Popryadukhin, P.; Dobrovolskaya, I.; Ivan'kova, E.; Yudin, V. Long-Term Functioning Aneurysmal Free Tissue-Engineered Vascular Graft Based on Composite Bi-Layered (PLLA/FPL) Scaffold. *Eur. J. Vasc. Endovasc. Surg.* **2019**, *58*, e817–e818. [CrossRef]
55. Kutuzova, L.; Athanasopulu, K.; Schneider, M.; Kandelbauer, A.; Kemkemer, R.; Lorenz, G. In Vitro Bio-Stability Screening of Novel Implantable Polyurethane Elastomers: Morphological Design and Mechanical Aspects. *Curr. Dir. Biomed. Eng.* **2018**, *4*, 535–538. [CrossRef]
56. Broadwater, S.J.; Roth, S.L.; Price, K.E.; Kobašlija, M.; McQuade, D.T. One-Pot Multi-Step Synthesis: A Challenge Spawning Innovation. *Org. Biomol. Chem.* **2005**, *3*, 2899–2906. [CrossRef]
57. Athanasopulu, K.; Kutuzova, L.; Thiel, J.; Lorenz, G.; Kemkemer, R. Enhancing the Biocompatibility of Siliconepolycarbonate Urethane Based Implant Materials. *Curr. Dir. Biomed. Eng.* **2019**, *5*, 453–455. [CrossRef]
58. Schindelin, J.; Arganda-Carreras, I.; Frise, E.; Kaynig, V.; Longair, M.; Pietzsch, T.; Preibisch, S.; Rueden, C.; Saalfeld, S.; Schmid, B.; et al. Fiji: An Open-Source Platform for Biological-Image Analysis. *Nat. Methods* **2012**, *9*, 676–682. [CrossRef]
59. Laterreur, V.; Ruel, J.; Auger, F.A.; Vallières, K.; Tremblay, C.; Lacroix, D.; Tondreau, M.; Bourget, J.M.; Germain, L. Comparison of the Direct Burst Pressure and the Ring Tensile Test Methods for Mechanical Characterization of Tissue-Engineered Vascular Substitutes. *J. Mech. Behav. Biomed. Mater.* **2014**, *34*, 253–263. [CrossRef]
60. Hinderer, S.; Seifert, J.; Votteler, M.; Shen, N.; Rheinlaender, J.; Schäffer, T.E.; Schenke-Layland, K. Engineering of a Bio-Functionalized Hybrid off-the-Shelf Heart Valve. *Biomaterials* **2014**, *35*, 2130–2139. [CrossRef]
61. Becker, M.; Schneider, M.; Stamm, C.; Seifert, M. A Polymorphonuclear Leukocyte Assay to Assess Implant Immunocompatibility. *Tissue Eng. Part C Methods* **2019**, *25*, 500–511. [CrossRef]
62. Schneider, M.; Stamm, C.; Brockbank, K.G.M.; Stock, U.A.; Seifert, M. The Choice of Cryopreservation Method Affects Immune Compatibility of Human Cardiovascular Matrices. *Sci. Rep.* **2017**, *7*, 1–14. [CrossRef]
63. Pusch, J.; Votteler, M.; Göhler, S.; Engl, J.; Hampel, M.; Walles, H.; Schenke-Layland, K. The Physiological Performance of a Three-Dimensional Model That Mimics the Microenvironment of the Small Intestine. *Biomaterials* **2011**, *32*, 7469–7478. [CrossRef] [PubMed]
64. Piccirillo, G.; Carvajal Berrio, D.A.; Laurita, A.; Pepe, A.; Bochicchio, B.; Schenke-Layland, K.; Hinderer, S. Controlled and Tuneable Drug Release from Electrospun Fibers and a Non-Invasive Approach for Cytotoxicity Testing. *Sci. Rep.* **2019**, *9*, 1–10. [CrossRef] [PubMed]
65. Al-Sabti, H.A.; Al Kindi, A.; Al-Rasadi, K.; Banerjee, Y.; Al-Hashmi, K.; Al-Hinai, A. Saphenous Vein Graft vs. Radial Artery Graft Searching for the Best Second Coronary Artery Bypass Graft. *J. Saudi Heart Assoc.* **2013**, *25*, 247–254. [CrossRef]

114

66.   Stekelenburg, M.; Rutten, M.C.M.; Snoeckx, L.H.E.H.; Baaijens, F.P.T. Dynamic Straining Combined with Fibrin Gel Cell Seeding Improves Strength of Tissue-Engineered Small-Diameter Vascular Grafts. *Tissue Eng. Part A* **2009**, *15*, 1081–1089. [CrossRef]

67.   Soletti, L.; Hong, Y.; Guan, J.; Stankus, J.J.; El-Kurdi, M.S.; Wagner, W.R.; Vorp, D.A. A Bilayered Elastomeric Scaffold for Tissue Engineering of Small Diameter Vascular Grafts. *Acta Biomater.* **2010**, *6*, 110–122. [CrossRef]

68.   Pukacki, F.; Jankowski, T.; Gabriel, M.; Oszkinis, G.; Krasinski, Z.; Zapalski, S. The Mechanical Properties of Fresh and Cryopreserved Arterial Homografts. *Eur. J. Vasc. Endovasc. Surg.* **2000**, *20*, 21–24. [CrossRef]

69.   Porter, T.R.; Taylor, D.O.; Fields, J.; Cycan, A.; Akosah, K.; Mohanty, P.K.; Pandian, N.G. Direct in Vivo Evaluation of Pulmonary Arterial Pathology in Chronic Congestive Heart Failure with Catheter-Based Intravascular Ultrasound Imaging. *Am. J. Cardiol.* **1993**, *71*, 754–757. [CrossRef]

70.   Abbott, W.M. Prosthetic Above-Knee Femoral-Popliteal Bypass: Indications and Choice of Graft. *Semin. Vasc. Surg.* **1997**, *10*, 3–7.

71.   Konig, G.; McAllister, T.N.; Dusserre, N.; Garrido, S.A.; Iyican, C.; Marini, A.; Fiorillo, A.; Avila, H.; Wystrychowski, W.; Zagalski, K.; et al. Mechanical Properties of Completely Autologous Human Tissue Engineered Blood Vessels Compared to Human Saphenous Vein and Mammary Artery. *Biomaterials* **2009**, *30*, 1542–1550. [CrossRef]

72.   Lamm, P.; Juchem, G.; Milz, S.; Schuffenhauer, M.; Reichart, B. Autologous Endothelialized Vein Allograft: A Solution in the Search for Small-Caliber Grafts in Coronary Artery Bypass Graft Operations. *Circulation* **2001**, *104*, I-108. [CrossRef]

73.   L'Heureux, N.; Pâquet, S.; Labbé, R.; Germain, L.; Auger, F.A. A Completely Biological Tissue-Engineered Human Blood Vessel. *FASEB J.* **1998**, *12*, 47–56.

74.   Caruso, A.; Licenziati, S.; Corulli, M.; Canaris, A.D.; De Francesco, M.A.; Fiorentini, S.; Peroni, L.; Fallacara, F.; Dima, F.; Balsari, A.; et al. Flow Cytometric Analysis of Activation Markers on Stimulated T Cells and Their Correlation with Cell Proliferation. *Cytometry* **1997**, *27*, 71–76. [CrossRef]

75.   Lerouge, S. Introduction to Sterilization: Definitions and Challenges. In *Sterilisation of Biomaterials and Medical Devices*; Elsevier: Amsterdam, The Netherlands, 2012; pp. 1–19.

76.   Ameer, J.M.; Anil Kumar, P.R.; Kasoju, N. Strategies to Tune Electrospun Scaffold Porosity for Effective Cell Response in Tissue Engineering. *J. Funct. Biomater.* **2019**, *10*, 30. [CrossRef]

77.   Bružauskaitė, I.; Bironaitė, D.; Bagdonas, E.; Bernotienė, E. Scaffolds and Cells for Tissue Regeneration: Different Scaffold Pore Sizes—Different Cell Effects. *Cytotechnology* **2016**, *68*, 355–369. [CrossRef]

78.   Murphy, C.M.; O'Brien, F.J. Understanding the Effect of Mean Pore Size on Cell Activity in Collagen-Glycosaminoglycan Scaffolds. *Cell Adhes. Migr.* **2010**, *4*, 377–381. [CrossRef]

79.   Arends, F.; Lieleg, O. Biophysical Properties of the Basal Lamina: A Highly Selective Extracellular Matrix. In *Composition and Function of the Extracellular Matrix in the Human Body*; InTech: London, UK, 2016.

80.   Liliensiek, S.J.; Nealey, P.; Murphy, C.J. Characterization of Endothelial Basement Membrane Nanotopography in Rhesus Macaque as a Guide for Vessel Tissue Engineering. *Tissue Eng. Part A* **2009**, *15*, 2643–2651. [CrossRef]

81.   Sage, H. Collagens of Basement Membranes. *J. Investig. Dermatol.* **1982**, *79*, 51s–59s. [CrossRef]

82.   Abrams, G.A.; Murphy, C.J.; Wang, Z.Y.; Nealey, P.F.; Bjorling, D.E. Ultrastructural Basement Membrane Topography of the Bladder Epithelium. *Urol. Res.* **2003**, *31*, 341–346.

83.   Inoguchi, H.; Kwon, I.K.; Inoue, E.; Takamizawa, K.; Maehara, Y.; Matsuda, T. Mechanical Responses of a Compliant Electrospun Poly(L-Lactide-Co-ε- Caprolactone) Small-Diameter Vascular Graft. *Biomaterials* **2006**, *27*, 1470–1478. [CrossRef]

84.   Nottelet, B.; Pektok, E.; Mandracchia, D.; Tille, J.-C.; Walpoth, B.; Gurny, R.; Möller, M. Factorial Design Optimization and *in Vivo* Feasibility of Poly(ε-Caprolactone)-Micro- and Nanofiber-Based Small Diameter Vascular Grafts. *J. Biomed. Mater. Res. Part A* **2009**, *89A*, 865–875. [CrossRef] [PubMed]

85.   Vaz, C.M.; van Tuijl, S.; Bouten, C.V.C.; Baaijens, F.P.T. Design of Scaffolds for Blood Vessel Tissue Engineering Using a Multi-Layering Electrospinning Technique. *Acta Biomater.* **2005**, *1*, 575–582. [CrossRef] [PubMed]

86.   Hironaka, K.; Makino, H.; Yamasaki, Y.; Ota, Z. Renal Basement Membranes by Ultrahigh Resolution Scanning Electron Microscopy. *Kidney Int.* **1993**, *43*, 334–345. [CrossRef] [PubMed]

87.   Takeuchi, T.; Gonda, T. Distribution of the Pores of Epithelial Basement Membrane in the Rat Small Intestine. *J. Vet. Med. Sci.* **2004**, *66*, 695–700. [CrossRef] [PubMed]

88.   Yurchenco, P.D.; Ruben, G.C. Basement Membrane Structure in Situ: Evidence for Lateral Associations in the Type IV Collagen Network. *J. Cell Biol.* **1987**, *105*, 2559–2568. [CrossRef]

89. Howat, W.J.; Holmes, J.A.; Holgate, S.T.; Lackie, P.M. Basement Membrane Pores in Human Bronchial Epithelium: A Conduit for Infiltrating Cells? *Am. J. Pathol.* **2001**, *158*, 673–680. [CrossRef]

90. Wierzbicka-Patynowski, I.; Schwarzbauer, J.E. Cell-Surface Transglutaminase Promotes Fibronectin Assembly via Interaction with the Gelatin-Binding Domain of Fibronectin: A Role in TGFbeta-Dependent Matrix Deposition. *J. Cell Sci.* **2003**, *116*, 3269–3276. [CrossRef]

91. Sevilla, C.A.; Dalecki, D.; Hocking, D.C. Regional Fibronectin and Collagen Fibril Co-Assembly Directs Cell Proliferation and Microtissue Morphology. *PLoS ONE* **2013**, *8*, e77316. [CrossRef]

92. Rico, P.; Mnatsakanyan, H.; Dalby, M.J.; Salmerón-Sánchez, M. Material-Driven Fibronectin Assembly Promotes Maintenance of Mesenchymal Stem Cell Phenotypes. *Adv. Funct. Mater.* **2016**, *26*, 6563–6573. [CrossRef]

93. Llopis-Hernández, V.; Cantini, M.; González-García, C.; Cheng, Z.A.; Yang, J.; Tsimbouri, P.M.; García, A.J.; Dalby, M.J.; Salmerón-Sánchez, M. Material-Driven Fibronectin Assembly for High-Efficiency Presentation of Growth Factors. *Sci. Adv.* **2016**, *2*, e1600188. [CrossRef]

94. Schmidt, G.; Hausser, H.; Kresse, H. Interaction of the Small Proteoglycan Decorin with Fibronectin. Involvement of the Sequence NKISK of the Core Protein. *Biochem. J.* **1991**, *280*, 411–414. [CrossRef] [PubMed]

95. Winnemöller, M.; Schmidt, G.; Kresse, H. Influence of Decorin on Fibroblast Adhesion to Fibronectin. *Eur. J. Cell Biol.* **1991**, *54*, 10–17. [PubMed]

96. Dee, K.C.; Puleo, D.A.; Bizios, R. Protein-Surface Interactions. In *An Introduction to Tissue-Biomaterial Interaction*; Wiley: Hoboken, NJ, USA, 2002; pp. 37–51.

97. Thyparambil, A.A.; Wei, Y.; Latour, R.A. Experimental Characterization of Adsorbed Protein Orientation, Conformation, and Bioactivity. *Biointerphases* **2015**, *10*, 019002. [CrossRef] [PubMed]

98. Latour, R.A. Molecular Simulation of Protein-Surface Interactions. In *Biological Interactions on Material Surfaces*; Puleo, D.A., Bizios, R., Eds.; Springer US: Berlin/Heidelberg, Germany, 2009; pp. 73–74.

99. Lebaron, R.G.; Athanasiou, K.A. Extracellular Matrix Cell Adhesion Peptides: Functional Applications in Orthopedic Materials. *Tissue Eng.* **2000**, *6*, 85–103. [CrossRef]

100. Hinderer, S.; Schesny, M.; Bayrak, A.; Ibold, B.; Hampel, M.; Walles, T.; Stock, U.A.; Seifert, M.; Schenke-Layland, K. Engineering of Fibrillar Decorin Matrices for a Tissue-Engineered Trachea. *Biomaterials* **2012**, *33*, 5259–5266. [CrossRef]

101. Ishizaki, T.; Saito, N.; Takai, O. Correlation of Cell Adhesive Behaviors on Superhydrophobic, Superhydrophilic, and Micropatterned Superhydrophobic/Superhydrophilic Surfaces to Their Surface Chemistry. *Langmuir* **2010**, *26*, 8147–8154. [CrossRef]

102. Schmidt, G.; Robenek, H.; Harrach, B.; Glössl, J.; Nolte, V.; Hörmann, H.; Richter, H.; Kresse, H. Interaction of Small Dermatan Sulfate Proteoglycan from Fibroblasts with Fibronectin. *J. Cell Biol.* **1987**, *104*, 1683–1691. [CrossRef]

103. Zhao, J.; Mitrofan, C.G.; Appleby, S.L.; Morrell, N.W.; Lever, A.M.L. Disrupted Endothelial Cell Layer and Exposed Extracellular Matrix Proteins Promote Capture of Late Outgrowth Endothelial Progenitor Cells. *Stem Cells Int.* **2016**, *2016*, 1406304. [CrossRef]

104. Brown, B.N.; Badylak, S.F. Expanded Applications, Shifting Paradigms and an Improved Understanding of Host-Biomaterial Interactions. *Acta Biomater.* **2013**, *9*, 4948–4955. [CrossRef]

105. Wang, Z.; Cui, Y.; Wang, J.; Yang, X.; Wu, Y.; Wang, K.; Gao, X.; Li, D.; Li, Y.; Zheng, X.L.; et al. The Effect of Thick Fibers and Large Pores of Electrospun Poly(ε-Caprolactone) Vascular Grafts on Macrophage Polarization and Arterial Regeneration. *Biomaterials* **2014**, *35*, 5700–5710. [CrossRef]

106. Dejana, E.; Orsenigo, F.; Molendini, C.; Baluk, P.; McDonald, D.M. Organization and Signaling of Endothelial Cell-to-Cell Junctions in Various Regions of the Blood and Lymphatic Vascular Trees. *Cell Tissue Res.* **2009**, *335*, 17–25. [CrossRef] [PubMed]

107. Lertkiatmongkol, P.; Liao, D.; Mei, H.; Hu, Y.; Newman, P.J. Endothelial Functions of Platelet/Endothelial Cell Adhesion Molecule-1 (CD31). *Curr. Opin. Hematol.* **2016**, *23*, 253–259. [CrossRef] [PubMed]

108. Yamaguchi, T.P.; Dumont, D.J.; Conlon, R.A.; Breitman, M.L.; Rossant, J. Flk-1, an Fit-Related Receptor Tyrosine Kinase Is an Early Marker for Endothelial Cell Precursors. *Development* **1993**, *118*, 489–498. [PubMed]

109. Smadja, D.M.; Bièche, I.; Helley, D.; Laurendeau, I.; Simonin, G.; Muller, L.; Aiach, M.; Gaussem, P. Increased VEGFR2 Expression during Human Late Endothelial Progenitor Cells Expansion Enhances in Vitro Angiogenesis with Up-Regulation of Integrin A6. *J. Cell. Mol. Med.* **2007**, *11*, 1149–1161. [CrossRef]

110. Kusuma, S.; Zhao, S.; Gerecht, S. The Extracellular Matrix Is a Novel Attribute of Endothelial Progenitors and of Hypoxic Mature Endothelial Cells. *FASEB J.* **2012**, *26*, 4925–4936. [CrossRef]

111. Ichii, M.; Frank, M.B.; Iozzo, R.V.; Kincade, P.W. The Canonical Wnt Pathway Shapes Niches Supportive of Hematopoietic Stem/Progenitor Cells. *Blood* **2012**, *119*, 1683–1692. [CrossRef]

112. Wijelath, E.S.; Rahman, S.; Murray, J.; Patel, Y.; Savidge, G.; Sobel, M. Fibronectin Promotes VEGF-Induced CD34+ Cell Differentiation into Endothelial Cells. *J. Vasc. Surg.* **2004**, *39*, 655–660. [CrossRef]

113. Shen, B.Q.; Lee, D.Y.; Gerber, H.P.; Keyt, B.A.; Ferrara, N.; Zioncheck, T.F. Homologous Up-Regulation of KDR/Flk-1 Receptor Expression by Vascular Endothelial Growth Factor in Vitro. *J. Biol. Chem.* **1998**, *273*, 29979–29985. [CrossRef]

114. Neill, T.; Schaefer, L.; Iozzo, R.V. Decorin: A Guardian from the Matrix. *Am. J. Pathol.* **2012**, *181*, 380–387. [CrossRef]

115. Mazor, R.; Alsaigh, T.; Shaked, H.; Altshuler, A.E.; Pocock, E.S.; Kistler, E.B.; Karin, M.; Schmid-Schönbein, G.W. Matrix Metalloproteinase-1-Mediated up-Regulation of Vascular Endothelial Growth Factor-2 in Endothelial Cells. *J. Biol. Chem.* **2013**, *288*, 598–607. [CrossRef]

116. Huttenlocher, A.; Werb, Z.; Tremble, P.; Huhtala, P.; Rosenberg, L.; Damsky, C.H. Decorin Regulates Collagenase Gene Expression in Fibroblasts Adhering to Vitronectin. *Matrix Biol.* **1996**, *15*, 239–250. [CrossRef]

117. Schönherr, E.; Schaefer, L.; O'Connell, B.C.; Kresse, H. Matrix Metalloproteinase Expression by Endothelial Cells in Collagen Lattices Changes during Co-Culture with Fibroblasts and upon Induction of Decorin Expression. *J. Cell. Physiol.* **2001**, *187*, 37–47. [CrossRef]

118. Murakami, M.; Nguyen, L.T.; Hatanaka, K.; Schachterle, W.; Chen, P.Y.; Zhuang, Z.W.; Black, B.L.; Simons, M. FGF-Dependent Regulation of VEGF Receptor 2 Expression in Mice. *J. Clin. Investig.* **2011**, *121*, 2668–2678. [CrossRef] [PubMed]

119. Penc, S.F.; Pomahac, B.; Winkler, T.; Dorschner, R.A.; Eriksson, E.; Herndon, M.; Gallo, R.L. Dermatan Sulfate Released after Injury Is a Potent Promoter of Fibroblast Growth Factor-2 Function. *J. Biol. Chem.* **1998**, *273*, 28116–28121. [CrossRef] [PubMed]

120. Chen, T.T.; Filvaroff, E.; Peng, J.; Marsters, S.; Jubb, A.; Koeppen, H.; Merchant, M.; Ashkenazi, A. MET Suppresses Epithelial VEGFR2 via Intracrine VEGF-Induced Endoplasmic Reticulum-Associated Degradation. *EBioMedicine* **2015**, *2*, 406–420. [CrossRef] [PubMed]

121. Chen, S.; Chakrabarti, R.; Keats, E.C.; Chen, M.; Chakrabarti, S.; Khan, Z.A. Regulation of Vascular Endothelial Growth Factor Expression by Extra Domain B Segment of Fibronectin in Endothelial Cells. *Investig. Ophthalmol. Vis. Sci.* **2012**, *53*, 8333–8343. [CrossRef]

122. Wijelath, E.S.; Rahman, S.; Namekata, M.; Murray, J.; Nishimura, T.; Mostafavi-Pour, Z.; Patel, Y.; Suda, Y.; Humphries, M.J.; Sobel, M. Heparin-II Domain of Fibronectin Is a Vascular Endothelial Growth Factor-Binding Domain. *Circ. Res.* **2006**, *99*, 853–860. [CrossRef]

123. Kou, R.; SenBanerjee, S.; Jain, M.K.; Michel, T. Differential Regulation of Vascular Endothelial Growth Factor Receptors (VEGFR) Revealed by RNA Interference: Interactions of VEGFR-1 and VEGFR-2 in Endothelial Cell Signaling. *Biochemistry* **2005**, *44*, 15064–15073. [CrossRef]

124. Scott, R.A.; Paderi, J.E.; Sturek, M.; Panitch, A. Decorin Mimic Inhibits Vascular Smooth Muscle Proliferation and Migration. *PLoS ONE* **2013**, *8*, e82456. [CrossRef]

125. Harding, A.; Cortez-Toledo, E.; Magner, N.L.; Beegle, J.R.; Coleal-Bergum, D.P.; Hao, D.; Wang, A.; Nolta, J.A.; Zhou, P. Highly Efficient Differentiation of Endothelial Cells from Pluripotent Stem Cells Requires the MAPK and the PI3K Pathways. *Stem Cells* **2017**, *35*, 909–919. [CrossRef]

126. Bryan, B.A.; Walshe, T.E.; Mitchell, D.C.; Havumaki, J.S.; Saint-Geniez, M.; Maharaj, A.S.; Maldonado, A.E.; D'Amore, P.A. Coordinated Vascular Endothelial Growth Factor Expression and Signaling during Skeletal Myogenic Differentiation. *Mol. Biol. Cell* **2008**, *19*, 994–1006. [CrossRef] [PubMed]

127. Zeng, Y.; Zhang, X.F.; Fu, B.M.; Tarbell, J.M. The Role of Endothelial Surface Glycocalyx in Mechanosensing and Transduction. In *Advances in Experimental Medicine and Biology*; Springer New York LLC: New York, NY, USA, 2018; Volume 1097, pp. 1–27.

128. Ballermann, B.J.; Dardik, A.; Eng, E.; Liu, A. Shear Stress and the Endothelium. *Kidney Int.* **1998**, *54*, S100–S108. [CrossRef] [PubMed]

129. Sato, M.; Kataoka, N.; Ohshima, N. Response of Vascular Endothelial Cells to Flow Shear Stress: Phenomenological Aspect. In *Biomechanics*; Springer Japan: Tokyo, Japan, 1996; pp. 3–27.

Appendices

130. Zhou, J.; Li, Y.S.; Chien, S. Shear Stress-Initiated Signaling and Its Regulation of Endothelial Function. *Arterioscler. Thromb. Vasc. Biol.* **2014**, *34*, 2191–2198. [CrossRef]

131. Sánchez-Duffhues, G.; García de Vinuesa, A.; ten Dijke, P. Endothelial-to-Mesenchymal Transition in Cardiovascular Diseases: Developmental Signaling Pathways Gone Awry. *Dev. Dyn.* **2018**, *247*, 492–508. [CrossRef] [PubMed]

132. Moonen, J.R.A.J.; Lee, E.S.; Schmidt, M.; Maleszewska, M.; Koerts, J.A.; Brouwer, L.A.; Van Kooten, T.G.; Van Luyn, M.J.A.; Zeebregts, C.J.; Krenning, G.; et al. Endothelial-to-Mesenchymal Transition Contributes to Fibro-Proliferative Vascular Disease and Is Modulated by Fluid Shear Stress. *Cardiovasc. Res.* **2015**, *108*, 377–386. [CrossRef]

133. Mahmoud, M.M.; Serbanovic-Canic, J.; Feng, S.; Souilhol, C.; Xing, R.; Hsiao, S.; Mammoto, A.; Chen, J.; Ariaans, M.; Francis, S.E.; et al. Shear Stress Induces Endothelial-To-Mesenchymal Transition via the Transcription Factor Snail. *Sci. Rep.* **2017**, *7*, 1–12. [CrossRef]

134. Melchiorri, A.J.; Bracaglia, L.G.; Kimerer, L.K.; Hibino, N.; Fisher, J.P. In Vitro Endothelialization of Biodegradable Vascular Grafts Via Endothelial Progenitor Cell Seeding and Maturation in a Tubular Perfusion System Bioreactor. *Tissue Eng.-Part C Methods* **2016**, *22*, 663–670. [CrossRef]

135. Dejana, E.; Hirschi, K.K.; Simons, M. The Molecular Basis of Endothelial Cell Plasticity. *Nat. Commun.* **2017**, *8*, 1–11. [CrossRef]

136. Lacorre, D.A.; Baekkevold, E.S.; Garrido, I.; Brandtzaeg, P.; Haraldsen, G.; Amalric, F.; Girard, J.P. Plasticity of Endothelial Cells: Rapid Dedifferentiation of Freshly Isolated High Endothelial Venule Endothelial Cells Outside the Lymphoid Tissue Microenvironment. *Blood* **2004**, *103*, 4164–4172. [CrossRef]

137. Nguyen, M.T.X.; Okina, E.; Chai, X.; Tan, K.H.; Hovatta, O.; Ghosh, S.; Tryggvason, K. Differentiation of Human Embryonic Stem Cells to Endothelial Progenitor Cells on Laminins in Defined and Xeno-Free Systems. *Stem Cell Rep.* **2016**, *7*, 802–816. [CrossRef]

Supplementary Materials

1. Mechanical characterization of the electrospun TPCU scaffold
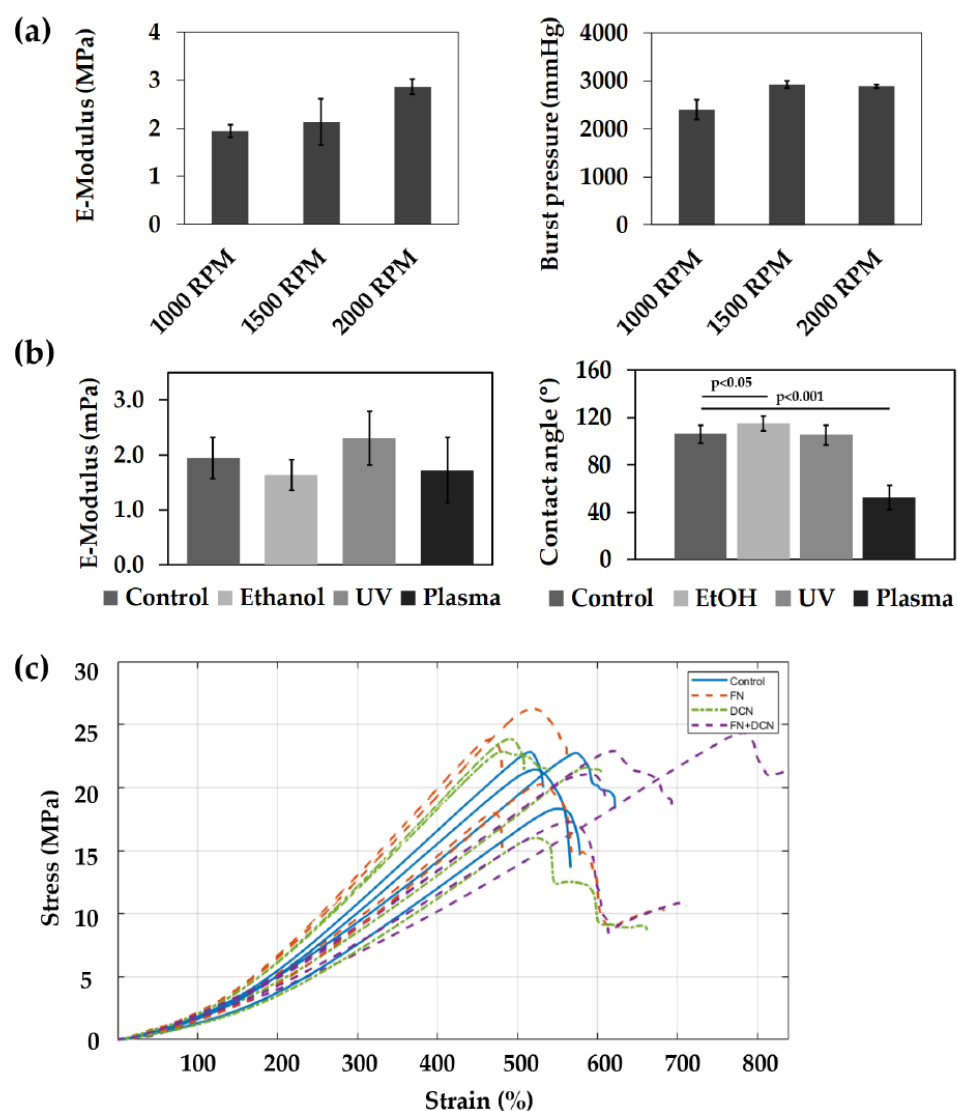
Figure S1. Mechanical characterization of the electrospun TPCU scaffold and biocompatibility of the materials. (**a**) E-modulus and burst pressure of tubular constructs spun with different mandrel rotating speeds. (**b**) Wettability and E-modulus of 70 % ethanol, UV and oxygen plasma treated electrospun TPCU scaffolds. Two-tailed t-test, n=3 (**c**) Stress-strain curves of control, FN, DCN and FN+DCN coated scaffolds.

2. Cytotoxicity of the materials used in the study
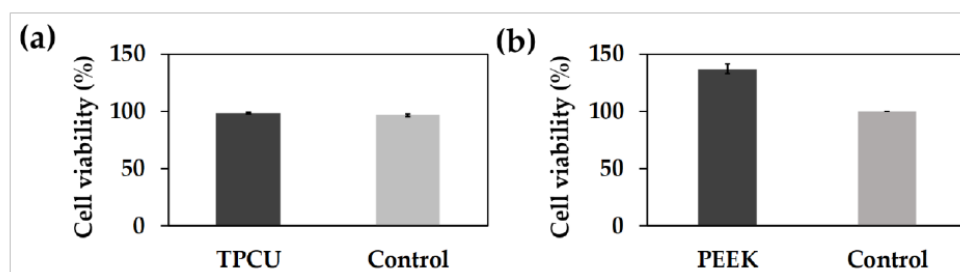
Figure S2. Cytotoxicity tests of the materials. Both (**a**) TPCU and (**b**) PEEK (used in the bioreactor) showed no cytotoxic effects.

3. Microbiological studies of the electrospun scaffolds

Method

In order to investigate the disinfection method, microbiological studies of the electrospun scaffolds were performed. For this approach, nine round TPCU scaffolds with a diameter of 3 cm were disinfected with 70% ethanol for 20 min. After washing three times with PBS under sterile conditions, each scaffold was transferred into 50 ml LB-medium (1% tryptone, 0.5% yeast extract, 1% sodium chloride in H_2O) and incubated for 48 hours at 37 °C. The medium without the scaffold served as a control. Subsequently, 0.1 mL of the LB-medium were plated on agar plates (4% LB-agar, Carl Roth, Karlsruhe, Germany) and incubated over night at 37 °C and 90% humidity. Finally, the germ load on the agar plates was examined macroscopically.

Results and Discussion

Two of the nine scaffolds showed a bacterial contamination after ethanol treatment (**Figure S3**). This result shows that our disinfection method does not guarantee 100% sterility. However, we are aware that ethanol treatment as a disinfection method does not necessarily inactivate all forms of microorganisms [1]. In order to take this into account in our study, penicillin-streptomycin was added to all cell culture experiments to suppress possible contamination. In a next step, sterilization methods should be investigated, such as gamma irradiation or ethylene oxide treatment.
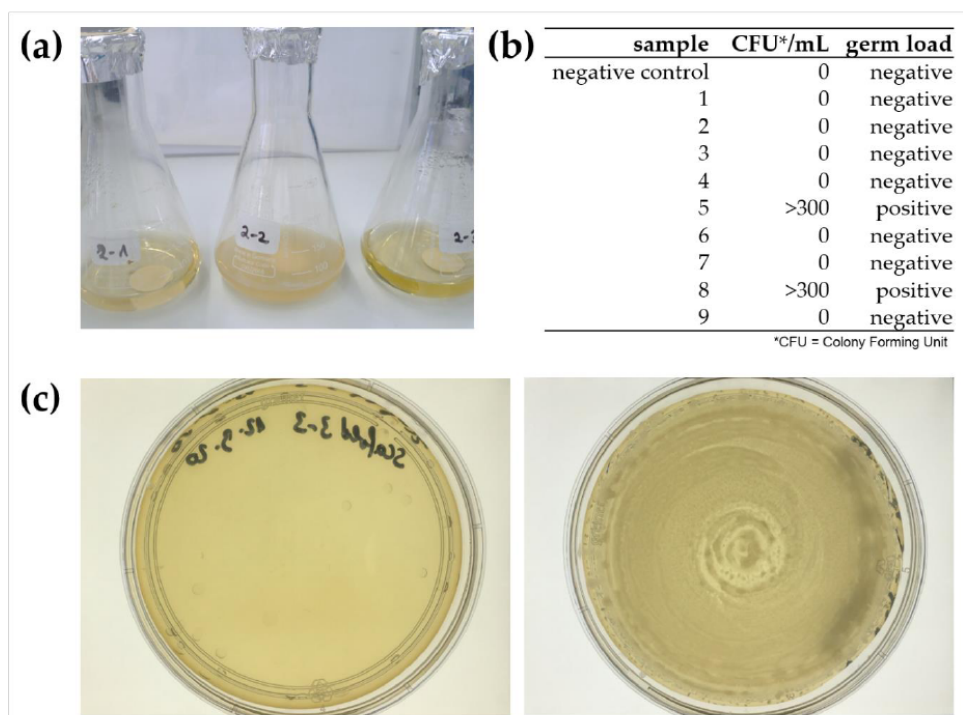
Figure S3. Microbiological studies of the ethanol disinfected electrospun TPCU scaffolds (**a**) Scaffolds were incubated in LB-medium for 48 hours at 37 °C. (**b**) In terms of germ load, two of nine scaffolds were positive. CFU stands for colony forming unit. (**c**) Macroscopic image of a germ-free (left) and a germ-contaminated (right) agar plate.

4. In silico CFD simulations

Methods

The CAD models were designed in Solidworks and consequently prepared for numerical fluid simulations. The three-dimensional surfaces of the bioreactor culture chamber model, which are in contact with the intraluminal medium, were imported into ANSYS Mesher, whilst omitting other irrelevant parts of the culturing chamber. The result practically resembled a 'pipe model' of the intraluminal circulation, with scaffold diameters ranging between 3.0 and 6.0 mm (**Error! Reference source not found.**). To assure a quicker convergence and stable results, the thee-dimensional pipe model was mostly meshed with a hexahedronal (six-sided) mesh structure. The resulting cell count in the meshed models was around 500.000 cells. The meshes were imported in Fluent 19, executed in the three-dimensional double precision mode and appointed all eight logical CPU cores on the computer. The simulation was carried out with a rigid model of the scaffold wall. A paraboloid velocity distribution was imposed on the inlet, representing an already fully developed flow profile at the entrance of the culture chamber. Furthermore, a no-slip velocity boundary condition was imposed on the walls. The numerical simulations in ANSYS Fluent were performed using the built-in pressure-based

solver and the second-order upwind momentum discretization scheme. Cell culture medium was approximated to have the same rheological properties as water at 37 °C, with a dynamic viscosity of 0.691 mPa s and a density of 993 kg m^{-3}. CFD simulations were carried out for a range of flow rates between 0.2 and 50.0 mL/min.
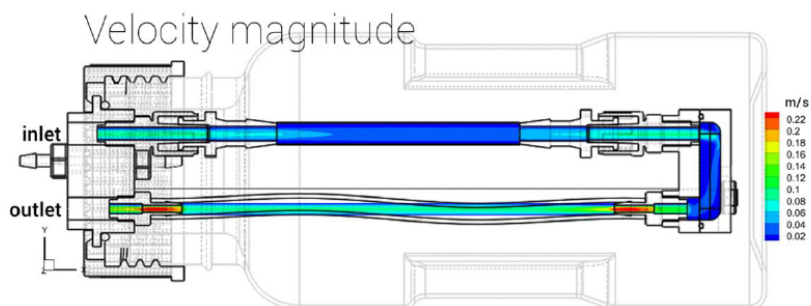
Figure S4. The part of the culture chamber that was considered for CFD simulations. Different flow rates and scaffold diameters were considered for which the geometry was adapted accordingly.

Results

The flow regime was analyzed and was found to be laminar within the operational range. The wall shear stress along the inner scaffold wall for different flow rates are plotted in **Error! Reference source not found.**. The observed Poiseuille values in the CFD simulations corresponded well to the analytical solution for the wall shear stress of a laminar flow in straight circular pipe according to the Hagen-Poiseuille equation for all flow rates between 0.2 and 20 ml/min.
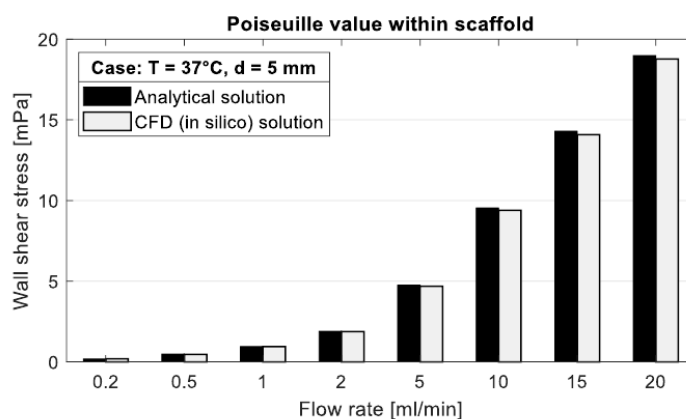
Figure S5. The Poiseuille values (developed wall shear stress value) within the scaffold for different flow rates. This plot compares the observed Poiseuille values to those of the analytical solution.

1.   Lerouge, S. Introduction to Sterilization: Definitions and Challenges. In *Sterilisation of Biomaterials and Medical Devices*; Elsevier, **2012**; pp. 1–19.

Journal of Materials Chemistry B

ROYAL SOCIETY OF CHEMISTRY

PAPER

Check for updates

Fibronectin adsorption on oxygen plasma-treated polyurethane surfaces modulates endothelial cell response†

Ruben Daum,‡[ab] Ivana Mrsic,‡[c] Johanna Hutterer, [c] Achim Junginger,[c] Svenja Hinderer, [ab] Alfred J. Meixner,[cd] Günter Gauglitz,[c] Thomas Chassé[cd] and Katja Schenke-Layland [*abef]

Fibronectin coating increases implant biocompatibility by enhancing surface endothelialization *via* integrin-mediated binding. Surface properties determine the fibronectin orientation and conformation, dictating which ligands are presented, and therefore altering the bioactivity of an implant surface. In this study, polyurethane was treated with oxygen plasma, which allowed for a simultaneous modification of the surface chemistry and topography to modulate fibronectin adsorption. By varying the parameters of the treatment, human plasma fibronectin adsorbed on the surfaces in different conformations, orientations, and binding affinities, which was investigated by atomic force microscopy, fluorescence microscopy, monoclonal and polyclonal antibody staining and reflectometric interference spectroscopy. Apart from the most hydrophilic rough surfaces, the adsorbed fibronectin showed a lower binding affinity and less conformational change on the more hydrophilic surfaces. A large amount of exposed fibronectin–cell binding was detected on the rough treated and the smooth untreated surfaces. Primary isolated human umbilical vein and human microvascular endothelial cells showed a significantly higher cell adherence on the absorbed fibronectin with a low binding affinity and low conformational changes. Significant differences in the formation of mature focal adhesions and the reorganization of F-actin were identified on the rough treated and the smooth untreated surfaces. Our data suggest that oxygen plasma treatment is a reliable technique for the modulation of fibronectin adsorption in order to adjust fibronectin bioactivity and impact cell responses to implant surfaces.

1. Introduction

The interaction between cardiovascular implants and cells in the human body is highly influenced by the layer of blood proteins initially adsorbed onto the synthetic material surfaces.[1] In order to trigger specific reactions in the body, an implant material can be functionalized with bioactive substances. An attractive candidate that has been reported to support endothelialization of the surface is fibronectin (FN), a well-studied glycoprotein of the extracellular matrix (ECM).[2–4] However, the influence of the surface properties on the deposition and thus bioactivity of FN is often neglected. FN fulfils a wide range of biological functions as it interacts with other ECM molecules and growth factors, binds to cell surface receptors and forms fibrils through intermolecular interactions.[5,6] It is a 440 kDa macromolecule that is secreted as a dimer connected by two disulfide S–S bonds at the C-terminus. The two peptide chains consist of several repeating domains (FNI, FNII and FNIII) that can associate with each other, resulting in a globular folding structure of FN.[7] Moreover, FN is very flexible and can change its conformation depending on the environment.[8] *In vivo*, FN is synthesized, for example, by hepatocytes and secreted into the blood plasma in an inactive globular conformation.[9] The soluble plasma FN

ª NMI Natural and Medical Sciences, Institute at the University of Tübingen, Markwiesenstr. 55, 72770 Reutlingen, Germany. Web: www.nmi.de/en

ᵇ Department of Women's Health, Research Institute for Women's Health, Eberhard Karls University Tübingen, Silcherstr. 7/1, 72076 Tübingen, Germany. E-mail: katja.schenke-layland@uni-tuebingen.de; Tel: +49-707-1298-5205; Web: www.schenke-layland-lab.de

ᶜ Institute of Physical and Theoretical Chemistry, Eberhard Karls University Tübingen, Auf der Morgenstelle 18, 72076 Tübingen, Germany

ᵈ Center for Light–Matter Interaction, Sensors & Analytics (LISA+) at the University of Tübingen, Auf der Morgenstelle 18, 72076 Tübingen, Germany

ᵉ Cluster of Excellence iFIT (EXC 2180) "Image-Guided and Functionally Instructed Tumor Therapies", Eberhard Karls University Tübingen, 72076 Tübingen, Germany

ᶠ Department of Medicine/Cardiology, Cardiovascular Research Laboratories, David Geffen School of Medicine at UCLA, Los Angeles, CA, 90095, USA

† Electronic supplementary information (ESI) available. See DOI: 10.1039/d0tb02757j

‡ These authors contributed equally to this work.

This journal is © The Royal Society of Chemistry 2021

J. Mater. Chem. B, 2021, **9**, 1647–1660 | **1647**

binds poorly to many cell types. In early wound-healing responses; however, it undergoes conformational changes by interacting with fibrin and platelets.[10] During this finely tuned unfolding process of the protein, cell- and FN-binding sides are exposed, which leads to further stages of tissue repair.[10] The folding of FN adsorbed on biomaterial surfaces has been shown to be influenced by surface properties such as wettability,[11] surface chemistry,[12] and roughness.[13] In recent years, several studies have investigated the influence of modified substrates on the conformation of FN and its effect on cell behavior.[14–17] Based on this knowledge, research now aims to specifically control cell attachment, proliferation, and differentiation through substrate-dependent changes.[18–20] Cells interact with FN mainly *via* the $\alpha 5 \beta 1$ integrin, which binds to the RGD loop on $FNIII_{10}$ and the neighboring PHSRN sequence in $FNIII_9$.[21–23] This interaction induces integrin clustering and the formation of focal adhesion complexes.[10] These protein complexes are dynamic structures that form mechanical links between FN and the cell cytoskeleton, and mediate the transduction of signaling events, which in turn affects the growth, differentiation, adhesion, and motility of the cell.[9] At the same time, the cell assembles FN into a fibrillar network through an integrin-dependent mechanism.[24] All these processes are strongly influenced by the conformation and the adhesive force of the adsorbed FN, and ultimately determine cell behavior.[20]

In this study, we investigated the adsorption behavior of FN and subsequently the endothelial cell–surface interaction through the fine-tuning of the surface wettability with oxygen plasma treatment of polyurethane (PU). The selected material is a commercially available PU of the Pellethane® series, which is being currently studied in cardiovascular devices.[3] The effects of oxygen plasma on the wettability of Pellethane® was examined in a recent study over a wide range of plasma treatment parameters.[25] Using this method allows the incorporation of oxygen-rich functional groups onto the material surface changing the chemical composition.[26] Simultaneously to functionalization, the competing plasma etching of low molecular contaminations and upper polymer surface layers is modifying the surface topography and therefore material roughness.[27,28] The objective of this study was a defined modification of the surface chemistry and roughness of PU in order to modulate the adsorption behavior and conformation of FN, which affects its bioactivity and subsequently influences endothelial cell responses, potentially providing surfaces for various cardiovascular applications.

2. Materials & methods

2.1 Sample preparation

2.1.1 Polyurethane spin-coating and oxygen plasma treatment. The commercially available PU Pellethane 2363-55DE (Lubrizol, Wickliffe, OH, USA) was dissolved in dimethylacetamide (99+% extra pure, Acros Organics, Fair Lawn, NJ, USA) to obtain a 5% (w/w) solution. The solution was spin-coated (Convac 1001, Fairchild Semiconductor, Stuttgart, Germany) at

Table 1 Plasma modification parameters of the PU samples

Sample	Pressure (mbar)	Time (min)
A	0.2	3.0
B	0.2	0.2
C	0.8	3.0
D	0.5	1.6
E	0.8	0.2
F[a]	—	—

[a] Sample F was not plasma treated and served as control.

2400 rpm for 40 seconds onto heated pre-cut silicon wafers (Siegert Wafer, Aachen, Germany) and glass slides, resulting in film thicknesses ranging between 270 and 300 nm. For reflectometric interference spectroscopy (RIfS), the PU solution was spin-coated onto glass substrates with a thin layer of tantalpentoxide (1 mm glass, 10 nm Ta_2O_5). Here, the spin-coated layer of PU served as the interference layer for the RIfS measurements. The concentration of the PU solution was adapted to result in a 310–380 nm optical thickness of the layer after the plasma treatment.

Plasma surface modifications of the polymer films were performed in a FEMTO low pressure plasma system (Diener electronic, Ebhausen, Germany) consisting of a borosilicate glass round vacuum and a low-frequency (40 kHz) generator using oxygen plasma. A previous study investigated the plasma modification of PU according to a statistical experimental design.[25] Based on this study, to achieve varied modifications with few plasma parameters, the process time and pressure were varied between 0.2–3.0 minutes and 0.2–0.8 mbar (Table 1). The applicable power was kept constant at 100 W.

2.1.2 DY-490 labeling of fibronectin. For covalent, fluorescence labeling of human FN (F1056-2MG, Sigma-Aldrich, St. Louis, USA), Dyomics DY-490 N-Hydroxysuccinimid-Ester (FluoroSpin 490 Protein Labeling & Purification Kit, emp biotech, Berlin, Germany) was used according to the manufacturer's instructions with a 20-fold molar excess of reactive dye to protein molecules. The resulting concentration and the degree of labeling (2.6 dye molecules per FN) was determined optically, measuring the absorbance at 280 nm and 493 nm with a NanoDrop 2000 spectrophotometer (Thermo Fisher Scientific, Waltham, USA).

2.1.3 Fibronectin adsorption. After oxygen plasma treatment, samples were disinfected with 70% ethanol for 10 min and rinsed in phosphate buffered saline (PBS). The samples were then incubated for 1 hour at 37 °C with 10 μg ml^{-1} human FN (10 μg ml^{-1}, F1056-2MG, Sigma-Aldrich, St. Louis, USA) that was dissolved in PBS.

2.2 Characterization of the surfaces

2.2.1 X-ray photoelectron spectroscopy. Photoelectron spectroscopy (XPS) was carried out using a multi-chamber ultrahigh vacuum system (base pressure 8×10^{-10} mbar) equipped with a Phoibos 100 analyzer and a 1 d – Delay Line detector (SPECS, Berlin, Germany). Al-Kα radiation of a conventional Al/Mg anode (XR-50 m X-ray source, $h\nu$ = 1486.6 eV)

1648 | *J. Mater. Chem. B*, 2021, **9**, 1647–1660

This journal is © The Royal Society of Chemistry 2021

was used for the measurements. The core-level spectra of the C 1s peaks were collected with 20 eV pass energy. The program Unifit version 2018 (Unifit scientific software, Leipzig, Germany) was used for spectral analysis identifying the plasma-induced groups (Fig. S1 and Table S1, ESI†).[29]

2.2.2 Contact angle measurements. Changes in wettability were determined through static contact angle measurements at room temperature using the sessile drop method on the CAM 200 optical angle goniometer (KSV Instruments LTD, Helsinki, Finland). The time between the flooding of the plasma chamber and the placement of the first test liquid drop of H_2O was 2.5 minutes. 5 drops were placed on different areas on each sample. The drop volume was 2 µl. The protein-coated samples were rinsed with distilled water and dried under a cold nitrogen stream before measurements were taken.

2.2.3 Atomic force microscopy. The surface topography of the samples was investigated with atomic force microscopy (AFM) using a Nanoscope III multi-mode AFM system operating in ScanAsyst PeakForce and TappingMode (Bruker, Billerica, MA, USA). ScanAsyst-Air-HR probes (Bruker) were selected with a spring constant of 0.4 N m^{-1} and a resonance frequency of 130 kHz for the PeakForce measurements, while the RTESPA-150 probes (Bruker) with a 150 kHz frequency were used for tapping mode. The open source program Gwyddion version 2.49 was used for AFM image analysis and qualitative root-mean-squared roughness r(RMS) estimations on a 1 µm^2 area.[30]

2.2.4 Reflectometric interference spectroscopy. RIfS, a label-free optical method, was used to investigate the adsorption of FN onto the modified PU surfaces in a time-resolved manner.[31] The PU films were incubated in PBS for 40 min before the FN adsorption measurements were started. This process was monitored by RIfS. In case of no further drift, different concentrations of FN in PBS (1 µg ml^{-1}, 3.3 µg ml^{-1}, 6.6 µg ml^{-1}, 10 µg ml^{-1}, 13.3 µg ml^{-1}, 16.6 µg ml^{-1} and 20 µg ml^{-1}) were pumped across the PU surface (pumping speed: 0.5 µl s^{-1}, flow cell diameters: width: 1 mm, height: 0.1 mm) for 33 minutes (Fig. S2, ESI†). The change in optical thickness ($\Delta n \cdot d$) was calculated from the recorded interference spectrum as described by Kraus et al.[31] The kinetic parameters, the association rate constant k_a, and the dissociation rate constant k_d of the FN adsorption onto the PU surface were evaluated from the binding curves of FN at different concentrations according to O'Shannessy et al.[32] The application of this basic model results in the mean k_a and k_d of the adsorption process over the investigated time and different binding sites of the protein.

2.2.5 Laser scanning confocal fluorescence microscopy of fluorescence-labeled fibronectin. Adsorption of the fluorescence-labeled FN on glass slides with plasma-treated PU was determined with a custom-built confocal microscope. An oil immersion objective lens (NA = 1.46) was used to focus laser light of 488 nm (LDH-D-C-485, PicoQuant, Berlin, Germany) with a repetition frequency of 20 MHz and a power of 15 nW to a diffraction limited spot. The fluorescence was detected with the same objective and guided through a pinhole and a long-pass filter (F76-490, AHF, Tübingen, Germany) to an avalanche photodiode (SPCM-AQR-13, PerkinElmer, Waltham,

USA). The fluorescence signal was collected by scanning the sample with a piezo-electric scanning stage over a square area of 100 µm^2 at several positions on three different samples (Fig. S3, ESI†).

2.2.6 Anti-fibronectin immunofluorescence staining. After FN adsorption, the surfaces were washed once with PBS and blocked with 2% (w/w) goat block solution for 30 minutes. Subsequently, the surfaces were incubated over night at 4 °C with a polyclonal anti-FN antibody (1 : 500, F3648-100UL, Sigma-Aldrich, St. Louis, USA) and a monoclonal anti-FN antibody, which is described to bind against the flexible linker between the 9th and 10th type III repeat of FN[33] (HFN7.1, 1 : 200, ABIN284417, antibodies-online, Aachen, Germany). After washing once with PBS, the samples were incubated with goat anti-rabbit IgG-Alexa Fluor® 546 and goat anti-mouse IgG-Alexa FluorΔ 488 (both 1 : 250, Thermo Fisher Scientific) for 45 minutes in the dark.[34] Images were acquired by using a Zeiss fluorescence microscope (Cell Observer, Carl Zeiss AG, Oberkochen, Germany). The focal plane was adjusted manually for each image.

2.3 Cell culture

For cell–material studies, human primary-isolated microvascular endothelial cells (HMVECs) were isolated from the foreskin biopsies under the ethics approval no. 495/2018BO2 (IRB, University Hospital Tübingen) by enzymatic digestion with dispase and trypsin as previously described.[35] Cells were cultured in endothelial cell growth medium MV (C-22020, PromoCell, Heidelberg, Germany) and used between passages 2 and 4. Human umbilical vein endothelial cells (HUVECs, C-12205, PromoCell, Heidelberg, Germany) were cultured in endothelial cell growth medium (C-22010, PromoCell) and used between passages 4 and 6.[36] For cell–material–interaction experiments, 400 cells mm^{-2} were seeded on the FN-adsorbed surfaces and incubated for 24 hours at 37 °C and 5% CO_2.

2.4 Immunocytochemistry

After cell culture experiments, the cell-seeded PU samples were washed with PBS$^-$ and fixed with 4% (w/w) paraformaldehyde in PBS for 10 minutes. In order to reduce nonspecific binding, the cells were incubated with 2% (w/w) goat block solution for 30 minutes. Cells were incubated with anti-FN (1 : 200, ab2413, Abcam, Cambridge, UK), anti-CD31 (PECAM-1; 1 : 100, sc-71872, Santa Cruz, USA), anti-von Willebrand factor (1 : 200, A0082, DAKO, Glostrup, Denmark), anti-focal adhesion kinase (FAK; 1 : 100, PA5-17591, Thermo Fisher scientific, Waltham, USA), anti-VE-Cadherin (1 : 250, HPA004726, Sigma-Aldrich, St. Louis, USA) and anti-vinculin (1 : 500, MAP3574, Milipore, Burlington, USA) over night at 4 °C. One primary antibody of the same species was used per sample. After washing with PBS, samples were incubated with goat anti-mouse IgG-Alexa Fluor® 488, goat anti-rabbit IgG-Alexa Fluor® 546 (both 1 : 250, Thermo Fisher Scientific) and Alexa Fluor® 647 Phalloidin (1 : 1000, A22283, Thermo Fisher Scientific) for 45 minutes in the dark. Finally, nuclei were counterstained with DAPI (10236276001, Roche, Basel, Switzerland). Images were observed by using a

This journal is © The Royal Society of Chemistry 2021

J. Mater. Chem. B, 2021, **9**, 1647–1660 | **1649**

Zeiss fluorescence microscope (Cell Observer, Carl Zeiss AG, Oberkochen, Germany).

2.5 Image analysis

Polyclonal and monoclonal anti-FN IF staining was quantified by measuring the relative pixel intensity (RPI) of the immuno-fluorescence images. Counting the DAPI-stained cell nuclei per area determined the number of adherent cells. The formation of focal adhesions was quantified by counting the vinculin and FAK foci per cell. To assess VE-cadherin and PECAM-1 expression as well as F-actin organization, the area within a defined fluorescence intensity threshold was measured and normalized to the cell number. All images were analyzed using ImageJ.[37]

2.6 Statistical analysis

Results are presented as mean ± standard deviation. For statistical analysis, a one-way ANOVA/Fisher's Least Significant Difference test was performed using Origin 2018 (OriginLab, Northampton, MA, USA). Probability values of 95%, 99% and 99.9% were used to determine significance.

3. Results

3.1 Analysis of the surface chemistry and its influence on FN adsorption

XPS, AFM and contact angle measurements showed that surface roughness affects the hydrophilic character of the polymers and FN adsorption behavior (Fig. 1). According to the XPS data (Fig. 1a, Fig. S1, ESI†), the chemical composition of the sample surfaces was separable into plasma-incorporated

functional groups and PU-specific functionalities. The plasma-generated −OH functional groups and the polymers C–O–C species peaks are situated on identical binding energies, and therefore could not be adequately separated within the functional group content calculations. From the XPS data analysis it was discernible that samples A and B had a higher –COOH and C=O content than all other samples, while the C, D and E surfaces had a high content of –OH and C–O–C functionalities (Fig. 1a). The untreated control surface F had no new plasma-created species. In terms of surface roughness, the untreated sample F showed a smooth surface that was only little impacted by most plasma treatments (Fig. 1b). Only surface A, treated for a longer time under low oxygen pressure, exhibited a clearly higher surface roughness compared to the other samples. (Fig. 1b). This effect was also seen in the water contact angle measurements of the series (Fig. 1c). The untreated F surface had the highest contact angle with $71.1° \pm 1.6°$. In contrast, the surfaces C, D and E, which were similar in chemical composition and roughness, were only slightly more hydrophilic with similar contact angle values ranging around $50°$ (C: $48.2° \pm 0.6°$ versus D: $50.8° \pm 1.7°$, $p < 0.05$; C versus E: $54.3° \pm 1.0°$, $p < 0.001$; D versus E, $p < 0.05$). Since the roughness was less impacted by these plasma treatments, the biggest contribution to the hydrophilization of these surfaces came from the introduced hydroxyl groups. While the –COOH and C=O surface coverage of the samples A and B was very similar, the contact angle of surface A ($17.5° \pm 1.9°$) was half as high compared with surface B ($33.4° \pm 2.7°$). The major contribution to this additional lowering of the contact angle of the longer plasma-treated sample came from the increased surface roughness,
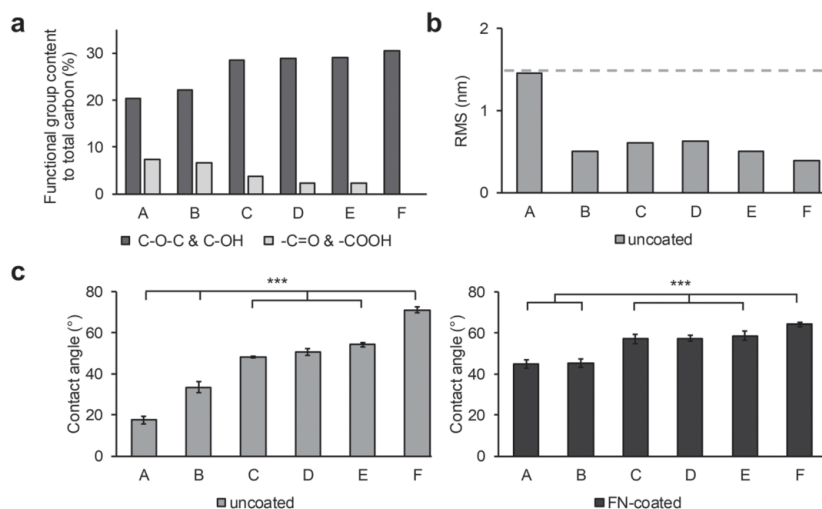

Fig. 1 Investigation of plasma modifications on the PU surfaces and adsorption of fibronectin. (a) XPS obtained chemical composition of plasma-induced functional groups on the polymer surface before FN coating. (b) Qualitative roughness analysis r(RMS) of the polymer surfaces after plasma treatment. The dash line represents the maximum roughness value. (c) Contact angle analysis of plasma-treated and untreated surfaces before (left, "uncoated", one-way ANOVA, $n = 3$, $p*** < 0.001$) and after FN coating (right, "FN-coated", one-way ANOVA, $n = 3$, $p*** < 0.001$). (d) AFM topography images of sample surfaces after FN coating. Scale bar equals 200 nm.

1650 | J. Mater. Chem. B, 2021, 9, 1647–1660

This journal is © The Royal Society of Chemistry 2021

which was twice as high as every other sample (A: 1.45 nm *versus* B: 0.5 nm, C: 0.61 nm, D: 0.63 nm, E: 0.5 nm and F: 0.39 nm).

The water contact angles and r(RMS) were also measured after FN coating of the samples (Fig. 1c, "FN-coated", Fig. 2a). As with the previous contact angle series, surface F ($64.2° \pm 1.1°$) was the least hydrophilic with the lowest change in the contact angle after FN coating (Table S2, ESI†). Samples C, D, and E had a contact angle of around 57° (C: $57.2° \pm 2.3°$, D: $57.4° \pm 1.5°$, E: $58.7° \pm 2.1°$, not significant). Unlike surface F, the A ($45.0° \pm 2.0°$) and B ($45.3° \pm 2.0°$) surfaces showed an increase in contact angle with the same result at about 45°. The AFM images, recorded after FN coating, resulted in visible topographic changes and increase in roughness compared with their uncoated counterparts only for the control sample F (Fig. 1d). From the height contrast images, and extracted height profiles of the images, no difference between the plasma treated FN-coated surfaces was visible (Fig. 2). The protein domains and the polymer background were indistinguishable, as was the case with phase AFM imaging (Fig. S4 and S5, ESI†). Through the plasma treatment of the samples, the FN proteins lost their material contrast with the polymer. The untreated surface (sample F) had a noticeable increased roughness after the protein coating, from approximately 0.4 to 3.1 nm, which was due to topographical changes caused by the protein network rather than modifications in the PU layer. This network was partially up to 10 nm high with differently sized pores ranging from 200 nm to 500 nm in diameter.

In order to study protein adsorption kinetics, the adsorption of FN on the oxygen plasma-treated PU surfaces was monitored by RIfS. An exemplary binding curve is depicted in Fig. 3a showing the baseline (with PBS), followed by the association of FN (with the FN solution), starting at the time point 0 s, and the dissociation (rinsing with PBS) of FN from 2000 s to 4000 s. The recorded binding curves (Fig. S2, ESI†) showed a different adsorption behavior of FN on the surfaces. These differences were evaluated by calculating the respective association rate constant k_a and dissociation rate constant k_d using a basic kinetic model (Fig. 3b and c). FN showed on all surfaces small k_d values in the magnitude of 10^{-3} s^{-1}. On surface F, FN exhibited the highest k_d value compared to all other investigated surfaces, indicating an easier desorption of FN from surface F. The calculated k_a values showed faster rates of the forward adsorption process on surface A, E and F in comparison to the surfaces B, C and D. The larger error of the fit of the calculated rate constants on the surfaces A, E and F in respect to the surfaces B, C and D demonstrated a larger discrepancy
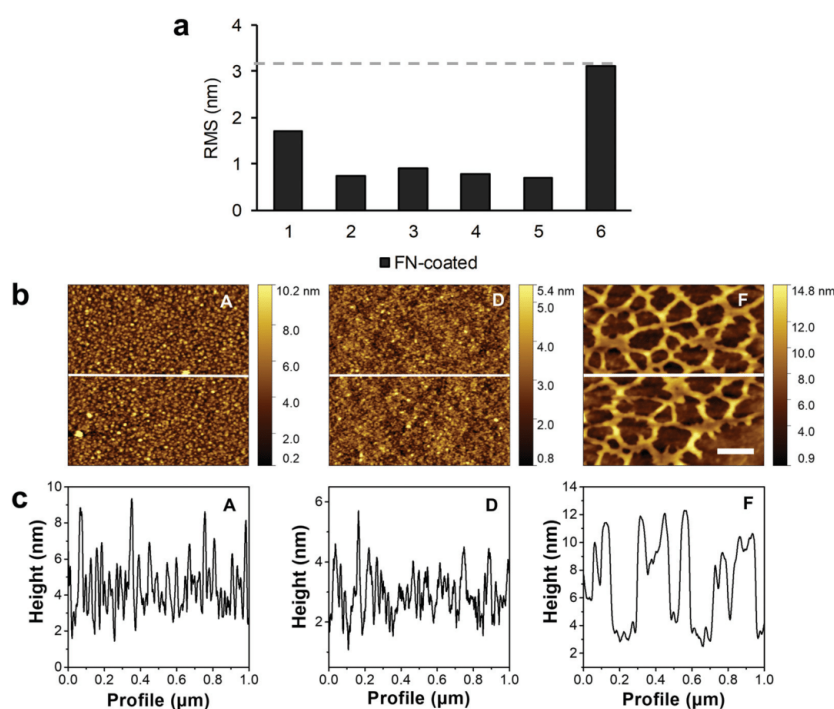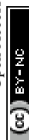

Fig. 2 Qualitative analysis of the polymer surface topography after protein coating. (a) r(RMS) results of the AFM measurements of the sample control and plasma-treated surfaces after FN coating. The dash line represents the highest r(RMS) value of the series. (b) AFM height contrast images of the FN-coated surfaces. The white line shows the profile extraction region. The scale bar equals 200 nm. (c) Extracted line profiles from the AFM images showing the structure of the surface.
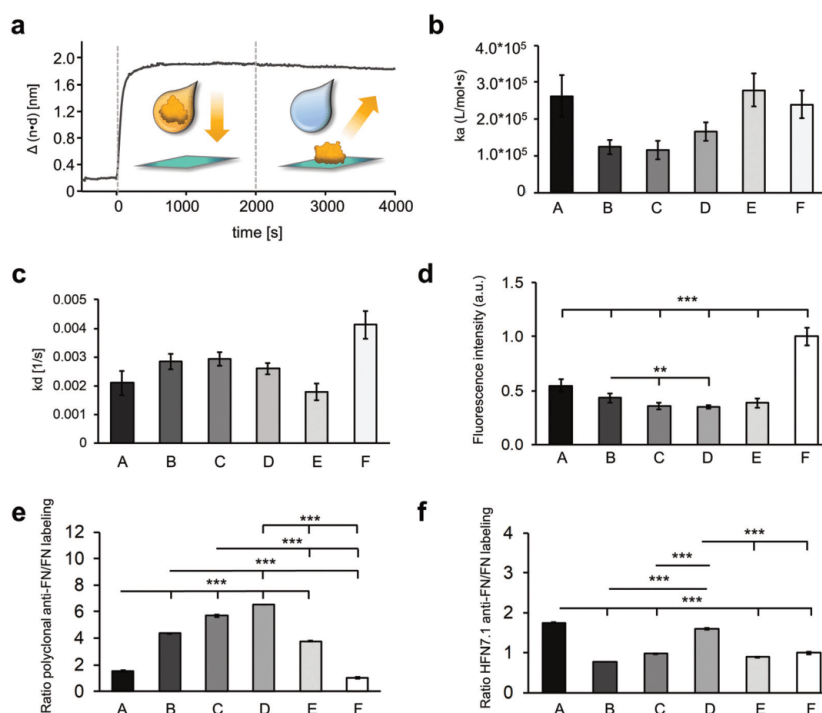
This journal is © The Royal Society of Chemistry 2021

J. Mater. Chem. B, 2021, **9**, 1647–1660 | **1651**

Paper

Fig. 3 The adsorbed fibronectin varies in adsorption kinetics, amount and conformation on different hydrophilic surfaces. (a) Exemplary binding curve of 10 µg ml^{-1} FN on surface F. Association (with the FN solution) of FN starting at time point 0 s and dissociation (with PBS) of FN from 2000 s to 4000 s. Calculated association rate constants (k_a) (b) and calculated dissociation rate constants (k_d) (c) of FN adsorption. Error bars depict the error of the fit. (d) Fluorescence intensity of labeled FN that was coated on the different surfaces. Data is shown relative to surface F. (e) Ratio of the polyclonal anti-FN immunofluorescence staining and the labeled FN. (f) Ratio of the monoclonal anti-FN immunofluorescence staining targeting the cell binding domain and the labeled FN. One-way ANOVA, $n = 3$, **$p < 0.01$, ***$p < 0.001$; RPI = relative pixel intensity.

from the assumed first order kinetic model on the surfaces A, E and F.

The relative amount of the total adsorbed FN on the different plasma-treated samples was determined indirectly by comparing the fluorescence intensity of DY-490 labeled FN after laser excitation (Fig. 3d). As the degree of labeling is consistent throughout the FN molecules, the amount of fluorescence intensity is directly linked to the amount of FN molecules on the surface. While sample F showed the highest fluorescence signal and therefore the highest amount of FN (1.00 ± 0.08), sample A revealed about half of it (0.54 ± 0.06). Samples C, D and E showed the same fluorescence intensity, which was significantly lower than sample A (A *versus* C: 0.36 ± 0.03, $p < 0.001$; A *versus* D: 0.35 ± 0.02, $p < 0.001$; A *versus* E: 0.39 ± 0.04, $p < 0.001$), sample B (B: 0.43 ± 0.04 *versus* C, $p < 0.01$; B *versus* D, $p < 0.01$), and sample F (F *versus* B, $p < 0.001$; F *versus* C, $p < 0.001$; F *versus* D, $p < 0.001$), which indicated fewer FN amounts on these surfaces.

The orientation and conformation of the adsorbed FN was further investigated with IF staining using a polyclonal antibody against the full-length FN (Fig. 3e and Fig. S6a, ESI†).

The ratio of the anti-FN staining to the amount of adsorbed FN, determined by the fluorescence-labeled FN, indicates conformational and orientation changes of the protein. Comparing the polyclonal anti-FN/FN labeling ratios of the different surfaces, a similar result was found on the surfaces C and D. Compared to them, the ratios on the A, B, E and F surfaces were significantly lower (A: 1.54 ± 0.05 *versus* C: 5.68 ± 0.07, A *versus* D: 6.51 ± 0.01, B: 4.35 ± 0.01 *versus* C, B *versus* D, E: 3.77 ± 0.05 *versus* C, E *versus* D, F: 1.00 ± 0.06 *versus* C, F *versus* D, all $p < 0.001$). The FN coating on the A and F surfaces even showed a significantly lower value compared with the B and E surfaces (all $p < 0.001$). Additionally, the adsorbed FN was stained with a monoclonal antibody (Fig. S6b, ESI†), whose epitope maps to a segment between the 9th and 10th type III repeat (HFN7.1), indicating the availability of the cell binding domain.[38] The ratio of the monoclonal antibody to the amount of adsorbed FN showed significantly higher signals on the A and D surfaces compared with the surfaces B, C, E and F (A: 1.74 ± 0.01 *versus* B: 0.77 ± 0.00, A *versus* C: 0.98 ± 0.01, A *versus* E: 0.89 ± 0.01, A *versus* F: 1.00 ± 0.03, D: 1.60 ± 0.02 *versus* B, D *versus* C, D *versus* E, D *versus* F, all $p < 0.001$),

Paper
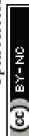
suggesting a more exposed cell binding domain of the FN on these surfaces (Fig. 3f).

3.2 Investigation of the endothelial cell–material–interaction on the FN-coated surfaces

The investigation of the endothelial cell–material–interaction on the different surfaces was of particular interest as it provides information to predict the behavior of the cells depending on surface properties and FN deposition. For this purpose, HUVECs and HMVECs were utilized.

First, the number of adherent HUVECs and HMVECs was investigated 24 hours after seeding showing a rather similar distribution of adherent cells on the different surfaces (Fig. 4a and b). However, on surfaces A and E, significantly less adherent HUVECs and HMVECs were found when compared with the surfaces B and D (HUVECs: A: 0.97 ± 0.01 versus B: 1.16 ± 0.04, $p < 0.01$ and D: 1.15 ± 0.05, $p < 0.05$; E: 0.95 ± 0.10 versus B and D, $p < 0.01$; HMVECs: A: 0.87 ± 0.04 versus B: 1.04 ± 0.05 and D: 1.05 ± 0.07, $p < 0.001$; E: 0.92 ± 0.60 versus B, $p < 0.001$ and D, $p < 0.01$, cell count was normalized to surface F). In addition, the HUVECs showed a significantly increased cell count on surface C compared to surface A and E (C: 1.11 ± 0.13 versus A and E, $p < 0.05$). For the HUVECs, but not for the HMVECs, significantly fewer adherent cells were found on surface F compared to surfaces B and D (F: 1.00 ± 0.09 versus B and D, $p < 0.05$). Both cell types showed no significant differences in the number of adherent cells between the B, C and D surfaces, and between the A and E samples.

The different surfaces did not appear to influence the size of the two cell types, although the HUVECs tended to be smaller on the surfaces B and C compared to the other samples, and larger on surfaces C, D and E (Fig. S7, ESI†).

The interaction of HUVECs and HMVECs with the pre-adsorbed FN layer led to a FN reorganization, which was demonstrated by anti-FN IF staining (Fig. 5a and Fig. S8, ESI†). Both cell types showed fibrillar structures on the A surface in the area of the cells (Fig. 5a, white arrow). In addition, FN reorganization appeared on all surfaces as dark areas around the cells, most notably in the C and D samples (Fig. 5a, white dotted arrow).

The cytoskeleton was examined by using F-actin staining, as its distribution provides information about the barrier function of an endothelial cell.[39] A distinct reorganization of the F-actin was observed on the different surfaces (Fig. 5 and Fig. S9, ESI†). For both cell types, peripheral ventral stress fibers were found on the A and F surfaces with more prominent F-actin bundles on the A surface (Fig. 5b). In contrast, in the cells on the samples B, C, D and E, the stress fibers were distributed over the entire cell. A semi-quantitative analysis of the F-actin-stained areas revealed a significantly lower amount of stress fibers in the cells cultured on the A surfaces compared with cells grown on surfaces B, D and E for both cell types (HUVECs: A: 0.71 ± 0.06 versus B: 1.39 ± 0.31, D: 1.35 ± 0.19 and E: 1.50 ± 0.50, $p < 0.05$; HMVECs: A: 0.60 ± 0.12 versus B: 1.23 ± 0.12, D: 1.25 ± 0.15 and E: 1.36 ± 0.13, $p < 0.05$). In addition, the HMVECs showed a significantly lower signal on surface A compared with surface C (A versus C: 1.10 ± 0.30, $p < 0.05$; Fig. 5c).

The integrin–mediated cell adhesion is associated with the formation of focal adhesions.[40] Vinculin, a scaffolding protein that is involved in the mechanical regulation of focal adhesions, was studied by statistically analyzing the number of vinculin foci per cell (Fig. 6).[41] Both cell types showed a significantly higher number of vinculin foci per cells on surface A compared with the other surfaces (HUVECs: A: 113 ± 40 versus B: 46 ± 16, $p < 0.01$; A versus C: 57 ± 41, D: 51 ± 10, E: 56 ± 7 and F: 53 ± 16, $p < 0.05$; HMVECs: A: 51 ± 21 versus B: 26 ± 9 and E: 27 ± 11, $p < 0.05$; A versus C: 19 ± 4 and D: 21 ± 5, $p < 0.01$), with the exception of surface F (49 ± 8) where a similar number of vinculin foci were counted in the HMVECs (Fig. 6a and b). For both cell types, the average number of foci per cell was similar for surfaces B, C, D and E.

Furthermore, the FAK, which plays a critical role in integrin–mediated signal transduction, was examined (Fig. 6).[42] For the HUVECs, the number of FAK foci per cell tended to be higher on the very hydrophilic surfaces (A: 40 ± 10, B: 32 ± 18 and C: 54 ± 35) than on the less hydrophilic surfaces (D: 25 ± 10, E: 27 ± 5 and F: 20 ± 7). Due to a high variation within the experiments, statistically significant more FAK foci per cells were only found on the C surface compared with the surface F (C: 54 ± 35 versus F: 20 ± 7, $p < 0.05$) (Fig. 6c and d). The HMVECs showed a slightly different behavior. They inclined to
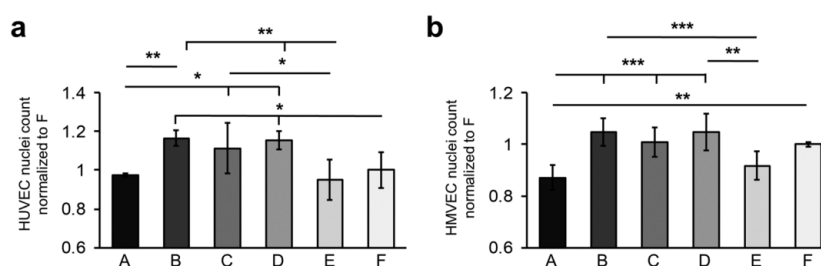

Fig. 4 Fibronectin coating on different hydrophilic surfaces impacts the number of adherent cells. The number of adherent (a) HUVECs and (b) HMVECs 24 h after cell seeding. Data is shown as change relative to F. One-way ANOVA, $n = 3$, $*p < 0.05$, $**p < 0.01$, $***p < 0.001$.

This journal is © The Royal Society of Chemistry 2021
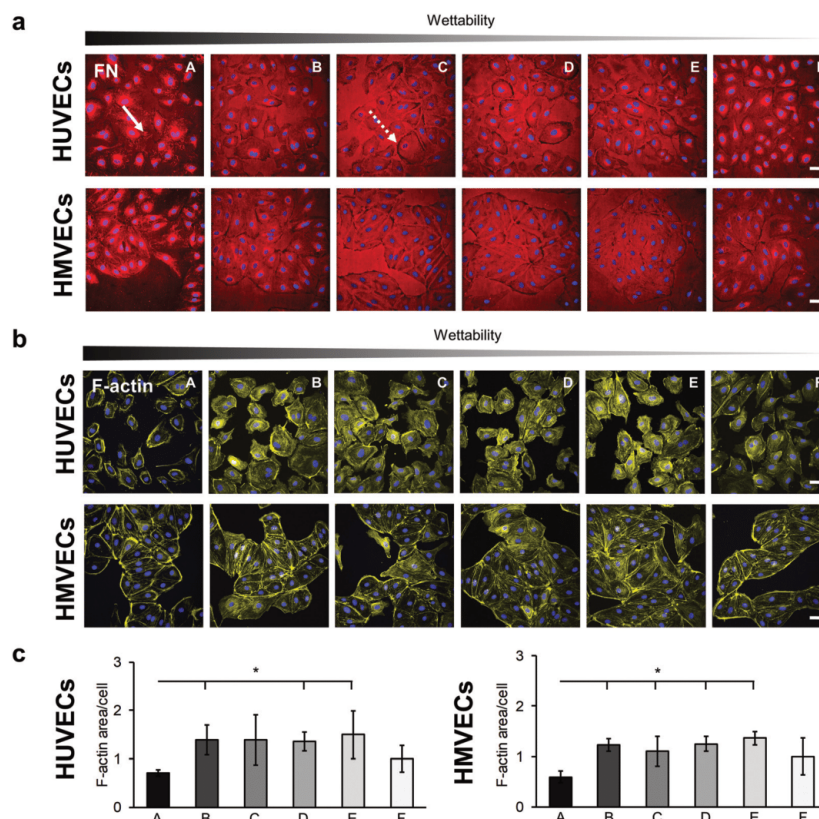
J. Mater. Chem. B, 2021, **9**, 1647–1660 | **1653**

Fig. 5 Cell–fibronectin-interaction and F-actin reorganization in HUVECs and HMVECs. (a) Anti-FN immunofluorescence staining shows the interaction of HUVECs and HMVECs with the adsorbed FN, which is indicated by fibrillar structures (white arrow) and dark areas (white dotted arrow). Scale bars equal 100 μm. (b) Peripheral F-actin bundles are formed in HUVECs and HMVECs that are seeded on A and F surfaces. Scale bars equal 100 μm. (c) Semi-quantitative area analysis of F-actin distribution in HUVECs and HMVECs. Data is shown relative to F. One-way ANOVA, $n = 3$, $*p < 0.05$.

form less FAK foci on the very hydrophilic surfaces compared with moderately hydrophilic surfaces. In detail, on surface B, significantly fewer FAK foci per cell were found compared to surfaces C and D (B: 12 ± 12 versus C: 42 ± 18 and D: 47 ± 24, $p < 0.05$). Both cell types tended to form few FAK foci on the F surface; however, in the case of HMVECs the number of FAK foci per cell was significantly lower compared to surface D (D: 47 ± 24 versus F: 17 ± 4, $p < 0.05$).

Cell–cell interactions were investigated by studying the expression of the endothelial cell type-specific markers VE-cadherin and PECAM-1 (Fig. 7). Both proteins are located on the surface of endothelial cells and account for a large portion of the endothelial cell–to–cell junctions that contribute to the maintenance of the endothelial permeability barrier.[43] Expression levels were evaluated by the IF-stained area per cell (Fig. 7b and d). The VE-cadherin staining showed similar expression levels for the HUVECs on all surfaces. Significant differences were found for the HMVECs (Fig. 7b and Fig. S10, ESI†). In detail, a higher VE-cadherin signal was detected on the A

surface compared with surfaces B and F (A: 1.59 ± 0.24 versus B: 1.02 ± 0.38 and F: 1.00 ± 0.39, $p < 0.05$). In addition, the cells on the C surface revealed a higher expression level compared with the B, D, E and F surfaces (C: 1.78 ± 0.52 versus D: 1.21 ± 0.28 and E: 1.30 ± 0.34, $p < 0.05$ and versus B and F, $p < 0.01$).

The PECAM-1 expression was the same for the HMVECs on all samples (Fig. 7c and d). For the HUVECs, less PECAM-1 was expressed in the cells on surface B compared with surface A. Interestingly, the HUVECs on surface B showed also a significantly lower expression of the endothelial cell marker von Willebrand factor (vWF) when compared with cells grown on surfaces D and F (B: 0.43 ± 0.12 versus D: 0.89 ± 0.26 and versus F: 1.00 ± 0.57, $p < 0.05$; Fig. 8).

4. Discussion

In the present study, oxygen plasma surface treatment was used to incorporate hydroxyl, carbonyl, carboxyl and other oxygen-rich
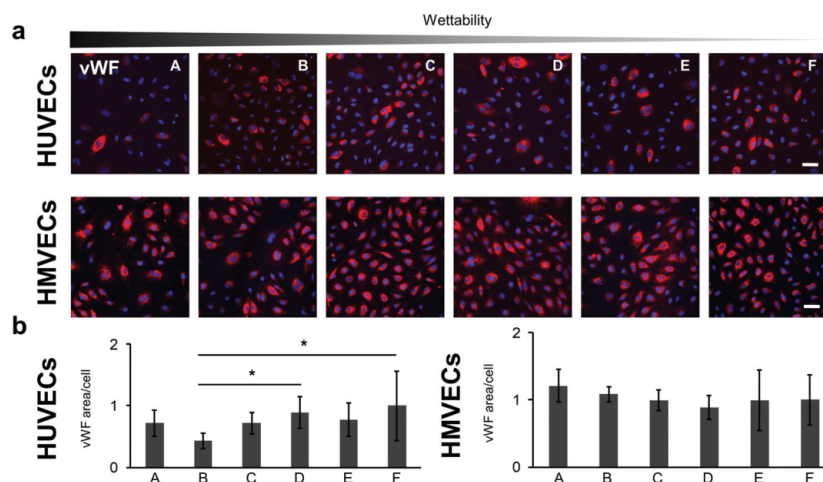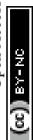
Paper

Fig. 6 The formation of focal adhesion complexes influenced by fibronectin coating on different hydrophilic surfaces. (a) Anti-vinculin immunofluorescence-stained HUVECs and HMVECs on the FN-coated surfaces. Vinculin foci are indicated by white arrows. Scale bars equal 100 μm. (b) Semi-quantitative analysis of the anti-vinculin staining for HUVECs (left) and HMVECs (right). Data is shown relative to surface F. (c) FAK-stained HUVECs and HMVECs seeded on the different hydrophilic FN-coated surfaces. FAK foci are indicated by white arrows. Scale bars equal 100 μm. (d) Semi-quantitative analysis of the anti-FAK staining for HUVECs (left) and HMVECs (right). Data is shown relative to surface F. One-way ANOVA, $n = 3$, $*p < 0.05$, $**p < 0.01$.

groups onto PU surfaces in order to modify the polarity and chemical structure of the surface.[44–49] During the plasma treatment, removal of material from the surface layer through plasma etching processes with UV irradiation and ion bombardment resulted in topographical changes.[27,44,47] The impact of the plasma modification on the different surfaces was evaluated using AFM imaging, XPS analysis and contact angle measurements. The XPS and contact angle results showed that higher oxidized functional groups were incorporated with low oxygen pressure treatments, which led to a greater impact on PU surface hydrophilicity.[25] From the contact angle measurements, specifically the low standard deviations of the samples, it can be concluded that the plasma treatment of the polymer surfaces had a high reproducibility. AFM measurements showed that an increased surface roughness contributed to lowering the contact angle, demonstrating a more hydrophilic surface.[50] Especially with surface A, which has a similar chemical composition to surface B, the higher wettability can be attributed to surface roughness effects. This roughening of the sample topography was caused by the ablative nature of the oxygen plasma, which had a larger effect during the longer plasma treatment of sample A under low oxygen pressure conditions. FN-coated plasma-treated samples were difficult to distinguish using AFM topographic imaging; however, contact angle analysis showed differences between the plasma-treated samples. Only on the FN-coated control surface F, AFM images showed a fibrillar network that may be attributed to material-driven fibrillogenesis where FN molecules unfold and bind to each other.[1,19,51]

RIfS was employed to investigate the conformation and orientation of FN on the samples. Here, the kinetic inspection of the binding curves revealed different rate constants for the chemical forward and reverse process, indicating different interaction sites on the reactants. Surface A and B had a similar chemical composition; however, there was a pronounced difference in the calculated k_a on these surfaces, which could be attributed to the changed surface roughness and different reaction sites on the adsorbed FN. In contrast, the increase of k_a from surface B to E was induced by the changes in the chemical composition of the surfaces and the corresponding different reaction sites on FN. In our study, we identified the lowest k_a values for the surfaces B, C and D, and larger k_a values for the more hydrophilic surface A as well as for the more hydrophobic surfaces E and F. This may be explained by the different influences of surface chemistry and surface roughness of the investigated PU surfaces on FN adsorption. A higher flexibility of FN on surface F in comparison to the other surfaces was found by a large k_a value and a coincidental large k_d value. Although FN appeared in a very stable fibrillary form on surface F, it exhibited a more dynamic interaction towards the surface. The oversimplification of the actual processes at the surface by the applied kinetic model is reflected in the calculated error accompanying the results.[52] The error was particularly large on surface A, E and F, indicating that the discrepancy from the Langmuir adsorption model was pronounced on these surfaces. On surface F, the lateral interactions between the adsorbed proteins in the network demonstrated by the AFM measurements (Fig. 1 and 2) can cause the discrepancy from the adsorption model. It is also very plausible that FN underwent greater conformational changes on surfaces A, E and F during adsorption when compared with surfaces B, C

This journal is © The Royal Society of Chemistry 2021

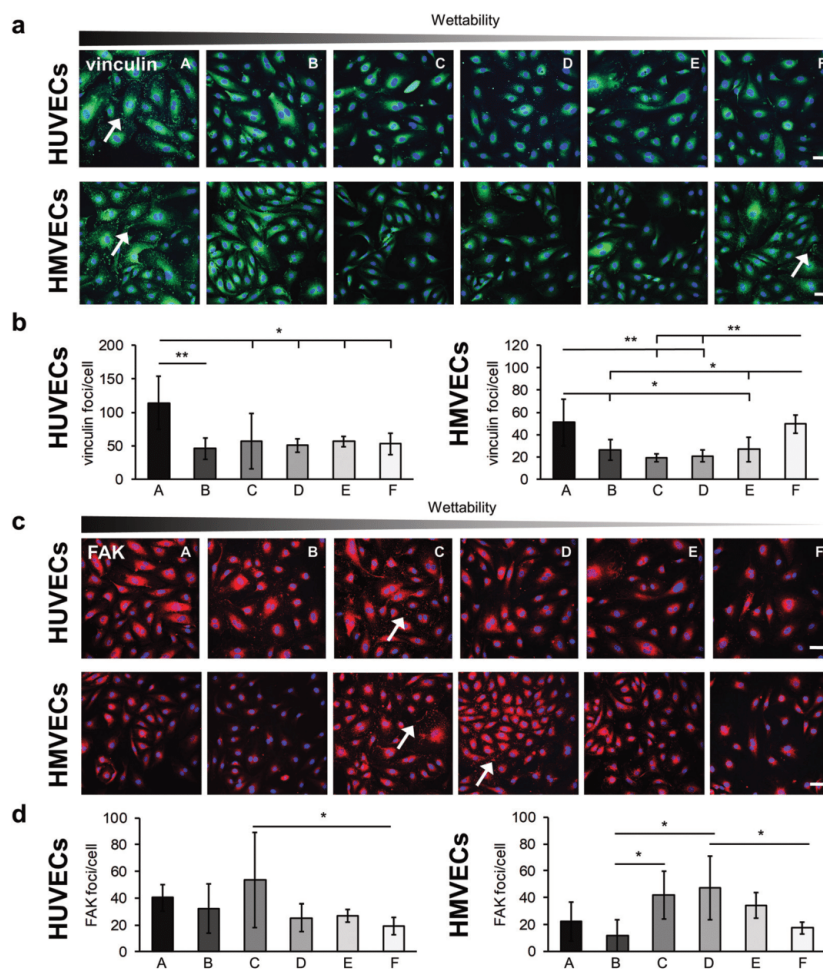*J. Mater. Chem. B*, 2021, **9**, 1647–1660 | **1655**

Fig. 7 Endothelial cell–to–cell junction variation on the different fibronectin-coated surfaces for both HUVECs and HMVECs. (a) VE-cadherin immunofluorescence staining of HUVECs (upper row) and HMVECs (lower row) on the different hydrophilic surfaces coated with FN. Scale bars equal 100 μm. (b) Semi-quantitative analysis of the anti-VE-cadherin-stained area for HUVECs (left) and HMVECs (right). Data is shown relative to surface F. (c) PECAM-1 immunofluorescence staining of HUVECs and HMVECs on the FN-coated surfaces. Scale bars equal 100 μm. (d) Semi-quantitative analysis of the anti-PECAM-1-stained area for HUVECs (left) and HMVECs (right). Data is shown relative to surface F. One-way ANOVA, $n = 3$, $*p < 0.05$, $**p < 0.01$.

and D. To test this hypothesis, the adsorption of FN was further examined with fluorescence-labeled FN as well as with polyclonal and monoclonal antibody IF staining.

The total amount of adsorbed FN was determined with fluorescence-labeled FN. Here, the measured fluorescence intensity of the covalently labeled FN is directly proportional to the amount of adsorbed FN. This is, because the fluorescence DY-490 FN labeling took place prior to the adsorption. Compared to the antibody staining, the fluorescence signal is not affected by the protein adsorption and the associated changes in protein conformation and orientation. As we had a mean number of 2.6 dye molecules per FN, we do not expect

that our labeling impaired the function and adsorption behavior of FN. A study by Hoffmann et al. analyzed the influence of FITC (a dye that is chemically related to DY-490) when covalently binding it to FN. For three dye molecules per FN, they could not detect significant modifications to the structure and biological function compared with unlabeled FN.[53] Especially for surface A and F, the amount of coated FN was significantly higher when compared with the other surfaces. While for surface A the surface roughness probably allowed an increased FN adsorption, the amount of adsorbed FN on surface F was influenced by the material-driven FN fibrillogenesis, where the FN molecules were probably adsorbed in several layers.[54,55]

Journal of Materials Chemistry B

Paper
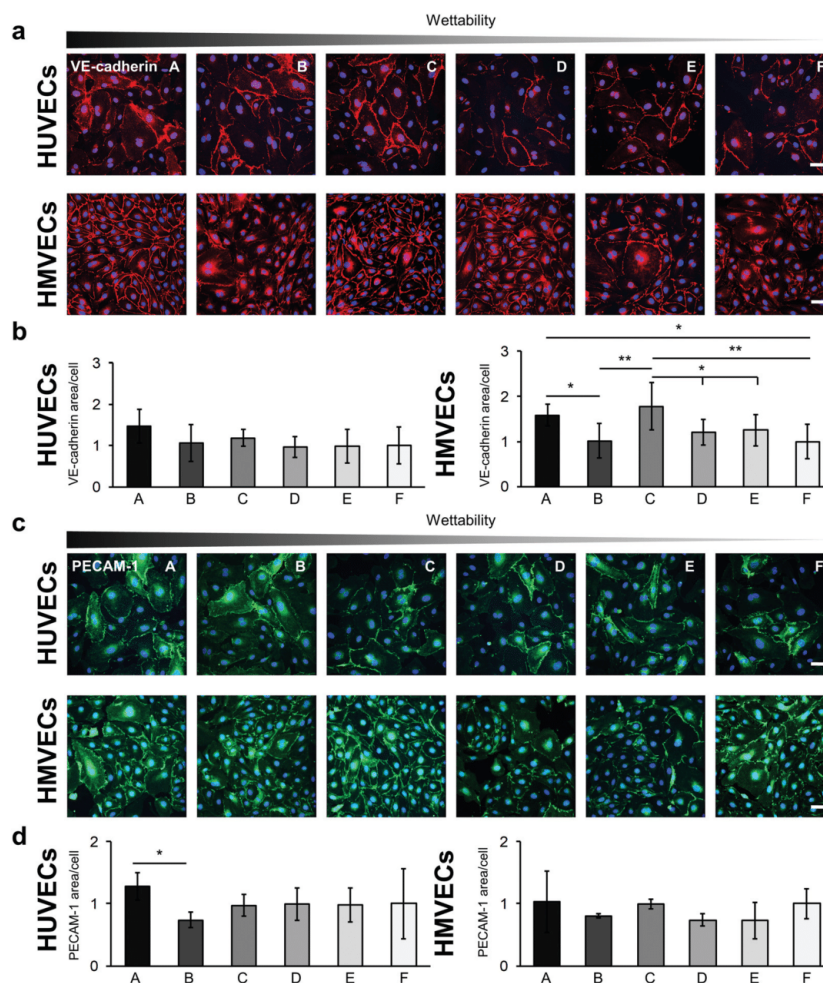
Fig. 8 von Willebrand factor (vWF) expression in HUVECs and HMVECs cultured on the FN-coated surfaces. (a) Anti-vWF immunofluorescence staining of HUVECs and HMVECs. The scale bar equals 100 μm. (b) Semi-quantitative analysis of the anti-vWF-stained cells. Data is shown relative to surface F. One-way ANOVA, $n = 3$, $*p < 0.05$.

The ratio of the amount of bound monoclonal and polyclonal anti-FN antibodies to the total amount of adsorbed fluorescence-labeled FN provides information about the conformation and orientation of the adsorbed protein. In our study, the individual surfaces showed different ratios, which indicates a varying adsorption behavior of FN on the surfaces (Fig. 3e and f). Since the polyclonal antibody binds to many different epitopes of FN, we hypothesize that the lower the antibody signal, the more the conformation of the protein is altered and thus fewer epitopes are present or accessible to the antibody. Interestingly, there seems to be a reciprocal correlation between the results of the polyclonal antibody staining and the k_a values of the RIfS measurements (Fig. 3). Since the k_a

value indirectly indicates the strength of the interaction between protein and surface, a greater conformational change can be assumed with stronger FN-material interaction.[56] Thus, the results of the polyclonal antibody support the observations of the RIfS measurements, which indicates a slight conformational change of the FN on the surfaces B, C and D, and a stronger FN unfolding and expansion on the surfaces E and F. This observation is consistent with the results of several studies that have described more drastic conformational changes on more hydrophobic surfaces.[14,57] Interestingly, despite their hydrophilic properties, conformational changes of the protein also occurred on the surface A. We assume that the surface roughness caused by oxygen plasma treatment influenced the

This journal is © The Royal Society of Chemistry 2021

J. Mater. Chem. B, 2021, **9**, 1647–1660 | **1657**

133

conformational change of the protein. Several studies have already described that surface roughness can lead to a widespread and rigid protein conformation.[13,58]

An additional indication of the conformational change of the adsorbed FN was provided by the results of the monoclonal HFN7.1 antibody, which binds near the cell binding domain consisting of the PHSRN and RGD integrin binding sites.[33] In literature, an increased HFN7.1 antibody binding to unfolded FN has been described.[14,59] In our study, especially samples A and D showed a high level of accessible cell binding domain indicating an extended FN conformation. However, our data suggest that the accessibility of the cell-binding-domain is not necessary and is solely associated with the conformational change, but also with the orientation of the protein. The FN adsorbed on surface D suggested only small conformational changes, but nevertheless showed a high availability of the cell binding domain. In contrast, the data for surface F indicates a more unfolded adsorbed protein, but with a low-exposed cell binding domain (Fig. 3b, e and f). From this we can conclude that depending on the surface properties, the adsorbed FN can take a more or less favorable conformation and orientation with respect to the accessibility of the cell binding domain, which ultimately influences its bioactivity. Since the surface chemistry and roughness of the surfaces C, D and E are similar, the difference in FN adsorption behavior on sample D could not be explained from the gathered information. Protein adsorption onto biomaterial surfaces is affected by many additional factors such as the stiffness, which have not been investigated.[60] Methods such as fluorescence resonance energy transfer could be helpful to obtain further details about the conformation of the adsorbed FN.

Bridging these results to later applications, the key question of how these differences influence cell behavior was studied. For both HUVECs and HMVECs we found the same trend of differences in the number of adherent cells on the different surfaces. It should be noted that the cells were examined 24 hours after seeding. Thus, the cell count is not only determined by the number of initially attached cells but also by cell proliferation. Interestingly, our results show that the number of adherent cells does neither correlate with the amount of the exposed FN cell binding side nor with the wettability or polarity of the underlying surface. Rather, a correlation between the k_a value of the RIfS measurements and the cell count is observed (Fig. 3 and 4). We hypothesize that due to the stronger interaction with the surface and the resulting conformational change of the FN, certain domains are exposed, which influence the cell cycle. In the literature it is described that binding to the first type III repeat or the heparin binding site of FN inhibits endothelial cell growth.[61,62] It is also possible that a phenomenon described by Podestá et al. took place.[63] In their study, the authors observed a decreased endothelial cell proliferation due to a reorganization of the cytoskeleton into actin filament bundles, which was induced by an increased density of focal contacts. Reduced cell growth associated with cytoskeletal reorganization may also be related to the CaMKK2/AMPK signaling pathway. It is described that

the activation of AMPK leads to the maturation of contractile actomyosin bundles and causes cell cycle arrest.[64–66] In our study, a reduced cell number was observed for both cell types on surfaces A and F, accompanied by the formation of actin bundles and an increased density of vinculin foci. This cytoskeletal organization indicates a resting endothelium, while stress fibers, as observed on surfaces B, C, D and E, occur when the endothelium is activated, a condition associated with cell proliferation and migration.[67]

During cell–FN interaction, which is mainly mediated by the integrins $\alpha5\beta1$ and $\alpha v\beta3$, focal adhesions are formed.[68] On surfaces A and F, we think that the more unfolded conformation of FN, associated with an increased presentation of the cell binding side, facilitates the formation of mature focal adhesions composed of vinculin and $\alpha v\beta3$.[69–71] In addition, a stronger FN–material interaction, as found on surface A, causes proper transmission of force through the actin cytoskeleton, allowing the maturation of vinculin-associated focal adhesions.[72]
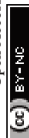
Probably due to the stronger adhesion of the FN to the surface A, the cells can also form FN fibrils and develop actin bundles.[67] It should be noted that the increased surface roughness of sample A to the other plasma treated samples can also influence the cell behavior.[73]

The more compact form of the FN molecule, which is assumed to be found on surfaces B, C and D, is only available for binding to $\alpha5\beta1$ and not to $\alpha v\beta3$.[74] Interestingly, higher levels of FAK foci, which are linked to integrin $\beta1$, were usually found on these surfaces.[75] The higher cell count and pronounced stress fibers in the cells on these surfaces can be attributed to FAK, as it enhances cell proliferation and cell motility by stimulating the formation of actin stress fibers and promoting the turnover of integrin-based adhesions.[76–78] In addition, the potentially weaker FN-material interaction on these surfaces hinder the cells to form vinculin-rich mature focal adhesions. Instead, when the cells exert a traction force on the FN, they detach it from the surface, which is indicated by the dark areas on the anti-FN-stained surfaces[79] (Fig. 4).

In our study, the expression of the endothelial cell markers vWF, VE-cadherin, and PECAM-1 was confirmed for both cell types. With regard to the formation of a functional endothelium on the FN-coated surfaces, the cell-to-cell junctions that establish the endothelial permeability barrier play an important role.[43] The slightly increased VE-cadherin and PECAM-1 expression in both cell types on surface A and for the HMVECs on surface C may indicate a more advanced formation of a functional endothelium compared to the other samples.

5. Conclusion

In our study, we showed that oxygen plasma treatment of PU surfaces through minor parameter changes induced large variations in the affinity, conformation and orientation of adsorbed FN, which in turn, significantly influenced the endothelial cell–material and cell–cell interactions. Due to the many simultaneous effects of plasma treatment on the surface

1658 | J. Mater. Chem. B, 2021, **9**, 1647–1660

This journal is © The Royal Society of Chemistry 2021

Paper

through the introduction of a variety of functional groups and changes in surface topography, a direct link between a single parameter to the bioactivity of adsorbed FN or on the cell behavior could not be established; however, it was demonstrated that oxygen plasma treatment is a reliable, fast and reproducible technique with a high application potential in the adjustment of FN bioactivity and subsequent endothelial cell response.

Source of funding

Conflicts of interest

None.

Acknowledgements

References

1 V. Llopis-Hernández, P. Rico, J. Ballester-Beltrán, D. Moratal and M. Salmerón-Sánchez, *PLoS One*, 2011, **6**, e19610.

2 J. M. Seeger and N. Klingman, *J. Vasc. Surg.*, 1988, **8**, 476–482.

3 W. S. Choi, Y. K. Joung, Y. Lee, J. W. Bae, H. K. Park, Y. H. Park, J.-C. Park and K. D. Park, *ACS Appl. Mater. Interfaces*, 2016, **8**, 4336–4346.

4 R. Daum, D. Visser, C. Wild, L. Kutuzova, M. Schneider, G. Lorenz, M. Weiss, S. Hinderer, U. A. Stock, M. Seifert and K. Schenke-Layland, *Cells*, 2020, **9**, 778.

5 J. Zhu and R. A. F. Clark, *J. Invest. Dermatol.*, 2014, **134**, 895–901.

6 B. Geiger, A. Bershadsky, R. Pankov and K. M. Yamada, *Nat. Rev. Mol. Cell Biol.*, 2001, **2**, 793–805.

7 T. P. Ugarova, C. Zamarron, Y. Veklich, R. D. Bowditch, M. H. Ginsberg, J. W. Weisel and E. F. Plow, *Biochemistry*, 1995, **34**, 4457–4466.

8 R. Mezzenga and M. Mitsi, *Biomacromolecules*, 2019, **20**, 55–72.

9 R. Pankov and K. M. Yamada, *J. Cell Sci.*, 2002, **115**, 3861–3863.

10 W. S. To and K. S. Midwood, *Fibrog. Tissue Repair*, 2011, **4**, 21.

11 M. Cantini, P. Rico, D. Moratal and M. Salmerón-Sánchez, *Soft Matter*, 2012, **8**, 5575–5584.

12 P. Thevenot, W. Hu and L. Tang, *Curr. Top. Med. Chem.*, 2008, **8**, 270–280.

13 M. B. Hovgaard, K. Rechendorff, J. Chevallier, M. Foss and F. Besenbacher, *J. Phys. Chem. B*, 2008, **112**, 8241–8249.

14 A. J. García, M. D. Vega and D. Boettiger, *Mol. Biol. Cell*, 1999, **10**, 785–798.

15 B. G. Keselowsky, D. M. Collard and A. J. García, *J. Biomed. Mater. Res., Part A*, 2003, **66**, 247–259.

16 A. J. Campillo-Fernández, R. E. Unger, K. Peters, S. Halstenberg, M. Santos, M. S. Sánchez, J. M. M. Dueñas, M. M. Pradas, J. L. G. Ribelles and C. J. Kirkpatrick, *Tissue Eng., Part A*, 2009, **15**, 1331–1341.

17 F. A. Vanterpool, M. Cantini, F. P. Seib and M. Salmerón-Sánchez, *BioRes. Open Access*, 2014, **3**, 286–296.

18 E. Grigoriou, M. Cantini, M. J. Dalby, A. Petersen and M. Salmeron-Sanchez, *Biomater. Sci.*, 2017, **5**, 1326–1333.

19 V. Llopis-Hernández, M. Cantini, C. González-García, Z. A. Cheng, J. Yang, P. M. Tsimbouri, A. J. García, M. J. Dalby and M. Salmerón-Sánchez, *Sci. Adv.*, 2016, **2**, E1600188.

20 C. González-García, M. Cantini, J. Ballester-Beltrán, G. Altankov and M. Salmerón-Sánchez, *Acta Biomater.*, 2018, **77**, 74–84.

21 K. M. Yamada and D. W. Kennedy, *J. Cell Biol.*, 1984, **99**, 29–36.

22 M. D. Pierschbacher, E. G. Hayman and E. Ruoslahti, *J. Cell. Biochem.*, 1985, **28**, 115–126.

23 S. I. Aota, M. Nomizu and K. M. Yamada, *J. Biol. Chem.*, 1994, **269**, 24756–24761.

24 P. Singh, C. Carraher and J. E. Schwarzbauer, *Annu. Rev. Cell Dev. Biol.*, 2010, **26**, 397–419.

25 I. Mrsic, T. Bäuerle, S. Ulitzsch, G. Lorenz, K. Rebner, A. Kandelbauer and T. Chassé, *Appl. Surf. Sci.*, 2021, **536**, 147782.

26 P. Alves, S. Pinto, H. C. de Sousa and M. H. Gil, *J. Appl. Polym. Sci.*, 2011, **122**, 2302–2308.

27 O. Mrad, J. Saunier, C. Aymes-Chodur, V. Rosilio, S. Bouttier, F. Agnely, P. Aubert, J. Vigneron, A. Etcheberry and N. Yagoubi, *Microscopy and Microanalysis*, Cambridge University Press, 2010, vol. 16, pp. 764–778.

28 M. Griffin, R. Palgrave, V. G. Baldovino-Medrano, P. E. Butler and D. M. Kalaskar, *Int. J. Nanomed.*, 2018, **13**, 6123–6141.

29 R. Hesse, T. Chassé, P. Streubel and R. Szargan, *Surf. Interface Anal.*, 2004, **36**, 1373–1383.

30 D. Nečas and P. Klapetek, *Cent. Eur. J. Phys.*, 2012, **10**, 181–188.

31 G. Kraus and G. Gauglitz, *Fresenius' J. Anal. Chem.*, 1994, **349**, 399–402.

32 D. J. O'Shannessy, M. Brigham-Burke, K. Karl Soneson, P. Hensley and I. Brooks, *Anal. Biochem.*, 1993, **212**, 457–468.

33 R. Bowditch, C. Halloran, S. Aota, M. Obara, E. Plow, K. Yamada and M. Ginsberg, *J. Biol. Chem.*, 1991, **266**, 23323–23328.

34 E. Brauchle, J. Kasper, R. Daum, N. Schierbaum, C. Falch, A. Kirschniak, T. E. Schäffer and K. Schenke-Layland, *Matrix Biol.*, 2018, **68–69**, 180–193.

35 J. Pusch, M. Votteler, S. Göhler, J. Engl, M. Hampel, H. Walles and K. Schenke-Layland, *Biomaterials*, 2011, **32**, 7469–7478.

36 A. Zbinden, M. Urbanczyk, S. L. Layland, L. Becker, J. Marzi, M. Bosch, P. Loskill, G. P. Duffy and K. Schenke-Layland, *Tissue Eng., Part A*, DOI: 10.1089/ten.tea.2020.0250.

37 J. Schindelin, I. Arganda-Carreras, E. Frise, V. Kaynig, M. Longair, T. Pietzsch, S. Preibisch, C. Rueden, S. Saalfeld, B. Schmid, J. Y. Tinevez, D. J. White, V. Hartenstein, K. Eliceiri, P. Tomancak and A. Cardona, *Nat. Methods*, 2012, **9**, 676–682.

38 J. Ballester-Beltrán, P. Rico, D. Moratal, W. Song, J. F. Mano and M. Salmerón-Sánchez, *Soft Matter*, 2011, **7**, 10803–10811.

39 N. V. Bogatcheva and A. D. Verin, *Microvasc. Res.*, 2008, **76**, 202–207.

40 C. Wu, *Cell Adhes. Migr.*, 2007, **1**, 13–18.

41 E. Spanjaard and J. De Rooij, *Curr. Biol.*, 2013, 23.

42 X. Zhao and J. L. Guan, *Adv. Drug Delivery Rev.*, 2011, **63**, 610–615.

43 M. G. Lampugnani, *Cold Spring Harbor Perspect. Med.*, 2012, **2**, a006528.

44 J. Friedrich, *The Plasma Chemistry of Polymer Surfaces*, Wiley-VCH Verlag GmbH & Co. KGaA, Weinheim, Germany, 2012.

45 B. Mutel, M. Bigan and H. Vezin, *Appl. Surf. Sci.*, 2004, **239**, 25–35.

46 L. Yang, J. Chen, Y. Guo and Z. Zhang, *Appl. Surf. Sci.*, 2009, **255**, 4446–4451.

47 F. Arefi-Khonsari, M. Tatoulian, F. Bretagnol, O. Bouloussa and F. Rondelez, *Surf. Coatings Technol.*, 2005, **200**, 14–20.

48 J. Lai, B. Sunderland, J. Xue, S. Yan, W. Zhao, M. Folkard, B. D. Michael and Y. Wang, *Appl. Surf. Sci.*, 2006, **252**, 3375–3379.

49 N. Inagaki, K. Narushim, N. Tuchida and K. Miyazaki, *J. Polym. Sci., Part B: Polym. Phys.*, 2004, **42**, 3727–3740.

50 R. N. Wenzel, *J. Phys. Colloid Chem.*, 1949, **53**, 1466–1467.

51 M. Salmerón-Sánchez, P. Rico, D. Moratal, T. T. Lee, J. E. Schwarzbauer and A. J. García, *Biomaterials*, 2011, **32**, 2099–2105.

52 R. A. Latour, *J. Biomed. Mater. Res., Part A*, 2015, **103**, 949–958.

53 C. Hoffmann, J. Leroy-Dudal, S. Patel, O. Gallet and E. Pauthe, *Anal. Biochem.*, 2008, **372**, 62–71.

54 D. Khang, S. Y. Kim, P. Liu-Snyder, G. T. R. Palmore, S. M. Durbin and T. J. Webster, *Biomaterials*, 2007, **28**, 4756–4768.

55 Y. Zhang, C. Chai, X. S. Jiang, S. H. Teoh and K. W. Leong, *Mater. Sci. Eng., C*, 2007, **27**, 213–219.

56 P. Roach, D. Farrar and C. C. Perry, *J. Am. Chem. Soc.*, 2005, **127**, 8168–8173.

57 V. Vadillo-Rodríguez, M. A. Pacha-Olivenza, M. L. Gónzalez-Martín, J. M. Bruque and A. M. Gallardo-Moreno, *J. Biomed. Mater. Res., Part A*, 2013, **101A**, 1397–1404.

58 M. S. Lord, B. G. Cousins, P. J. Doherty, J. M. Whitelock, A. Simmons, R. L. Williams and B. K. Milthorpe, *Biomaterials*, 2006, **27**, 4856–4862.

59 D. Gagné, Y. D. Benoit, J. F. Groulx, P. H. Vachon and J. F. Beaulieu, *BMC Mol. Cell Biol.*, 2020, **21**, 14.

60 N. B. Guerra, C. González-García, V. Llopis, J. C. Rodríguez-Hernández, D. Moratal, P. Rico and M. Salmerón-Sánchez, *Soft Matter*, 2010, **6**, 4748–4755.

61 A. Ambesi, R. M. Klein, K. M. Pumiglia and P. J. McKeown-Longo, *Cancer Res.*, 2005, **65**, 148–156.

62 G. A. Homandberg, J. Kramer-Bjerke, D. Grant, G. Christianson and R. Eisenstein, *Biochim. Biophys. Acta, Protein Struct. Mol. Enzymol.*, 1986, **874**, 61–71.

63 F. Podestá, T. Roth, F. Ferrara, E. Cagliero and M. Lorenzi, *Diabetologia*, 1997, **40**, 879–886.

64 L. Miranda, S. Carpentier, A. Platek, N. Hussain, M. A. Gueuning, D. Vertommen, Y. Ozkan, B. Sid, L. Hue, P. J. Courtoy, M. H. Rider and S. Horman, *Biochem. Biophys. Res. Commun.*, 2010, **396**, 656–661.

65 S. Fogarty, F. A. Ross, D. V. Ciruelos, A. Gray, G. J. Gowans and D. G. Hardie, *Mol. Cancer Res.*, 2016, **14**, 683–695.

66 S. Tojkander, K. Ciuba and P. Lappalainen, *Cell Rep.*, 2018, **24**, 11–19.

67 H. Schnittler, M. Taha, M. O. Schnittler, A. A. Taha, N. Lindemann and J. Seebach, *Cell Tissue Res.*, 2014, **355**, 529–543.

68 E. H. J. Danen, P. Sonneveld, C. Brakebusch, R. Fässler and A. Sonnenberg, *J. Cell Biol.*, 2002, **159**, 1071–1086.

69 J. L. Coll, A. Ben-Ze'ev, R. M. Ezzell, J. L. Rodríguez Fernández, H. Baribault, R. G. Oshima and E. D. Adamson, *Proc. Natl. Acad. Sci. U. S. A.*, 1995, **92**, 9161–9165.

70 R. M. Saunders, M. R. Holt, L. Jennings, D. H. Sutton, I. L. Barsukov, A. Bobkov, R. C. Liddington, E. A. Adamson, G. A. Dunn and D. R. Critchley, *Eur. J. Cell Biol.*, 2006, **85**, 487–500.

71 V. Schaufler, H. Czichos-Medda, V. Hirschfeld-Warnecken, S. Neubauer, F. Rechenmacher, R. Medda, H. Kessler, B. Geiger, J. P. Spatz and E. A. Cavalcanti-Adam, *Cell Adhes. Migr.*, 2016, **10**, 505–515.

72 A. Sales, K. Ende, J. Diemer, A. R. Kyvik, J. Veciana, I. Ratera, R. Kemkemer, J. P. Spatz and J. Guasch, *ACS Omega*, 2019, **4**, 1791–1800.

73 H. Amani, H. Arzaghi, M. Bayandori, A. S. Dezfuli, H. Pazoki-Toroudi, A. Shafiee and L. Moradi, *Adv. Mater. Interfaces*, 2019, **6**, 1900572.

74 S. Huveneers, H. Truong, R. Fässler, A. Sonnenberg and E. H. J. Danen, *J. Cell Sci.*, 2008, **121**, 2452–2462.

75 X. K. Zhao, Y. Cheng, M. Liang Cheng, L. Yu, M. Mu, H. Li, Y. Liu, B. Zhang, Y. Yao, H. Guo, R. Wang and Q. Zhang, *Sci. Rep.*, 2016, **6**, 1–12.

76 A. P. Gilmore and L. H. Romer, *Mol. Biol. Cell*, 1996, 7, 1209–1224.

77 K. Katoh, *PeerJ*, 2017, **2017**, e4063.

78 C. Lawson and D. D. Schlaepfer, *Cell Adhes. Migr.*, 2012, **6**, 302–306.

79 D. K. Pettit, T. A. Horbett and A. S. Hoffman, *J. Biomed. Mater. Res.*, 1992, **26**, 1259–1275.

Daum R, Mrsic I et al., Supplementary data
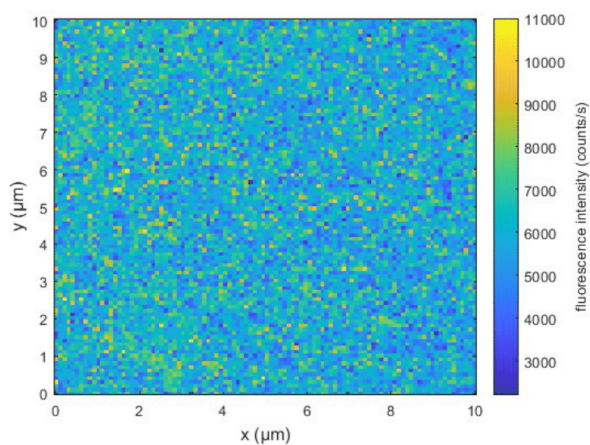Fibronectin adsorption on oxygen plasma-treated polyurethane surfaces modulates endothelial cell response

Supplementary data

Fibronectin adsorption on oxygen plasma-treated polyurethane surfaces modulates endothelial cell response

Ruben Daum[1,2,3§], Ivana Mrsic[4§], Johanna Hutterer[4], Achim Junginger[4], Svenja Hinderer[1], Alfred

J. Meixner[4,5], Günter Gauglitz[4], Thomas Chassé[4,5] and Katja Schenke-Layland[1,2,3,6,7] *

[1] NMI Natural and Medical Sciences Institute at the University of Tübingen, Markwiesenstr. 55, 72770 Reutlingen,

Germany

[2] Department of Women's Health, Research Institute for Women's Health, University of Tübingen, Silcherstr. 7/1,

72076 Tübingen, Germany

[3] Department of Bioengineering, University of Tübingen, Silcherstr. 7/1, 72076 Tübingen, Germany

[4] Institute of Physical and Theoretical Chemistry, University of Tübingen, Auf der Morgenstelle 18, 72076 Tübingen,

Germany

[5] Center for Light-Matter Interaction, Sensors & Analytics (LISA+) at the University of Tübingen, Auf der Morgenstelle

18, 72076 Tübingen, Germany

[6] Cluster of Excellence iFIT (EXC 2180) "Image-Guided and Functionally Instructed Tumor Therapies", University

of Tübingen, 72076 Tübingen, Germany

[7] Department of Medicine/Cardiology, Cardiovascular Research Laboratories, David Geffen School of Medicine at

UCLA, Los Angeles, CA 90095, USA

*Correspondence: katja.schenke-layland@uni-tuebingen.de; Tel.: +49-707-1298-5205; www.schenke-layland-

lab.de

§These authors contributed equally to this work

Supplementary Figure 1. XPS peak fit example of sample B (GP-FWHM = 1.205 eV; LP-FWHM = 0.42 eV; FWHM = 1.445 eV). Spectra were collected with 20 eV pass energy, 0.2 s dwell time, and 0.05 eV step size. The pink peaks represent the plasma generated functional groups, except C-O-C which is part of the polyurethane structure. The green peaks come from the polyurethane carbon groups (PU: O(O**C**)N at 289.6 eV; **C**–O(OC)N at 287.1 eV); C–O–C at 286.3 eV; O(OC)N–**C** at 285.8 eV; **C**–C at 285.1 eV; **C**=C at 284.7; plasma-induced: **C**–OH at 286.3 eV; –**C**=O at 287.7 eV; –**C**OOH at 288.8 eV).
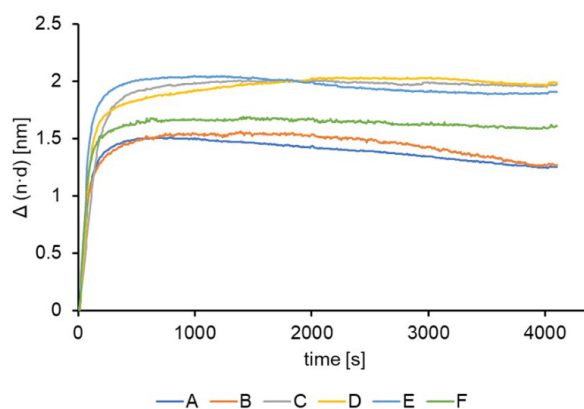
Supplementary Figure 2. Binding curves of 10 µg/ml fibronectin on surfaces A, B, C, D, E and F measured with Reflectometric Interference Spectroscopy.

Supplementary Figure 3. Exemplary laser confocal scanning microscopy image of DY-490 labeled FN coated on sample F. The samples showed homogeneous fluorescence signals. Pixel size is 100 nm.
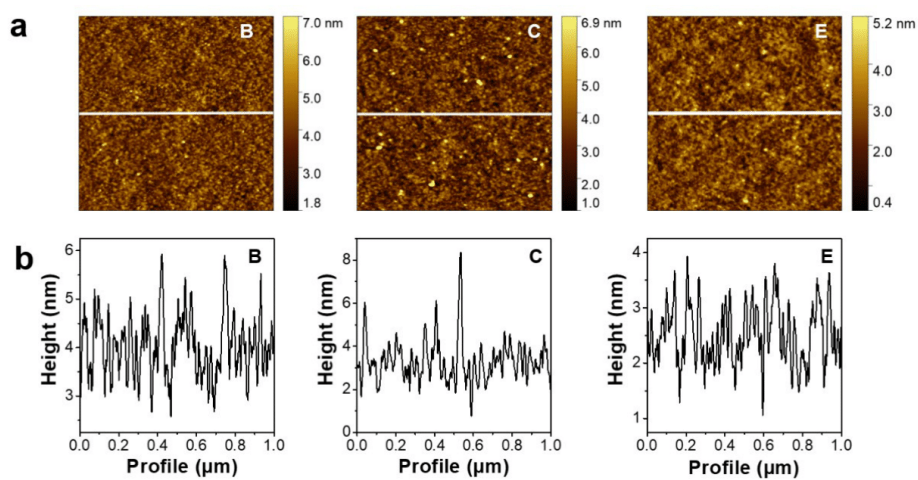
Supplementary Figure 4. AFM (**a**) height contrast images of plasma treated surfaces with FN coating. The white line represents the region of the extracted height profiles. (**b**) Extracted height profile lines of the FN-coated polymer surfaces showcasing the surface structuration.
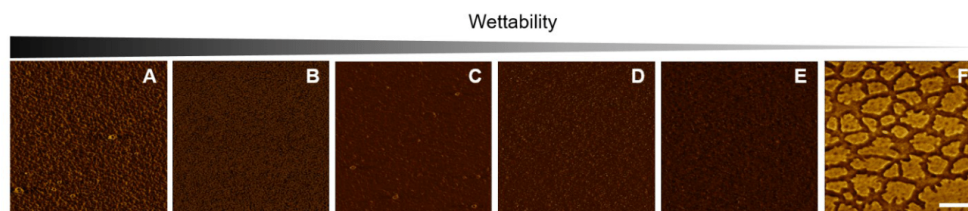
Supplementary Figure 5. AFM material contrast images of the sample surfaces after FN coating. The scale bar equals 200 nm.
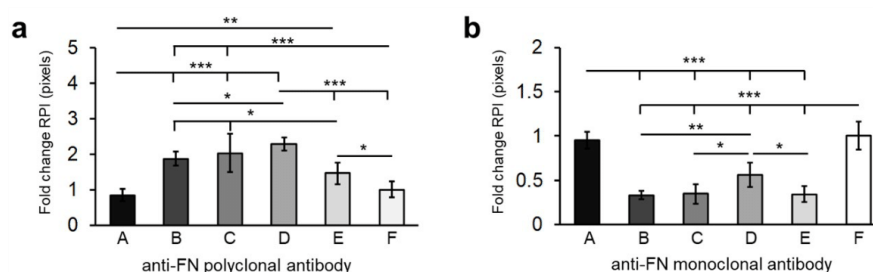
Supplementary Figure 6. (**a**) Semi-quantitative pixel intensity analysis of the polyclonal anti-FN immunofluorescence staining. Data is shown relative to surface F. (**b**) Monoclonal anti-FN immunofluorescence staining against the cell binding domain. Data is shown relative to surface F. One-way ANOVA, n=3, *p<0.05, **p<0.01, ***p<0.001; RPI = relative pixel intensity.
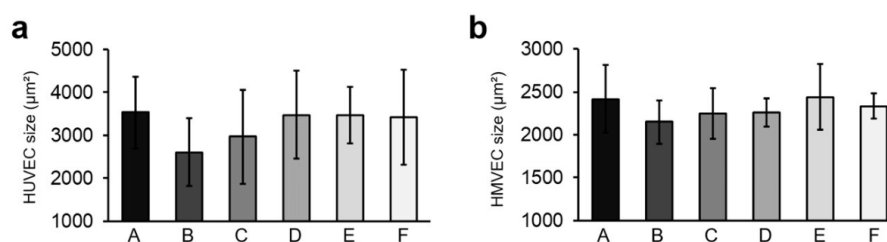
Supplementary Figure 7. The size of adherent (**a**) HUVECs and (**b**) HMVECs 24 h after cell seeding. Data is shown as change relative to F. n=3, no significant differences between the samples.
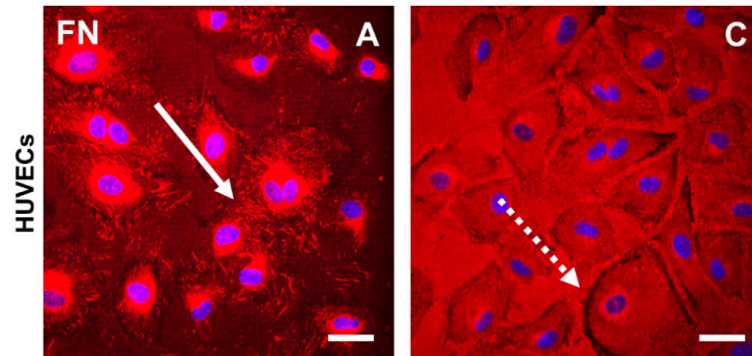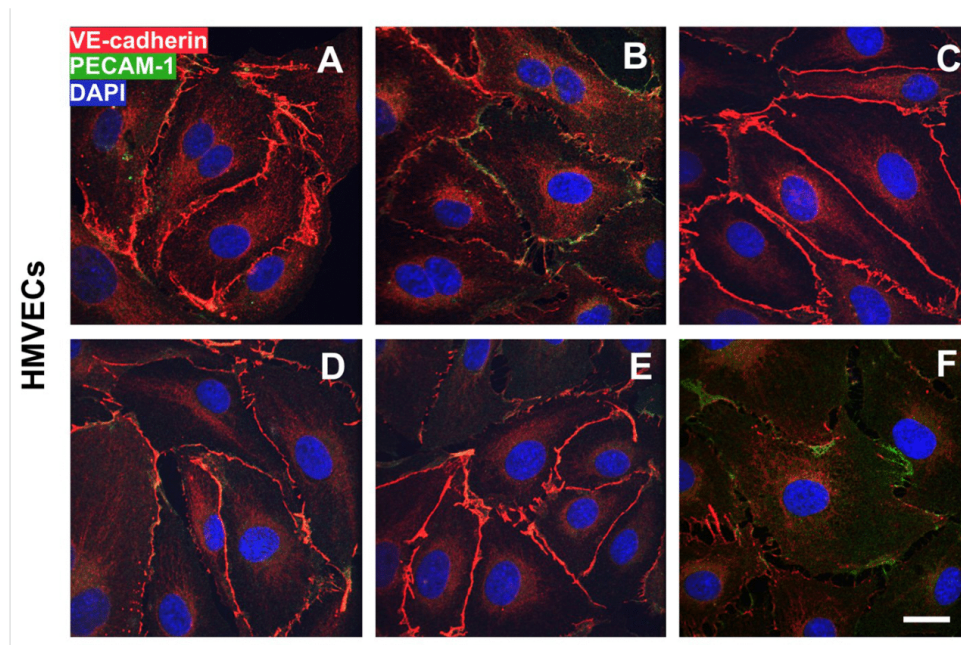
Supplementary Figure 8. Cell–fibronectin-interaction in HUVECs on surface A and C. Anti-FN immunofluorescence staining shows the interaction of HUVECs with the adsorbed FN, which is indicated by fibrillar structures (white arrow) and dark areas (white dotted arrow). Scale bars equal 100 µm.
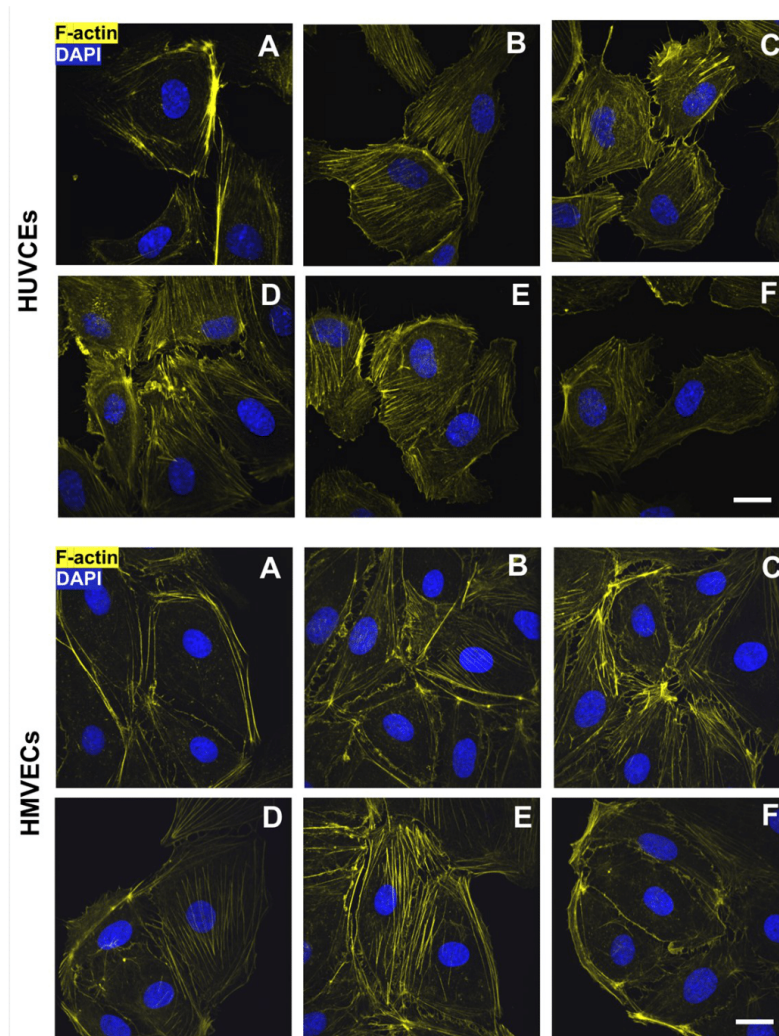
Supplementary Figure 9. F-actin staining of HUVECs and HMVECs on the different fibronectin-coated surfaces. Scale bars equal 20 μm.

Supplementary Figure 10. VE-cadherin and PECAM-1 immunofluorescence staining of HMVECs on the different fibronectin-coated surfaces. Scale bars equal 20 µm.

Supplementary Table 1. C 1s core level peak fit parameters for sample B. Full width at half maximum values were established from the urethane peak at 289.6 eV and kept constant for all peaks (GP-FWHM = 1.206 eV; LP-FWHM = 0.418 eV; FWHM = 1.445 eV)

Peak name	Peak position, eV	rel. Area, %
C-O-C/C-OH	286.32	22.15
-C=O	287.70	4.38
-COOH	288.73	2.26

Supplementary Table 2. Mean values, standard deviations and statistical analysis of contact angles from uncoated and FN-coated samples.

Sample	uncoated		FN-coated		uncoated versus FN-coated
	Mean	SD	Mean	SD	p-value*
A	17.5	1.9	45.0	2.0	$2.8*10^{-18}$
B	33.4	2.7	45.3	2.0	$1.3*10^{-9}$
C	48.2	0.6	57.2	2.3	$1.3*10^{-7}$
D	50.8	1.7	57.4	1.5	$5.2*10^{-6}$
E	54.3	1.0	58.7	2.1	0.00241
F	71.1	1.6	64.2	1.1	$1.0*10^{-5}$

* One-way ANOVA, n=3